天津大学
Tianjin University

多功能管状折纸超材料的机构设计与性能编程

Kinematic Design and Property Programmability of Multifunctional Tubular Origami Metamaterials

一级学科：工程力学

研究方向：折纸结构

作者姓名：李梦岳

指导教师：陈焱 教授

答辩时间	2025 年 05 月 07 日		
答辩委员会	姓名	职称	工作单位
主席	汪越胜	教授	天津大学
委员	陈常青	教授	清华大学
	魏国武	教授	英国索尔福德大学
	朱睿	教授	北京理工大学
	刘洋	副教授	天津大学

天津大学机械工程学院

二〇二六年五月

摘要

管状折纸结构及其衍生的超材料凭借其独特的几何构型与优异的空间折展性能，在先进工程结构设计中极具应用前景。然而，现有设计多受限于平面截面假设，缺乏针对空间多边形截面折纸管状结构的广义运动学综合理论，制约了折纸结构的构型创新。伴随着超材料从单一功能向多功能集成化的发展，其物理性能的可编程性研究显得尤为紧迫。然而，多功能超材料普遍面临着不同物理属性间相互耦合的制约，即难以在满足某一特定性能指标的同时，实现对另一类物理属性的独立编程。

针对上述构型设计的理论局限与多物理场性能耦合难题，本文聚焦于折纸超材料的运动学分析与多物理场性能编程研究，旨在建立一套从运动学综合到性能编程的完整设计方法。

在折纸机构学方面，建立了一套基于四折痕顶点的单自由度管状折纸结构运动学综合框架。推导了具有广义空间四边形截面管状结构的协调性条件，并将解析模型扩展至多顶点系统。在此基础上，构建了单、双、三通路折纸超材料，实现了从单一管状单元到复杂空间超材料的系统化设计。

在单通路折纸超材料方面，系统研究了折痕图案的山谷线分布对超材料多物理场性能的影响。通过构建一系列具有不同空间构型的折纸单元，揭示了山谷线排布对几何形态、力学性能及声学特性的影响，验证了山谷线分布是实现超材料性能编程的关键设计维度。

在双通路折纸超材料方面，通过建立设计参数、初始折叠状态与物理响应之间的非唯一映射关系，实现了在保持力学刚度或声学带隙恒定的前提下，对另一物理属性进行大幅独立编程。此外，基于热塑性聚合物验证了通过热机械重构实现性能调控的可行性。

在三通路折纸超材料方面，所构建的结构在三个正交方向上表现出各向异性力学性能。研究揭示了其在正交方向上截然不同的变形机理，并阐明了设计角与初始折叠角对性能的非线性影响，从而实现了单一结构中多种力学机制的集成。

本文围绕多功能管状折纸超材料的机构设计与性能编程，构建了从广义运动学综合、性能机理揭示到多物理场性能编程的完整设计方法。不仅突破了传统管状折纸的几何束缚，也为实现超材料在多物理场中的按需定制提供了技术支撑。

关键词：刚性折纸；折纸超材料；管状折纸结构；多物理场性能编程

ABSTRACT

Tubular origami structures and their derived metamaterials hold significant promise for advanced engineering applications due to their unique geometric configurations and excellent spatial deployability. However, existing designs are often constrained by the assumption of planar cross-sections. The lack of a generalized kinematic synthesis framework for tubular structures with spatial polygonal cross-sections severely limits configurational innovation. As metamaterials evolve from single functionality to multifunctional integration, investigating the programmability of their physical properties becomes increasingly urgent. Nevertheless, multifunctional metamaterials are universally challenged by strong coupling between different physical properties; specifically, it remains difficult to independently program one target property without affecting others.

To address these theoretical limitations in structural design and the challenges of multiphysical coupling, this dissertation focuses on the kinematic analysis and multiphysical property programming of origami metamaterials, aiming to establish a comprehensive design methodology extending from kinematic synthesis to performance programming.

In terms of origami mechanisms, a generalized kinematic synthesis framework for single-DOF tubular origami structures based on 4-crease vertices is established. Compatibility conditions for tubular structures with generalized spatial quadrilateral cross-sections are derived, and the analytical model is extended to multi-vertex systems. On this basis, single-, double-, and triple-tubular origami metamaterials are constructed, enabling systematic design from individual tubular units to complex spatial metamaterials.

For single-tubular origami metamaterials, the effects of mountain-valley crease assignments on the multiphysical properties are systematically investigated. By constructing a series of structures with distinct spatial configurations, the effects of crease assignments on geometric, mechanical, and acoustic properties are revealed. These findings confirm that the crease assignment serves as a key design dimension for programmable metamaterial performance.

For double-tubular origami metamaterials, a non-unique mapping between design parameters, initial folding states, and physical responses enables substantial independent programming of one physical property while maintaining constant mechanical stiffness or acoustic bandgaps. Experimental validation using thermoplastic polymers further demonstrates that performance can be tuned through thermo-mechanical reconfiguration.

For triple-tubular origami metamaterials, the constructed structures exhibit anisotropic mechanical performance along three orthogonal directions. The distinct deformation mechanisms along these directions are revealed. Moreover, the nonlinear relationships between the anisotropic performance and both the design angles and initial folding angles are clarified. These characteristics enable the integration of multiple mechanical mechanisms within a single structure.

In summary, focusing on the kinematic design and property programmability of multifunctional tubular origami metamaterials, this dissertation constructs a comprehensive design methodology covering generalized kinematic synthesis, performance mechanism investigation, and multiphysical programming. This work not only breaks through the geometric constraints of traditional tubular origami but also provides a solid foundation for the on-demand customization of metamaterials across multiphysical fields.

KEY WORDS: Rigid origami; Origami metamaterials; Tubular origami structures; Multiphysical performance programming

Contents

List of Figures

List of Tables

Notation

Nomenclature

a, b, c, h, l	Side lengths of the origami panels
$a_{i(i+1)}$	Link lengths of linkages between joint i and joint i+1
l_x, l_y, l_z	Geometric dimensions of the double-tubular origami unit
$l^{K(K+1)}$	Length of the link connecting vertices K and K+1
$\boldsymbol{L}^{IJ}$	Link vector directed from vertex I to vertex J
L_x, L_y, L_z	Geometric dimensions of the double-tubular origami metamaterial
w, h, l	Geometric dimensions in the x, y, and z directions of the double-corrugated unit and the triple-tubular unit
W, H, L	Geometric dimensions in the x, y, and z directions of the double-corrugated metamaterial and the triple-tubular metamaterial
v_{xy}, v_{xz}	The Poisson's ratios in different directions
v	The Poisson's ratio of the material
x_i, y_i, z_i	x, y, z coordinate axes of system i
t	Thickness of the origami panels
E	Young's module
F	Force
$\boldsymbol{T}_{\mathrm{U}}^{(K+1)K}$	Transformation from the coordinate frame $\{ x_2^{K+1},\ z_2^{K+1}\}$ to $\{ x_2^{K},\ z_2^{K} \}$ in the upper part
$\boldsymbol{T}_{\mathrm{L}}^{K(K+1)}$	Transformation from the coordinate frame $\{ x_4^{K},\ z_4^{K} \}$ to $\{ x_4^{K+1},\ z_4^{K+1}\}$ in the lower part
$\boldsymbol{R}_x$	The rotation matrix about the x axis
$\boldsymbol{R}z$	The rotation matrix about the z axis
$\boldsymbol{T}_z$	The translation matrix along the z axis
$\boldsymbol{Q}_{(i+1)i}$	3×3 transformation matrix from the i th coordinate system to the i+1 th coordinate system

$\boldsymbol{T}_{(i+1)i}$	4×4 transformation matrix from the i th coordinate system to the i+1 th coordinate system

Greek Alphabets

α, β	The interior angles of a parallelogram
$\alpha_{i(i+1)}$	Twist angle of link i(i+1) between joints i and i+1 o
$\varphi_i, \theta_i, \delta_i, \varepsilon_i, \gamma_i$	Dihedral angles between panels
η_i	Line angle of two origami panels
σ_y	Yield stress
σ_u	Ultimate stress
ε_u	Ultimate strain
σ_0	Plastic flow stress
λ	The coefficient representing non-uniform deformation during multi-layer honeycomb buckling
σ	Stress
ε	Strain

Abbreviations

2D	Two dimensional
3D	Three dimensional
4D	Four dimensional
DOF	Degree of freedom
D-H	Denavit-Hartenberg
SVD	Singular value decomposition
M-V	Mountain-valley
ZCH	Zigzag unit cell with hole
TMP	Tachi-Miura polyhedron
FE	Finite element
PEEQ	Equivalent plastic strain
SEA	Specific energy absorption

IBZ	Irreducible Brillouin zone
TL	Transmission loss
TPU	Thermoplastic polyurethanes
ABS	Acrylonitrile butadiene styrene
PLA	Polylactic acid
LCE	Liquid crystal elastomer
SMP	Shape memory polymers
PDMS	Polydimethylsiloxane
PVA	Polyvinyl alcohol

Chapter 1 Introduction

1.1 Background and Significance

Metamaterials are artificial structures rationally designed to exhibit extraordinary properties that transcend the limits of their constituent natural materials. Unlike conventional materials, whose properties are derived primarily from their chemical composition and microscopic lattice structure, the macroscopic behavior of metamaterials is governed by the geometric arrangement of their internal architectures. Since the initial conceptualization[1], metamaterials have garnered significant attention across various disciplines due to their unprecedented capabilities in manipulating physical fields. In the domains of electromagnetics, optics, and acoustics, metamaterials have enabled revolutionary applications such as invisibility cloaks[2], super-resolution imaging[3], and sound absorption[4]. Extending the scope of metamaterial design, the concept of structure-property mapping has been applied to the regime of static and dynamic mechanics, giving rise to the field of mechanical metamaterials.

Mechanical metamaterials represent a distinct class of structural materials designed to achieve unusual mechanical responses through the topology optimization of their unit cells[5,6]. By tailoring the geometry, connectivity, and hierarchy of the microstructures, these materials can exhibit unique mechanical characteristics that are counterintuitive or impossible to achieve with standard solids. Prominent examples include negative Poisson's ratio[7,8], multi-stability[9,10], and mechanical logical gate[11,12]. At the same time, these excellent mechanical properties also pave the way for their applications in various fields, such as energy storage[13], biomedical[14], acoustics[15,16], optics[17], thermal management[18,19], flexible electronics[20,21], etc.

To realize these complex mechanical responses, origami—the ancient art of paper folding—has emerged as a powerful platform for designing mechanical metamaterials. Origami offers a unique geometric approach to transforming two-dimensional (2D) sheets into complex three-dimensional (3D) structures with continuous folding motions. By treating the crease patterns as bars and linkages, origami structures can be designed to possess programmable mechanical properties, ranging from rigid-foldable mechanisms to deformable compliant structures. This geometric versatility has been extensively explored in many areas, including sound absorption[22], vibration control[23], thermal conductivity[24], energy absorbers[25–27], and so on, as shown in Fig. 1-1.

However, the design of complex origami assemblies is often impeded by the challenge of satisfying rigid foldability constraints without relying on restrictive geometric assumptions, such as the requirement for co-planar cross-sections, inevitably excluding a wide range of valid geometries. Consequently, there remains a critical need for a generalized framework capable of systematically solving compatibility conditions for complex origami patterns without reliance on restrictive geometric constraints.

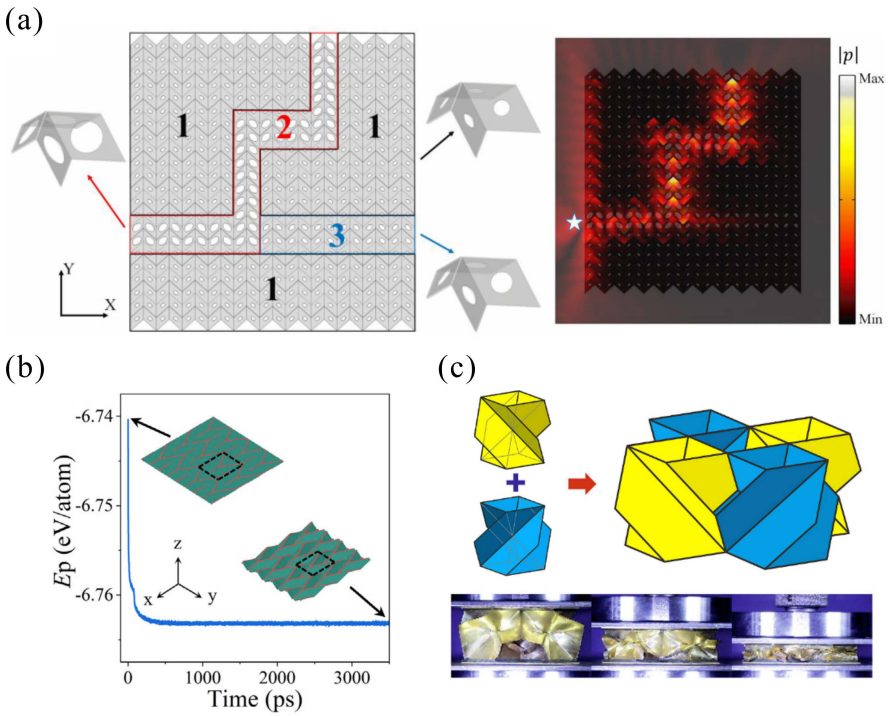

Fig. 1-1 Applications of origami structures in various fields. (a) The pre-folded Miura-ori capable of programmable acoustic waveguides[22]; (b) the origami metamaterial with tunable thermal conductivity[24]; (c) a sandwich structure with a foldcore for energy absorption[27].

Although origami and other topological designs have achieved success in specific mechanical domains, modern engineering applications, such as aerospace deployable structures and soft robotics, are increasingly demanding materials that offer multifunctional integration. Consequently, research is shifting from optimizing single physical properties to developing multifunctional metamaterials that provide versatile cross-domain capabilities, such as combining energy absorption with sound insulation[28,29], or thermal expansion and phononic bandgap properties[30–32]. However, the advancement of such integrated systems is currently impeded by a fundamental limitation: the absence of independent programmability in existing multifunctional

metamaterials. Because diverse physical responses are typically governed by the same set of shared design variables, altering a structure to achieve a target performance in one domain almost inevitably induces unintended variations in others. This mutually restrictive nature severely limits the precise and independent tailoring of specific functionalities. As a result, the design process often transforms into inefficient "trial-and-error" iterations, restricting the on-demand development of intelligent integrated systems.

Therefore, the exploration of novel origami structural designs, systematic programming frameworks, and strategies for independent programming can pave the way for the development of multifunctional origami metamaterials. This research not only holds significant value in advancing the configuration synthesis and performance characterization of origami structures but also facilitates their implementation in critical engineering applications, such as adaptive aerospace structures, soft robotics, and intelligent devices.

1.2 Literature Review

1.2.1 Kinematic Theory

To systematically analyze the motion of spatial mechanisms and origami structures, a variety of mathematical modeling techniques have been established, each with distinct advantages and limitations depending on the complexity of the target structure, such as the vector method[33], the quaternion method[34], screw theory[35–37], truss method[38,39], and the SVD method[40–42]. Among these frameworks, the matrix-based method (Denavit-Hartenberg notation) stands out for its capability to simultaneously account for the mechanism's topology and geometric parameters. Its primary advantage lies in its ability to determine the DOF and, more importantly, derive accurate analytical solutions for the full-period motion[43]. Consequently, the D-H notation is widely adopted for the design and analysis of rigid origami, thick-panel origami, and modular origami structures. As schematically illustrated in Fig. 1-2, this notation provides a notation for attaching a local coordinate frame to each link in a kinematic chain and describing the transformation between adjacent frames using homogeneous transformation matrices.

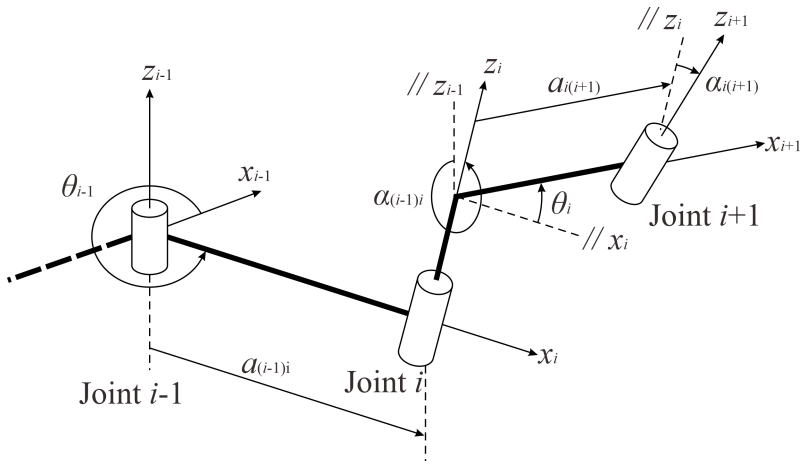

Fig. 1-2 The D-H notation of adjacent links connected by revolute joints.

The D-H method uniquely defines the spatial relationship between two adjacent links using four geometric parameters, which are defined based on the common normal between the joint axes, as shown in Fig. 1-2. The z_i axis aligns with the rotational axis of the ith revolute joint. The x_i axis is established as the common normal between z_{i-1} and z_i. The twist angle $\alpha_{i(i+1)}$ denotes the rotation from z_i to z_{i+1} about the x_{i+1} axis. The joint angle θ_i describes the rotation from x_i to x_{i+1} about the z_i axis. The parameter $a_{i(i+1)}$ represents the shortest distance between z_i and z_{i+1} along their common normal. The offset distance R_i corresponds to the displacement between x_i and x_{i+1} along the z_i axis. Based on these definitions, the general homogeneous transformation matrix $\boldsymbol{T}_{(i+1)i}$ describing the relative pose between adjacent coordinate frames is given by:

$$\boldsymbol{T}_{(i+1)i}=\begin{bmatrix}\cos\theta_i & -\sin\theta_i\cos\alpha_{i(i+1)} & \sin\theta_i\sin\alpha_{i(i+1)} & a_{i(i+1)}\cos\theta_i\\ \sin\theta_i & \cos\theta_i\cos\alpha_{i(i+1)} & -\cos\theta_i\sin\alpha_{i(i+1)} & a_{i(i+1)}\sin\theta_i\\ 0 & \sin\alpha_{i(i+1)} & \cos\alpha_{i(i+1)} & R_i\\ 0 & 0 & 0 & 1\end{bmatrix}, \tag{1-1}$$

which transforms the kinematic representations from the (i+1)th coordinate system to the ith system, and when i+1>n, it is replaced by 1. For closed-loop linkages comprising n links, the kinematic closure equation is derived through matrix transformation analysis of consecutive joint coordinate

$$\boldsymbol{T}_{21}\cdot\boldsymbol{T}_{32}\cdots\boldsymbol{T}_{n(n-1)}\cdot\boldsymbol{T}_{1n}=\mathbf{I}_4, \tag{1-2}$$

A specific and significant class of spatial mechanisms is the spherical linkage, with the spherical 4R linkage shown in Fig. 1-3 serving as a representative example. In this

mechanism, the axes of all four revolute joints intersect at a single point, known as the mechanism center. Due to this geometric concentricity, the linear dimensions associated with the link geometry naturally vanish; specifically, both the link length $a_{i(i+1)}$ and the link offset R_i become zero. Under these conditions, the translation components in the last column of the general matrix are eliminated, and the matrix degenerates into a pure rotation form. The kinematic transformation is thus solely governed by the two angular parameters: the link twist $\alpha_{i(i+1)}$ (representing the fixed angle between joint axes) and the joint angle θ_i (the variable governing motion). The simplified transformation matrix for a spherical link is expressed as:

$$\boldsymbol{Q}_{(i+1)i} = \begin{bmatrix} \cos\theta_i & -\cos\alpha_{i(i+1)}\sin\theta_i & \sin\alpha_{i(i+1)}\sin\theta_i \\ \sin\theta_i & \cos\alpha_{i(i+1)}\cos\theta_i & -\sin\alpha_{i(i+1)}\cos\theta_i \\ 0 & \sin\alpha_{i(i+1)} & \cos\alpha_{i(i+1)} \end{bmatrix}, \tag{1-3}$$

which transforms the coordinates from the (i+1)th system to the ith system through pure rotations about z_i axis by angle θ_i. And the general closure equation in Eq. (1-2) simplifies to

$$\boldsymbol{Q}_{21}\cdot\boldsymbol{Q}_{32}\cdot\boldsymbol{Q}_{43}\cdot\boldsymbol{Q}_{14} = \mathbf{I}_3. \tag{1-4}$$

For spherical 4R systems, the cyclic condition requires i+1 is replaced by 1 when i+1=5. By solving this matrix equation, the implicit or explicit relationships between the input and output joint angles can be derived, providing the rigorous mathematical basis for the configuration analysis and synthesis of complex spatial mechanisms.

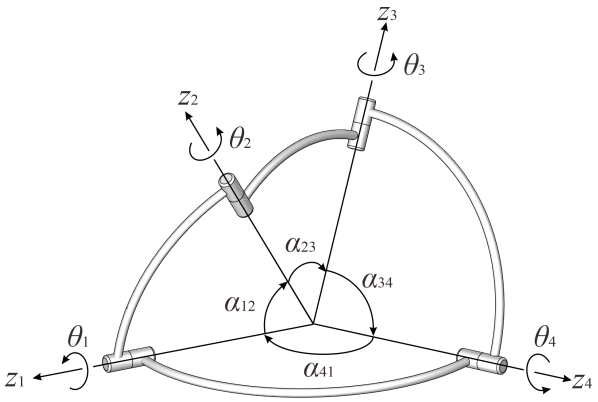

Fig. 1-3 A spherical 4R linkage.

1.2.2 Rigid Origami

Rigid origami, a pivotal subset of origami engineering, refers to a kinematic idealization where the material surfaces (facets) are modeled as infinitely rigid plates

that rotate about hinge-like creases without any stretching, bending, or shearing deformation. Unlike conventional compliant mechanisms that rely on material elasticity, the macroscopic deformation of rigid origami is governed solely by the geometric compatibility of its crease patterns. This rigid-foldability hypothesis transforms the continuous deformation problem into a mechanism analysis problem, allowing complex folding behaviors to be described using the kinematic theory of spatial linkages.

1.2.2.1 Rigid Foldability and Flat-Foldability of Origami Pattern

The assessment of rigid foldability in large-scale origami tessellations is predicated on the fundamental kinematic analysis of individual vertex. By abstracting a crease vertex into a spherical linkage system, wherein rigid sectors function as links and creases as concurrent revolute joints[44], as shown in Fig. 1-4, the problem is transposed into the domain of spatial mechanism theory. Guided by this kinematic relationship, a spectrum of analytical and numerical frameworks has been synthesized to elucidate folding mechanics. Initial theoretical contributions utilized rotation vector algebra and quaternions to derive loop closure constraints[34]. These were complemented by screw theory approaches, which proved effective in categorizing kinematic traits governed by symmetry[45]. In terms of computational modeling, techniques such as SVD[46] and the vector geometry[47] have been widely adopted to simulate kinematic trajectories and identify singularity bifurcations in general *n*-crease vertices.

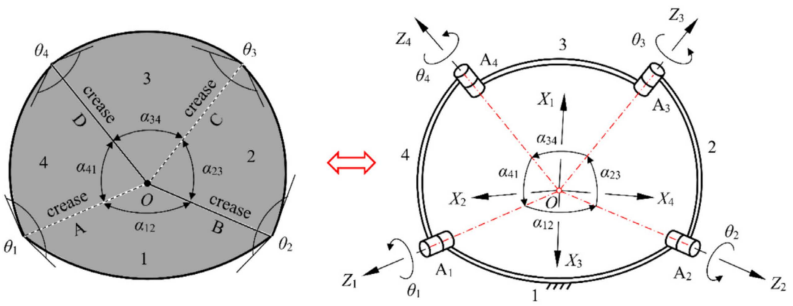

Fig. 1-4 A 4-crease origami vertex and its equivalent spherical 4*R* linkage[44].

Among the diverse analytical frameworks, the matrix-based method utilizing D-H notation distinguishes itself through its exceptional versatility[43]. Unlike purely geometric or numerical approaches, this method establishes a unified algebraic framework that seamlessly bridges the analysis of individual vertices and global

tessellations. For the fundamental vertex unit, it derives general explicit analytical solutions by solving the loop closure equations of the equivalent spherical linkage, thereby providing precise kinematic relationships between dihedral angles[44]. Crucially, this capability extends to complex multi-vertex systems, where the entire crease pattern is modeled as a network of interconnected spherical mechanisms. By integrating kinematic formulas with motion path transmission strategies, this approach systematically resolves the single-DOF compatibility conditions for the global network[48], facilitating the rational design of novel rigid origami patterns without reliance on trial-and-error approximations.

Beyond the study of rigid foldability, the property of flat-foldability, defined as the capacity of an origami structure to fully fold into a compact 2D state, remains a critical attribute in both theoretical mechanics and practical engineering applications. To determine the flat-foldability of a *n*-crease vertex, three fundamental geometric and topological conditions are widely recognized:

(1) The Kawasaki-Justin Theorem[49]: Governing geometric compatibility, this theorem necessitates that the alternating sum of sector angles around a flat-foldable vertex must be zero; equivalently, the sum of odd-numbered angles must equal that of even-numbered angles, summing to π.

(2) The Maekawa-Justin Theorem[50]: Addressing topological validity, this theorem states that the difference between the number of mountain (M) and valley (V) folds at a flat-foldable interior vertex must be two, expressed as $|M - V| = 2$.

(3) The Big-Little-Big Angle Theorem[51]: This rule assumes that a sector angle strictly smaller than its two neighbors must be bounded by creases of opposite parities. Consequently, the two creases enclosing the minimal sector angle at any vertex must strictly consist of one mountain and one valley fold.

1.2.2.2 Classic Origami Patterns

The advancement of rigid origami has been significantly driven by the identification and mathematical characterization of specific crease patterns that exhibit distinct kinematic behaviors. Over the past few decades, a rich variety of classic patterns have been established, serving as the fundamental building blocks for designing deployable structures and mechanical metamaterials. Unlike random folds, these classic patterns are distinguished by their periodic tessellations and predictable

DOF, allowing them to transform planar sheets into complex 3D configurations with tailored mechanical properties, such as negative Poisson's ratio[52–56], multistability[57–60], and programmable stiffness[61–63]. These patterns not only provide diverse geometric solutions for spatial packaging but also function as the essential unit cells for programming advanced mechanical responses.

The 4-crease vertex constitutes the fundamental building block of rigid origami. Its geometric configuration is defined by four sector angles, denoted as α_1, α_2, α_3, α_4, surrounding a central intersection point, as shown in Fig. 1-5(a). Depending on the specific constraints imposed on these angular parameters, this generalized vertex can evolve into a variety of distinct kinematic families. When the sum of alternating sector angles is supplementary, i.e., $\alpha_1+\alpha_3=\alpha_2+\alpha_4=\pi$, the structure satisfies the Kawasaki-Justin theorem and forms a flat-foldable vertex, also known as the double-corrugated vertex[48], as shown in Fig. 1-5(b).

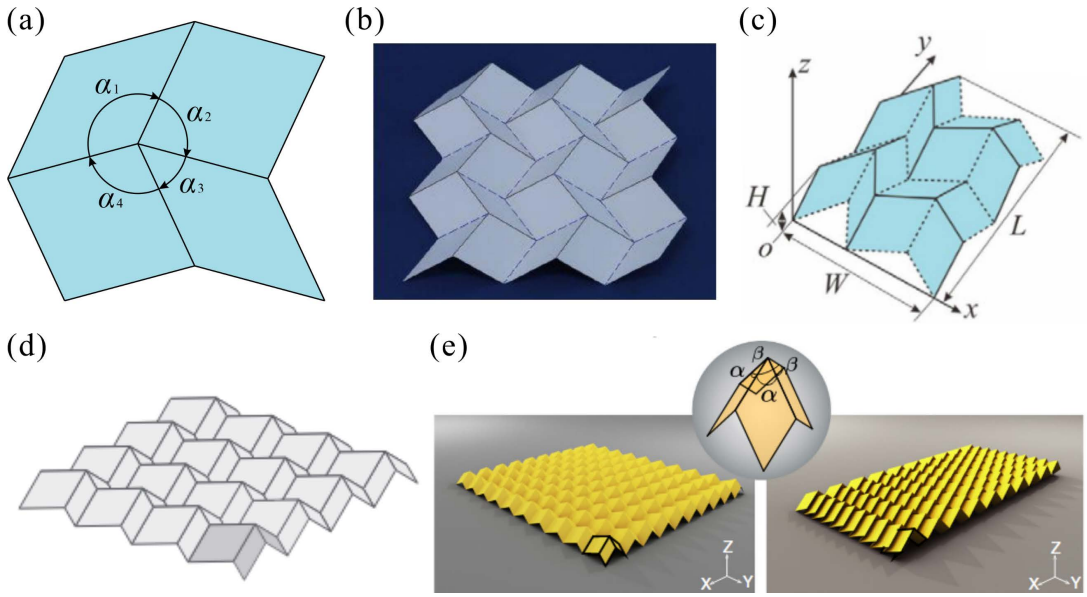

Fig. 1-5 The 4-crease vertex origami. (a) General 4-crease vertex origami with different sector angles; (b) the flat-foldable 4-crease vertex origami[48]; (c) the in-plane graded Miura-ori[64]; (d) the Miura-ori[65]; (e) eggbox origami[54].

Alternatively, if the constraints are altered such that adjacent angle pairs sum to π, i.e., $\alpha_1+\alpha_2=\alpha_3+\alpha_4=\pi$, the vertex forms the basis of the in-plane graded Miura pattern[64], as shown in Fig. 1-5(c). The classical Miura-ori pattern[65] emerges as a highly symmetric subset of the flat-foldable family. It must satisfy not only the flat-foldability

condition ($\alpha_1+\alpha_3=\alpha_2+\alpha_4=\pi$) but also the additional symmetry constraints of $\alpha_1=\alpha_4$ and $\alpha_2=\alpha_3$, as shown in Fig. 1-5(d). Beyond the realm of flat sheets lies the domain of non-Euclidean origami, characterized by a sector angle sum that deviates from 2π ($\alpha_1+\alpha_2+\alpha_3+\alpha_4\neq2\pi$). A quintessential representative of this class is the eggbox pattern[54], which is inherently not flat-deployable, as shown in Fig. 1-5(e).

The configuration of M-V folds serves as a determinant factor governing the folding mechanics of crease patterns, particularly within mechanism networks composed of interconnected vertices. Focusing on the double-corrugated pattern, Peng et al.[48] employed the D-H matrix method to model the kinematics of individual units. By extending this analysis to the network level, they systematically evaluated the rigid foldability of tessellations under various fold orientations, ultimately identifying a series of valid M-V assignment schemes that ensure structural rigidity, as shown in Fig. 1-6(a).

Parallel to these investigations, the origami twist family, characterized by a central polygon surrounded by parallel crease sets, has attracted significant research interest. For triangular twist variants, Feng et al.[66] synthesized kinematic compatibility conditions with flat-foldability criteria to exhaustively derive all feasible M-V assignments, as presented in Fig. 1-6(b), thereby establishing a complete theoretical library of folding modes for this geometry. In the case of square-twist patterns, foundational work by Hull et al. [67] utilized flat-foldability theory to isolate sixteen potential M-V distributions. By accounting for rotational and mirror symmetries, these redundant states were elegantly reduced to four classic, distinct configurations. Subsequent kinematic analysis by Ma et al.[68] classified these topologies into two rigid-foldable variants (Fig. 1-6(c)) and two non-rigid modes (Fig. 1-6(d)). Further advancing this domain, Feng et al.[69] demonstrated that non-rigid square twists could be converted into rigid mechanisms through the strategic introduction of auxiliary creases, as shown in Fig. 1-6(e). This research not only unveiled the kinematic bifurcation behaviors of the modified structures but also established an effective methodology for transforming non-rigid origami into rigid systems.

Building upon the principles established for simpler polygons, recent studies have expanded this modification strategy to more complex hexagonal geometries. Wei et al.[70] systematically constructed hexagonal twist patterns possessing distinct DOF, ranging from one to three, by selectively introducing auxiliary fold lines, as shown in

Fig. 1-7(a). Furthermore, by tessellating these modified units, they successfully synthesized a novel class of hexagonal twist networks that maintain a single-DOF, as shown in Fig. 1-7(b).

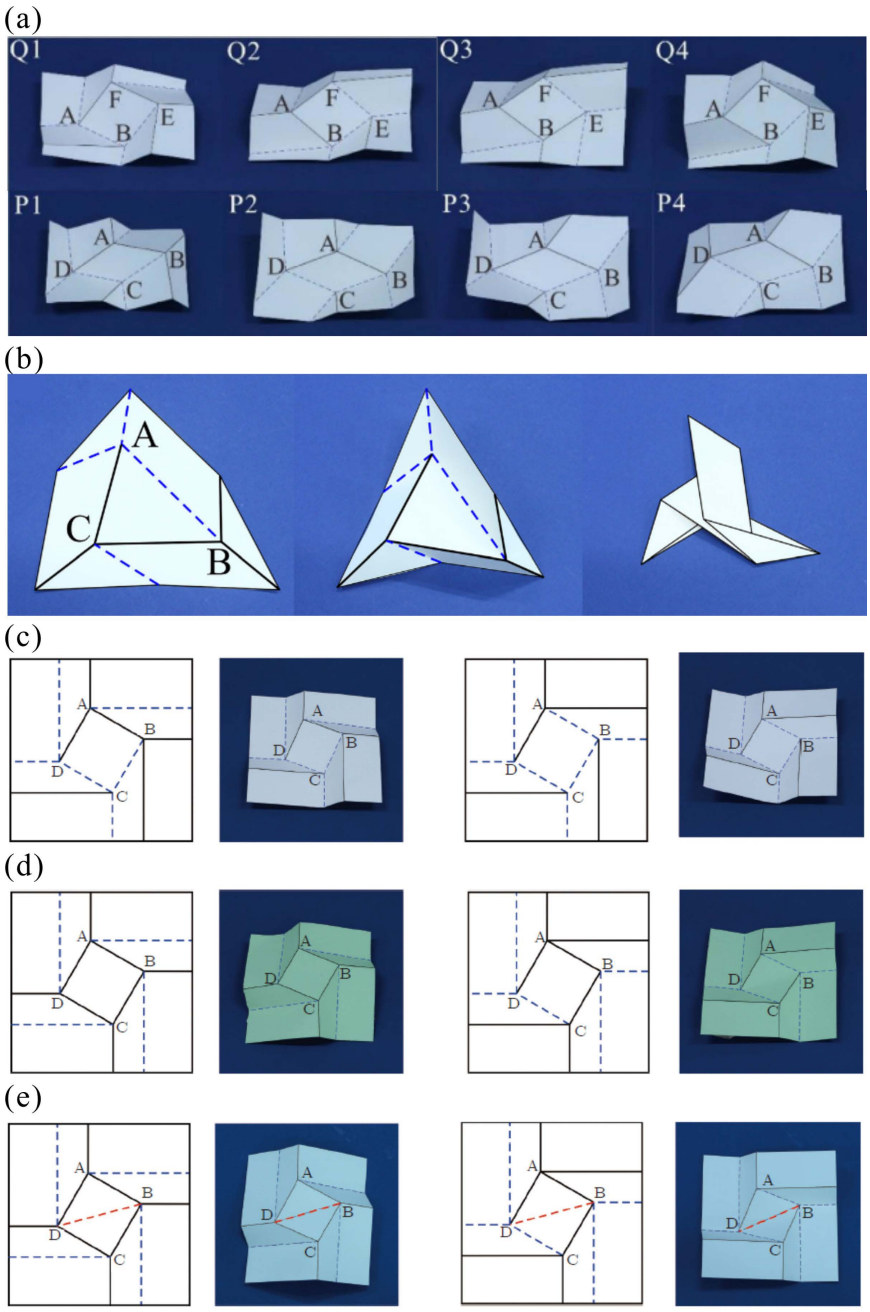

Fig. 1-6 Rigid foldability analysis and M-V assignments of representative origami patterns. (a) Valid M-V assignment schemes for the rigid double-corrugated pattern[48]; (b) the triangular twist pattern[66]; (c) two rigid-foldable variants of the square-twist pattern[68]; (d) two non-rigid variants of the square-twist pattern[68]; (e) rigid-foldable square twist converted from non-rigid variants via auxiliary creases[69].

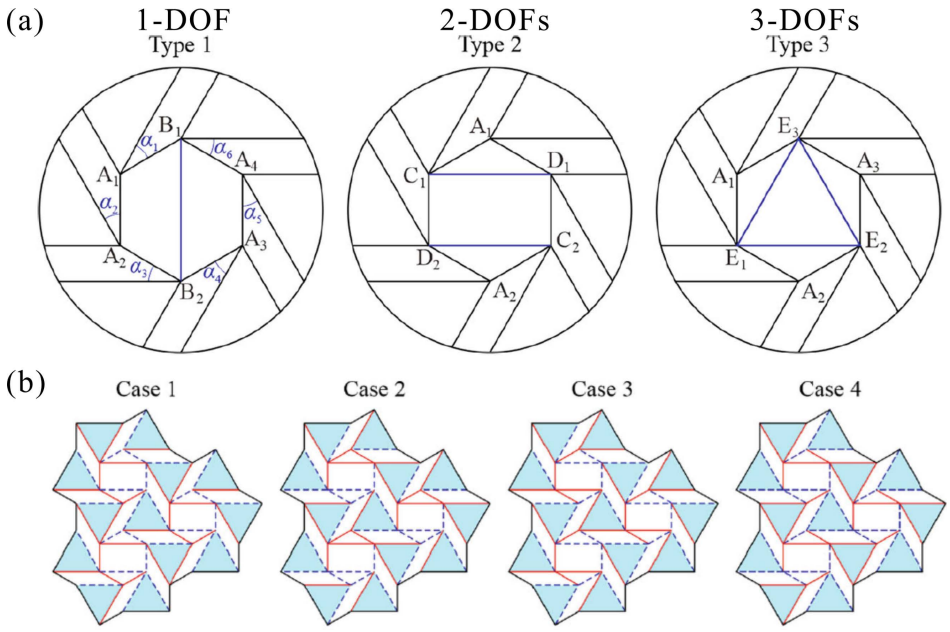

Fig. 1-7 Construction of variable-DOF hexagonal twist patterns and rigid tessellations via auxiliary creases. (a) Hexagonal twist units with distinct DOFs (ranging from 1 to 3) constructed by selective auxiliary fold lines; (b) single-DOF hexagonal twist tessellation networks.[70]

Origami tessellations composed of 6-crease vertices, such as the Resch pattern (Fig. 1-8(a))[71], the Waterbomb pattern (Fig. 1-8(b))[72], and the Yoshimura (diamond) pattern (Fig. 1-8(c))[73], are fundamentally distinct from 4-crease systems. These patterns possess multiple DOFs, giving them versatile structural deformability and diverse shape-shifting modes. Consequently, they have found extensive utility in engineering domains requiring shape adaptability, including energy-absorbing structures[74,75], deployable medical devices[76], soft robotics[77,78], and architecture[79]. However, this kinematic flexibility inevitably renders their analytical modeling significantly more intricate. In addition to kinematic methods employed to resolve motion compatibility conditions[80], numerical simulation algorithms, such as truss-equivalent models[81] and the finite particle method[82], have also been extensively applied to characterize the behavior of these multi-DOF patterns. Furthermore, to specifically address the analytical complexity of high-degree vertices, Zhang et al.[73] proposed an innovative vertex splitting methodology. This approach virtually decomposes a single 6-crease vertex into two coupled 4-crease or 5-crease sub-units. By enforcing constrained associations between these split nodes, the method effectively reduces the DOF of the analytical model while rigorously preserving the kinematic

equivalence of the original pattern, thereby providing a streamlined framework for analyzing complex folding paths.

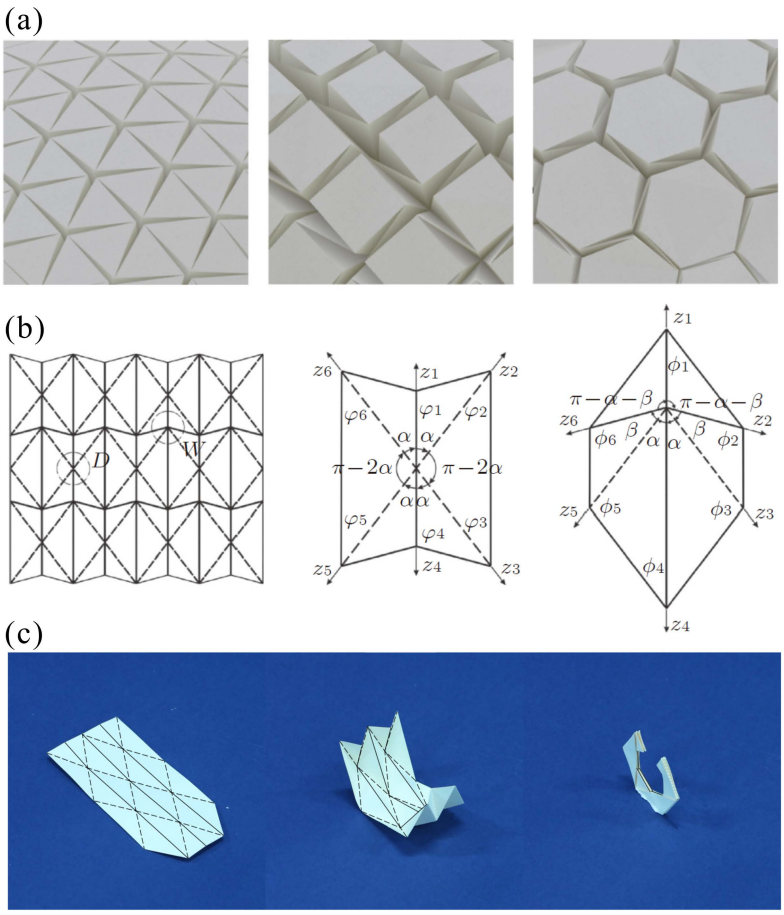

Fig. 1-8 Representative multi-DOF origami patterns composed of 6-crease vertices. (a) Resch patterns with diverse tessellation geometries: triangular, quadrilateral, and hexagonal configurations[71]; (b) Waterbomb origami pattern[72]; (c) Yoshimura (diamond) pattern[73].

1.2.2.3 Tubular Origami Structures

Tubular origami structures constitute a pivotal class of deployable systems that transform flexible sheets into volumetric deployable elements through topological closure. Unlike open planar tessellations, these structures are defined by a closed cross-sectional geometry. From the perspective of construction, origami tubes are generally realized through two distinct methodologies: the first involves enforcing cylindrical closure constraints on a single continuous crease pattern to form a seamless shell with open ends, while the second relies on the assembly and coupling of multiple origami

strips or panels to create a polygonal enclosure. This structural versatility allows origami tubes to serve as fundamental unit cells for cellular metamaterials, enabling the development of lightweight, reconfigurable systems that balance substantial volume reduction with high structural rigidity.

In tubular origami, extensive research has focused on complex kinematic structures, primarily categorized into multi-DOF patterns and non-rigid systems. For instance, the Waterbomb tube[80] exhibits highly versatile multi-DOF deployment. Meanwhile, non-rigid systems like the Yoshimura[83] and Kresling[84,85] rely heavily on the physical bending or stretching of constituent panels rather than pure hinge rotation. These multi-DOF and non-rigid structures are frequently investigated for their unique functional behaviors, particularly in energy absorption and multistability.

In contrast to these systems, single-DOF rigid tubular structures are characterized by their strict flat-foldability and diverse cross-sectional possibilities. The design of such structures demands rigorous adherence to kinematic compatibility conditions. Tachi et al.[86] pioneered a design methodology for single-DOF flat-foldable tubes, realizing configurations with various cross-sections, including quadrilateral and hexagonal forms, as shown in Fig. 1-9(a). Building on kinematic analysis, Liu et al.[87] derived compatibility equations for closed-loop assemblies composed of 4-crease vertices, facilitating the design of tubes with distinct polygonal cross-sections, as presented in Fig. 1-9(b). To expand the design space, Chen et al.[88] introduced constructive operations, such as summation, subtraction, and combination, to generate novel tubular forms, as shown in Fig. 1-9(c). Furthermore, Filipov et al. advanced geometric versatility through two distinct approaches: developing modular assembly strategies (zipper, aligned, and internal coupling) for tunable stiffness[89], as shown in Fig. 1-9(d), and designing tubes capable of accommodating arbitrary planar polygonal cross-sections[90], as shown in Fig. 1-9(e).

However, a prevailing limitation in the aforementioned studies is that the cross-sectional geometries are strictly confined to planar polygons. Although Liu et al.[87] formulated the necessary compatibility conditions, their analytical process incorporated a simplifying assumption of co-planar cross-sections. This simplification inevitably excludes a wide range of valid spatial geometries. Therefore, establishing a generalized kinematic framework is essential to overcome these geometric limitations, thereby

enabling the systematic resolution of compatibility conditions for complex origami patterns independent of restrictive coplanar assumptions.

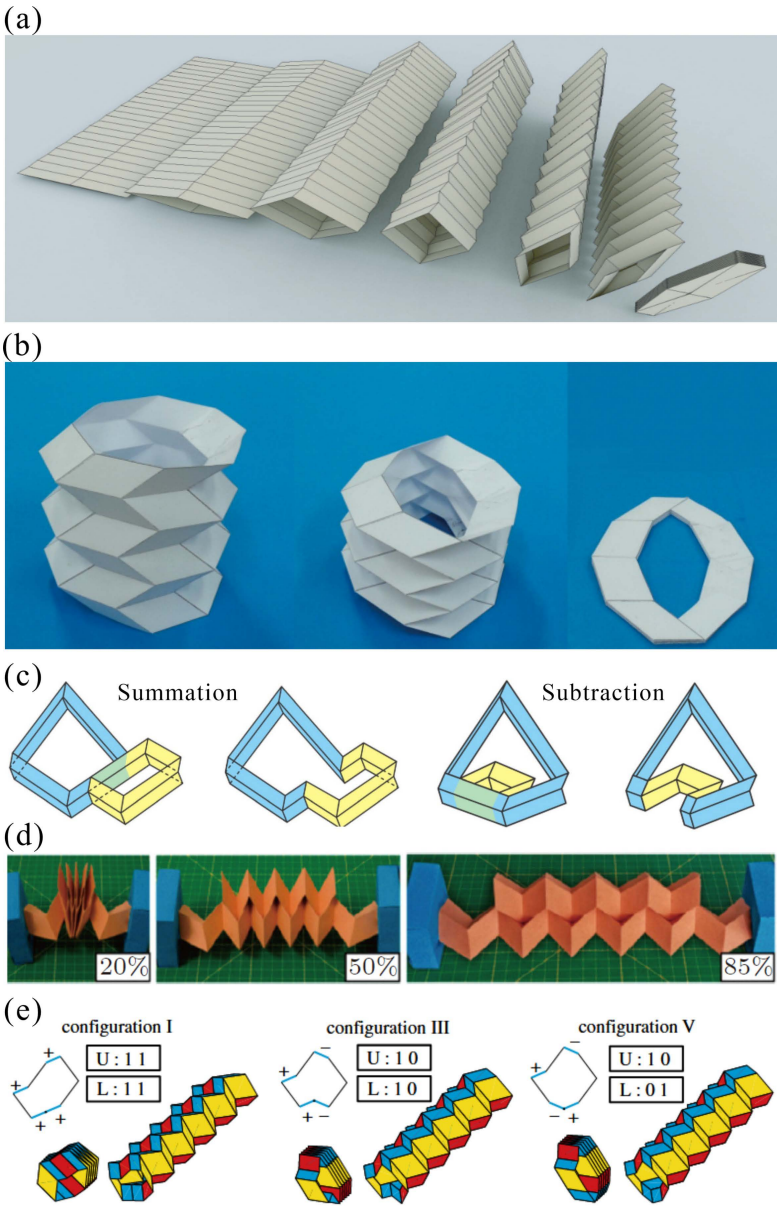

Fig. 1-9 Single-DOF rigid foldable origami tubes. Folding and deployment processes of origami tube with (a) planar quadrilateral cross-section[86] and (b) planar octagon cross-section[87]; (c) generation of origami tubes through summation and subtraction[88]; (d) tubular assemblies using zipper coupling schemes[89]; (e) origami tubes with planar polygonal cross-sections[90].

1.2.3 Origami Metamaterials

Origami-based mechanical metamaterials are created by transforming continuous 2D sheets into 3D architectures through predefined networks of creases. Rather than acting exclusively as simple rotational hinges, these interconnected creases establish a

fundamental geometric framework that coordinates the complex interplay between localized folding and global structural deformation. Crucially, the overarching mechanical behavior of these systems is governed by the distribution and evolution of elastic potential energy during the folding and deployment processes. Based on the spatial distribution of deformation, origami metamaterials can be systematically categorized into three distinct classes. The first class adheres to the rigid origami deformation mode, where deformation is exclusively localized at the hinge lines, leaving the constituent facets effectively non-deformable. The second class follows a non-rigid deformation mode, where the system relies primarily on the bending, twisting, or stretching of the panels themselves to accommodate kinematic incompatibilities or external loads. The third class exhibits a hybrid deformation mode, characterized by a complex coupling of rigid hinge rotation and elastic panel deformation. This rich scope of deformation mechanisms allows for the precise programming of diverse mechanical properties, such as multistability[91,92] and programmable stiffness[93,94], by simply manipulating the geometric layout of the crease pattern.

1.2.3.1 Origami Metamaterials with Rigid Origami Deformation Mode

Origami metamaterials under the rigid origami deformation mode constitute the most fundamental and extensively studied category within the field. In these systems, the structural deformation is strictly confined to the rotation of creases, which act as revolute joints, while the constituent facets remain rigid and undeformed throughout the deformation process. Consequently, the overall mechanical properties of these metamaterials are governed primarily by the geometric kinematics of the crease pattern rather than the elastic deformation of the constituent material.

As the quintessential representative of this class, the Miura-ori metamaterial has garnered extensive attention. Relative analytical studies[65] have derived explicit formulas that link the geometric parameters to the resulting geometric dimensions and Poisson's ratio. Utilizing its precise kinematics, Zhang et al.[95] investigated the mechanical response of Miura-ori metamaterials under quasi-static compression. By modeling the creases as ideal plastic hinges, as shown in Fig. 1-10(a), they established an analytical model that accurately characterizes the mechanical responses. Subsequently, Karagiozova et al.[96] extended this analysis to the dynamic regime using both analytical and numerical methods. Their findings revealed that the energy

absorption capacity of Miura-ori metamaterials is strain-rate dependent, enhancing significantly with increased loading velocities. On a geometric level, Dang et al.[97] conducted a systematic study on the deployment kinematics of axisymmetric Miura-ori, as shown in Fig. 1-10(b). They further developed an optimization framework to design hyperboloid tessellations capable of approximating complex surfaces of revolution.

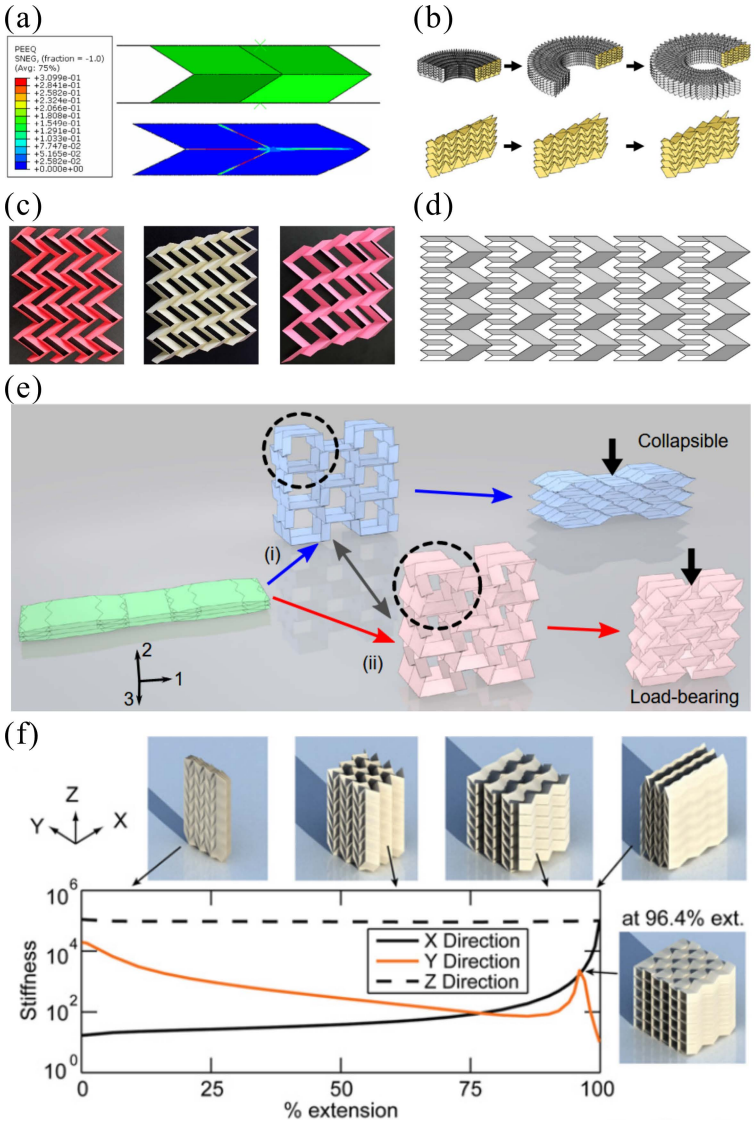

Fig. 1-10 The Miura-ori based origami metamaterials. (a) Deformed shapes of the cell and equivalent plastic strains under quasi-static compression[95]; (b) singly curved stacked axisymmetric Miura origami metamaterials[97]; (c) ZCH sheets created by changing the directions and/or the values of the offsets in the patterns[98]; (d) geometry of the zigzag-based metamaterials[99]; (e) the TMP structure can be folded into two distinctive configurations: collapsible and load-bearing modes[100]; (f) kinematic folding sequence of the cellular origami metamaterial and compression stiffness of the metamaterial in the three Cartesian directions vs. extension[89].

Beyond the standard configuration, researchers have explored systematic modifications of the unit cell geometry to engineer variants with unique mechanical properties. By integrating zigzag structural forms with the Miura-ori base, Eidini[98,101] proposed the Zigzag unit Cell with Hole (ZCH), as shown in Fig. 1-10(c). This variant not only achieves a more lightweight architecture but also demonstrates the capability to modulate the system's Poisson's ratio. Further investigating the zigzag-based metamaterials shown in Fig. 1-10(d), Zhang et al.[99] combined analytical and numerical approaches to analyze their large deformation and plastic behaviors under quasi-static in-plane compression. Their results demonstrated that the zigzag configuration exhibits superior energy absorption performance compared to the traditional Miura-ori counterpart. Another variant is the Tachi-Miura Polyhedron (TMP), which manifests as a bellows-like 3D structure derived from standard Miura-ori cells[102,103]. By strategically reconfiguring the M-V assignments of specific crease lines, this architecture enables the programmable tuning of critical mechanical properties, including Poisson's ratio and structural stiffness[100,104–106], as shown in Fig. 1-10(e). In terms of modular assembly, Filipov et al.[89] coupled Miura-ori tubes using a "zipper" coupling manner, successfully creating origami metamaterials that exhibit anisotropic stiffness characteristics in orthogonal directions, as shown in Fig. 1-10(f).

Origami metamaterials composed of high-degree vertices exhibit multi-DOF, offering multistate shape morphing ability. The Resch pattern serves as a prime example of a multi-DOF network. In its fully compacted planar state, the dense sixfold structural arrangement creates a rigid plate capable of supporting significant static loads. This mechanical robustness extends to tubular configurations, where the structure demonstrates superior resistance to axial compression[107], as shown in Fig. 1-11(a). Meanwhile, waterbomb origami serves as another typical multi-DOF pattern, distinguished by its rich kinematic versatility. Beyond its utility in robotic wheels[108] and pneumatic grippers[109], the waterbomb base also serves as a fundamental platform for constructing mechanical metamaterials, where its multi-DOF nature allows for the precise programming of stiffness profiles and deformation modes. Feng et al.[110] discovered a twist motion in waterbomb origami tubes that significantly enhances stiffness, proving that a purely rigid twist is only possible when the tube is fully squeezed with specific symmetry, while further twisting requires material deformation, as shown in Fig. 1-11(b). Mukhopadhyay et al.[62] demonstrated a distant actuation

feature in waterbomb metamaterials where far-field forces control local shape and stiffness, creating a programmable transition from rigid folding to high-stiffness structural deformation upon vertex contact, as shown in Fig. 1-11(c).

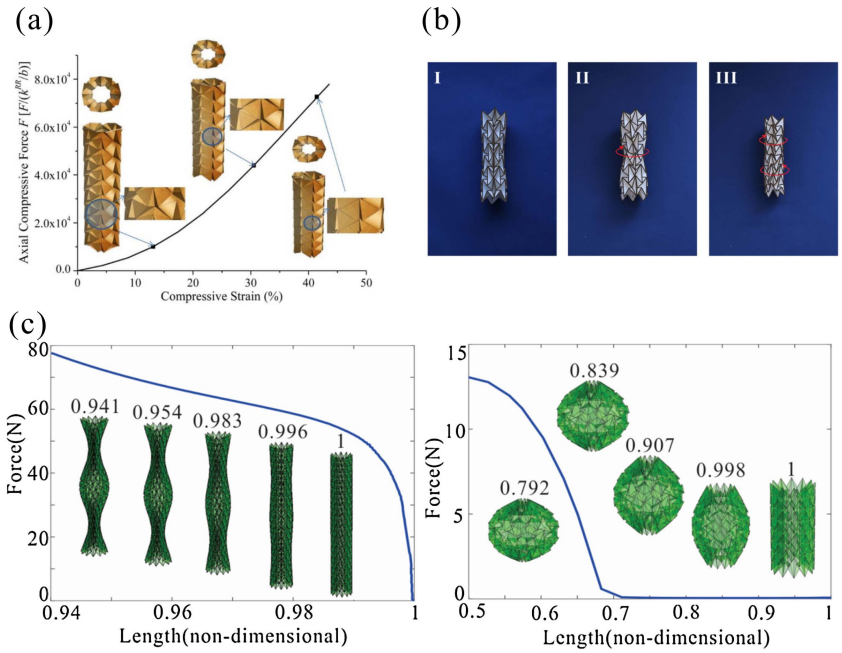

Fig. 1-11 Mechanical metamaterials based on multi-DOF origami patterns. (a) Normalized axial compression behavior of Resch based tubular metamaterial[107]; (b) twist motion of a waterbomb tube which starts from the fully squeezed row and then spreads row to row till the ends of the tube[110]; (c) programmable distant actuation feature in the tubular waterbomb metamaterial[62].

1.2.3.2 Origami Metamaterials with Non-Rigid Origami Deformation Mode

Distinct from rigid systems, origami metamaterials characterized by non-rigid deformation modes rely on the deformation of constituent facets, such as bending, twisting, or stretching, to accommodate folding motions. Non-rigid metamaterials enable rich nonlinear mechanical behaviors, such as bistability[111,112] and superior energy absorption[113–119], which are fundamentally unattainable through purely rigid kinematics.

Prominent among these systems are the Kresling and diamond patterns, which exploit panel deformation to achieve unique functional properties. The Kresling pattern, formed by the folding of a thin-walled tube under torque, as shown in Fig. 1-12(a), utilizes the non-rigid stretching or bending of panels to induce bistable snap-through transitions coupled with axial-torsional motion[120,121], as shown in Fig. 1-12(b). This

distinct energy landscape makes it a preferred candidate for developing tunable stiffness isolators and mechanical switches[122–124]. Meanwhile, the diamond pattern, effectively originating from the buckling modes of thin-walled cylinders, relies on the coordinated bending of facets to accommodate significant axial shortening during the crushing process, as demonstrated in Fig. 1-12(c). This topology enables the design of metamaterials with exceptional load-bearing efficiencies and programmable post-buckling responses, allowing for precise modulation of the cylindrical stiffness profile[125–129].

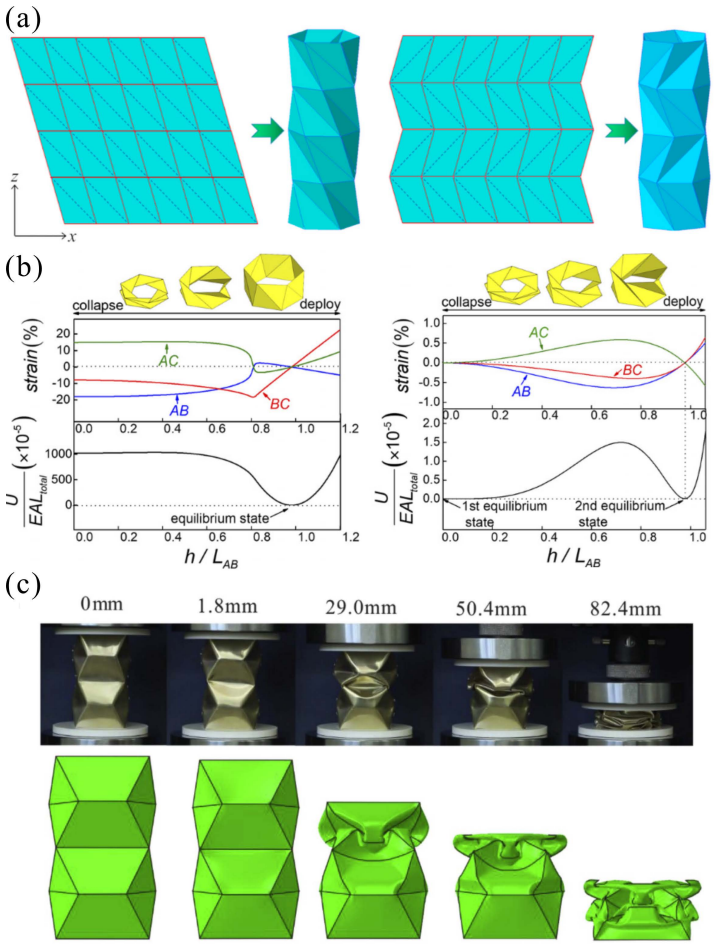

Fig. 1-12 Origami metamaterials with non-rigid deformation mode. (a) Kresling origami structure formed by array and mirror series connection method[123]; (b) monostable and bistable characteristic of the Kresling origami unit[124]; (c) panel buckling of the diamond origami crash box[129].

1.2.3.3 Origami Metamaterials with Hybrid Deformation Mode

Representing the frontier of origami engineering, metamaterials with hybrid deformation modes integrate the kinematic determinism of rigid folding with the panel

buckling of non-rigid distortion. Unlike systems governed by a single dominant mechanism, hybrid metamaterials operate through a programmable sequential transition between rigid mechanism motion and facet deformation. This synergistic interaction allows for the precise tailoring of the global force-displacement response, enabling advanced functionalities such as multi-stage energy absorption[130,131]. By strategically designing the geometric constraints to trigger transitions between rigid and deformable states, these systems offer a versatile platform for applications requiring both high shape adaptability during deployment and substantial structural load-bearing capability in service.

One highly effective and practical strategy to induce such programmable hybrid behaviors is the introduction of geometric gradients. As illustrated in Fig. 1-13(a), the unit cell geometry of the Miura pattern can be spatially varied within each layer[65] to create a functionally graded architecture. This geometric inhomogeneity introduces kinematic constraints that disrupt the standard synchronized folding path typically observed in uniform origami. Investigating this effect, Ma et al.[132] and Yuan et al.[64] thoroughly analyzed the complex mechanical response of graded Miura metamaterials. They observed a distinct, sequential deformation mechanism under compressive loading: the structure initially undergoes a rigid folding mode, characterized by remarkably low stiffness and a relatively smooth, extended force-displacement plateau. Upon reaching a geometrically self-locked state, the continued compression forces the system into a non-rigid regime dominated by panel buckling, resulting in a sudden and significant surge in structural stiffness and energy dissipation capacity, as shown in Fig. 1-13(b).

Beyond geometric gradients, adopting a composite structural design strategy provides another powerful avenue for achieving hybrid deformation. For instance, Li et al.[133] developed a hybrid metamaterial by integrating stacked Miura layers with rhombic honeycomb structures. This architecture exhibits a two-stage programmable compressive strength, as shown in Fig. 1-13(c). By systematically tuning the geometric parameters of both the origami and honeycomb constituents, the distinct mechanical responses across the different deformation stages, including the initial yield strength, the transition threshold, and the final densification strain, can be precisely programmed. Similar design strategies utilizing hybrid deformation modes have been widely adopted to engineer metamaterials with superior mechanical performance[134,135].

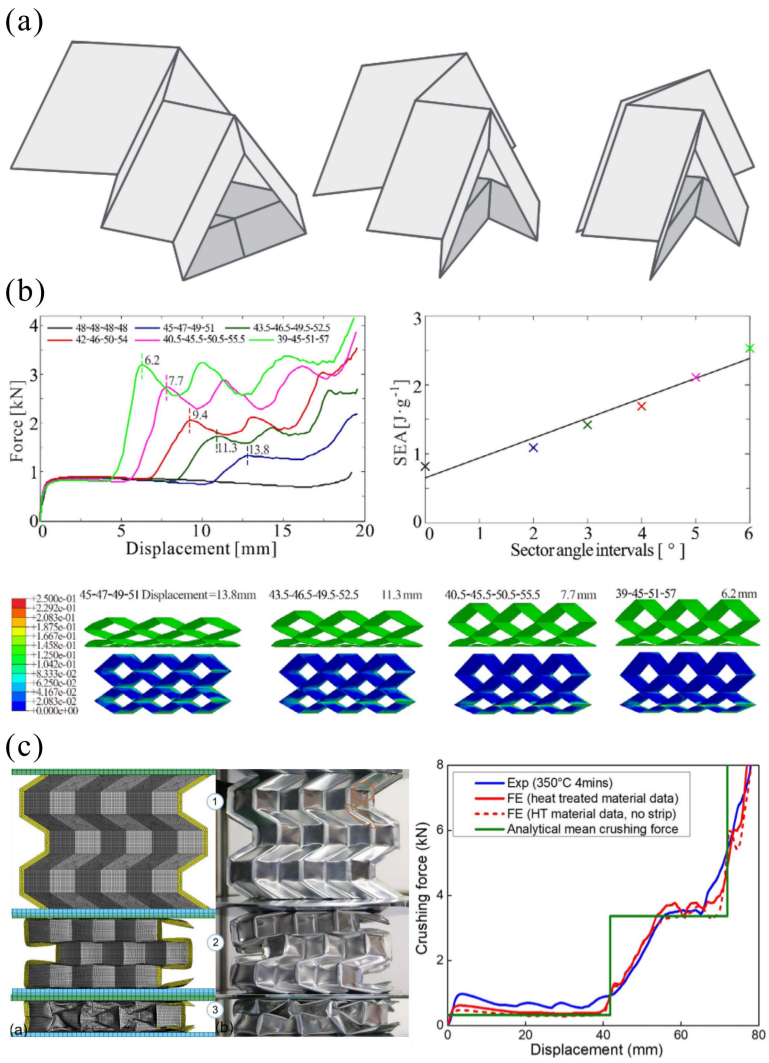

Fig. 1-13 Origami metamaterials with hybrid deformation modes. (a) Schematic of a Miura-ori with spatially varied unit cell geometry[65]; (b) sequential deformation mechanism and graded stiffness of the graded Miura-ori metamaterials[132]; (c) deformation modes and the two stage force-displacement response of the hybrid metamaterial[133].

1.2.3.4 Fabrication Techniques for Origami Metamaterials

In addition to design methodologies and mechanical characterizations, the practical realization of origami-inspired mechanical metamaterials strongly depends on advanced fabrication techniques. A variety of manufacturing approaches have been developed to translate foldable geometries into physical prototypes, ranging from conventional 3D/4D printing and moulding to laser cutting of thin sheets, modular assembly, electrospinning, and hybrid processes. Each technique offers distinct advantages in terms of material compatibility, structural complexity, scalability, and

integration of actuation or sensing functionalities. To provide a clear overview, Table 1-1 summarizes the main fabrication routes, typical materials, and representative applications.

Table 1-1 Summary of fabrication techniques for origami-inspired mechanical metamaterials.

Fabrication method	Materials examples	Typical applications
3D printing	PLA, ABS, TPU	Ref. [166, 167]
4D printing	SMP, LCE	Ref. [168, 169]
Moulding	PDMS, Ecoflex, Dragon Skin, silicone rubber, Copper	Ref. [170, 171, 132]
Laser cutting + manual folding	PET, PVC, paperboard, polycarbonate	Ref. [172, 173]
Modular assembly	Polycarbonate panels + silicone rubber sheets	Ref. [174]
Electrospinning	PVA nanofibrous membrane	Ref. [175]
Hybrid processes	LCE + conductive wires + 3D-printed frame	Ref. [176]

1.2.4 Multifunctional metamaterials

The preceding discussions have primarily focused on metamaterials tailored for a specific mechanical property. However, practical engineering scenarios often necessitate structures that can satisfy concurrent performance objectives rather than maximizing a single function. Addressing this complexity, the research focus has progressively shifted towards multifunctional metamaterials. Unlike their mono-functional counterparts, these advanced architectures are designed to integrate multiple programmable physical properties simultaneously within a unified geometric configuration. This design philosophy enables a single structure to efficiently fulfill diverse operational requirements without the need for assembling distinct components for each function.

To achieve such integrated capabilities, researchers have extensively exploited strategic geometric designs to coordinate distinct physical mechanisms. For instance, microlattice architectures based on face-centered cubic plate-truss configurations

presented in Fig. 1-14(a) have been adopted to simultaneously enhance acoustic and mechanical energy absorption[29]. Additionally, unit cells obtained from topology optimization have successfully synthesized negative thermal expansion and phononic bandgap properties [30], as shown in Fig. 1-14(b).

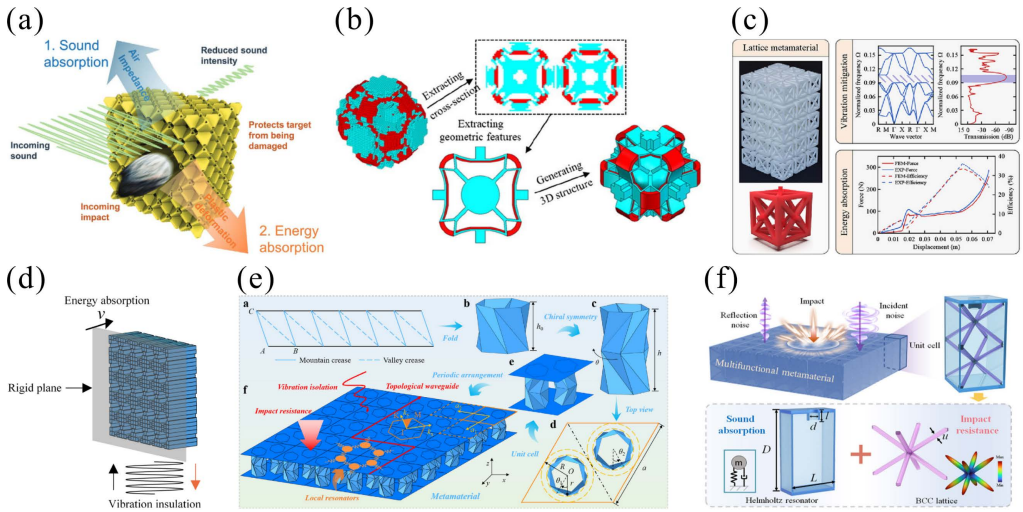

Fig. 1-14 Strategic geometric designs for multifunctional metamaterials. (a) Microlattice architecture based on face-centered cubic plate-truss configurations[29]; (b) unit cells obtained from topology optimization[30]; (c) hierarchical face-centered cubic frameworks[136]; (d) hierarchical square tube microstructures[137]; (e) multifunctional sandwich origami-based topological metamaterials[138]; (f) lattice architectures integrated with Helmholtz resonators[139].

Beyond elemental unit cells, hierarchical structuring offers another effective pathway. The strategic integration of strut elements within hierarchical microstructures, including face-centered cubic frameworks[136] in Fig. 1-14(c), and square tubes[137] in Fig. 1-14(d), enables metamaterials to concurrently achieve vibration suppression and energy dissipation functionalities. Similarly, sandwich architectures incorporating chiral Kresling origami cores, as depicted in Fig. 1-14(e), have been engineered to synergize topological wave transport with substantial mechanical robustness, utilizing local resonances for effective vibration isolation[138]. Recent innovations demonstrate that systems combining Helmholtz resonance principles with lattice architectures can effectively integrate broadband sound absorption and impact-resistant characteristics through multi-scale energy dissipation mechanisms[139], as shown in Fig. 1-14(f).

In addition to static geometric configurations, the incorporation of reconfigurable structural mechanisms and stimuli-responsive materials introduces dynamic tunability

over these multifunctional properties. For instance, Liu et al.[140] developed a tunable sandwich panel by integrating quasi-zero stiffness lattice cores with kirigami-style surfaces, as shown in Fig. 1-15(a), utilizing mechanical stretching to modulate load-bearing capacity, energy absorption, and vibration isolation capabilities simultaneously. Similarly, the synthesis of shape memory polymers with bistable beams creates reconfigurable metamaterials exhibiting tunable Poisson's ratios and bandgap characteristics through reversible phase transformations[141], as presented in Fig. 1-15(b). Likewise, magneto-active metamaterials, as shown in Fig. 1-15(c), demonstrate field-responsive modulation of both mechanical stiffness and acoustic band structures via external magnetic manipulation[142].

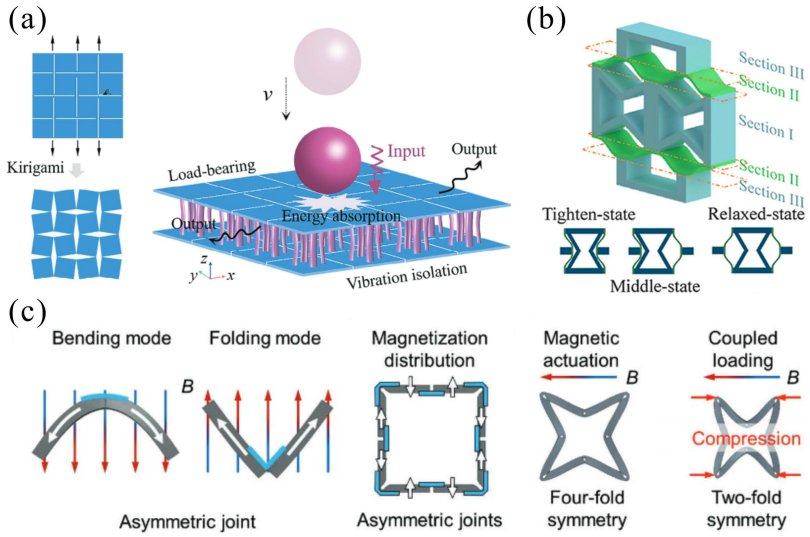

Fig. 1-15 Tunability of multifunctional metamaterials via reconfigurable mechanisms and stimuli-responsive materials. (a) A tunable sandwich panel integrating quasi-zero stiffness lattice cores with mechanically stretchable kirigami-style surfaces[140]; (b) reconfigurable metamaterials utilizing shape memory polymers with bistable beams for reversible phase transformations[141]; (c) magneto-active metamaterials demonstrating field-responsive property modulation under external magnetic manipulation[142].

However, a persistent challenge in the development of advanced multifunctional metamaterials remains the inherent parameter coupling among multiple physical properties. Because distinct physical behaviors are typically governed by the exact same set of underlying geometric parameters, attempting to optimize or vary one property inevitably alters the others. This fundamental interdependence severely

restricts the independent programmability of each individual function. Consequently, it poses a significant constraint for complex engineering applications that demand customized, independent control over distinct physical responses without unwanted functional trade-offs.

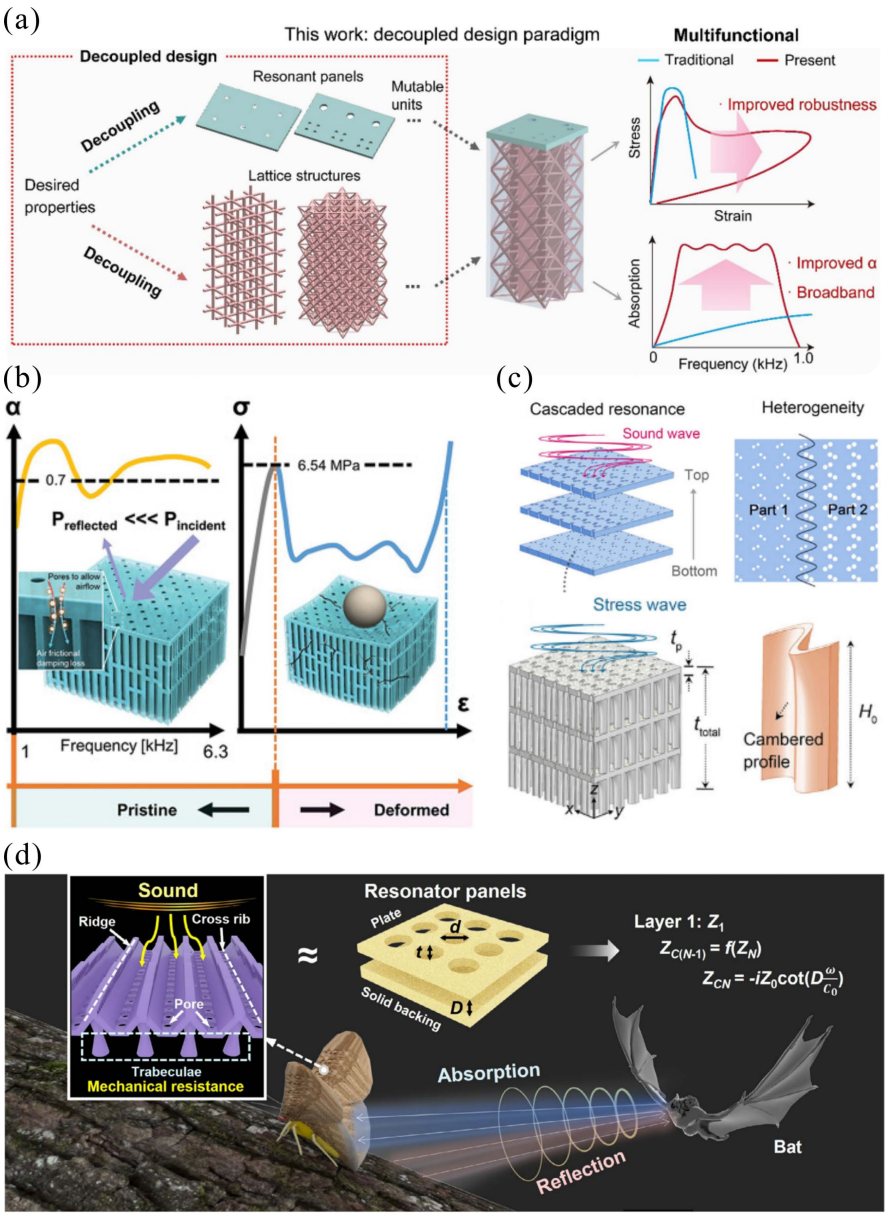

Fig. 1-16 Strategies for achieving independent programmability in multifunctional metamaterials. (a) Integration of resonant plates and lattice structures for decoupled acoustic and mechanical control[143]; (b) bio-inspired multi-level microlattices utilizing geometrical heterogeneities[144]; (c) weakly-coupled designs featuring asymmetric cambered cell walls[145]; (d) moth wing-inspired metamaterials integrating acoustic, mechanical, and thermal functionalities[146].

To mitigate this coupling and attain independent programmability, recent research efforts have focused on spatially or physically compartmentalizing functions. This is typically achieved by incorporating distinct, highly specialized sub-units within a larger composite structure, where each discrete module is dedicated to governing a specific physical function. For example, Li et al. [143] employs a hybrid architecture combining resonant plates and lattice structures, as presented in Fig. 1-16(a), to control acoustic and mechanical responses, respectively. Advancing this modular framework through bio-inspiration, a multi-level microlattice[144] was subsequently proposed, as shown in Fig. 1-16(b), which utilizes geometrical heterogeneities to achieve broadband sound absorption and deformation tolerance. Additionally, a weakly-coupled design featuring asymmetric cambered cell walls was developed to further optimize mechanical wave energy absorption without compromising structural integrity[145], as presented in Fig. 1-16(c). More recently, Pei et al.[146] drew inspiration from moth wings to construct a multifunctional metamaterial, as shown in Fig. 1-16(d), which integrates broadband acoustic absorption, mechanical energy dissipation, and thermal insulation within a unified framework.

While this compartmentalized approach effectively realizes independent programmability, it inevitably leads to a dramatic increase in structural and geometric complexity. Furthermore, these physically separated designs are predominantly static; once fabricated, they completely lack the capability for post-manufacturing structural reconfigurability and on-demand property tunability. Consequently, achieving both independent programmability and tunability within a single geometric design remains a critical, unresolved challenge.

1.3 Aim and Scope

The primary objective of this dissertation is to establish a generalized kinematic theoretical framework for the design of origami metamaterials, and to further develop multifunctional metamaterials with independently programmable and tunable properties. This research is expected to offer novel solutions for complex engineering challenges in emerging domains.

This research begins with exploring the fundamental kinematic mechanisms of origami, aiming to construct a generalized theoretical framework for the synthesis of

tubular structures. Building upon this foundation, the study systematically investigates the intrinsic mapping mechanisms linking M-V assignments and geometric parameters to mechanical and acoustic performance of metamaterials. Subsequently, it proposes design strategies for multifunctional metamaterials that feature independently programmable and tunable mechanical and acoustic properties. Finally, the research presents novel multifunctional metamaterials exhibiting distinct anisotropic mechanical properties in three orthotropic directions.

1.4 Outlines of Dissertation

This dissertation consists of six chapters. Their main contents are outlined below, and a schematic illustration is provided in Fig. 1-17.

Chapter 1 reviews the existing kinematic theories and their applications to the analysis and design of origami structures. In addition, tubular origami structures, origami metamaterials, and multifunctional metamaterials are introduced and discussed.

Chapter 2 establishes a generalized analytical framework for the kinematic synthesis of single-DOF tubular origami structures composed of 4-crease vertices. Beginning with a fundamental tubular unit comprising four such vertices, geometric compatibility conditions are systematically derived and subsequently generalized to multi-vertex systems. Building upon this theoretical foundation, a novel class of double-tubular origami structures is developed, which are then systematically expanded into complex spatial metamaterials using a tailored rotational assembly strategy.

Chapter 3 establishes a programmable framework for single-tubular origami metamaterials by manipulating M-V assignments. Analytical and numerical results reveal that these topological distributions inherently affect mechanical responses: normalized stiffness is governed by the varying rate of folding angles, while specific energy absorption (SEA) depends on the magnitude of angle changes and local panel buckling. The study is further extended to the acoustic domain, demonstrating that specific M-V configurations can induce directional bandgaps and thereby enable effective wave manipulation. Consequently, this chapter verifies M-V assignments as a critical and independent dimension for programming mechanical and acoustic functionalities in origami metamaterials.

Chapter 4 proposes a family of double-tubular origami metamaterials that exhibit unique rigid origami folding kinematics in two orthogonal directions. By correlating

the design parameters and initial folding states with the mechanical and acoustic responses, this chapter demonstrates that these two properties are independently programmable. This capability allows for varying one property over a wide range while maintaining the other nearly unchanged. Specifically, the frequency range of the bandgap can be tuned by up to 10.4 times while the stiffness remains constant; conversely, the stiffness can vary by up to 16.9 times without altering the bandgap frequency range. Furthermore, prototypes fabricated from thermoplastic polymers demonstrate on-site tunability via thermomechanical reconfiguration.

Chapter 5 presents a novel origami metamaterial which demonstrates remarkably programmable anisotropic mechanical properties in three orthotropic directions under quasi-static compression. Through a combination of theoretical analysis, experiments and numerical simulations, this newly designed metamaterial is proved to exhibit a rigid origami folding mode when loaded in the *x* direction, resulting in low SEA and compressive stiffness. Conversely, when loaded in the *y* direction, the metamaterial achieves high SEA and stiffness due to buckling deformation, which is three times larger than the corresponding data in the *x* direction. Furthermore, in the *z* direction, the metamaterial initially undergoes a rigid origami folding mode followed by panel buckling, resulting in a graded response with intermediate SEA and stiffness.

As the conclusion of this dissertation, Chapter 6 summarizes main achievements and future works. This dissertation first investigates the generalized analytical framework established for the kinematic synthesis of tubular and double-tubular origami structures, which serves as the theoretical foundation for the subsequent designs. Based on these kinematics, it investigates the programming of mechanical and acoustic properties in single-tubular metamaterials achieved through diverse M-V assignments. Subsequently, the dissertation highlights the unique independent programmability and tunability of mechanical and acoustic properties in the double-tubular metamaterial. Finally, the programmable anisotropic mechanical responses of triple-tubular metamaterial in three orthotropic directions are synthesized, followed by a discussion on the limitations of the current study and perspectives for future research.

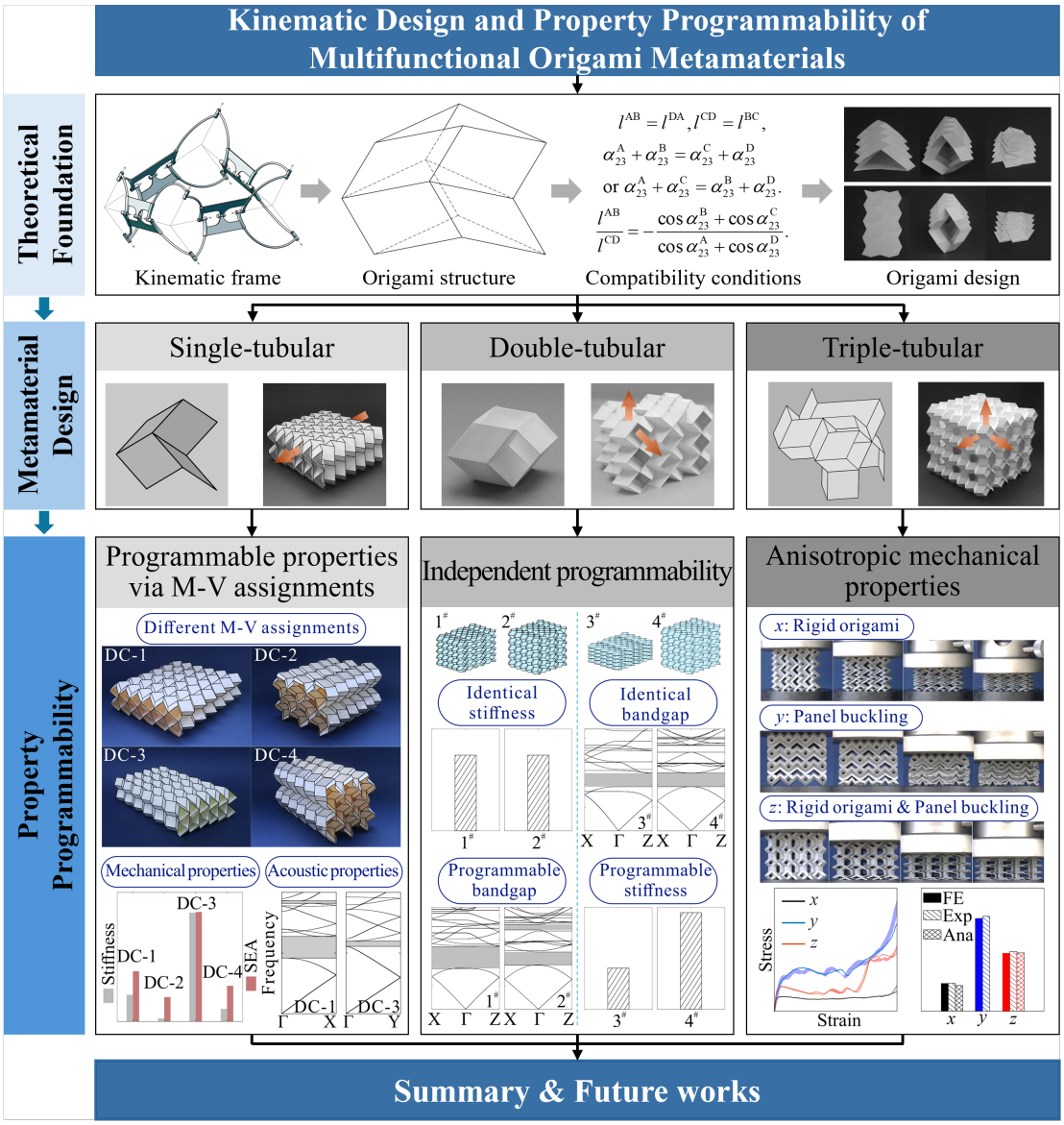

Fig. 1-17 Main contents of this dissertation.

Chapter 2 Kinematic Synthesis of Single-DOF Tubular Origami Structures Composed of 4-Crease Vertices

2.1 Introduction

Origami-inspired structures have garnered significant attention in engineering for their potential to create foldable mechanisms with tailored mechanical properties. However, the design of complex origami assemblies is often impeded by the challenge of satisfying rigid foldability constraints without relying on restrictive geometric assumptions, such as the requirement for co-planar cross-sections.

Thus, the objective of this chapter is to establish a generalized framework for the systematic synthesis of single-DOF tubular origami structures featuring spatial polygonal cross-sections. For this purpose, the investigation begins by deriving the compatibility conditions for a basic tubular mobile assembly formed by four 4-crease vertices. This analysis is subsequently extended to generalize the compatibility conditions for tubular assemblies comprising multiple 4-crease vertices. Guided by these theoretical criteria, a diverse range of single-tubular origami structures is constructed. Building upon this foundation, a novel class of double-tubular origami structures is synthesized via a geometric coupling strategy, followed by the establishment of a systematic methodology for tessellating these units into 3D cellular metamaterials.

The outline of this chapter is as follows. Section 2.2 establishes the compatibility conditions for a mobile assembly of four 4-crease vertices and derives explicit solutions of origami structures with spatial polygonal cross-sections. Section 2.3 extends these conditions to structures comprising multiple 4-crease vertices. Section 2.4 details the geometric construction of a novel double-tubular origami unit based on the derived theoretical cases and establishes a systematic tessellation strategy for cellular metamaterials. Finally, Section 2.5 summarizes the main findings.

2.2 Compatibility Conditions on Tubular Assembly of Four 4-Crease Vertices

This section presents the kinematic analysis of a closed-loop origami assembly composed of four 4-crease vertices (A, B, C, D), as illustrated in Fig. 2-1. A global

coordinate system {*X*, *Y*, *Z*} is established to define the spatial reference of the structure. To facilitate the kinematic formulation, local coordinate frames are established on the links and joints employing the D-H notation. Specifically, the z_i axis aligns with the rotational axis of the *i*th revolute joint. The x_i axis is established as the common normal between z_{i-1} and z_i. The twist angle $\alpha_{i(i+1)}$ denotes the rotation from z_i to z_{i+1} about the x_{i+1} axis. The joint angle θ_i describes the rotation from x_i to x_{i+1} about the z_i axis, which is defined within the range [0, 2π]. In this study, to better correlate the kinematic parameters with the physical geometry of the origami structure, the dihedral angle φ_i is introduced. As explicitly highlighted in red in Fig. 2-1, the relationship between these two angles is defined as $\varphi_i = \pi - \theta_i$, resulting in a value range of [-π, π] for φ_i. Within this convention, the range [0, π] corresponds to a mountain fold, whereas the range [-π, 0] denotes a valley fold. Consequently, to facilitate the subsequent analysis, φ_i is adopted to represent the folding angles throughout the remainder of this paper. Focusing first on the constraints by neglecting link lengths, the input and output parameters for the closed-loop assembly must satisfy the closure condition:

$$\varphi_1^{\mathrm{A}} \to \varphi_3^{\mathrm{A}} = \varphi_1^{\mathrm{B}} \to \varphi_3^{\mathrm{B}} = \varphi_1^{\mathrm{C}} \to \varphi_3^{\mathrm{C}} = \varphi_1^{\mathrm{D}} \to \varphi_3^{\mathrm{D}} = \varphi_1^{\mathrm{A}}. \tag{2-1}$$

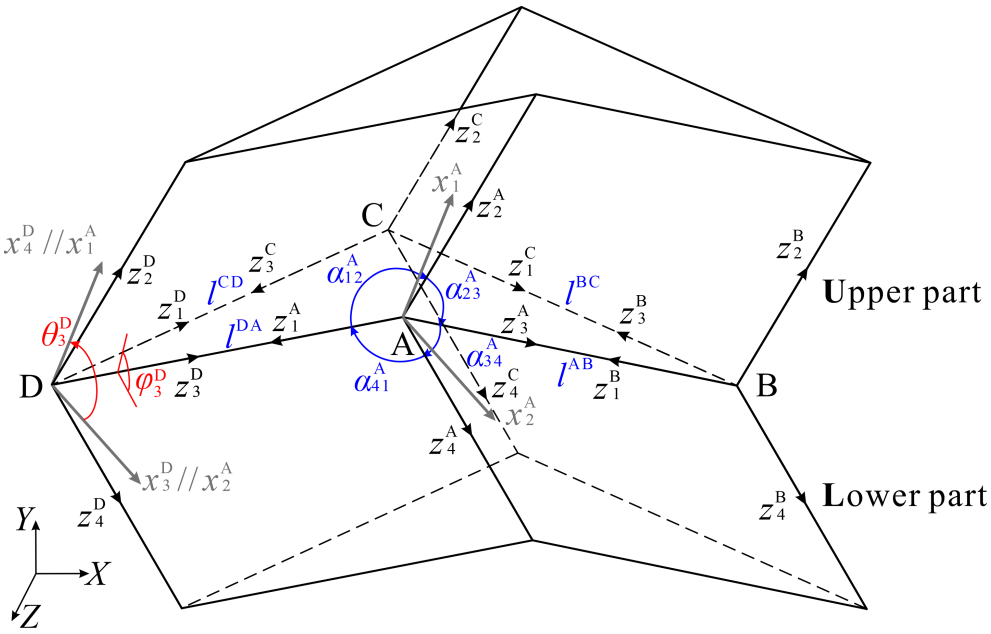

Fig. 2-1 Schematic of an origami structure composed of four 4-crease vertices.

Following the methodology in the research by Liu et al. [87], to ensure the system functions as a mobile assembly with a single-DOF, the geometric constraints among the

vertices are governed by:

$$z_2^{\mathrm{A}} /\!/ z_2^{\mathrm{B}} /\!/ z_2^{\mathrm{C}} /\!/ z_2^{\mathrm{D}},\ z_4^{\mathrm{A}} /\!/ z_4^{\mathrm{B}} /\!/ z_4^{\mathrm{C}} /\!/ z_4^{\mathrm{D}}. \tag{2-2}$$

To incorporate the physical dimensions of the structure, the link length l between adjacent vertices is introduced. As shown in Fig. 2-1, the structure is conceptually decomposed into an upper part and a lower part, bounded by the spatial quadrilateral ABCD. For the upper part, the spatial loop-closure equation is established by enforcing the sequential coordinate transformations traversing from the local frame $\{x_2^{\mathrm{A}},\ z_2^{\mathrm{A}}\}$, through $\{x_2^{\mathrm{B}},\ z_2^{\mathrm{B}}\}$, $\{x_2^{\mathrm{C}},\ z_2^{\mathrm{C}}\}$, and $\{x_2^{\mathrm{D}},\ z_2^{\mathrm{D}}\}$, and ultimately returning to the initial frame $\{x_2^{\mathrm{A}},\ z_2^{\mathrm{A}}\}$. Similarly, the compatibility condition for the lower part is determined by the coordinate transformation sequence traversing from the local frame $\{x_4^{\mathrm{D}},\ z_4^{\mathrm{D}}\}$, through $\{x_4^{\mathrm{A}},\ z_4^{\mathrm{A}}\}$, $\{x_4^{\mathrm{B}},\ z_4^{\mathrm{B}}\}$, $\{x_4^{\mathrm{C}},\ z_4^{\mathrm{C}}\}$, back to the starting frame $\{x_4^{\mathrm{D}},\ z_4^{\mathrm{D}}\}$. Consequently, to ensure structural integrity and compatibility, the following two geometric conditions must be satisfied:

$$\boldsymbol{T}_{\mathrm{U}}^{\mathrm{AD}}\boldsymbol{T}_{\mathrm{U}}^{\mathrm{DC}}\boldsymbol{T}_{\mathrm{U}}^{\mathrm{CB}}\boldsymbol{T}_{\mathrm{U}}^{\mathrm{BA}} = \mathbf{I}_4, \tag{2-3}$$

$$\boldsymbol{T}_{\mathrm{L}}^{\mathrm{DA}}\boldsymbol{T}_{\mathrm{L}}^{\mathrm{AB}}\boldsymbol{T}_{\mathrm{L}}^{\mathrm{BC}}\boldsymbol{T}_{\mathrm{L}}^{\mathrm{CD}} = \mathbf{I}_4, \tag{2-4}$$

where

$$\begin{aligned}
\boldsymbol{T}_{\mathrm{U}}^{(K+1)K} &= \boldsymbol{R}_x\left(\pi\text{-}\alpha_{12}^{K+1}\right)\boldsymbol{T}_z\left(l^{K(K+1)}\right)\boldsymbol{R}_x\left(2\pi\text{-}\alpha_{23}^{K}\right)\boldsymbol{R}_z\left(\pi+\varphi_2^{K}\right),\\
\boldsymbol{T}_{\mathrm{L}}^{K(K+1)} &= \boldsymbol{R}_x\left(\pi\text{-}\alpha_{34}^{K}\right)\boldsymbol{T}_z\left(l^{K(K+1)}\right)\boldsymbol{R}_x\left(2\pi\text{-}\alpha_{41}^{K+1}\right)\boldsymbol{R}_z\left(\pi+\varphi_4^{K+1}\right),
\end{aligned} \tag{2-5}$$

in which $l^{K(K+1)}$ denotes the length of the link connecting vertices K and K+1. Here, K represents vertices A, B, C, D, with the convention that K+1=A when K=D. The matrix $\boldsymbol{T}_{\mathrm{U}}^{(K+1)K}$ represents the transformation from the coordinate frame $\{x_2^{K+1},\ z_2^{K+1}\}$ to $\{x_2^{K},\ z_2^{K}\}$ in the upper part. The matrix $\boldsymbol{T}_{\mathrm{L}}^{K(K+1)}$ represents the transformation from the coordinate frame $\{x_4^{K},\ z_4^{K}\}$ to $\{x_4^{K+1},\ z_4^{K+1}\}$ in the lower part. The matrix $\boldsymbol{R}_x(\alpha_{i(i+1)})$ is the rotation matrix by angle $\alpha_{i(i+1)}$ about the x_i axis

$$\boldsymbol{R}_x\left(\alpha_{i(i+1)}\right) = \begin{bmatrix} 1 & 0 & 0 & 0 \\ 0 & \cos\alpha_{i(i+1)} & -\sin\alpha_{i(i+1)} & 0 \\ 0 & \sin\alpha_{i(i+1)} & \cos\alpha_{i(i+1)} & 0 \\ 0 & 0 & 0 & 1 \end{bmatrix}, \tag{2-6}$$

$\boldsymbol{R}_z\left(\varphi_i\right)$ denotes the rotation matrix by angle φ_i about the z_i axis

$$\boldsymbol{R}_z\left(\varphi_i\right)=\begin{bmatrix}\cos\varphi_i & -\sin\varphi_i & 0 & 0\\ \sin\varphi_i & \cos\varphi_i & 0 & 0\\ 0 & 0 & 1 & 0\\ 0 & 0 & 0 & 1\end{bmatrix}, \tag{2-7}$$

and $\boldsymbol{T}_z\left(l^{K(K+1)}\right)$ is the translation matrix along the z_i axis

$$\boldsymbol{T}_z\left(l^{K(K+1)}\right)=\begin{bmatrix}1 & 0 & 0 & 0\\ 0 & 1 & 0 & 0\\ 0 & 0 & 1 & l^{K(K+1)}\\ 0 & 0 & 0 & 1\end{bmatrix}. \tag{2-8}$$

Equations (2-3) and (2-4) constitute the fundamental compatibility conditions for the upper and lower parts, respectively. The system initially involves twenty unknown design parameters, comprising sixteen angle parameters and four length parameters. However, due to the geometric constraint in Eq. (2-2):

$$\alpha_{12}^{K+1}+\alpha_{23}^{K}=\pi,\ \ \alpha_{41}^{K+1}+\alpha_{34}^{K}=\pi, \tag{2-9}$$

the number of independent angle parameters can be reduced to eight. Solving this system reveals that the assembly behaves as a closed chain composed of four parallelograms. The explicit solution to Eq. (2-3) yields

$$\begin{aligned}\cos\left(\varphi_2^{\mathrm{A}}+\varphi_2^{\mathrm{B}}\right)&=\cos\left(\varphi_2^{\mathrm{C}}+\varphi_2^{\mathrm{D}}\right),\\ \sin\left(\varphi_2^{\mathrm{A}}+\varphi_2^{\mathrm{B}}\right)&=-\sin\left(\varphi_2^{\mathrm{C}}+\varphi_2^{\mathrm{D}}\right),\end{aligned} \tag{2-10}$$

$$l^{\mathrm{AB}}\sin\alpha_{12}^{\mathrm{B}}\sin\varphi_2^{\mathrm{A}}-l^{\mathrm{BC}}\sin\alpha_{12}^{\mathrm{C}}\sin\left(\varphi_2^{\mathrm{A}}+\varphi_2^{\mathrm{B}}\right)-l^{\mathrm{CD}}\sin\alpha_{12}^{\mathrm{D}}\sin\varphi_2^{\mathrm{D}}=0,$$

$$l^{\mathrm{DA}}\sin\alpha_{12}^{\mathrm{A}}-l^{\mathrm{AB}}\sin\alpha_{12}^{\mathrm{B}}\cos\varphi_2^{\mathrm{A}}+l^{\mathrm{BC}}\sin\alpha_{12}^{\mathrm{C}}\cos\left(\varphi_2^{\mathrm{A}}+\varphi_2^{\mathrm{B}}\right)-l^{\mathrm{CD}}\sin\alpha_{12}^{\mathrm{D}}\cos\varphi_2^{\mathrm{D}}=0, \tag{2-11}$$

$$l^{\mathrm{DA}}\cos\alpha_{12}^{\mathrm{A}}+l^{\mathrm{AB}}\cos\alpha_{12}^{\mathrm{B}}+l^{\mathrm{BC}}\cos\alpha_{12}^{\mathrm{C}}+l^{\mathrm{CD}}\cos\alpha_{12}^{\mathrm{D}}=0. \tag{2-12}$$

Similarly, the solution to Eq. (2-4) is given by

$$\begin{aligned}\cos\left(\varphi_4^{\mathrm{A}}+\varphi_4^{\mathrm{B}}\right)&=\cos\left(\varphi_4^{\mathrm{C}}+\varphi_4^{\mathrm{D}}\right),\\ \sin\left(\varphi_4^{\mathrm{A}}+\varphi_4^{\mathrm{B}}\right)&=-\sin\left(\varphi_4^{\mathrm{C}}+\varphi_4^{\mathrm{D}}\right),\end{aligned} \tag{2-13}$$

$$-l^{\mathrm{AB}}\sin\alpha_{34}^{\mathrm{A}}\sin\varphi_4^{\mathrm{A}}-l^{\mathrm{BC}}\sin\alpha_{34}^{\mathrm{B}}\sin\left(\varphi_4^{\mathrm{C}}+\varphi_4^{\mathrm{D}}\right)+l^{\mathrm{CD}}\sin\alpha_{34}^{\mathrm{C}}\sin\varphi_4^{\mathrm{D}}=0,$$

$$l^{\mathrm{DA}}\sin\alpha_{34}^{\mathrm{D}}-l^{\mathrm{AB}}\sin\alpha_{34}^{\mathrm{A}}\cos\varphi_4^{\mathrm{A}}+l^{\mathrm{BC}}\sin\alpha_{34}^{\mathrm{B}}\cos\left(\varphi_4^{\mathrm{C}}+\varphi_4^{\mathrm{D}}\right)-l^{\mathrm{CD}}\sin\alpha_{34}^{\mathrm{C}}\cos\varphi_4^{\mathrm{D}}=0, \tag{2-14}$$

$$l^{\mathrm{AB}}\cos\alpha_{34}^{\mathrm{A}}+l^{\mathrm{BC}}\cos\alpha_{34}^{\mathrm{B}}+l^{\mathrm{CD}}\cos\alpha_{34}^{\mathrm{C}}+l^{\mathrm{DA}}\cos\alpha_{34}^{\mathrm{D}}=0. \tag{2-15}$$

Equations (2-10), (2-11), (2-13), and (2-14) describe relationships for the dihedral angle φ_i, which varies during folding and deployment processes. To provide a geometric

interpretation of these results, we consider the planar quadrilaterals $A_1B_1C_1D_1$ and $A_2B_2C_2D_2$, obtained by projecting the spatial quadrilateral ABCD onto the planes with normal vectors $\mathbf{AA}_1$ and $\mathbf{AA}_2$, respectively, as shown in Fig. 2-2(a). The projections of axes x_2^{A} and x_3^{A} are axis x_2^{A1} and x_3^{A1}, respectively, as illustrated in Fig. 2-2(b). In this planar configuration, φ_2^{A}, φ_2^{B}, φ_2^{C}, and φ_2^{D} denote the internal angles of the quadrilateral $A_1B_1C_1D_1$. Consequently, the summation of φ_2^K satisfies

$$\varphi_2^{\mathrm{A}}+\varphi_2^{\mathrm{B}}+\varphi_2^{\mathrm{C}}+\varphi_2^{\mathrm{D}}=2\pi. \tag{2-16}$$

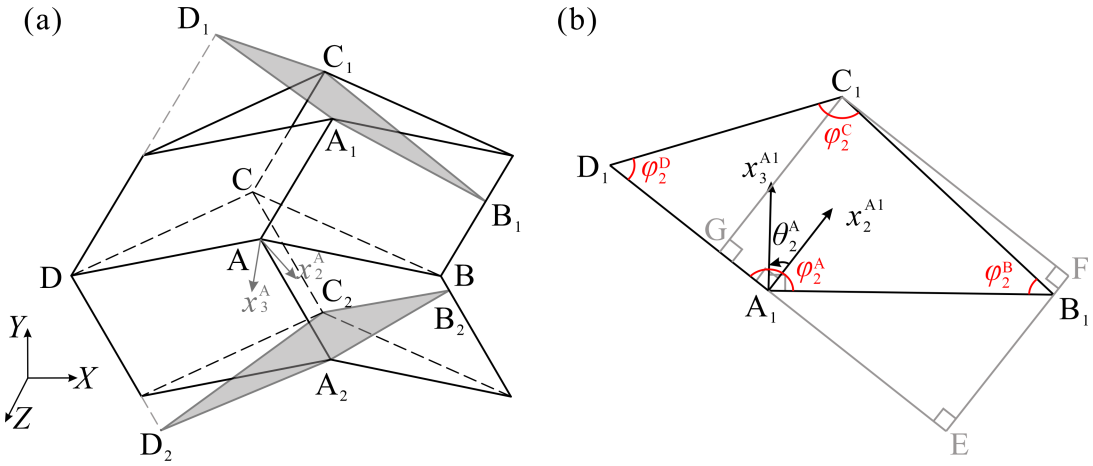

Fig. 2-2 (a) Projections of spatial quadrilateral ABCD, (b) geometric details of the planar quadrilateral $A_1B_1C_1D_1$.

Hence, the relationship among the dihedral angles φ_i described by Eq. (2-10) is automatically satisfied when the upper part forms a closed loop. Furthermore, regarding the quadrilateral $A_1B_1C_1D_1$, the notation $|A_1B_1|$ is employed to denote the linear distance between vertices A_1 and B_1; similar definitions apply to the lengths of the remaining sides, i.e., $|B_1C_1|$, $|C_1D_1|$, and $|D_1A_1|$. Then Eq. (2-11) can be reformulated as

$$\begin{aligned}
&|\mathrm{A_1B_1}|\sin\varphi_2^{\mathrm{A}}-|\mathrm{B_1C_1}|\sin\left(\varphi_2^{\mathrm{A}}+\varphi_2^{\mathrm{B}}\right)-|\mathrm{C_1D_1}|\sin\varphi_2^{\mathrm{D}}=0,\\
&|\mathrm{D_1A_1}|-|\mathrm{A_1B_1}|\cos\varphi_2^{\mathrm{A}}+|\mathrm{B_1C_1}|\cos\left(\varphi_2^{\mathrm{A}}+\varphi_2^{\mathrm{B}}\right)-|\mathrm{C_1D_1}|\cos\varphi_2^{\mathrm{D}}=0.
\end{aligned} \tag{2-17}$$

To further analyze the geometry of the planar quadrilateral $A_1B_1C_1D_1$, auxiliary lines are constructed as shown in Fig. 2-2(b): a perpendicular from point B_1 to line D_1A_1 intersects at point E, a perpendicular from C_1 to line B_1E intersects at point F, and a perpendicular from C_1 to line D_1A_1 intersects at G. Consequently, the relationships between the dihedral angles φ_i and the edge length described by Eq. (2-17) simplify to

$$\begin{aligned}\left|\mathrm{B_1E}\right|+\left|\mathrm{B_1F}\right|-\left|\mathrm{C_1G}\right|=0,\\ \left|\mathrm{D_1A_1}\right|+\left|\mathrm{A_1E}\right|-\left|\mathrm{C_1F}\right|-\left|\mathrm{D_1G}\right|=0.\end{aligned}\tag{2-18}$$

Based on the geometry presented in Fig. 2-2(b), the length constraint within the planar quadrilateral $A_1B_1C_1D_1$ described by Eq. (2-18) is naturally satisfied.

Then, consider the planar quadrilateral $A_2B_2C_2D_2$ illustrated in Fig. 2-3. Let the projections of axes x_1^{A} and x_4^{A} be denoted as x_1^{A1} and x_4^{A1}, respectively. The summation of φ_4^K satisfies

$$\varphi_4^{\mathrm{A}}+\varphi_4^{\mathrm{B}}+\varphi_4^{\mathrm{C}}+\varphi_4^{\mathrm{D}}=2\pi.\tag{2-19}$$

Consequently, Eq. (2-13) is inherently satisfied. Within the quadrilateral $A_2B_2C_2D_2$, Eq. (2-14) can be reformulated as

$$\begin{aligned}-\left|\mathrm{A_2B_2}\right|\sin\varphi_4^{\mathrm{A}}-\left|\mathrm{B_2C_2}\right|\sin\left(\varphi_4^{\mathrm{C}}+\varphi_4^{D}\right)+\left|\mathrm{C_2D_2}\right|\sin\varphi_4^{D}=0,\\ \left|\mathrm{A_2D_2}\right|-\left|\mathrm{A_2B_2}\right|\cos\varphi_4^{\mathrm{A}}+\left|\mathrm{B_2C_2}\right|\cos\left(\varphi_4^{\mathrm{C}}+\varphi_4^{D}\right)-\left|\mathrm{C_2D_2}\right|\cos\varphi_4^{D}=0.\end{aligned}\tag{2-20}$$

To facilitate the geometric analysis of the planar quadrilateral $A_2B_2C_2D_2$, auxiliary construction lines are introduced as depicted in Fig. 2-3. Specifically, a perpendicular line is drawn from point B_2 to line D_2A_2, intersecting at point E. Similarly, a perpendicular from C_2 to line B_2E intersects at point F, and a perpendicular from C_2 to line D_2A_2 intersects at G. Based on this geometric construction, Eq. (2-20) simplifies to

$$\begin{aligned}-\left|\mathrm{B_2E}\right|-\left|\mathrm{B_2F}\right|+\left|\mathrm{C_2G}\right|=0,\\ \left|\mathrm{A_2D_2}\right|+\left|\mathrm{A_2E}\right|-\left|\mathrm{C_2F}\right|-\left|\mathrm{D_2G}\right|=0.\end{aligned}\tag{2-21}$$

Finally, considering the geometric relationships presented in Fig. 2-3, Eq. (2-20) is naturally satisfied.

Therefore, the correlations between the edge lengths and twist angles $\alpha_{i(i+1)}$ for the upper and lower parts, represented by Eqs. (2-12) and (2-15), constitute the essential compatibility conditions.

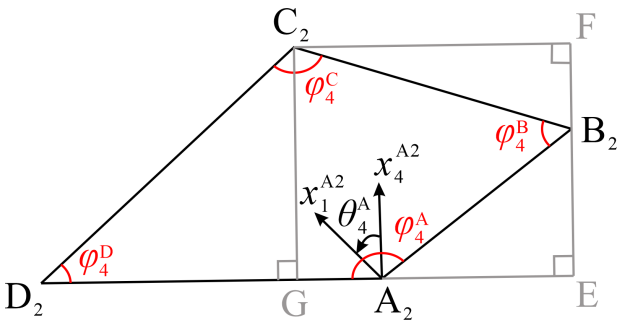

Fig. 2-3 Geometric details of the planar quadrilateral $A_2B_2C_2D_2$.

Next, considering a specific geometric constraint, the link vector directed from vertex *I* to vertex *J* is denoted as $\boldsymbol{L}^{IJ}$, and its modulus is represented by l^{IJ}, i.e., $|\boldsymbol{L}^{IJ}|= l^{IJ}$. Based on this notation, the constraint is formulated as

$$\boldsymbol{L}^{\mathrm{DA}} + \boldsymbol{L}^{\mathrm{AB}} = \boldsymbol{L}^{\mathrm{DC}} + \boldsymbol{L}^{\mathrm{CB}}. \tag{2-22}$$

However, with four length parameters and eight angular parameters remaining, the high dimensionality of the unknowns complicates the solution process. Therefore, we impose the constraints in Eq. (2-23) to reduce the angular parameters, which are expressed as

$$\begin{aligned} \alpha_{12}^{\mathrm{A}} + \alpha_{34}^{\mathrm{A}} = \pi, \;\; \alpha_{23}^{\mathrm{A}} + \alpha_{41}^{\mathrm{A}} = \pi, \\ \alpha_{12}^{\mathrm{C}} + \alpha_{34}^{\mathrm{C}} = \pi, \;\; \alpha_{23}^{\mathrm{C}} + \alpha_{41}^{\mathrm{C}} = \pi. \end{aligned} \tag{2-23}$$

From a physical perspective, these equations dictate that vertices A and C must be flat-foldable 4-crease vertices. This geometric restriction effectively reduces the number of unknown angle parameters to four, facilitating the subsequent analysis.

By rotating the origami structure shown in Fig. 2-2(a) clockwise by 90° about the *X* axis, the configuration transforms into that illustrated in Fig. 2-4. For clarity of representation and derivation, the structure is visually decomposed into two segments. It is important to note that the node pairs (D, D′), (B, B′), (K, K′), (L, L′), (M, M′), and (N, N′) represent coincident nodes in the physical assembly. A Cartesian coordinate system is established with the origin located at vertex D (or D′). Consequently, the fundamental geometry relationships are defined as follows:

$$\begin{aligned} \boldsymbol{L}^{\mathrm{DA}} + \boldsymbol{L}^{\mathrm{AB}} = \boldsymbol{L}^{\mathrm{DB}} = \left(x(\mathrm{B}), y(\mathrm{B}), z(\mathrm{B})\right), \\ \boldsymbol{L}^{\mathrm{DC}} + \boldsymbol{L}^{\mathrm{CB}} = \boldsymbol{L}^{\mathrm{D'B'}} = \left(x(\mathrm{B'}), y(\mathrm{B'}), z(\mathrm{B'})\right). \end{aligned} \tag{2-24}$$

To facilitate the geometric derivation, a series of auxiliary lines are constructed: a perpendicular line AQ is drawn from point A to the line DM, intersecting at point Q; a perpendicular line AP is drawn from point A to the plane DMN, with the foot of the perpendicular denoted as P; and a perpendicular line BO is drawn from point B to the line AP, intersecting at point O. Additionally, let B_0 denote the projection of point B (or B′) onto the *x* axis.

Applying spherical trigonometry to the spherical triangle associated with vertex D (spherical triangle D-AMN), the following relationships are obtained:

$$\begin{aligned} \cos\angle\mathrm{MDN} = \cos\alpha_{23}^{\mathrm{A}}\cos\alpha_{23}^{\mathrm{D}} + \sin\alpha_{23}^{\mathrm{A}}\sin\alpha_{23}^{\mathrm{D}}\cos\varphi_{3}^{\mathrm{D}}, \\ \cos\angle\mathrm{AQP}= \frac{\cos\alpha_{23}^{\mathrm{D}} - \cos\angle\mathrm{MDN}\cos\alpha_{23}^{\mathrm{A}}}{\sin\alpha_{23}^{\mathrm{A}}\sin\angle\mathrm{MDN}}. \end{aligned} \tag{2-25}$$

Hence, there exist:

$$\begin{aligned}\left|\mathrm{AP}\right| &= l^{\mathrm{DA}} \sin\alpha_{23}^{\mathrm{A}} \sin\angle\mathrm{AQP},\\ \left|\mathrm{AO}\right| &= l^{\mathrm{AB}} \sin\alpha_{23}^{\mathrm{A}} \sin\angle\mathrm{AQP}.\end{aligned} \tag{2-26}$$

Furthermore, considering the geometry of the right-angled triangle PDQ, the following relation holds:

$$\angle\mathrm{PDQ} = \arctan\frac{\left|\mathrm{PQ}\right|}{\left|\mathrm{DQ}\right|} = \frac{\sqrt{\left|\mathrm{AQ}\right|^2 - \left|\mathrm{AP}\right|^2}}{\left|\mathrm{DQ}\right|}. \tag{2-27}$$

This leads to:

$$\angle\mathrm{PDB}_0 = \angle\mathrm{PDQ} - \frac{\angle\mathrm{MDN}}{2}. \tag{2-28}$$

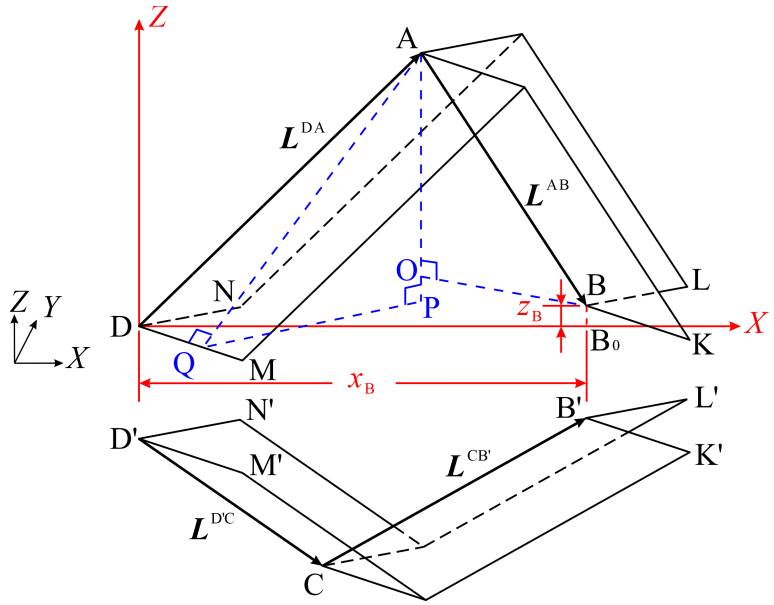

Fig. 2-4 Setup of the Cartesian coordinates in the origami structure.

Synthesizing the preceding derivations, the general coordinate expression can be determined as:

$$\boldsymbol{L}^{\mathrm{DB}} = \begin{bmatrix} x(\mathrm{B}) \\ y(\mathrm{B}) \\ z(\mathrm{B}) \end{bmatrix} = \begin{bmatrix} \dfrac{\sqrt{2}}{2}\left(l^{\mathrm{DA}} + l^{\mathrm{AB}}\right)\dfrac{\cos\alpha_{23}^{\mathrm{A}} + \cos\alpha_{23}^{\mathrm{D}}}{\sqrt{1+\cos\angle\mathrm{MDN}}} \\ 0 \\ \left(l^{\mathrm{DA}} - l^{\mathrm{AB}}\right)\sin\alpha_{23}^{\mathrm{A}}\sqrt{1-\left(\dfrac{\cos\alpha_{23}^{\mathrm{D}} - \cos\angle\mathrm{MDN}\cos\alpha_{23}^{\mathrm{A}}}{\sin\alpha_{23}^{\mathrm{A}}\sin\angle\mathrm{MDN}}\right)^2} \end{bmatrix}. \tag{2-29}$$

Similarly, applying the same geometric principles to the counterpart segment of the structure yields:

$$\boldsymbol{L}^{\mathrm{D'B'}}=\begin{bmatrix} x(\mathrm{B'}) \\ y(\mathrm{B'}) \\ z(\mathrm{B'}) \end{bmatrix}=\begin{bmatrix} \dfrac{\sqrt{2}}{2}\left(l^{\mathrm{BC}}+l^{\mathrm{CD}}\right)\dfrac{-\cos\alpha_{23}^{\mathrm{C}}-\cos\alpha_{23}^{\mathrm{B}}}{\sqrt{1+\cos\angle\mathrm{MDN}}} \\ 0 \\ \left(l^{\mathrm{CD}}-l^{\mathrm{BC}}\right)\sin\alpha_{23}^{\mathrm{C}}\sqrt{1-\left(\dfrac{-\cos\alpha_{23}^{\mathrm{B}}+\cos\angle\mathrm{MDN}\cos\alpha_{23}^{\mathrm{C}}}{\sin\alpha_{23}^{\mathrm{C}}\sin\angle\mathrm{MDN}}\right)^2} \end{bmatrix}. \quad (2\text{-}30)$$

Equating corresponding terms in Eqs. (2-29) and (2-30), the following equations are derived

$$\begin{aligned} &\left(l^{\mathrm{DA}}+l^{\mathrm{AB}}\right)\left(\cos\alpha_{23}^{\mathrm{A}}+\cos\alpha_{23}^{\mathrm{D}}\right)=\left(l^{\mathrm{BC}}+l^{\mathrm{CD}}\right)\left(-\cos\alpha_{23}^{\mathrm{C}}-\cos\alpha_{23}^{\mathrm{B}}\right), \\ &\left(l^{\mathrm{AB}}-l^{\mathrm{DA}}\right)^2\left(\sin^2\alpha_{23}^{\mathrm{A}}-\cos^2\angle\mathrm{D_2DD_1}-\cos^2\alpha_{23}^{\mathrm{D}}+2\cos\angle\mathrm{D_2DD_1}\cos\alpha_{23}^{\mathrm{A}}\cos\alpha_{23}^{\mathrm{D}}\right) \\ &=\left(l^{\mathrm{CD}}-l^{\mathrm{BC}}\right)^2\left(\sin^2\alpha_{23}^{\mathrm{C}}-\cos^2\angle\mathrm{D_2DD_1}-\cos^2\alpha_{23}^{\mathrm{B}}+2\cos\angle\mathrm{D_2DD_1}\cos\alpha_{23}^{\mathrm{C}}\cos\alpha_{23}^{\mathrm{B}}\right). \end{aligned} \quad (2\text{-}31)$$

To ensure the validity of Eq. (2-31) and obtain precise solutions, it is necessary to perform a case analysis based on the link length parameters. Specifically, we examine the difference between (l^{AB}-l^{DA}) and (l^{CD}-l^{BC}). If the condition l^{AB}-l^{DA}=l^{CD}-l^{BC}=0 is satisfied, the general constraint in Eq. (2-31) simplifies to

$$\frac{l^{\mathrm{DA}}+l^{\mathrm{AB}}}{l^{\mathrm{BC}}+l^{\mathrm{CD}}}=-\frac{\cos\alpha_{23}^{\mathrm{B}}+\cos\alpha_{23}^{\mathrm{C}}}{\cos\alpha_{23}^{\mathrm{A}}+\cos\alpha_{23}^{\mathrm{D}}}. \quad (2\text{-}32)$$

By integrating the relationship between the twist angles given in Eq. (2-32) with the expressions for edge lengths and twist angles $\alpha_{i(i+1)}$ for the upper and lower parts (Eqs. (2-12) and (2-15)), we derive the following compatibility conditions:

Case 1:

$$\begin{aligned} &l^{\mathrm{AB}}=l^{\mathrm{DA}}, l^{\mathrm{CD}}=l^{\mathrm{BC}}, \\ &\frac{l^{\mathrm{AB}}}{l^{\mathrm{CD}}}=-\frac{\cos\alpha_{23}^{\mathrm{B}}+\cos\alpha_{23}^{\mathrm{C}}}{\cos\alpha_{23}^{\mathrm{A}}+\cos\alpha_{23}^{\mathrm{D}}}. \end{aligned} \quad (2\text{-}33)$$

Based on the compatibility conditions derived in case 1, two types of origami structures featuring spatial quadrilateral cross-sections are designed, as illustrated in Fig. 2-5. These structures are constructed by tessellating the fundamental kinematic unit four times to form a tubular assembly. This construction strategy is consistently applied to all subsequent models discussed in this work. Figure 2-5 presents the physical folding sequences of these configurations and the corresponding relationships between the dihedral angles. The analysis reveals that the folding characteristics are critically governed by the selection of geometric parameters. Specifically, when the parameters are chosen to possess high symmetry, the kinematic curve in Fig. 2-5(a) shows that

φ_4^{D}, φ_3^{D}, and φ_4^{A} reach 0 or π when the input angle φ_1^{D} is 0 or π. This quantitative result confirms that the structure possesses two compact 2D states, corresponding to fully flat-folded (φ_1^{D}=0, state i) and flat-deployed (φ_1^{D}=π, state v) states. In contrast, adopting a more general set of parameters results in the configuration shown in Fig. 2-5(b). Here, the kinematic curve demonstrates that φ_4^{D}, φ_3^{D}, and φ_4^{A} remain neither 0 nor π when φ_1^{D} is 0 or π, thereby verifying the absence of any compact 2D states. Furthermore, the kinematic curves in Fig. 2-5 reveal discontinuities during the motion. At these critical points, the dihedral angle satisfies φ_4^{D}=π (or -π). Physically, this condition indicates a transition in the M-V assignment of φ_4^{D}, signifying that a crease switches from a mountain fold to a valley fold (or vice versa) during the continuous folding process. To ensure the structure can achieve a fully flat-folded state, the geometric arrangement must allow the adjacent layers to come into contact without physical intersection. This requirement leads to the following constraint:

$$2l^{\mathrm{AB}}\cos\frac{\alpha_{23}^{\mathrm{A}}+\alpha_{23}^{\mathrm{D}}}{2}=-2l^{\mathrm{CD}}\cos\frac{\alpha_{23}^{\mathrm{B}}+\alpha_{23}^{\mathrm{C}}}{2}. \tag{2-34}$$

Substituting Eq. (2-34) into Eq. (2-33) yields the flat-foldability conditions for this graded configuration:

$$\begin{gathered} l^{\mathrm{AB}}=l^{\mathrm{DA}}, l^{\mathrm{CD}}=l^{\mathrm{BC}}, \\ \alpha_{23}^{\mathrm{A}}+\alpha_{23}^{\mathrm{B}}=\alpha_{23}^{\mathrm{C}}+\alpha_{23}^{\mathrm{D}} \text{ or } \alpha_{23}^{\mathrm{A}}+\alpha_{23}^{\mathrm{C}}=\alpha_{23}^{\mathrm{B}}+\alpha_{23}^{\mathrm{D}}, \\ \frac{l^{\mathrm{AB}}}{l^{\mathrm{CD}}}=-\frac{\cos\alpha_{23}^{\mathrm{B}}+\cos\alpha_{23}^{\mathrm{C}}}{\cos\alpha_{23}^{\mathrm{A}}+\cos\alpha_{23}^{\mathrm{D}}}. \end{gathered} \tag{2-35}$$

Based on the solution space derived in Eq. (2-35), two distinct origami configurations are constructed, as illustrated in Fig. 2-6. In these two configurations, the parameters α_{23}^{B} and α_{23}^{C} are switched. The kinematic curves demonstrate that when the input angle φ_1^{D} is 0, the remaining dependent dihedral angles reach 0 or π. This verifies that both configurations possess a flat-folded state. Furthermore, the folding behaviors are distinguished by the relative magnitudes of the twist angles. For the case where $\alpha_{23}^{\mathrm{A}}>\alpha_{23}^{\mathrm{D}}$, if the condition (π-$\alpha_{23}^{\mathrm{B}}$) < (π-$\alpha_{23}^{\mathrm{C}}$) is met, the structure folds into the configuration shown in Fig. 2-6(a). The kinematic curve for this configuration exhibits a discontinuity, corresponding to a physical transition in the M-V assignment of φ_4^{D}. Conversely, if (π-α_{23}^{B}) > (π-α_{23}^{C}), the structure folds into the configuration shown in Fig. 2-6(b), where the kinematic curve remains continuous throughout the motion. It is worth noting that when $\alpha_{23}^{\mathrm{A}}<\alpha_{23}^{\mathrm{D}}$, these relationships are switched, leading

to the opposite correspondence between the geometric conditions and the resulting folded states.

Alternatively, we consider the special geometric condition satisfying l^{AB}-l^{DA}=l^{CD}-l^{BC}≠0, and the solution is given by

$$\begin{aligned} \cos\alpha_{23}^{A}\cos\alpha_{23}^{D} &= \cos\alpha_{23}^{B}\cos\alpha_{23}^{C}, \\ \cos^{2}\alpha_{23}^{A}+\cos^{2}\alpha_{23}^{D} &= \cos^{2}\alpha_{23}^{B}+\cos^{2}\alpha_{23}^{C}. \end{aligned} \tag{2-36}$$

To derive the explicit kinematic relationship for this case, a similar analysis is performed by combining this simplified constraint with the previously defined expressions (Eqs. (2-12) and (2-15)). Solving this system of equations yields a distinct solution set, denoted as case 2:

Case 2:

$$\begin{aligned} & l^{AB}=l^{CD}, l^{BC}=l^{DA}, \\ & \cos\alpha_{23}^{A}=-\cos\alpha_{23}^{C}, \cos\alpha_{23}^{B}=-\cos\alpha_{23}^{D}, \\ & \left(\text{or } \cos\alpha_{23}^{A}=-\cos\alpha_{23}^{D}, \cos\alpha_{23}^{B}=-\cos\alpha_{23}^{C}\right). \end{aligned} \tag{2-37}$$

Utilizing the relationships derived in case 2, an origami structure characterized by a parallelogram cross-section is designed, as illustrated in Fig. 2-7. The kinematic relationship and the folding process demonstrate that the structure possesses two compact 2D states.

In summary, this section has established a rigorous kinematic foundation for the fundamental closed-loop assembly of four 4-crease vertices. By integrating D-H kinematics with spatial loop-closure constraints, explicit compatibility equations were derived, revealing that the rigid foldability of such structures is not limited to planar cross-sections. Two distinct solution spaces were identified: case 1, corresponding to those with generalized spatial quadrilateral cross-sections, and case 2, corresponding to structures with parallelogram cross-sections. Furthermore, the derivation of flat-foldability conditions ensures that these assemblies can achieve compact folded states. These findings demonstrate that the geometric design space for single-DOF rigid-foldable tubular origami structures is significantly broader than previously assumed, providing the theoretical basis for the generalized multi-vertex analysis in the subsequent section.

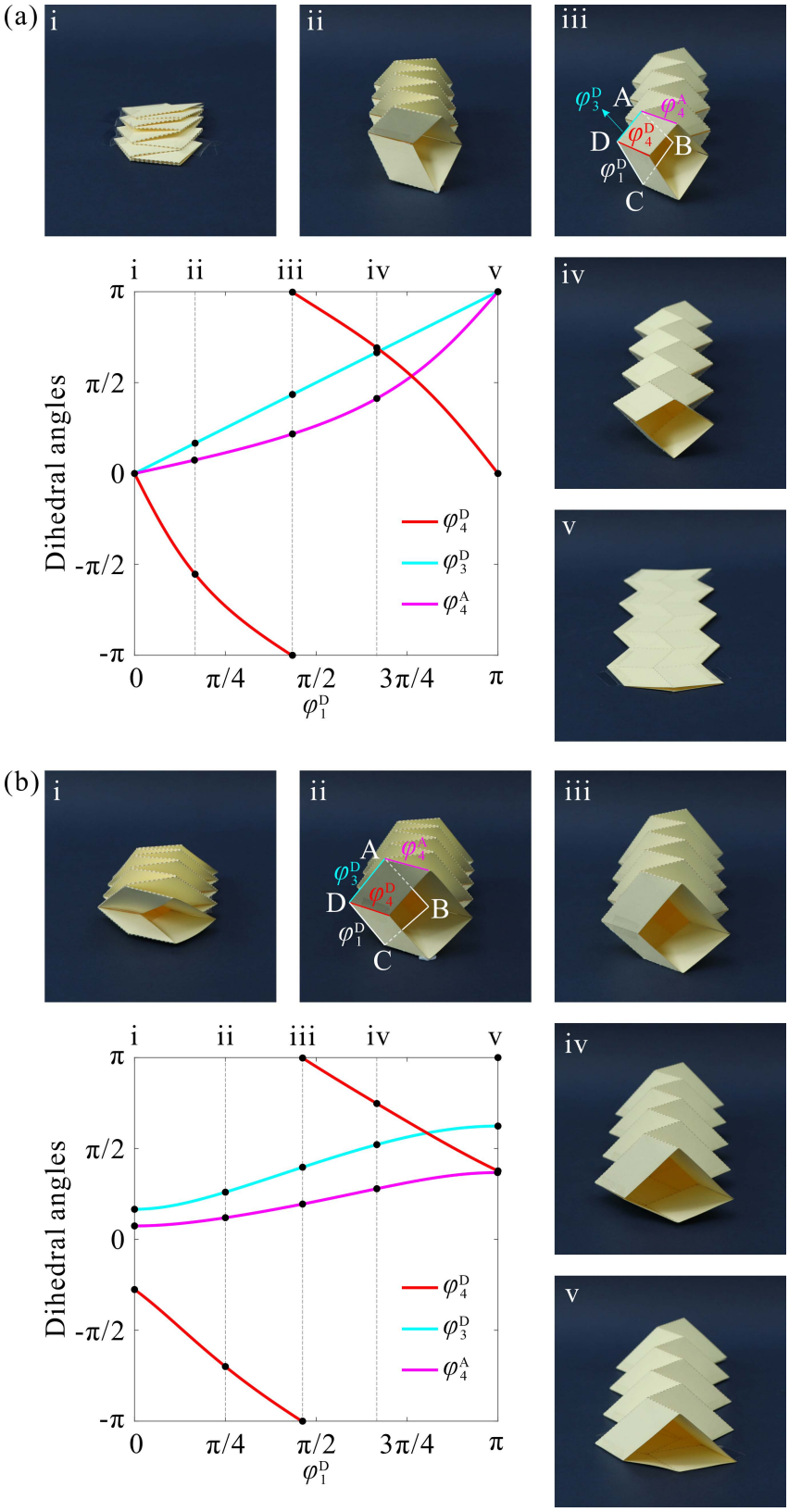

Fig. 2-5 Kinematic relationships of dihedral angles and the corresponding folding processes for configurations based on case 1, with (a) $l^{AB}=l^{BC}=l^{CD}=l^{DA}, \alpha_{23}^{A}=5\pi/18, \alpha_{23}^{B}=13\pi/18, \alpha_{23}^{C}=5\pi/9, \alpha_{23}^{D}=4\pi/9$; (b) $l^{DA}=l^{AB}, l^{BC}=l^{CD}, \alpha_{23}^{A}=4\pi/9, \alpha_{23}^{B}=5\pi/6, \alpha_{23}^{C}=11\pi/18, \alpha_{23}^{D}=5\pi/18$.

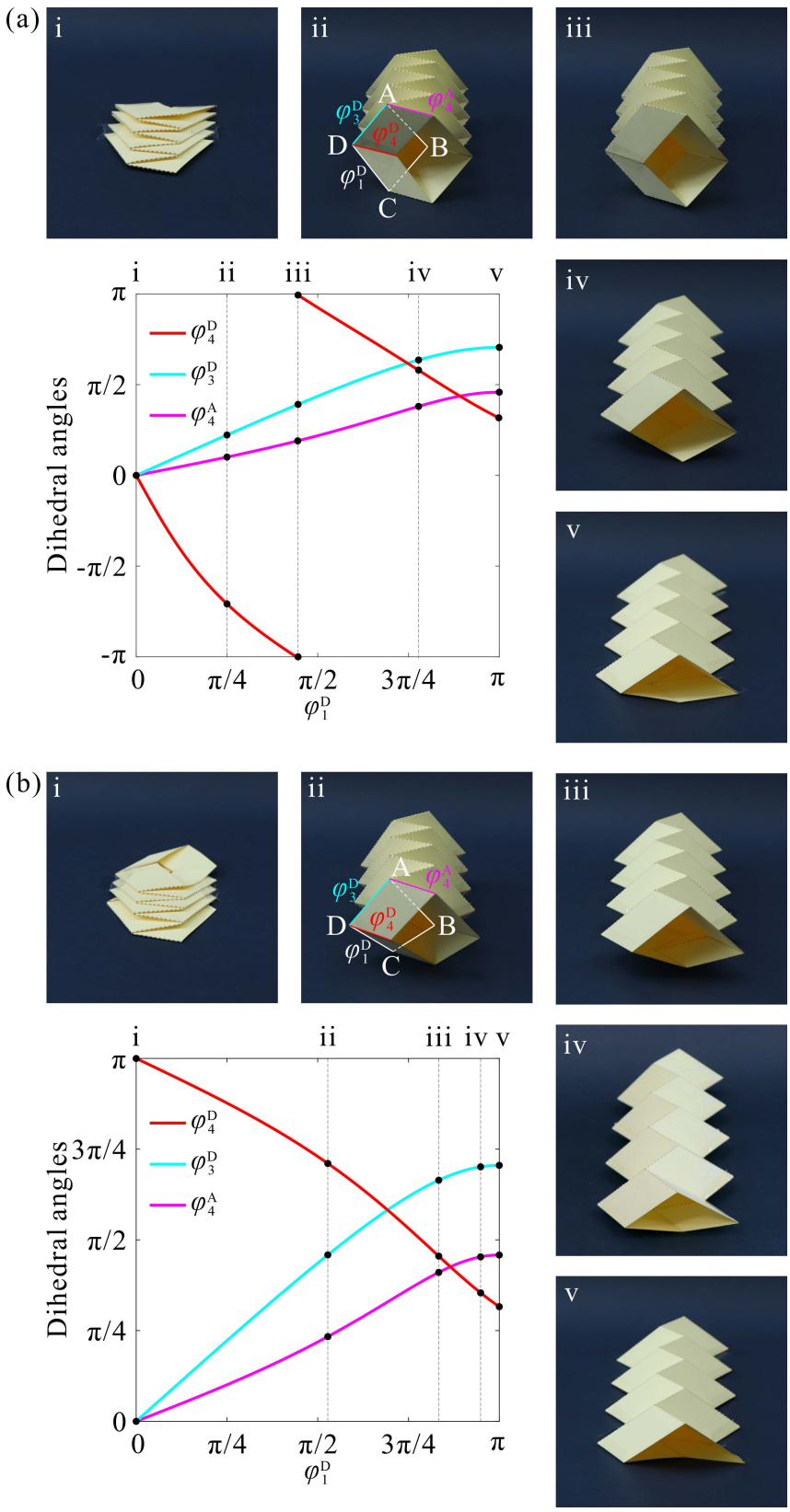

Fig. 2-6 Kinematic relationships of dihedral angles and the corresponding folding processes for configurations based on Eq. (2-35), with (a) $l^{DA}=l^{AB}, l^{BC}=l^{CD}, \alpha_{23}^{A}=4\pi/9, \alpha_{23}^{B}=7\pi/9, \alpha_{23}^{C}=11\pi/18, \alpha_{23}^{D}=5\pi/18$; (b) $l^{DA}=l^{AB}, l^{BC}=l^{CD}, \alpha_{23}^{A}=4\pi/9, \alpha_{23}^{B}=11\pi/18, \alpha_{23}^{C}=7\pi/9, \alpha_{23}^{D}=5\pi/18$.

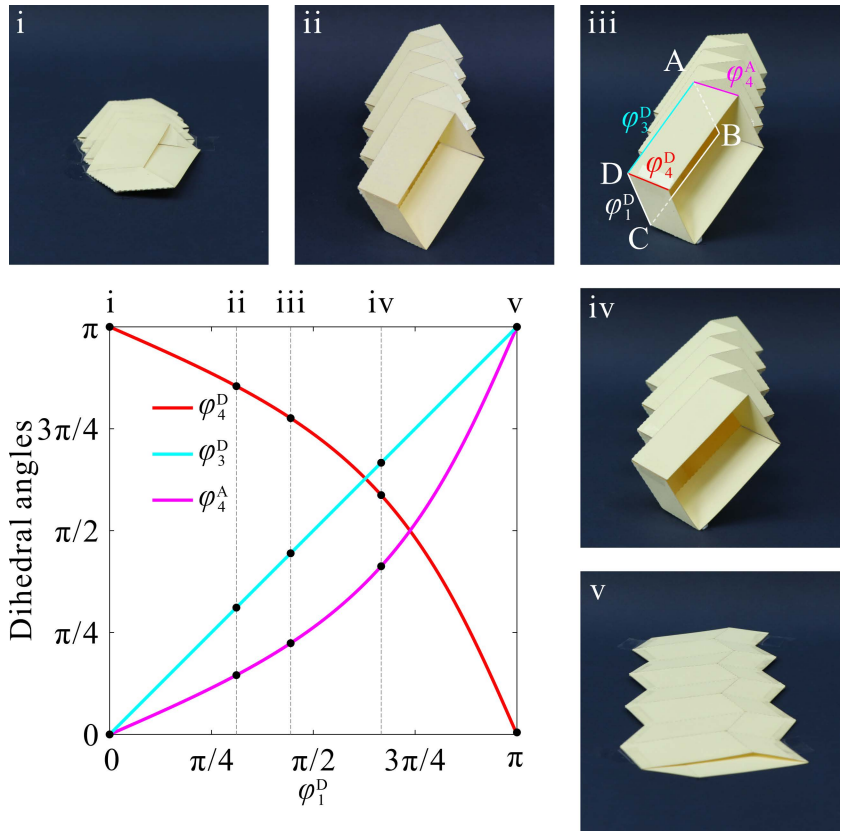

Fig. 2-7 Kinematic relationships of dihedral angles and the corresponding folding processes for configurations based on case 2, with $l^{BC}=2l^{AB}$, $l^{AB}=l^{CD}$, $l^{BC}=l^{DA}$, $\alpha_{23}^{A}=\pi-\alpha_{23}^{C}=4\pi/9$, $\alpha_{23}^{D}=\pi-\alpha_{23}^{B}=5\pi/18$.

2.3 Compatibility Conditions on Tubular Assembly of Multiple 4-Crease Vertices

The kinematic analysis is now extended to generalized origami assemblies composed of multiple 4-crease vertices, as illustrated in Fig. 2-8. The assembly is conceptually partitioned along the reference plane (designated as the *XOY* plane) into two distinct regions, denoted as region M (highlighted in blue) and region N (highlighted in gray). Region M comprises a serial chain of P 4-crease vertices (labeled I, II, …, P), while region N contains Q 4-crease vertices (labeled I, II, …, Q).

Although the cross-sectional profile of such a structure typically forms a spatial concave polygon, the strategic modification of M-V assignments allows for transformation into a spatial convex polygon, as indicated by the transparent overlay in Fig. 2-8. In this configuration, vertices P_0 and Q_0 serve as the inflection points connecting the distinct geometric chains of regions M and N, respectively. To facilitate kinematic analysis, the view presented in Fig. 2-9(a) is derived by rotating the

configuration in Fig. 2-9 counter-clockwise by 90° about the *X* axis. In this rotated orientation, the structure is further decomposed into an upper part and a lower part by a spatial dividing polygon (highlighted in red in Fig. 2-9(a)). Consequently, the intersection of the vertical (M/N) and horizontal (U/L) divisions create four structural quadrants: MU, ML, NU, and NL. Using vertex P_0 and its adjacent nodes as a representative case, local coordinate systems are established based on the D-H notation, as detailed in Fig. 2-9(b). For region M (and similarly for N), the vertices indexed from II to P (and II to Q) are designed as flat-foldable 4-crease vertices, while maintaining the parallelism constraint described in Eq. (2-2). For notational brevity, we use α to represent the acute angle of the constituent parallelograms. For instance, $\alpha_{ML}^{P_0}$ denotes the acute angle corresponding to the edge connecting P_0 and P_0+1 within the lower part of region M, as shown in Fig. 2-9(b).

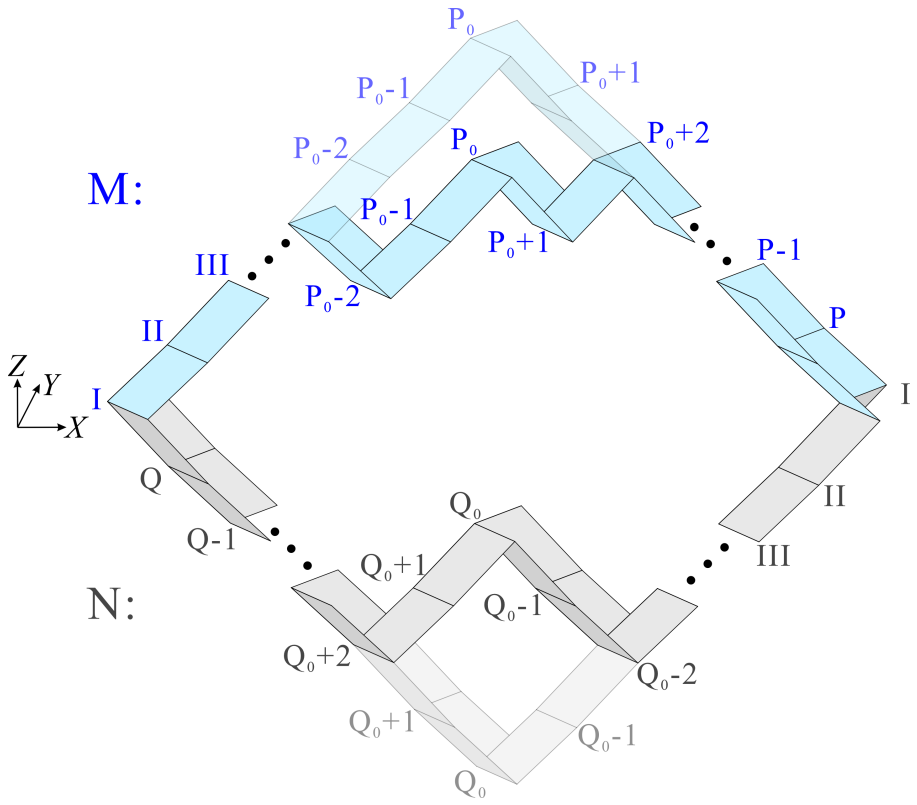

Fig. 2-8 An origami structure composed of multiple 4-crease vertices.

Similar to the derivation for the origami structure composed of four 4-crease vertices, the compatibility conditions that must be satisfied for the upper and lower parts in this multi-vertex assembly are:

$$\begin{aligned}\prod_{K=\mathrm{I}}^{\mathrm{P}}\boldsymbol{T}_{\mathrm{MU}}^{(K+1)K}\cdot\prod_{K=\mathrm{I}}^{\mathrm{Q}}\boldsymbol{T}_{\mathrm{NU}}^{(K+1)K}&=\mathbf{I}_4,\\ \prod_{K=\mathrm{I}}^{\mathrm{P}}\boldsymbol{T}_{\mathrm{ML}}^{K(K+1)}\cdot\prod_{K=\mathrm{I}}^{\mathrm{Q}}\boldsymbol{T}_{\mathrm{NL}}^{K(K+1)}&=\mathbf{I}_4,\end{aligned}\tag{2-38}$$

in which

$$\begin{aligned}\boldsymbol{T}_{\mathrm{M/NU}}^{(K+1)K}&=\boldsymbol{R}_x\left(\alpha_{\mathrm{M/NU}}^{K+1}\right)\boldsymbol{T}_z\left(l_{\mathrm{M/N}}^{K(K+1)}\right)\boldsymbol{R}_x\left(2\pi\text{-}\alpha_{\mathrm{M/NU}}^{K}\right)\boldsymbol{R}_z\left(\pi+\varphi_2^K\right),\\ \boldsymbol{T}_{\mathrm{M/NL}}^{K(K+1)}&=\boldsymbol{R}_x\left(\pi\text{-}\alpha_{\mathrm{M/NL}}^{K}\right)\boldsymbol{T}_z\left(l_{\mathrm{M/N}}^{K(K+1)}\right)\boldsymbol{R}_x\left(\pi\text{-}\alpha_{\mathrm{M/NL}}^{K+1}\right)\boldsymbol{R}_z\left(\pi+\varphi_4^{K+1}\right).\end{aligned}\tag{2-39}$$

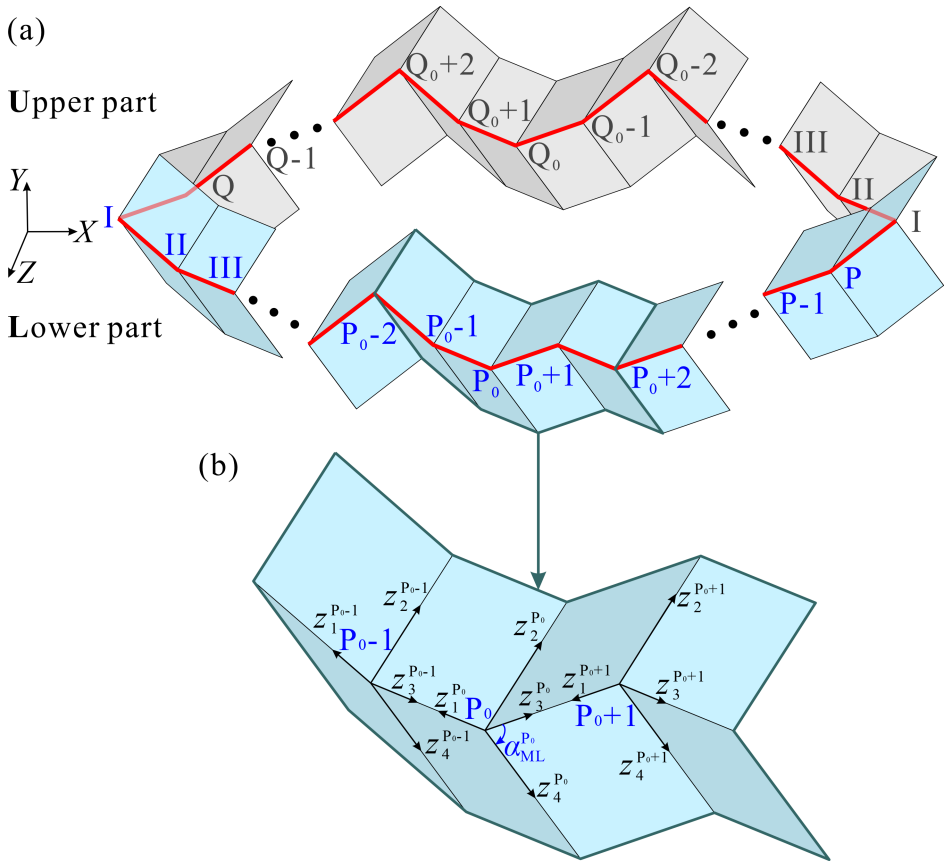

Fig. 2-9 Geometric definition and coordinate system setup of the rotated origami structure. (a) division into upper and lower parts, (b) coordinate system setup near vertex P_0.

By simultaneously solving the system of kinematic equations established in Eq. (2-38), we derive the explicit compatibility conditions that govern the independent motions of the upper and lower parts:

$$\begin{aligned}&l_{\mathrm{M}}^{\mathrm{I\,II}}\cos\alpha_{\mathrm{MU}}^{\mathrm{I}}+l_{\mathrm{M}}^{\mathrm{II\,III}}\cos\alpha_{\mathrm{MU}}^{\mathrm{II}}+\cdots+l_{\mathrm{M}}^{\mathrm{P_0(P_0+1)}}\cos\alpha_{\mathrm{MU}}^{\mathrm{P_0}}+\cdots+l_{\mathrm{M}}^{\mathrm{PI}}\cos\alpha_{\mathrm{MU}}^{\mathrm{P}}\\ &=l_{\mathrm{N}}^{\mathrm{I\,II}}\cos\alpha_{\mathrm{NU}}^{\mathrm{I}}+l_{\mathrm{N}}^{\mathrm{II\,III}}\cos\alpha_{\mathrm{NU}}^{\mathrm{II}}+\cdots+l_{\mathrm{N}}^{\mathrm{Q_0(Q_0+1)}}\cos\alpha_{\mathrm{NU}}^{\mathrm{Q_0}}+\cdots+l_{\mathrm{N}}^{\mathrm{QI}}\cos\alpha_{\mathrm{NU}}^{\mathrm{Q}},\end{aligned}\tag{2-40}$$

$$\begin{aligned} &l_{\mathrm{M}}^{\mathrm{I\,II}}\cos\alpha_{\mathrm{ML}}^{\mathrm{I}}+l_{\mathrm{M}}^{\mathrm{II\,III}}\cos\alpha_{\mathrm{ML}}^{\mathrm{II}}+\cdots+l_{\mathrm{M}}^{\mathrm{P}_0(\mathrm{P}_0+1)}\cos\alpha_{\mathrm{ML}}^{\mathrm{P}_0}+\cdots+l_{\mathrm{M}}^{\mathrm{PI}}\cos\alpha_{\mathrm{ML}}^{\mathrm{P}}\\ &=l_{\mathrm{N}}^{\mathrm{I\,II}}\cos\alpha_{\mathrm{NL}}^{\mathrm{I}}+l_{\mathrm{N}}^{\mathrm{II\,III}}\cos\alpha_{\mathrm{NL}}^{\mathrm{II}}+\cdots+l_{\mathrm{N}}^{\mathrm{Q}_0(\mathrm{Q}_0+1)}\cos\alpha_{\mathrm{NL}}^{\mathrm{Q}_0}+\cdots+l_{\mathrm{N}}^{\mathrm{QI}}\cos\alpha_{\mathrm{NL}}^{\mathrm{Q}}. \end{aligned} \tag{2-41}$$

Furthermore, to ensure the kinematic compatibility between regions M and N, the following geometric constraint is imposed:

$$\boldsymbol{L}_{\mathrm{M}}^{\mathrm{I\,II}}+\boldsymbol{L}_{\mathrm{M}}^{\mathrm{II\,III}}+\cdots+\boldsymbol{L}_{\mathrm{M}}^{\mathrm{PI}}=-\left(\boldsymbol{L}_{\mathrm{N}}^{\mathrm{I\,II}}+\boldsymbol{L}_{\mathrm{N}}^{\mathrm{II\,III}}+\cdots+\boldsymbol{L}_{\mathrm{N}}^{\mathrm{QI}}\right), \tag{2-42}$$

Consequently, solving this constraint equation leads to the derivation of the following relationships:

$$\frac{l_{\mathrm{M}}^{\mathrm{I\,II}}+l_{\mathrm{M}}^{\mathrm{II\,III}}+\cdots l_{\mathrm{M}}^{\mathrm{PI}}}{l_{\mathrm{N}}^{\mathrm{I\,II}}+l_{\mathrm{N}}^{\mathrm{II\,III}}+\cdots l_{\mathrm{N}}^{\mathrm{QI}}}=\frac{\cos\alpha_{\mathrm{NU}}^{\mathrm{I}}+\cos\alpha_{\mathrm{NU}}^{\mathrm{II}}}{\cos\alpha_{\mathrm{MU}}^{\mathrm{I}}+\cos\alpha_{\mathrm{MU}}^{\mathrm{II}}}, \tag{2-43}$$

$$\begin{gathered} \left(\Delta_{\mathrm{M}}\right)^2=\left(\Delta_{\mathrm{N}}\right)^2,\\ \left(\Delta_{\mathrm{M}}\right)^2\cos\alpha_{\mathrm{MU}}^{\mathrm{I}}\cos\alpha_{\mathrm{MU}}^{\mathrm{II}}=\left(\Delta_{\mathrm{N}}\right)^2\cos\alpha_{\mathrm{MU}}^{\mathrm{I}}\cos\alpha_{\mathrm{NU}}^{\mathrm{II}}, \\ \left(\Delta_{\mathrm{M}}\right)^2\left(\sin^2\alpha_{\mathrm{MU}}^{\mathrm{II}}-\cos^2\alpha_{\mathrm{MU}}^{\mathrm{I}}\right)=\left(\Delta_{\mathrm{N}}\right)^2\left(\sin^2\alpha_{\mathrm{NU}}^{\mathrm{II}}-\cos^2\alpha_{\mathrm{NU}}^{\mathrm{I}}\right). \end{gathered} \tag{2-44}$$

In these expressions, Δ_{M} and Δ_{N} represent the length parameters associated with regions M and N, respectively, and

$$\begin{aligned} \Delta_{\mathrm{M}}&=l_{\mathrm{M}}^{\mathrm{I\,II}}+l_{\mathrm{M}}^{\mathrm{II\,III}}+\cdots+l_{\mathrm{M}}^{(\mathrm{P}_0-1)\mathrm{P}_0}-l_{\mathrm{M}}^{\mathrm{P}_0(\mathrm{P}_0+1)}-\cdots-l_{\mathrm{M}}^{\mathrm{PI}},\\ \Delta_{\mathrm{N}}&=l_{\mathrm{N}}^{\mathrm{I\,II}}+l_{\mathrm{N}}^{\mathrm{II\,III}}+\cdots+l_{\mathrm{N}}^{(\mathrm{Q}_0-1)\mathrm{Q}_0}-l_{\mathrm{N}}^{\mathrm{Q}_0(\mathrm{Q}_0+1)}-\cdots-l_{\mathrm{N}}^{\mathrm{QI}}. \end{aligned} \tag{2-45}$$

The analysis reveals that the kinematic solutions are governed by the parameters $(\Delta\mathrm{M})^2$ and $(\Delta\mathrm{N})^2$. Consequently, integrating this finding with the fundamental compatibility conditions established in Eqs. (2-40) and (2-41), we identify specific solution cases based on the classification of these length parameters.

Case 3: When $(\Delta_{\mathrm{M}})^2=(\Delta_{\mathrm{N}})^2\neq 0$:

Under this specific condition, the angular parameters are strictly constrained by the geometry, leading to the expression:

$$\begin{gathered} \alpha_{\mathrm{MU}}^{\mathrm{I}}=\alpha_{\mathrm{NU}}^{\mathrm{II}},\ \alpha_{\mathrm{MU}}^{\mathrm{II}}=\alpha_{\mathrm{NU}}^{\mathrm{I}},\\ \left(\text{or } \alpha_{\mathrm{MU}}^{\mathrm{I}}=\alpha_{\mathrm{NU}}^{\mathrm{I}},\ \alpha_{\mathrm{MU}}^{\mathrm{II}}=\alpha_{\mathrm{NU}}^{\mathrm{II}}\right),\\ l_{\mathrm{M}}^{\mathrm{I\,II}}+l_{\mathrm{M}}^{\mathrm{II\,III}}+\cdots+l_{\mathrm{M}}^{(\mathrm{P}_0-1)\mathrm{P}_0}=l_{\mathrm{N}}^{\mathrm{I\,II}}+l_{\mathrm{N}}^{\mathrm{II\,III}}+\cdots+l_{\mathrm{N}}^{(\mathrm{Q}_0-1)\mathrm{Q}_0},\\ l_{\mathrm{M}}^{\mathrm{P}_0(\mathrm{P}_0+1)}+l_{\mathrm{M}}^{(\mathrm{P}_0+1)(\mathrm{P}_0+2)}+\cdots+l_{\mathrm{M}}^{\mathrm{PI}}=l_{\mathrm{N}}^{\mathrm{Q}_0(\mathrm{Q}_0+1)}+l_{\mathrm{N}}^{(\mathrm{Q}_0+1)(\mathrm{Q}_0+2)}+\cdots+l_{\mathrm{N}}^{\mathrm{QI}}. \end{gathered} \tag{2-46}$$

To demonstrate the physical implementation of this case, we consider a specific configuration where P=III, Q=II, and $\mathrm{P}_0=\mathrm{Q}_0=\mathrm{II}$. Substituting these values into Eq. (2-46), the relationship between the length parameters simplifies to:

$$\begin{aligned} l_{\mathrm{M}}^{\mathrm{I\,II}} &= l_{\mathrm{N}}^{\mathrm{I\,II}}, \\ l_{\mathrm{M}}^{\mathrm{II\,III}} + l_{\mathrm{M}}^{\mathrm{III\,I}} &= l_{\mathrm{N}}^{\mathrm{II\,I}}. \end{aligned} \tag{2-47}$$

Guided by these derived parameters, the origami tubular structure illustrated in Fig. 2-10 is constructed. This assembly comprises a total of five 4-crease vertices and features a spatial parallelogram cross-section. The kinematic relationships and folding process demonstrate that this structure possesses two distinct compact 2D states.

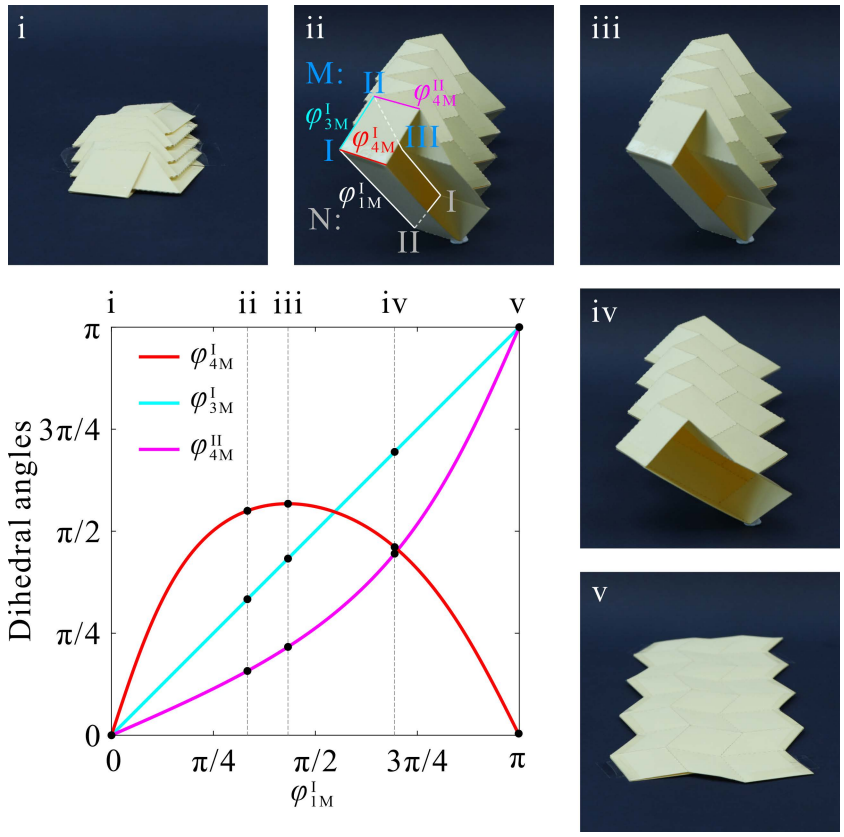

Fig. 2-10 Kinematic relationships of dihedral angles and the corresponding folding processes for configurations based on case 3, with $l_{\mathrm{M}}^{\mathrm{I\,II}} = l_{\mathrm{M}}^{\mathrm{II\,III}} = l_{\mathrm{N}}^{\mathrm{I\,II}}, l_{\mathrm{M}}^{\mathrm{II\,III}} + l_{\mathrm{M}}^{\mathrm{III\,I}} = l_{\mathrm{N}}^{\mathrm{II\,I}}, \alpha_{\mathrm{MU}}^{\mathrm{I}} = 5\pi/18, \alpha_{\mathrm{MU}}^{\mathrm{II}} = 4\pi/9.$

Finally, we investigate the special case where $(\Delta_{\mathrm{M}})^2=(\Delta_{\mathrm{N}})^2=0$. This condition leads to the emergence of three distinct sub-cases, classified as follows:

Case 4.1:

$$\cos\alpha_{\mathrm{MU}}^{\mathrm{I}} = \cos_{\mathrm{MU}}^{\mathrm{II}}, \quad \cos\alpha_{\mathrm{NU}}^{\mathrm{I}} = \cos_{\mathrm{NU}}^{\mathrm{II}}. \tag{2-48}$$

Case 4.2: In this sub-case, the solution depends on the specific parity of vertex indices P, Q, P_0 and Q_0. Accordingly, there exist the following relationships:

$$
\begin{aligned}
f(\mathrm{P}_0) &= \begin{cases} l_{\mathrm{M}}^{\mathrm{I\,II}} + l_{\mathrm{M}}^{\mathrm{III\,IV}} + \cdots + l_{\mathrm{M}}^{(\mathrm{P}_0-2)(\mathrm{P}_0-1)} = l_{\mathrm{M}}^{(\mathrm{P}_0+1)(\mathrm{P}_0+2)} + l_{\mathrm{M}}^{(\mathrm{P}_0+3)(\mathrm{P}_0+4)} & (\text{if } \mathrm{P}_0 \text{ is odd}) \\ l_{\mathrm{M}}^{\mathrm{I\,II}} + l_{\mathrm{M}}^{\mathrm{III\,IV}} + \cdots + l_{\mathrm{M}}^{(\mathrm{P}_0-1)\mathrm{P}_0} = l_{\mathrm{M}}^{\mathrm{P}_0(\mathrm{P}_0+1)} + l_{\mathrm{M}}^{(\mathrm{P}_0+2)(\mathrm{P}_0+3)} & (\text{if } \mathrm{P}_0 \text{ is even}) \end{cases}, \\
g(\mathrm{P}) &= \begin{cases} l_{\mathrm{M}}^{(\mathrm{P}_0-1)\mathrm{P}_0} & (\text{if P is odd}) \\ l_{\mathrm{M}}^{\mathrm{P}_0(\mathrm{P}_0+1)} & (\text{if P is even}) \end{cases}, \\
f(\mathrm{Q}_0) &= \begin{cases} l_{\mathrm{N}}^{\mathrm{I\,II}} + l_{\mathrm{N}}^{\mathrm{III\,IV}} + \cdots + l_{\mathrm{N}}^{(\mathrm{P}_0-2)(\mathrm{P}_0-1)} = l_{\mathrm{N}}^{(\mathrm{P}_0+1)(\mathrm{P}_0+2)} + l_{\mathrm{N}}^{(\mathrm{P}_0+3)(\mathrm{P}_0+4)} & (\text{if } \mathrm{Q}_0 \text{ is odd}) \\ l_{\mathrm{N}}^{\mathrm{I\,II}} + l_{\mathrm{N}}^{\mathrm{III\,IV}} + \cdots + l_{\mathrm{N}}^{(\mathrm{P}_0-1)\mathrm{P}_0} = l_{\mathrm{N}}^{\mathrm{P}_0(\mathrm{P}_0+1)} + l_{\mathrm{N}}^{(\mathrm{P}_0+2)(\mathrm{P}_0+3)} & (\text{if } \mathrm{Q}_0 \text{ is even}) \end{cases}, \\
g(\mathrm{Q}) &= \begin{cases} l_{\mathrm{M}}^{(\mathrm{Q}_0-1)\mathrm{Q}_0} & (\text{if Q is odd}) \\ l_{\mathrm{M}}^{\mathrm{Q}_0(\mathrm{Q}_0+1)} & (\text{if Q is even}) \end{cases}.
\end{aligned}
\tag{2-49}
$$

And the compatibility conditions are derived as

$$
\begin{gathered}
f(\mathrm{P}_0) + g(\mathrm{P}), \\
f(\mathrm{Q}_0) + g(\mathrm{Q}), \\
l_{\mathrm{M}}^{\mathrm{I\,II}} + l_{\mathrm{M}}^{\mathrm{II\,III}} + \cdots + l_{\mathrm{M}}^{(\mathrm{P}_0-1)\mathrm{P}_0} = l_{\mathrm{M}}^{\mathrm{P}_0(\mathrm{P}_0+1)} + l_{\mathrm{M}}^{(\mathrm{P}_0+1)(\mathrm{P}_0+2)} + \cdots + l_{\mathrm{M}}^{\mathrm{PI}}, \\
l_{\mathrm{N}}^{\mathrm{I\,II}} + l_{\mathrm{N}}^{\mathrm{II\,III}} + \cdots + l_{\mathrm{N}}^{(\mathrm{Q}_0-1)\mathrm{Q}_0} = l_{\mathrm{N}}^{\mathrm{Q}_0(\mathrm{Q}_0+1)} + l_{\mathrm{N}}^{(\mathrm{Q}_0+1)(\mathrm{Q}_0+2)} + \cdots + l_{\mathrm{N}}^{\mathrm{QI}}, \\
\frac{l_{\mathrm{M}}^{\mathrm{I\,II}} + l_{\mathrm{M}}^{\mathrm{II\,III}} + \cdots + l_{\mathrm{M}}^{(\mathrm{P}_0-1)\mathrm{P}_0}}{l_{\mathrm{N}}^{\mathrm{I\,II}} + l_{\mathrm{N}}^{\mathrm{II\,III}} + \cdots + l_{\mathrm{N}}^{(\mathrm{Q}_0-1)\mathrm{Q}_0}} = \frac{\cos\alpha_{\mathrm{NU}}^{\mathrm{I}} + \cos\alpha_{\mathrm{NU}}^{\mathrm{II}}}{\cos\alpha_{\mathrm{MU}}^{\mathrm{I}} + \cos\alpha_{\mathrm{MU}}^{\mathrm{II}}}.
\end{gathered}
\tag{2-50}
$$

Case 4.3:

$$
\begin{gathered}
l_{\mathrm{M}}^{\mathrm{I\,II}} + l_{\mathrm{M}}^{\mathrm{II\,III}} + \cdots + l_{\mathrm{M}}^{(\mathrm{P}_0-1)\mathrm{P}_0} = l_{\mathrm{M}}^{\mathrm{P}_0(\mathrm{P}_0+1)} + l_{\mathrm{M}}^{(\mathrm{P}_0+1)(\mathrm{P}_0+2)} + \cdots + l_{\mathrm{M}}^{\mathrm{PI}}, \\
l_{\mathrm{N}}^{\mathrm{I\,II}} + l_{\mathrm{N}}^{\mathrm{II\,III}} + \cdots + l_{\mathrm{N}}^{(\mathrm{Q}_0-1)\mathrm{Q}_0} = l_{\mathrm{N}}^{\mathrm{Q}_0(\mathrm{Q}_0+1)} + l_{\mathrm{N}}^{(\mathrm{Q}_0+1)(\mathrm{Q}_0+2)} + \cdots + l_{\mathrm{N}}^{\mathrm{QI}}, \\
\frac{l_{\mathrm{M}}^{\mathrm{I\,II}} + l_{\mathrm{M}}^{\mathrm{III\,IV}} + l_{\mathrm{M}}^{\mathrm{V\,VI}} + \cdots - \left(l_{\mathrm{M}}^{\mathrm{II\,III}} + l_{\mathrm{M}}^{\mathrm{IIII\,V}} + l_{\mathrm{M}}^{\mathrm{VI\,VII}} + \cdots\right)}{l_{\mathrm{N}}^{\mathrm{I\,II}} + l_{\mathrm{N}}^{\mathrm{III\,IV}} + l_{\mathrm{N}}^{\mathrm{V\,VI}} + \cdots - \left(l_{\mathrm{N}}^{\mathrm{II\,III}} + l_{\mathrm{N}}^{\mathrm{IIII\,V}} + l_{\mathrm{N}}^{\mathrm{VI\,VII}} + \cdots\right)} = \frac{\cos\alpha_{\mathrm{NU}}^{\mathrm{I}} - \cos\alpha_{\mathrm{NU}}^{\mathrm{II}}}{\cos\alpha_{\mathrm{MU}}^{\mathrm{I}} - \cos\alpha_{\mathrm{MU}}^{\mathrm{II}}}, \\
\frac{l_{\mathrm{M}}^{\mathrm{I\,II}} + l_{\mathrm{M}}^{\mathrm{II\,III}} + \cdots + l_{\mathrm{M}}^{(\mathrm{P}_0-1)\mathrm{P}_0}}{l_{\mathrm{N}}^{\mathrm{I\,II}} + l_{\mathrm{N}}^{\mathrm{II\,III}} + \cdots + l_{\mathrm{N}}^{(\mathrm{Q}_0-1)\mathrm{Q}_0}} = \frac{\cos\alpha_{\mathrm{NU}}^{\mathrm{I}} + \cos\alpha_{\mathrm{NU}}^{\mathrm{II}}}{\cos\alpha_{\mathrm{MU}}^{\mathrm{I}} + \cos\alpha_{\mathrm{MU}}^{\mathrm{II}}}.
\end{gathered}
\tag{2-51}
$$

The theoretical framework established above provides a robust basis for synthesizing a diverse range of origami structures. Notably, the solution in case 4.1 mathematically recovers the geometry of the classical Miura-ori pattern, validating the generality of the results. Applying the conditions derived in cases 4.2 and 4.3 allows for the construction of the alternative origami configurations shown in Fig. 2-11. For these specific configurations, the kinematic curves in Figs. 2-11(a) and 2-11(b) indicate that these structures can neither achieve a fully flat-folded state nor a flat-deployed state, where the gray shaded regions denote ranges physically inaccessible due to model interference.

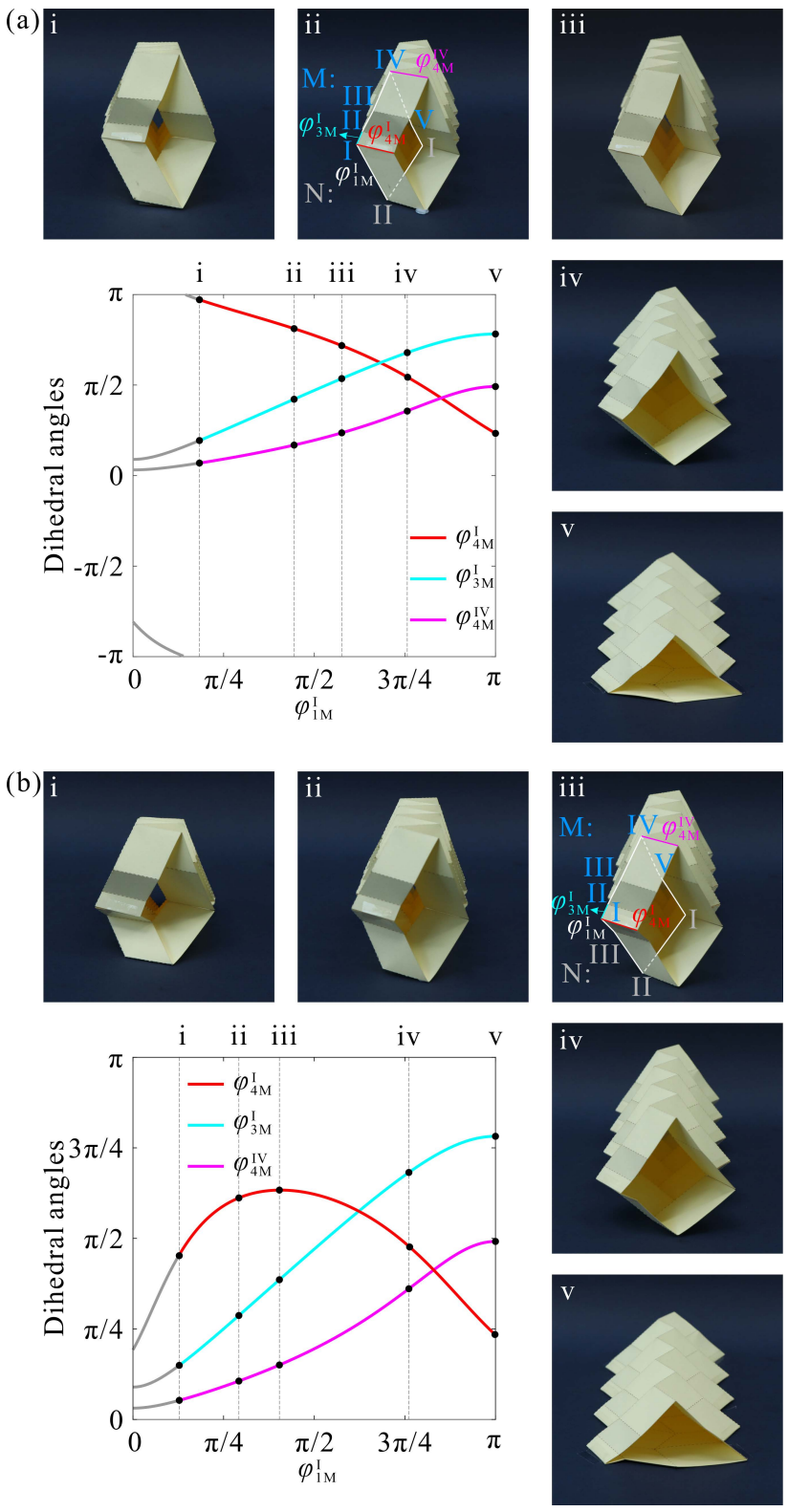

Fig. 2-11 Kinematic relationships of dihedral angles and the corresponding folding processes for configurations based on (a) case 4.2 and (b) case 4.3, with (a) $l_{\mathrm{M}}^{\mathrm{II\,III}}=2l_{\mathrm{M}}^{\mathrm{I\,II}}, l_{\mathrm{M}}^{\mathrm{III\,IV}}=3l_{\mathrm{M}}^{\mathrm{I\,II}}, l_{\mathrm{N}}^{\mathrm{I\,II}}=l_{\mathrm{N}}^{\mathrm{II\,III}}$, $\alpha_{\mathrm{MU}}^{\mathrm{I}}=\pi/3, \alpha_{\mathrm{MU}}^{\mathrm{II}}=4\pi/9, \alpha_{\mathrm{NU}}^{\mathrm{I}}=5\pi/18, \alpha_{\mathrm{NU}}^{\mathrm{II}}=5\pi/12$, and (b) $l_{\mathrm{M}}^{\mathrm{II\,III}}=2l_{\mathrm{M}}^{\mathrm{I\,II}}, l_{\mathrm{M}}^{\mathrm{III\,IV}}=3l_{\mathrm{M}}^{\mathrm{I\,II}}, l_{\mathrm{M}}^{\mathrm{IV\,V}}=2.5l_{\mathrm{M}}^{\mathrm{I\,II}}$, $\alpha_{\mathrm{MU}}^{\mathrm{I}}=\pi/3, \alpha_{\mathrm{MU}}^{\mathrm{II}}=4\pi/9, \alpha_{\mathrm{NU}}^{\mathrm{I}}=5\pi/18, \alpha_{\mathrm{NU}}^{\mathrm{II}}=5\pi/12$.

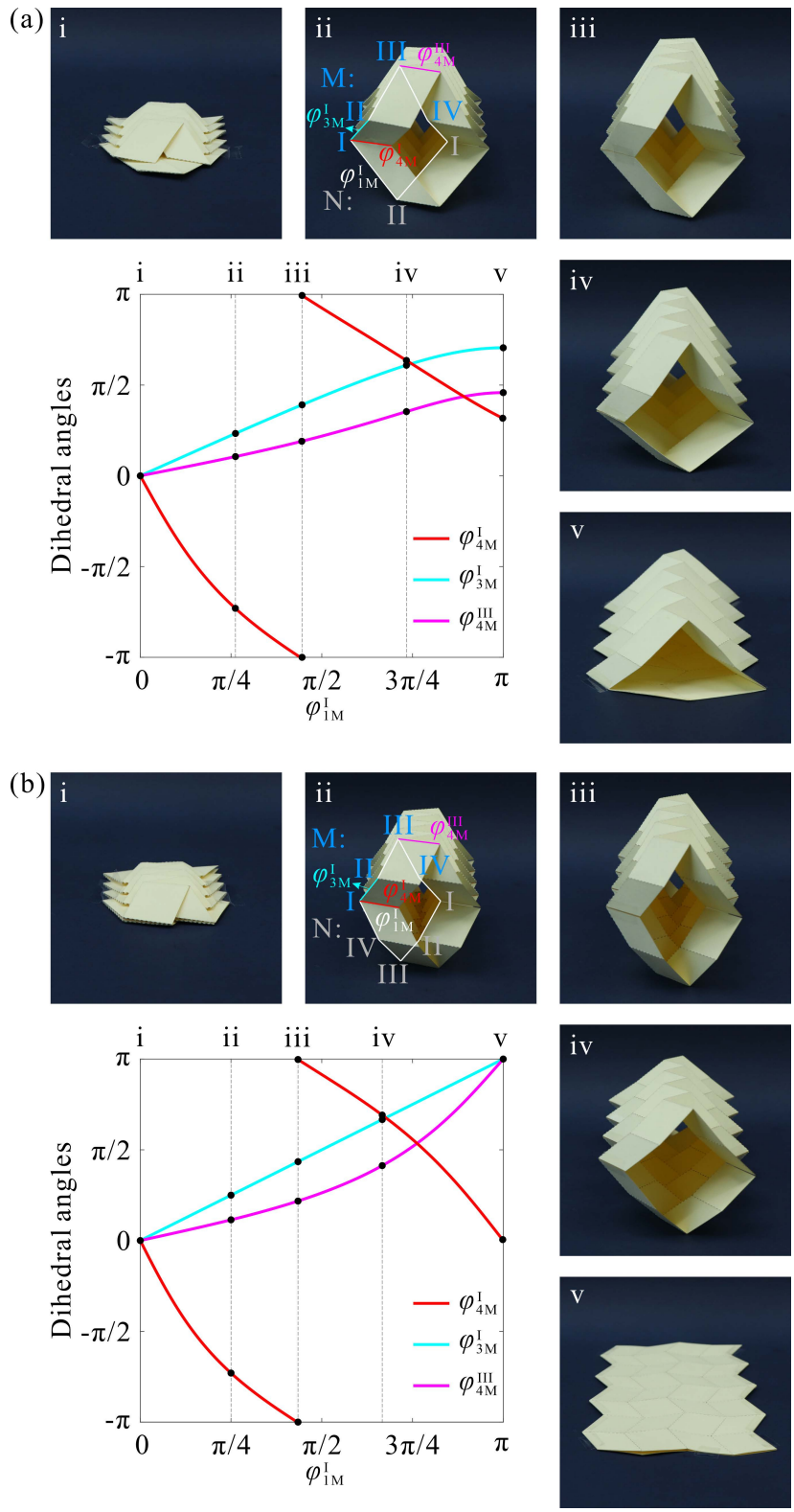

Fig. 2-12 Kinematic relationships of dihedral angles and the corresponding folding processes for configurations based on case 4.2, with (a) $l_{\mathrm{M}}^{\mathrm{I\,II}}=l_{\mathrm{M}}^{\mathrm{II\,III}}=l_{\mathrm{M}}^{\mathrm{III\,IV}}=l_{\mathrm{M}}^{\mathrm{IV\,P}}, l_{\mathrm{N}}^{\mathrm{I\,II}}=l_{\mathrm{N}}^{\mathrm{II\,I}}, \alpha_{\mathrm{MU}}^{\mathrm{I}}=5\pi/18, \alpha_{\mathrm{MU}}^{\mathrm{II}}=4\pi/9, \alpha_{\mathrm{NU}}^{\mathrm{I}}=2\pi/9, \alpha_{\mathrm{NU}}^{\mathrm{II}}=7\pi/18$, and (b) $l_{\mathrm{M}}^{\mathrm{I\,II}}=l_{\mathrm{M}}^{\mathrm{II\,III}}=l_{\mathrm{M}}^{\mathrm{III\,IV}}=l_{\mathrm{M}}^{\mathrm{IV\,I}}=l_{\mathrm{N}}^{\mathrm{I\,II}}=l_{\mathrm{N}}^{\mathrm{II\,III}}=l_{\mathrm{N}}^{\mathrm{III\,IV}}=l_{\mathrm{N}}^{\mathrm{IV\,I}}, \alpha_{\mathrm{MU}}^{\mathrm{I}}=\alpha_{\mathrm{NU}}^{\mathrm{II}}=4\pi/9, \alpha_{\mathrm{MU}}^{\mathrm{II}}=\alpha_{\mathrm{NU}}^{\mathrm{I}}=5\pi/18$.

Nevertheless, by carefully selecting design parameters within these theoretical cases, complex flat-foldable assemblies can still be achieved. As demonstrated in Figs. 2-12(a) and 2-12(b), origami structures composed of six or eight 4-crease vertices can be successfully constructed to allow for flat-foldability.

To conclude, this section has successfully generalized the kinematic analysis to origami assemblies composed of multiple 4-crease vertices. By decomposing the complex loop into discrete geometric chains, universal compatibility conditions governing the relative geometric parameters were derived. The analysis identified specific solution classes, case 3 and case 4, which enable the construction of single-DOF tubular origami structures with complex spatial polygonal cross-sections. Notably, this framework recovers classical patterns such as the Miura-ori as a subset (case 4.1) while unlocking novel configurations with tailored folding characteristics (cases 4.2 and 4.3). These theoretical advancements provide a robust methodology for synthesizing complex tubular origami structures with versatile spatial configurations, serving as the building blocks for the advanced metamaterial design discussed in the following section.

2.4 Design and Tessellation of Double-Tubular Origami Structures

Based on the compatibility conditions established in the previous sections, single-tubular origami structures oriented along specific axes can be systematically constructed. However, the proposed theoretical framework offers design flexibility that extends well beyond simple single-tubular configurations. This section utilizes the derived compatibility conditions to explore advanced construction possibilities, specifically focusing on the synthesis of double-tubular origami structures through constraint-based geometric coupling.

The construction process begins with a primary single-tubular structure derived from the case 4.2 compatibility conditions, as illustrated in Fig. 2-13(a). The boundary interface of this structure, specifically the section defined by the polygon ABCDEF, possesses the geometric characteristics to serve as a shared constraint boundary for an adjacent substructure. By treating this interface as a linkage foundation, a secondary origami assembly with a distinct spatial orientation can be coupled to the primary unit, as presented in Fig. 2-13(b). To ensure the rigid foldability of this coupled assembly, strict parameter matching is required at the connecting vertices. In the primary structure

(Fig. 2-13(a)), vertices B, C, and E, are fully defined flat-foldable 4-crease vertices. Taking vertex B as an example, its two angular parameters and four length parameters are intrinsic to the primary design. Consequently, for the secondary substructure shown in Fig. 2-13(b) (defined by the cross-section BHKG), the kinematic constraints propagate from vertex B. Thus, we have:

$$\begin{aligned} \alpha_{12}^{\mathrm{B}}+\alpha_{34}^{\mathrm{B}}=\pi,\ \alpha_{23}^{\mathrm{B}}+\alpha_{41}^{\mathrm{B}}=\pi, \\ \alpha_{12}^{\mathrm{K}}+\alpha_{34}^{\mathrm{K}}=\pi,\ \alpha_{23}^{\mathrm{K}}+\alpha_{41}^{\mathrm{K}}=\pi. \end{aligned} \tag{2-52}$$

If the lengths satisfy $l^{\mathrm{BG}}\neq l^{\mathrm{BH}}$, the governing compatibility equation corresponds to Eq. (2-46), satisfying:

$$\begin{aligned} l^{\mathrm{BG}}=l^{\mathrm{HK}},\ l^{\mathrm{BH}}=l^{\mathrm{GK}}, \\ \alpha_{12}^{\mathrm{B}}=\alpha_{12}^{\mathrm{K}},\ \alpha_{23}^{\mathrm{B}}=\alpha_{23}^{\mathrm{K}}. \end{aligned} \tag{2-53}$$

Conversely, if the geometric setup dictates an alternative relationship where $l^{\mathrm{BG}}=l^{\mathrm{BH}}$ under specific symmetric conditions, the system adheres to Eq. (2-50):

$$\begin{aligned} l^{\mathrm{KG}}=l^{\mathrm{KH}}, \\ \frac{l^{\mathrm{BG}}}{l^{\mathrm{KG}}}=\frac{\cos\alpha_{12}^{\mathrm{K}}+\cos\alpha_{23}^{\mathrm{K}}}{\cos\alpha_{34}^{\mathrm{B}}+\cos\alpha_{41}^{\mathrm{B}}}. \end{aligned} \tag{2-54}$$

Simultaneously, vertex D in the primary structure functions as an eggbox-type vertex, with its four angular and four length parameters already determined. Furthermore, vertex D shares fully defined parallelogram facets with the adjacent flat-foldable 4-crease vertices (C and E); a similar geometric constraint applies to vertex L. Due to these shared kinematic chains, the spatial position and angular parameters of the resulting vertex L are uniquely constrained. Thus, regardless of the specific case applied (Eq. (2-46) or Eq. (2-50)), the four angular and four length parameters of the eggbox vertex L are uniquely determined by the closure constraints of the adjacent loops. Consequently, by synthesizing the primary configuration from Fig. 2-13(a) with the derived secondary substructure from Fig. 2-13(b), a complete double-tubular origami unit is obtained, as shown in Fig. 2-13(c). This derivation confirms that once the geometry of the primary single-tubular structure is defined, the kinematic profile of the corresponding double-tubular configuration is uniquely determined by the governing compatibility conditions, ensuring a single-DOF motion for the combined assembly.

Due to the absence of inherent symmetry in the generalized double-tubular unit, assembling multiple units into a large-scale mechanism requires a specific rotational tessellation strategy to ensure geometric continuity. Unlike uniform tessellations that

rely solely on simple translation, the asymmetric nature of these units necessitates a more complex arrangement to maintain kinematic compatibility. Figure 2-14 illustrates the fundamental building blocks derived from this strategy. The reference configuration is designated as original unit ①. By performing spatial rotations on this primary unit along the coordinate axes, a series of complementary configurations, referred to as rotated units ②, ③, and ④, are generated. These derived variants are not merely reoriented duplicates but serve as essential distinct components that allow the structure to extend continuously in 3D space.

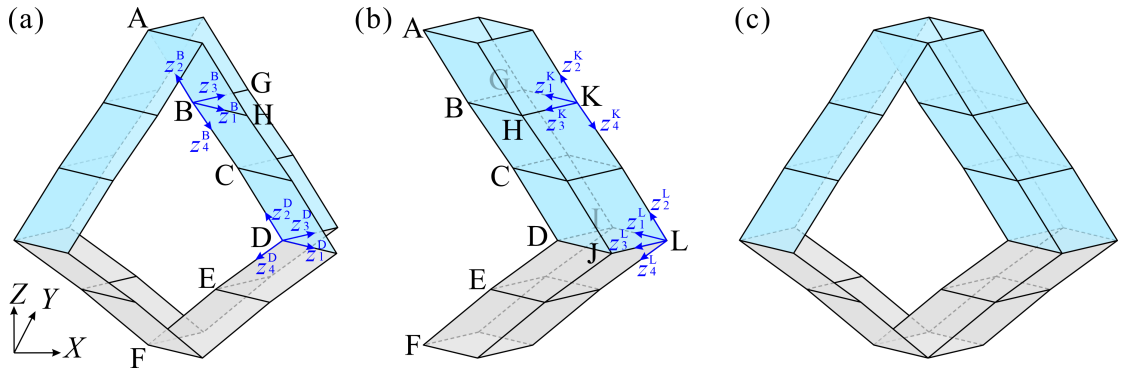

Fig. 2-13 Construction of double-tubular origami structure. (a) Primary single-tubular configuration based on case 4.2; (b) auxiliary origami substructure; (c) the double-tubular origami structure.

Crucially, Figure 2-15(a) provides the detailed geometric definition of the reference configuration, designated as original unit ①. To explicitly illustrate the geometric interface, the figure presents a 3D isometric view alongside a side view, in which the boundary contour is highlighted by red lines and the vertices are marked by red squares. The side view reveals that the outer boundary exhibits a distinct zig-zag profile, which acts as a specific geometric interface for connectivity. The assembly variants are generated through spatial rotations of this reference unit, as shown in Fig. 2-15(b)-(d). Notably, these spatial rotations not only reorient the structure in 3D space but also transform the alignment of this zig-zag profile. This transformation is vital because it ensures that the boundary profiles of adjacent units are mathematically compatible, allowing them to interlock perfectly without physical interference.

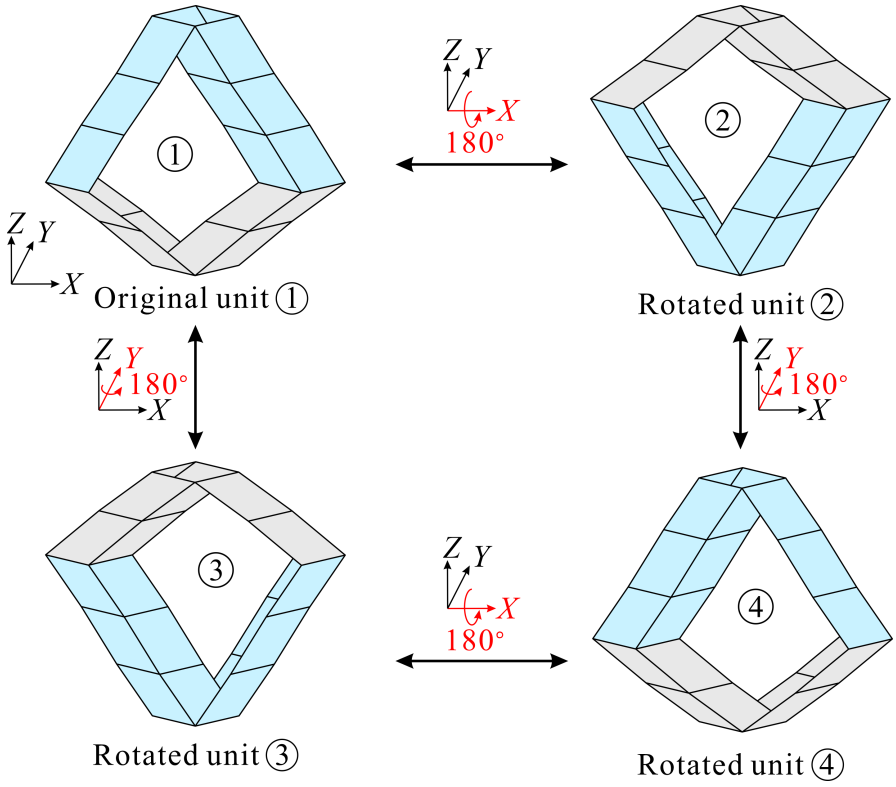

Fig. 2-14 Orientation variants of the double-tubular origami unit: original unit ① and the derived rotated units ②, ③, and ④.

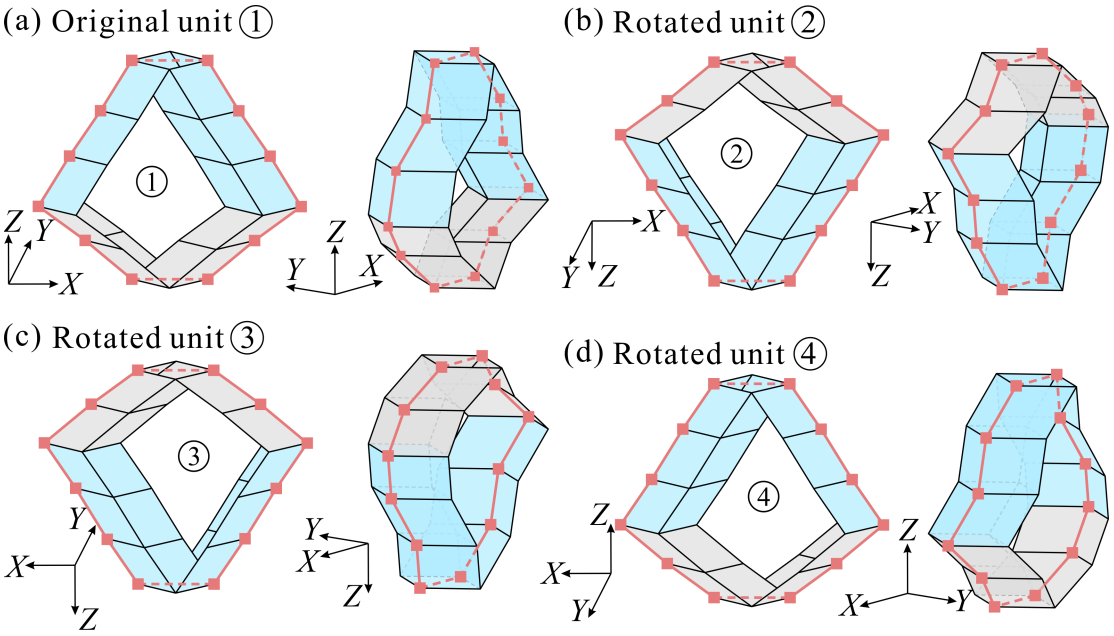

Fig. 2-15 Geometric definition and orientation variants of the double-tubular origami unit. (a) Original unit ①; (b) rotated unit ②; (c) rotated unit ③; (d) rotated unit ④.

Consequently, when interconnecting multiple double-tubular units to form an extensive structure, stringent connectivity rules must be satisfied to address the absence of inherent symmetry in the generalized double-tubular unit. As detailed in the geometric definition, the outer boundary of these units exhibits a distinct zig-zag profile. Since spatial rotations transform the alignment of this profile, adjacent units must not only connect via shared edges but also strictly maintain identical relative positions of their outer profiles along the interface to ensure compatibility. For example, as illustrated in Fig. 2-16(a), the tessellation requires a specific matching of rotated variants: the blue component of unit ① must connect exclusively with the blue component of unit ②, whereas the gray component of unit ① is compatible only with unit ③. Through this specific rotational tessellation strategy, which ensures geometric continuity across the boundaries, double-tubular origami structures can be systematically arranged in 3D space to construct extensive kinematic grids, ultimately forming an origami metamaterial with single-DOF mobility, as shown in Fig. 2-16(b).

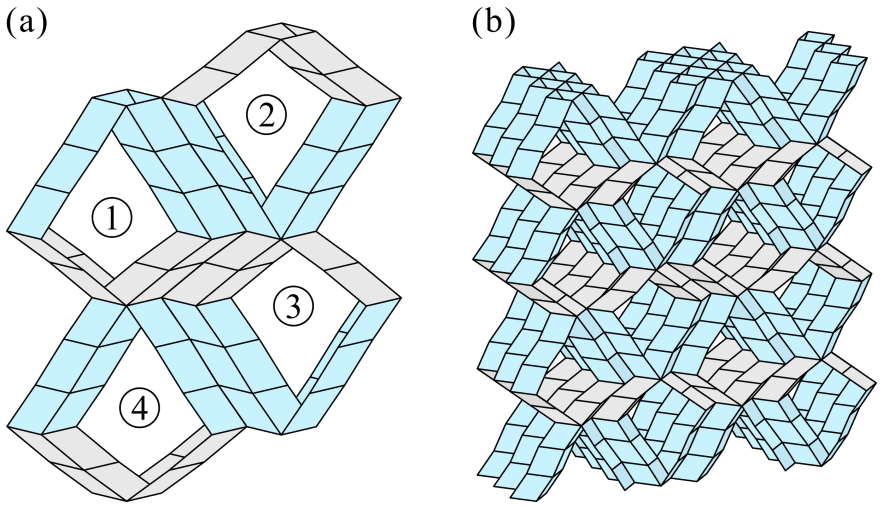

Fig. 2-16 Tessellation rules for the assembly of double-tubular structures. (a) Tessellation of distinct rotated origami units; (b) assembled origami metamaterial.

As a representative example, we adopt the specific unit configuration shown in Fig. 2-4(a), which features high symmetry and possesses two compact 2D states, as the primary structure. Through the systematic execution of the previously discussed tessellation strategy, these primary structures are interconnected to form the double-tubular origami metamaterial presented in Fig. 2-17. The kinematic analysis of this

metamaterial reveals a distinct coupling effect: the dihedral angles φ_3^{D} and φ_4^{D} exhibit opposite variation trends throughout the motion. Specifically, as one set of dihedral angles increases, the other set decreases, implying that the expansion of the structure along one tubular axis is coupled with a contraction or distinct geometric transformation along the orthogonal axis. Physically, this characteristic indicates that the tubular pathways aligned along the two distinct directions undergo inverse geometric evolutions during the folding process, thereby endowing the metamaterial with complex, direction-dependent spatial reconfiguration capabilities.

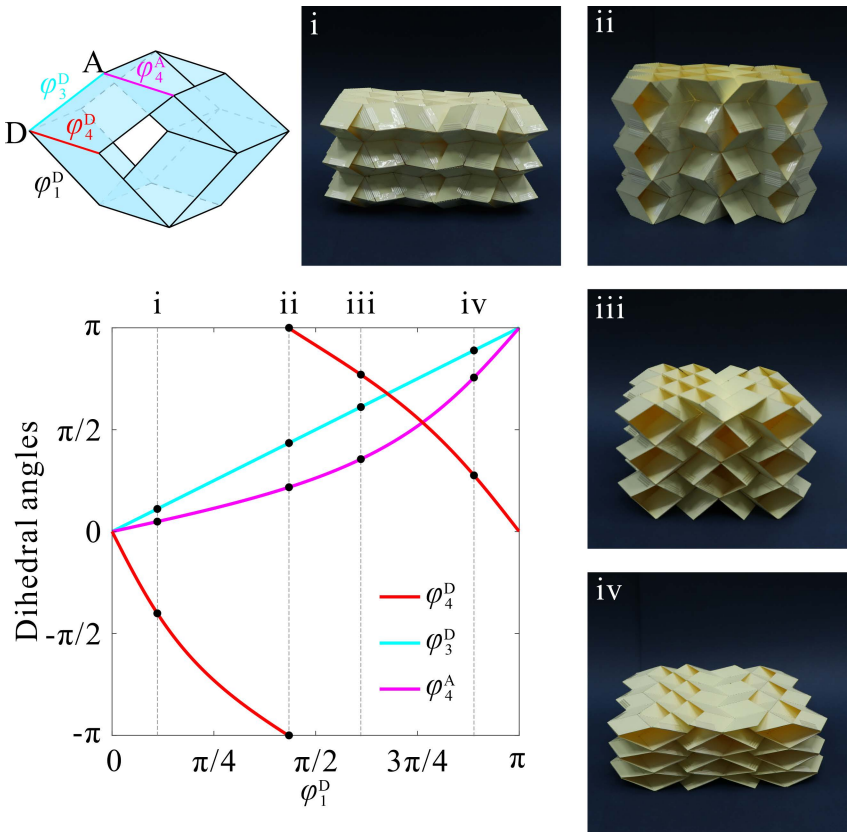

Fig. 2-17 Double-tubular origami metamaterial based on the origami structure in Fig. 2-4(a).

2.5 Conclusions and Discussion

In this chapter, a generalized kinematic framework has been established for the synthesis and analysis of rigid-foldable tubular origami structures constructed from 4-crease vertices, effectively eliminating the design limitations imposed by traditional co-planar cross-section assumptions. By decomposing the spatial assembly into upper and lower parts with loop-closure constraints, the research has derived explicit

compatibility conditions for both fundamental four-vertex loops and generalized multi-vertex chains. This rigorous analytical approach has significantly extended the feasible design space, enabling the construction of diverse configurations ranging from simple parallelograms to complex spatial polygonal cross-sections. Guided by these theoretical results, a novel double-tubular origami unit has been successfully constructed via constraint-based geometric coupling. Furthermore, a systematic tessellation strategy has been developed, employing specific rotational transformations to ensure the geometric and kinematic continuity of these units within cellular metamaterials. These advancements position the proposed framework as a versatile design methodology, paving the way for applications in deployable aerospace systems, soft robotics, and architectural structures.

In addition, although the generalized kinematic framework developed in this chapter significantly expands the feasible design space for tubular origami structures, practical considerations for subsequent metamaterial design indicate that symmetric configurations with coplanar cross-sectional vertices are often more advantageous. Symmetric designs provide more predictable and uniform folding behavior and simplify tessellation strategies. Therefore, while the theoretical design space accommodates highly diverse spatial polygonal cross-sections, prioritizing symmetry in future designs is expected to improve geometric compatibility and ease the implementation of complex origami metamaterials.

The present study is formulated within the framework of zero-thickness rigid origami, and the effect of panel thickness on foldability is therefore not considered. Meanwhile, the analytical solvability of the proposed framework relies on the flat-foldability constraint, which serves as a necessary dimensionality-reduction step. As a result, the present solution is limited to a specific class of tubular origami structures and does not include more general configurations containing three or more eggbox-type vertices. Future work may address these limitations from both physical and methodological perspectives. On the one hand, incorporating thickness effects would enable a more realistic kinematic synthesis of tubular origami structures. On the other hand, for tubular assemblies composed of general 4-crease vertices, numerical approaches could be introduced to handle the compatibility conditions in the resulting high-dimensional nonlinear design space.

Chapter 3 Single-Tubular Metamaterials with Programmable Mechanical and Acoustic Properties via M-V Assignments

3.1 Introduction

Based on the compatibility conditions discussed in Chapter 2, a variety of origami structures with distinct geometric characteristics and folding behaviors can be designed. By tessellating these units in 3D space, origami metamaterials can be constructed. Regarding the performance of such structures, systematic studies have been extensively conducted on the influence of geometric and material parameters, such as design angles, panel side lengths, folding angles, and wall thickness, on their physical properties. However, with respect to the influence of M-V assignments, previous studies have primarily focused on variations in geometry, with limited research dedicated to their specific effects on physical properties.

Thus, the objective of this chapter is to program the mechanical and acoustic properties of single-tubular metamaterials by varying M-V assignments. For this purpose, a series of single-DOF rigid foldable origami metamaterials based on the double-corrugated pattern are created by altering their crease assignments. The geometric dimensions and Poisson's ratios of these metamaterials are theoretically analyzed to establish their kinematic foundations. To further investigate the impact of M-V assignments on mechanical and acoustic performance, a combined approach utilizing finite element (FE) simulation and experiments is employed. By systematically correlating specific M-V configurations with their corresponding physical responses, this chapter demonstrates that altering M-V assignments is an effective strategy for performance programming.

The outline of this chapter is as follows. Section 3.2 presents the geometric design, identifying four distinct rigid foldable units, and derives their Poisson's ratios. Section 3.3 systematically investigates the mechanical properties, comparing the structural responses of uniform and mixed metamaterials. Subsequently, Section 3.4 extends this comparative framework to investigate the acoustic properties of both uniform and mixed designs. Finally, conclusions are included in Section 3.5, which ends this chapter.

3.2 Geometric Design

The double-corrugated pattern, shown in Fig. 3-1(a), represents a typical origami pattern consisting of degree-4 vertices. It composes two types of rhombi with identical side lengths a but varying internal angles, named α and β. Based on the Maekawa-Justin theory and the Big-Little-Big Angle theorem, numerous M-V assignments can be applied to this origami pattern. Figure 3-1(b) illustrates a rigid M-V assignment, while Fig. 3-1(c) shows a non-rigid one, where solid and dashed lines represent mountain and valley creases, respectively. In a study conducted by Peng et al. [48], the rigid foldability of the units ABCD and ABEF shown in Fig. 3-1(a) was examined using kinematic analysis, considering all possible M-V assignments. Based on the previous analysis, four distinct rigid foldable origami units with single DOF can be constructed within a 4×4 origami pattern, labeled as DC-1 to DC-4 in Fig. 3-2. The gray area shown in the figure represents the smallest unit of the origami structure. This unit can be repetitively arranged in a 2D plane to form a larger origami pattern. For the four types of origami units shown in Fig. 3-2, the angles φ_i, θ_i (i=1, 2, 3, 4), ε_i (i=2, 4) represent the dihedral angle between the panels, and δ_i and γ_i (i=1, 2, 3, 4) represent the dihedral angle between the panel and the plane spanned by vectors BA and BC. Additionally, creases of the same color correspond to identical dihedral angles. In this paper, we consider φ_i as the folding parameter of the origami units, and the relationships of other angles plotted in Fig. 3-3 can be obtained using the following equations[147,148]:

$$\theta_i = \begin{cases} \pi - 2\arctan\left(\cot\dfrac{\varphi_i}{2}\cos\dfrac{\beta-\alpha}{2} \Big/ \cos\dfrac{\beta+\alpha}{2} \right) & \text{when } i = 1, 2 \\ 2\arctan\left(\tan\dfrac{\varphi_i}{2}\sin\dfrac{\beta-\alpha}{2} \Big/ \sin\dfrac{\alpha+\beta}{2} \right) & \text{when } i = 3, 4 \end{cases}, \tag{3-1}$$

$$\delta_i = \begin{cases} \dfrac{\pi}{2} - \arctan\left[\left(\cos\beta\sin\alpha - \cos\alpha\sin\beta\cos\varphi_i\right) / \left(\sin\beta\sin\varphi_i\right) \right] & \text{when } i = 1, 2 \\ \dfrac{\pi}{2} + \arctan\left(\cos\alpha\cot\varphi_i + \cot\beta\csc\varphi_i\sin\alpha\right) & \text{when } i = 3, 4 \end{cases}, \tag{3-2}$$

$$\gamma_i = \begin{cases} \dfrac{\pi}{2} - \arctan\left[\left(\cos\alpha\sin\beta - \cos\beta\sin\alpha\cos\varphi_i\right) / \left(\sin\alpha\sin\varphi_i\right) \right] & \text{when } i = 1, 2 \\ \dfrac{\pi}{2} - \arctan\left(\cos\beta\cot\varphi_i + \cot\alpha\csc\varphi_i\sin\beta\right) & \text{when } i = 3, 4 \end{cases}, \tag{3-3}$$

$$\varepsilon_i = \begin{cases} 2\arctan\left(\tan\dfrac{\varphi_i}{2} \sin\dfrac{\alpha+\beta}{2} \Big/ \sin\dfrac{\beta-\alpha}{2} \right) & \text{when } i=2 \\ 2\operatorname{arccot}\left(\cot\dfrac{\varphi_i}{2} \cos\dfrac{\alpha+\beta}{2} \Big/ \cos\dfrac{\beta-\alpha}{2} \right) & \text{when } i=4 \end{cases}. \tag{3-4}$$

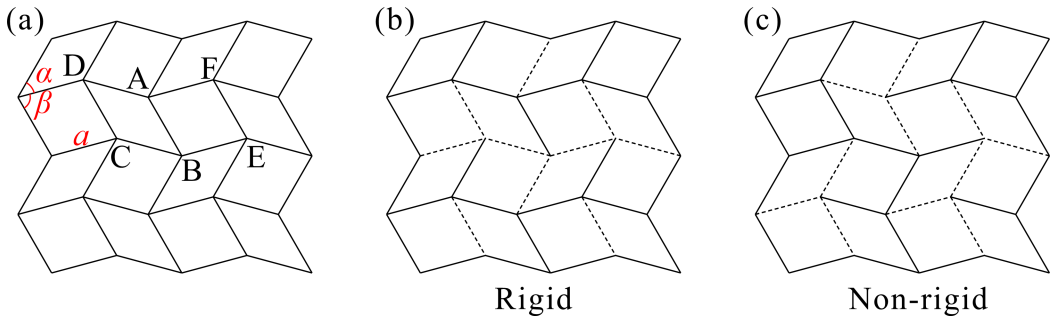

Fig. 3-1 (a) The double-corrugated origami pattern; (b) M-V assignments of a rigid origami pattern and (c) a non-rigid origami pattern.

The geometric dimensions are indicated in blue in Fig. 3-2, in which *w*, *l*, and *h* are the geometric dimensions in *x*, *y*, and *z* directions, representing the width, length, and height of the origami units, respectively. It is important to note that the plane spanned by vectors BA and BC and the plane spanned by vectors ED and EF are identical. Hence, the height *h* also represents the perpendicular distance from point G to this plane. The geometric dimensions can be derived by applying the following equations:

$$w_i = \begin{cases} 2a\sqrt{\left(1-\cos\alpha\cos\beta-\sin\alpha\sin\beta\cos\varphi_i\right)/2} & \text{when } i=1 \\ w_1 & \text{when } i=2 \\ 2a\sqrt{\left(1-\cos\alpha\cos\beta-\sin\alpha\sin\beta\cos\theta_i\right)/2} & \text{when } i=3 \\ 2w_3 & \text{when } i=4 \end{cases}, \tag{3-5}$$

$$l_i = \begin{cases} 2a\sqrt{\left(1+\cos\alpha\cos\beta-\sin\alpha\sin\beta\cos\theta_i\right)/2} & \text{when } i=1 \\ 2l_1 & \text{when } i=2 \\ 2a\sqrt{\left(1+\cos\alpha\cos\beta-\sin\alpha\sin\beta\cos\varphi_i\right)/2} & \text{when } i=3 \\ l_3 & \text{when } i=4 \end{cases}, \tag{3-6}$$

$$h_i = \begin{cases} a\sin\alpha\sin\delta_i & \text{when } i=1,3 \\ 2a\sin\alpha\sin\delta_i & \text{when } i=2,4 \end{cases}. \tag{3-7}$$

Then, the Poisson's ratios in different direction v_{xy} and v_{xz} can be calculated as

$$\upsilon_{xy} = -\frac{dl/l}{dw/w}, \tag{3-8}$$

$$\upsilon_{xz} = -\frac{dh/h}{dw/w}. \tag{3-9}$$

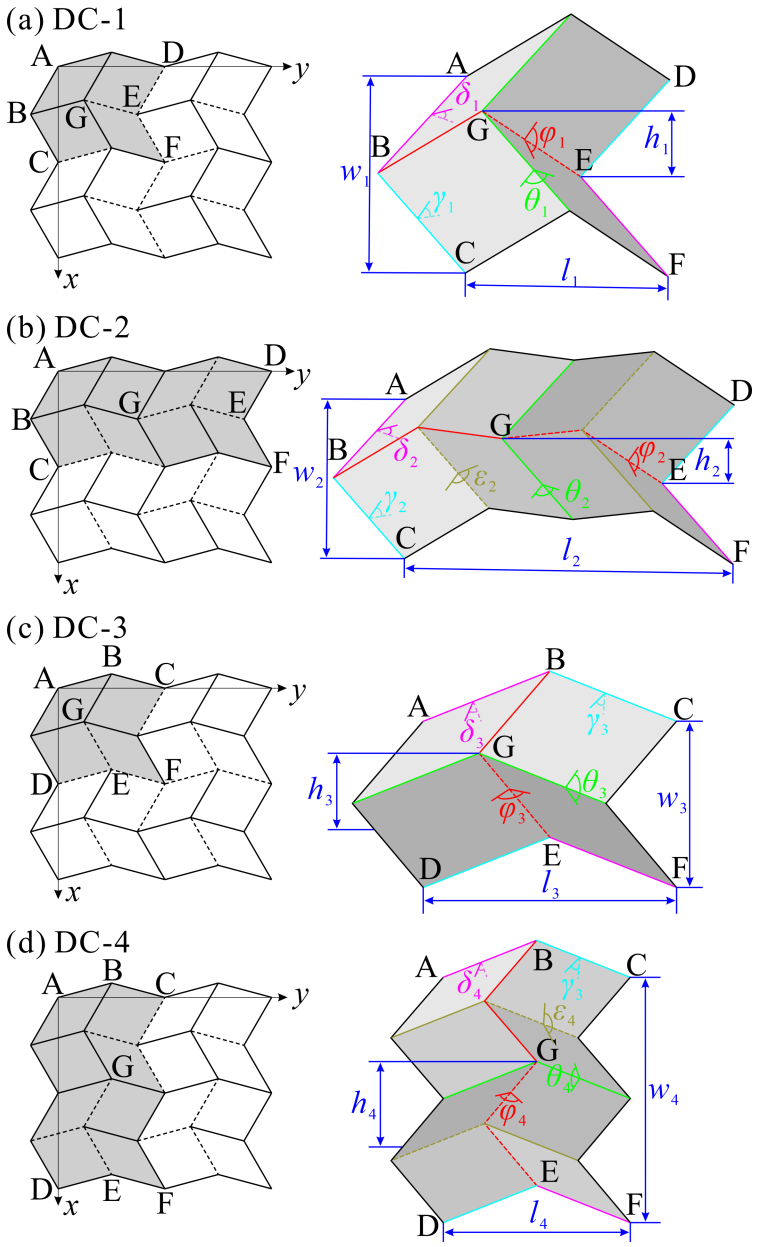

Fig. 3-2 The M-V assignments of four typical origami units and their corresponding geometry: (a) DC-1; (b) DC-2; (c) DC-3; (d) DC-4.

Figure 3-4 illustrates the geometric dimensions and Poisson's ratios of the four units, with the Poisson's ratios validated by simulations. It is evident from Figs. 3-4(a) and 3-4(b) that despite variations in the M-V assignments, the configurations DC-1 and DC-2 share identical v_{xy} and v_{xz}. Similarly, DC-3 and DC-4 also exhibit the same

Poisson's ratios. This behavior can be attributed to the fact that changes in the M-V assignments lead to alterations in the geometries of the units. However, there exists a two-fold relationship between their geometric dimensions, as shown in Eqs. (3-5)-(3-7). Consequently, according to the definition of Poisson's ratio outlined in Eqs. (3-8)-(3-9), the configurations display the same Poisson's ratio. These configurations exhibit a negative v_{xy} and a negative-positive v_{xz}. The positive Poisson's ratio of the origami structure attributes to the typically wine-rack mechanism[149-151]. The single-tubular origami metamaterials can be obtained by mirroring the origami sheets along the plane spanned by vectors BA and BC. The folding processes of these origami metamaterials are shown in Fig. 3-5.

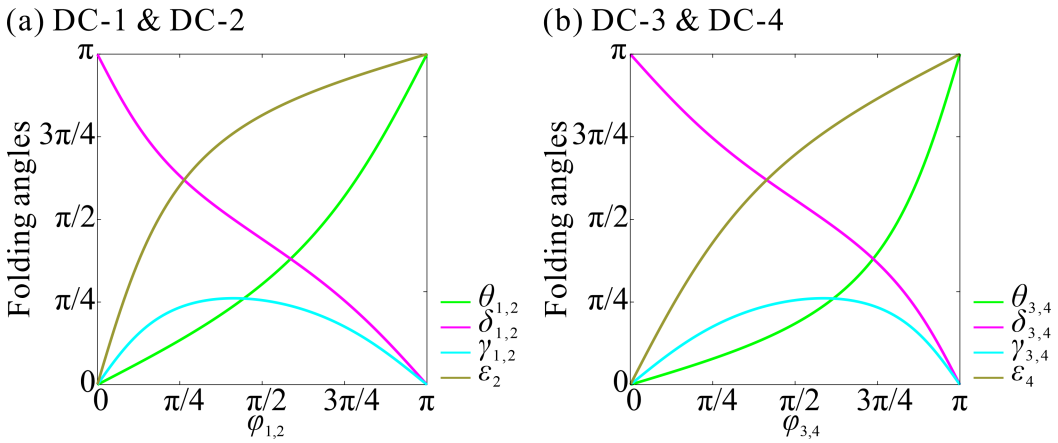

Fig. 3-3 Variations in different folding angles: (a) DC-1 and DC-2; (b) DC-3 and DC-4.

Mixed metamaterials are constructed under the premise of a finite number of units. For the current metamaterial size of 6×6×2, it can be regarded as being formed by the repeating arrangement of two types of unit cells. Specifically, mixed metamaterials are constructed by connecting origami configurations that share the same Poisson's ratio along the direction where their geometric dimensions are identical. To be more precise, DC-1 and DC-2 are connected in the *x* direction, while DC-3 and DC-4 are connected in the *y* direction. We use the variable *n*×6 to represent the number of DC-2 (or DC-4) units within a layer. For instance, when *n* is set to 1, it is denoted as DC-M*x*-1 (or DC-M*y*-1), meaning that there are 1×6 DC-2 (DC-4) units in a layer. By varying the value of *n*, we can construct several different origami metamaterials shown in Fig. 3-6, in which DC-M*x*-0, DC-M*x*-3, DC-M*y*-0, and DC-M*y*-3 are the uniform metamaterials, corresponding to DC-1 to DC-4, respectively, and DC-M*x*-1, DC-M*y*-1, DC-M*x*-2, and

DC-M*y*-2 are the mixed metamaterials. When the number of units is further increased, the mixed metamaterial can also be viewed as a single unit cell that tiles in three-dimensional space.

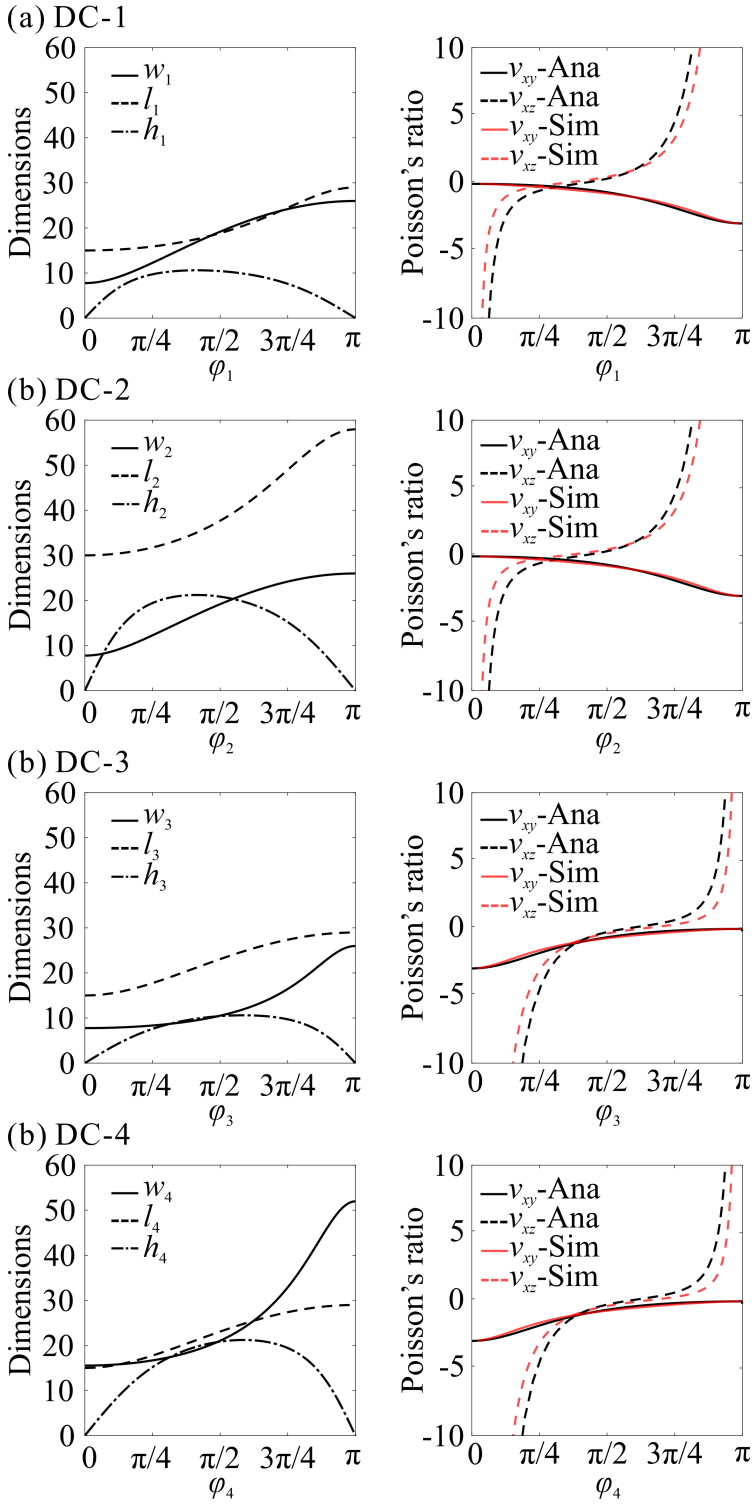

Fig. 3-4 Geometric dimensions and Poisson's ratio of the origami units: (a) DC-1; (b) DC-2; (c) DC-3; (d) DC-4.

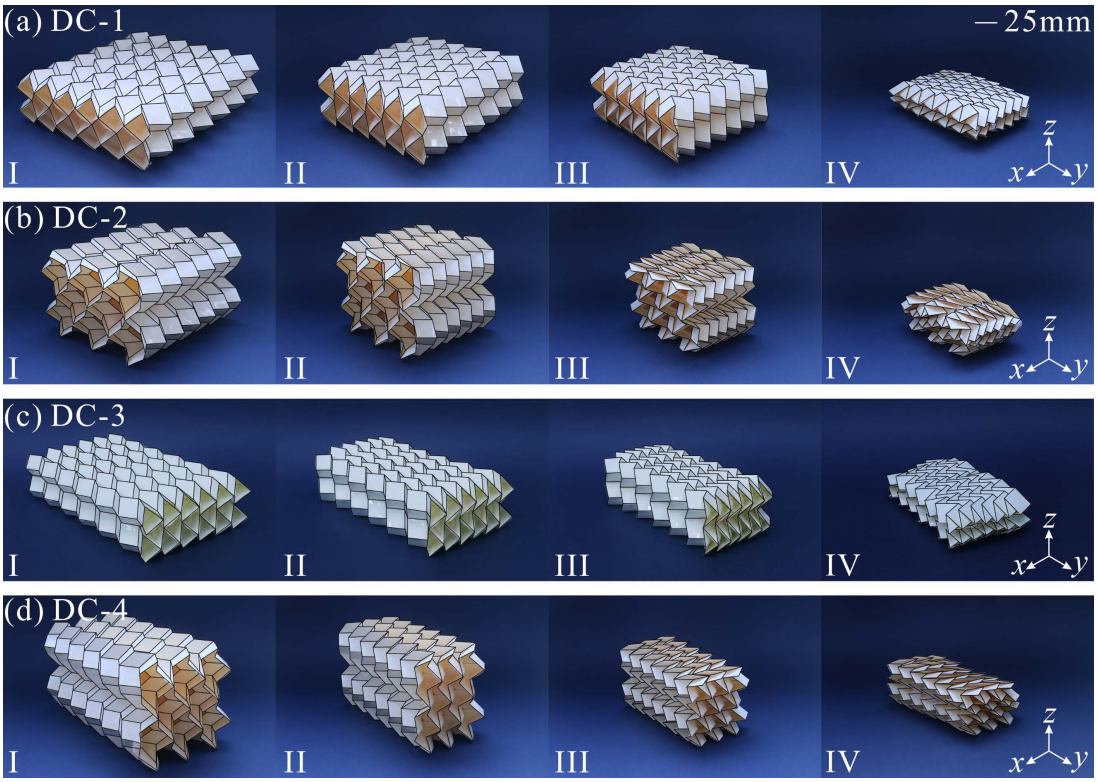

Fig. 3-5 The 6×6×4 origami metamaterials formed by origami units, in which each layer consists of 6×6 double-corrugated vertices and there is a total number of 4 layers: (a) DC-1; (b) DC-2; (c) DC-3; (d) DC-4.

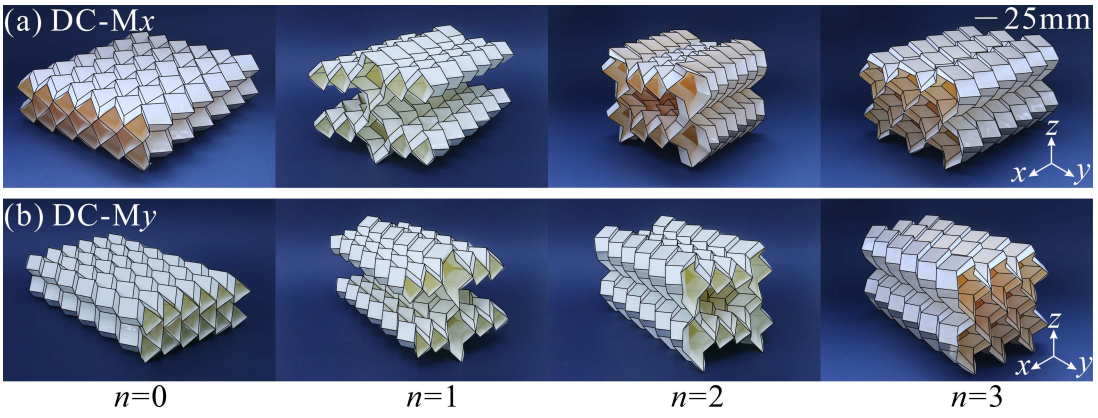

Fig. 3-6 Construction of different metamaterials by varying M-V assignments: (a) DC-M*x* with *n* = 0, 1, 2, 3, where *n* is the number of DC-2 per layer; (b) DC-M*y* with *n* = 0, 1, 2, 3.

3.3 Mechanical Properties

To gain a more comprehensive understanding of the metamaterial behaviors in the rigid foldable directions when changing the M-V assignments, numerical simulations

of the compression were performed using the commercial finite element software Abaqus/Explicit. The rigid foldable directions differ among these configurations. Taking DC-1 as an example, when choosing $\varphi_i=2\pi/3$ as the initial folding state and compressing in the x direction, the angles φ_1 and θ_1 exhibit a decreasing trend, while the angles δ_1 and γ_1 show an increasing trend. Different angles are compatible under the compression in the x direction, as shown in Fig. 3-3(a). When compressing in the y direction, the angles φ_1, δ_1, and γ_1 exhibit an increasing trend, while θ_1 has a decreasing trend, which is unable to be achieved compatibly according to Fig. 3-3(a). And when compressing in the z direction, the angles φ_1 and θ_1 have an increasing trend, while the angles δ_1 and γ_1 show a decreasing trend. It is compatible throughout the compression process. Therefore, the x and z directions serve as the two rigid foldable directions for DC-1 and DC-2, while the y and z directions are the rigid foldable directions for DC-3 and DC-4.

The compression scenario was simulated by modeling a structure placed on a stationary rigid plate and compressed by a moving plate. In the simulation, the stationary rigid plate was fully fixed in space, while all DOFs of the moving plate were constrained, except for the translational DOF in the corresponding directions. A prescribed downward displacement of 85% of the model dimension was assigned to the free DOF of the moving plate, allowing control over the compression process. The loading rate was controlled using the smooth amplitude definition feature provided by Abaqus. The model was meshed using four-node shell elements with reduced integration (S4R). General contact between the surfaces was taken into account, and friction was considered by assigning a friction coefficient μ of 0.3.

Before conducting the analysis, convergence tests were performed to assess the effects of mesh density and analysis time. Two principles recommended by Abaqus were considered during these tests. The first principle involved checking the ratio of artificial energy to internal energy, ensuring that it remained below 5%. This examination aimed to ensure that the hourglassing effect, which can introduce artificial energy into the system, did not significantly impact the results. The second principle involved evaluating the ratio of kinetic energy to internal energy throughout the compression process. It was necessary to verify that this ratio remained below 5% for the majority of the process, indicating that the dynamic effects could be considered insignificant. Based on the convergence tests, it was determined that a global mesh size

of 1 mm and an analysis time of 0.1 s produced satisfactory results. Both geometric nonlinearity and material nonlinearity are taken into account.

Four metamaterials have the same design and folding parameters, with a=15 mm, α=π/4, β=5π/12, and φ=2π/3. 316L stainless steel with a thickness of 0.8 mm is used as the material in the simulation process. And the material properties are consistent with the experiments.

To validate the numerical model, compression experiments in two rigid foldable different directions are conducted on the specimens. The geometric parameters of the specimens are as follows: a=10 mm, α=π/4, β=5π/12, and φ=2π/3. And the M-V assignments are the same as DC-2. The experiment setup is shown in Fig. 3-7. It is conducted on an Instron testing machine (type 5982). The measuring range of the load cell is 100 kN with an accuracy of 0.1%. The specimens are compressed with a displacement of 85% of the specimen height at the loading rate of 5 mm/min to eliminate dynamic effects. Each experiment was conducted three times to ensure accuracy and eliminate accidental errors.

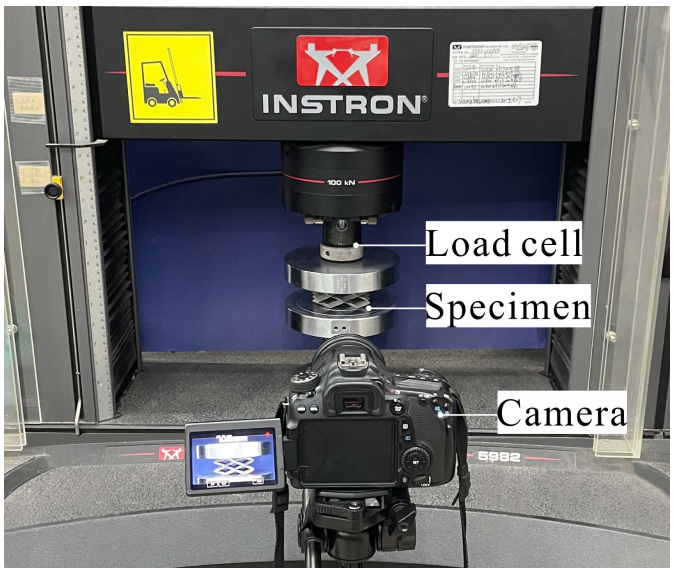

Fig. 3-7 Experimental setup of quasi-static compression.

The specimens are fabricated out of 316L stainless steel with a thickness of 0.8 mm through the 3D printing technique. The printing method employed is selective laser melting with a double laser powder sintering process. The material used is 316L stainless steel powder with particle sizes ranging from 15 to 53 μm. The printing layer thickness is 0.04 mm, with scanning spacings of 0.1 μm on the upper surface and 0.05

μm on the lower surface. The scanning speeds are 650 m/s on the upper surface and 2200 m/s on the lower surface, and the laser power settings are 160 kW on the upper surface and 180 kW on the lower surface.

The material properties obtained from the uniaxial tensile test are as follows: elastic modulus E=175 GPa, Poisson's ratio v=0.3, yield stress σ_y=486.71 MPa, ultimate stress σ_u=845.97 MPa, ultimate strain ε_u=29.06%. The density of the material is ρ=7.85 g/cm^3.

The comparative analysis between the experimental stress-strain curves and the corresponding numerical simulation results is illustrated in Fig. 3-8, while the morphological evolution and the distribution of equivalent plastic strain (PEEQ) during the deformation process are detailed in Fig. 3-9. A close examination reveals that the FE model successfully captures the fundamental mechanical characteristics of the structure, including its elastic stiffness and plateau stress trends. Due to the fact that the boundary conditions in the experiment and the finite element are not exactly the same, particularly friction, there was a slight synchronization difference in the x direction during compression, resulting in higher experimental values. Additionally, printing errors and surface roughness from the 3D printing process may cause the physical model to exhibit higher stress when compressed. The errors between the experimental and finite element results, measured by comparing integrating of the stress over the strain, are less than 10% in both directions, which is acceptable for origami metamaterials[130,132]. Therefore, the finite element modeling approach is considered appropriate for this study.

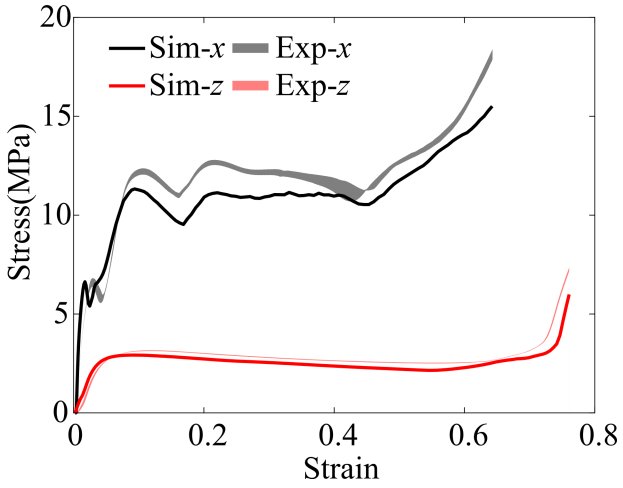

Fig. 3-8 The experimental stress versus strain curves compared with the simulations.

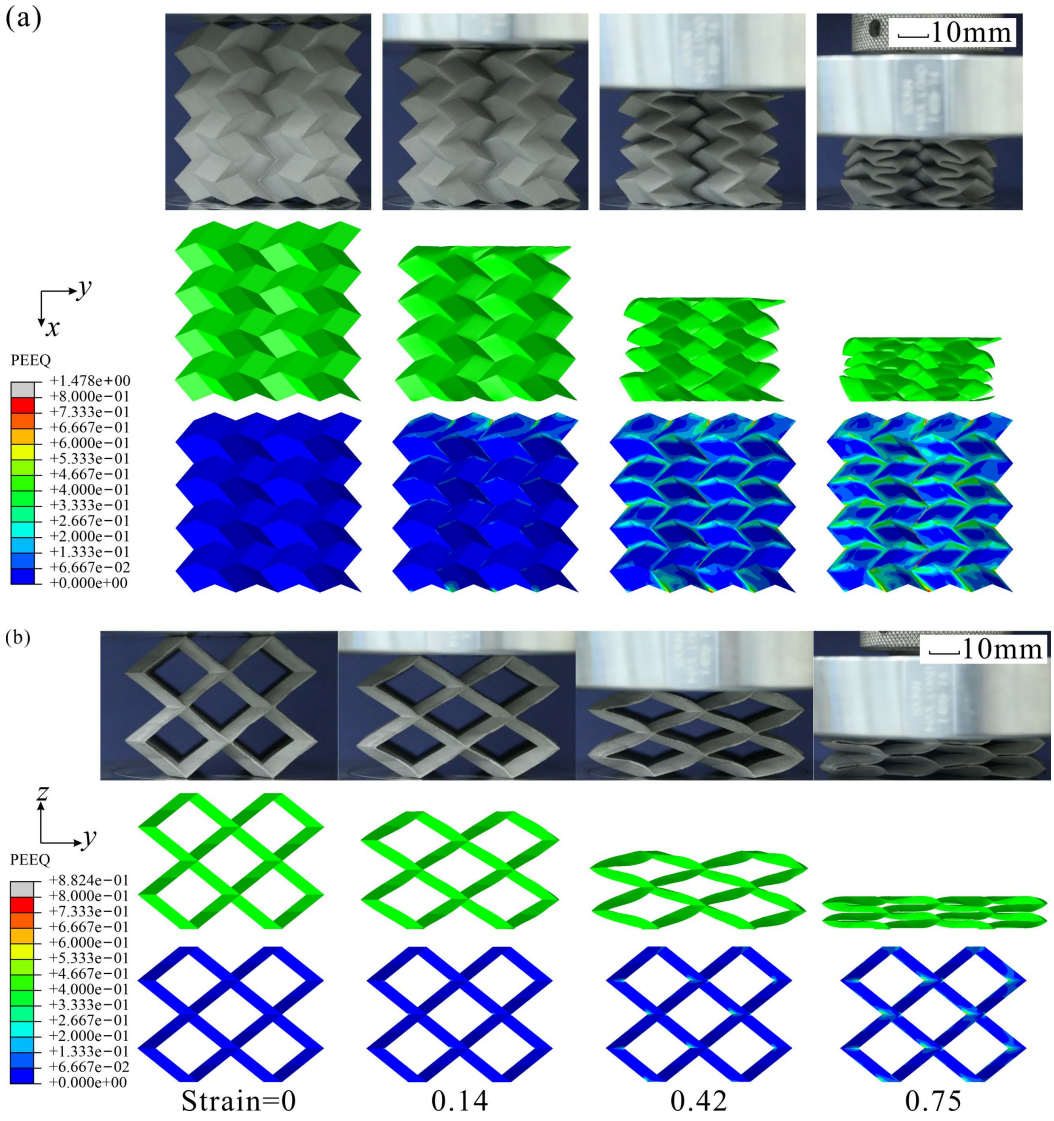

Fig. 3-9 Experimentally and numerically obtained deformation processes in two rigid foldable directions: (a) compression in the *x* direction; (b) compression in the *z* direction.

3.3.1 Mechanical Properties of the Uniform Metamaterials

The results obtained from the finite element simulations consist of the stress versus strain curves, stiffness within the elastic stage normalized by the projected area perpendicular to the loading direction, and the SEA, defined as the energy absorption per unit mass[152]. The results of DC-1 and DC-2 in the *x* direction, DC-3 and DC-4 in the *y* direction are plotted in Fig. 3-10. It can be seen from Fig. 3-10(a) that these curves display similar trends: initially increasing and then entering a plateau, then continuing to increase.

The deformation processes and the corresponding PEEQ contour maps are plotted in Fig. 3-11. It can be seen from Figs. 3-11(a) and 3-11(b) that the deformation processes of DC-1 and DC-2 basically follow the rigid origami folding mode. The plastic deformation mainly concentrates near the creases. While in the case of DC-3 and DC-4, buckling deformation of the panels is observed when the strain ranges from 0.42 to 0.55, as shown in Figs. 3-11(c) and 3-11(d). This behavior arises due to non-monotonic changes in the angle γ during compression in the x or y direction, as illustrated in Fig. 3-3. Setting $\varphi_0=2\pi/3$ as the initial folding state, γ undergoes a process of increasing and then decreasing. This non-monotonic change cannot be achieved through compression in a single direction. Therefore, as γ reaches its maximum and starts to decrease, buckling deformation occurs in the panel.

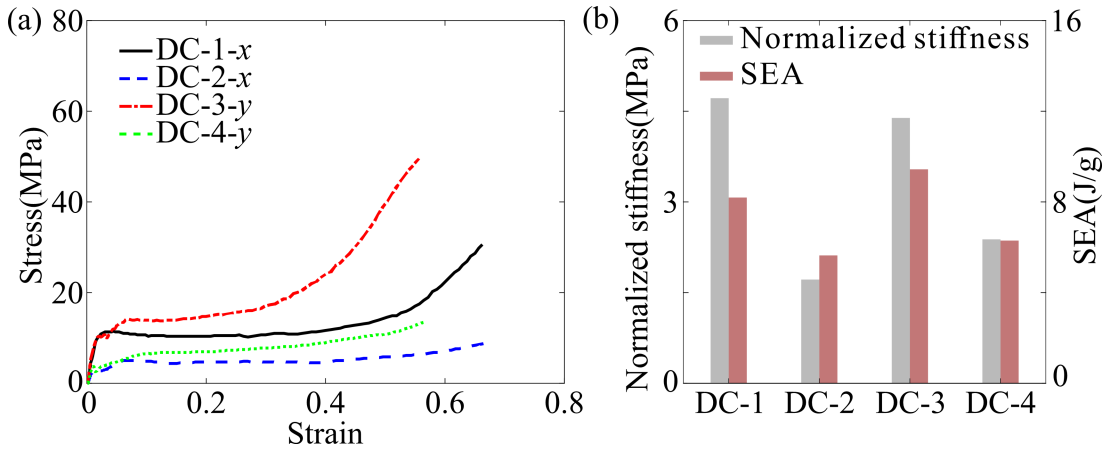

Fig. 3-10 (a) The stress versus strain curves of DC-1 and DC-2 when compressing in the x direction and DC-3 and DC-4 when compressing in the y direction; (b) corresponding normalized stiffness and SEA.

Consequently, when comparing the variations in γ shown in Figs. 3-3(a) and 3-3(b), it is evident that DC-3 and DC-4 exhibit more pronounced buckling deformation when compared to DC-1 and DC-2 due to the closer alignment of $\varphi_{3,4}$ with φ_0 when $\gamma_{3,4}$ is maximized. This geometric proximity to the critical threshold significantly diminishes the structural stiffness, thereby triggering earlier and more severe out-of-plane buckling. Additionally, all four metamaterials show buckling deformation at the boundary, which arises from the point contact between the metamaterial boundary and the two rigid plates.

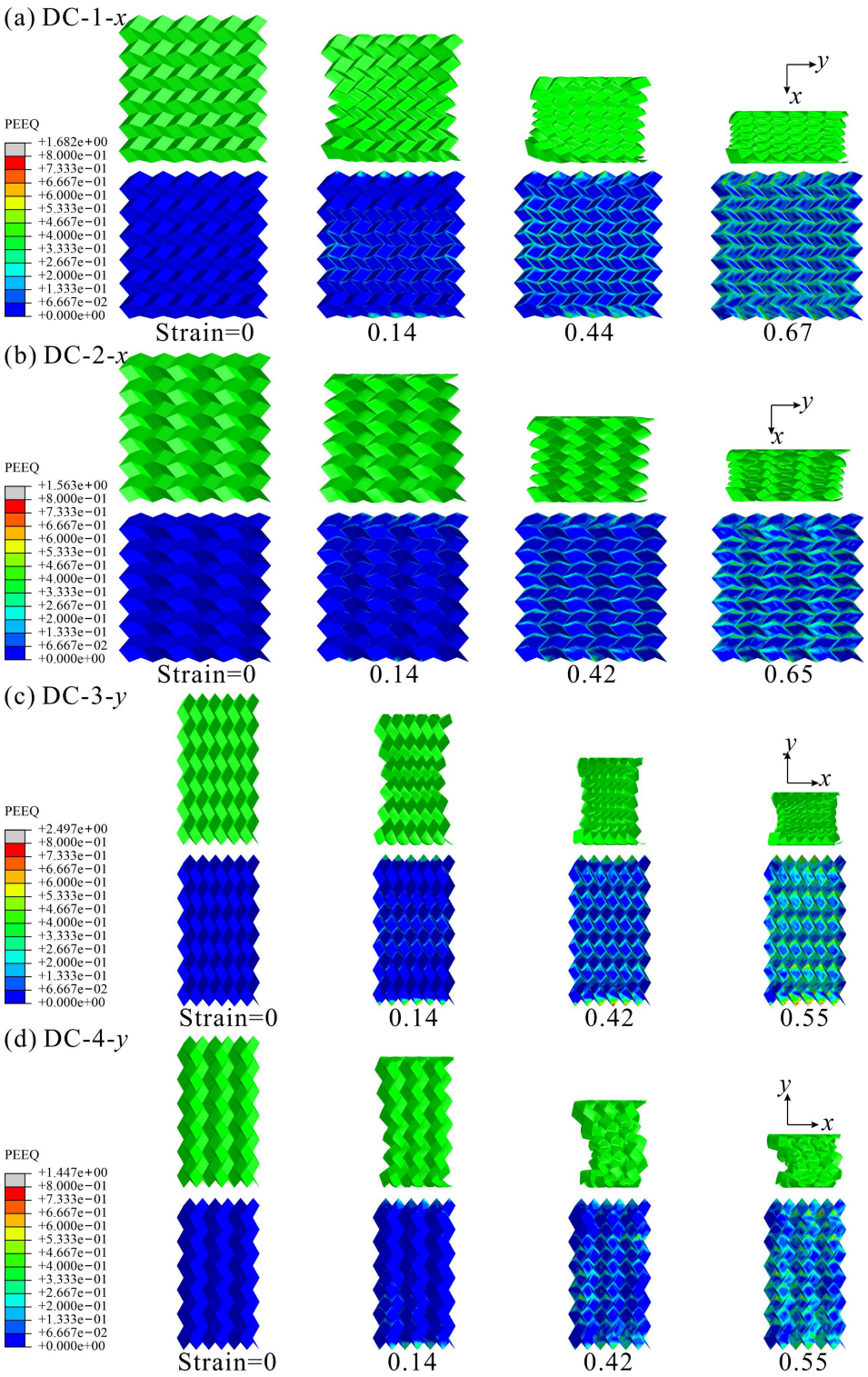

Fig. 3-11 Deformation processes and their corresponding PEEQ contour maps of the metamaterials: (a) and (b) DC-1 and DC-2 when compressing in the *x* direction; (c) and (d) DC-3 and DC-4 when compressing in the *y* direction.

The normalized stiffness and the SEA exhibit similar regularities across different metamaterials as shown in Fig. 3-10(b). This can be attributed primarily to the

variations in angles within the metamaterials when subjected to a compression load. In a 6×6×4 metamaterial, where the total number of creases remains constant, varying the M-V assignments leads to a variation in the number of different types of creases. The folding angles for different metamaterials are presented in Table 3-1. We denote the rate of angle changes in metamaterial as Dω_i, and the magnitude of angle changes in metamaterial as Sω_i. These values can be calculated as follows:

$$\mathrm{D}\omega_i = n_{\varphi i} + n_{\theta i}\frac{\partial \theta_i}{\partial \varphi_i} + n_{\delta i}\frac{\partial \delta_i}{\partial \varphi_i} + n_{\gamma i}\frac{\partial \gamma_i}{\partial \varphi_i} + n_{\varepsilon i}\frac{\partial \varepsilon_i}{\partial \varphi_i}, \tag{3-10}$$

$$\mathrm{S}\omega_i = n_{\varphi i}\left|\varphi_{0i} - \varphi_{\mathrm{end}i}\right| + n_{\theta i}\left|\theta_{0i} - \theta_{\mathrm{end}i}\right| + n_{\delta i}\left|\delta_{0i} - \delta_{\mathrm{end}i}\right| + n_{\gamma i}\left|\gamma_{0i} - \gamma_{\mathrm{end}i}\right| + n_{\varepsilon i}\left|\varepsilon_{0i} - \varepsilon_{\mathrm{end}i}\right|, \tag{3-11}$$

in which $n_{\varphi i}$, $n_{\theta i}$, $n_{\delta i}$, $n_{\gamma i}$, and $n_{\varepsilon i}$ represent the number of folding angles given in Table 3-1. θ_0, δ_0, γ_0, and ε_0 represent the folding angles when $\varphi_0=2\pi/3$, and φ_{end}, θ_{end}, δ_{end}, γ_{end}, and $\varepsilon_{\mathrm{end}}$ represent the target folding angles when the strain is up to 0.65.

Table 3-1 The number of folding angles in metamaterials DC-1 to DC-4.

	$N(\varphi_i)$	$N(\theta_i)$	$N(\delta_i)$	$N(\gamma_i)$	$N(\varepsilon_i)$
DC-1	528	528	48	48	0
DC-2	528	240	48	48	288
DC-3	528	528	48	48	0
DC-4	528	240	48	48	288

According to Eqs. (3-10) and (3-11), the variations of Dω_i and Sω_i can be obtained, as shown in Fig. 3-12. The normalized stiffness of the metamaterial is primarily determined by Dω_i, since it represents the changes in angles under small strains. A larger angle changes corresponds to a higher force requirement under a small strain, leading to increased stiffness. When the initial folding angle $\varphi_0=2\pi/3$, it is apparent from Fig. 3-12(a) that Dω_1>Dω_3>Dω_4>Dω_2. Therefore, the normalized stiffness of DC-1 to DC-4 exhibits the same order of magnitude, as shown in Fig. 3-10(b). The SEA is related to the magnitude of angle changes Sω_i. When treating the crease as a plastic hinge, the energy can be calculated by multiplying the rotation angle of the hinges by the bending moment of the hinges. As the material and side length of the hinges remain constant, the bending moment per radian is consistent across all plastic hinges.

Therefore, a larger Sω_i value indicates a larger energy by the hinges.

When compressing in the *x* or *y* direction, it can be seen from Fig. 3-12(b) that Sω_1>Sω_4>Sω_2>Sω_3, in which Sω_3 does not match the relationship in Fig. 3-10(b). This is attributed to the significant buckling deformation of the DC-3, as illustrated in Fig. 3-11(c). The pronounced buckling deformation contributes to an increase in the SEA of DC-3.

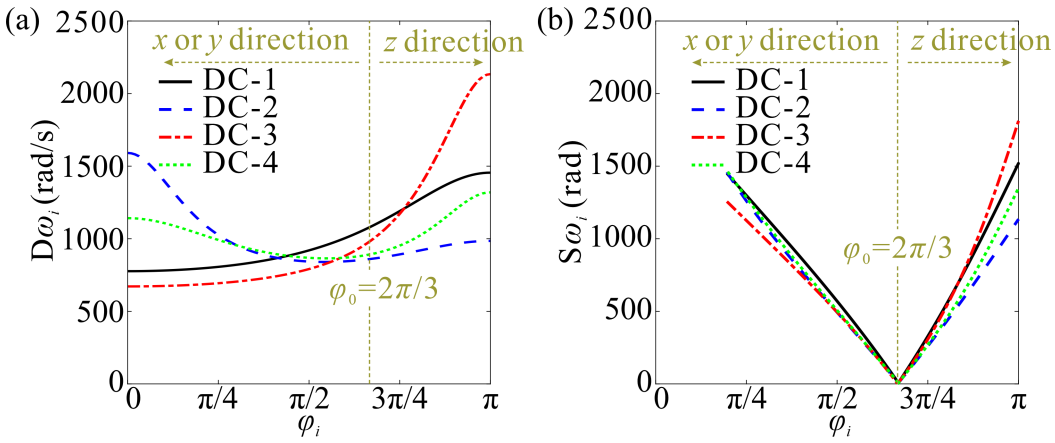

Fig. 3-12 (a) The rate of angle changes and (b) the magnitude of angle changes in DC-1 to DC-4.

The simulation results of the four metamaterials when compressing in the *z* direction are plotted in Fig. 3-13. From the deformation modes and the PEEQ contour maps shown in Fig. 3-14, it is obvious that the deformation of these configurations completely follows the rigid origami folding mode, and the plastic deformation mainly occurs near the creases, while the panels are free from distortion. We can obtain from Fig. 3-12 that Dω_1>Dω_3>Dω_4>Dω_2 and Sω_3>Sω_1>Sω_4>Sω_2. Therefore, the SEA shown in Fig. 3-13(b) follow the same order as Sω_i, as we analyzed before.

It is worth noting that the stress, SEA and stiffness of DC-3 are significantly higher than those of other configurations. This phenomenon can be attributed primarily to the boundary effect induced by the contact. Unlike the compressions in the *x* or *y* directions, the contact between the metamaterial boundaries and the two rigid plates in the *z* direction imposes a strong boundary constraint. As shown in Fig. 3-4, compression in the *z* direction induces significant extension in the *x* and *y* directions. However, this boundary constraint hinders such extension, restricting the deformation of the middle panels. This restriction leads to buckling deformation, as marked by the red box in Fig.

3-14(c). Consequently, the stress, SEA and stiffness of DC-3 are considerably higher than those of other configurations.

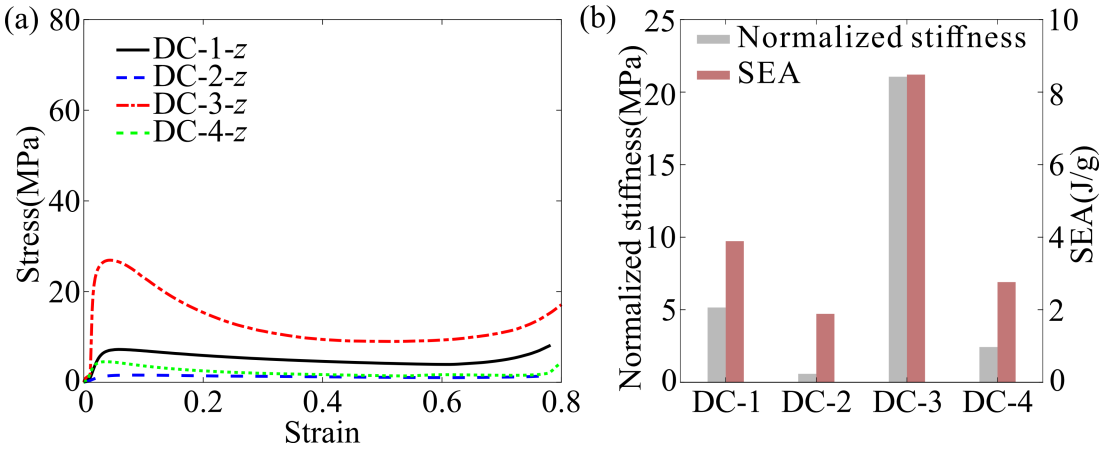

Fig. 3-13 (a) The stress versus strain curves of DC-1 to DC-4 when compressing in the *z* direction; (b) corresponding normalized stiffness and SEA.

Through a comprehensive finite element analysis of the various metamaterial configurations across their rigid foldable directions, a distinct correlation between the underlying kinematic design and the macroscopic mechanical response is established. Specifically, it is observed that paired metamaterials engineered with identical Poisson's ratios (DC-1 and DC-2, as well as DC-3 and DC-4), demonstrate highly analogous deformation modes and load-bearing capacities. The structural rigidity is intrinsically linked to the folding kinematics; the normalized stiffness across the DC-1 to DC-4 configurations is fundamentally governed by $D\omega_i$. When the metamaterials primarily undergo deformation following the rigid origami folding mode, the magnitude of the angle changes $S\omega_i$ plays an important role in determining the SEA. However, as the loading orientation shifts to the *y* direction, configurations such as DC-3 and DC-4 undergo a profound mechanistic transition. In these specific cases, the structural response deviates from pure kinematic folding, and the severe out-of-plane buckling of the constituent panels emerges as the dominant deformation mechanism. This critical shift from zero-energy rigid folding to energy-intensive facet buckling dissipates considerably more strain energy, thereby resulting in a significant and advantageous amplification of the SEA for these metamaterials.

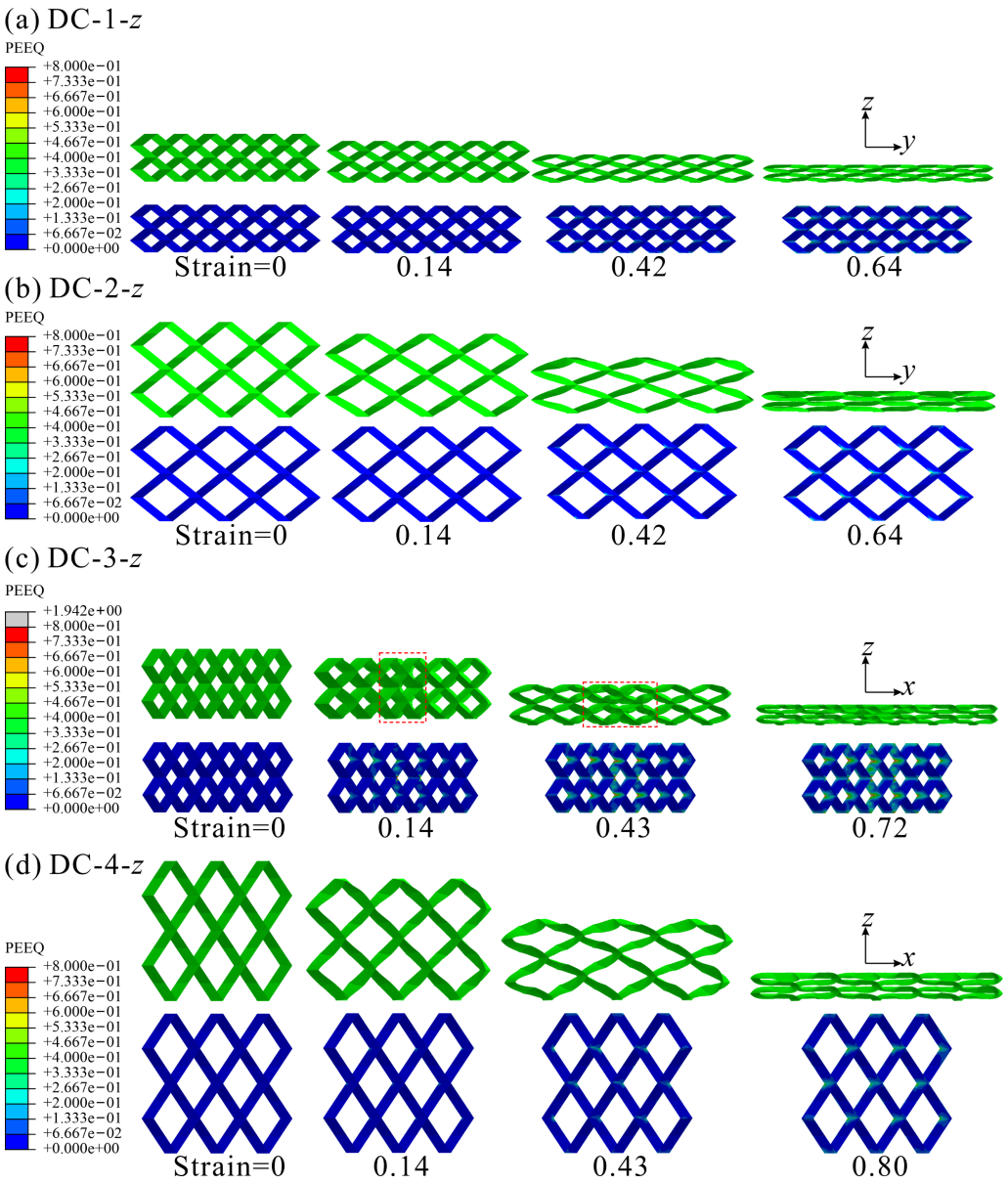

Fig. 3-14 Deformation processes and their corresponding PEEQ contour maps of the metamaterials when compressing in the *z* direction: (a) DC-1; (b) DC-2; (c) DC-3; (d) DC-4.

3.3.2 Mechanical Properties of the Mixed Metamaterials

To investigate the behavior of the mixed metamaterial, finite element simulations are conducted to simulate compression along the rigid foldable directions. The results of DC-M*x* when compressing in the *x* direction are presented in Fig. 3-15. Figures 3-16(a) and 3-16(b) illustrate the deformation processes of DC-M*x*-1 and DC-M*x*-2, which show similarities to the deformation processes of DC-M*x*-0 and DC-M*x*-3 presented in Figs. 3-11(a) and 3-11(b), respectively. The number of different folding angles in these metamaterials are shown in Table 3-2. From Figs. 3-17(a) and 3-17(b),

we can observe the following relationships when applying compression load in the *x* direction: $D\omega_{Mx\text{-}0}>D\omega_{Mx\text{-}1}>D\omega_{Mx\text{-}2}>D\omega_{Mx\text{-}3}$ and $S\omega_{Mx\text{-}0}>S\omega_{Mx\text{-}1}>S\omega_{Mx\text{-}2}>S\omega_{Mx\text{-}3}$. These results correspond precisely with the normalized stiffness and SEA plotted in Fig 3-15(b).

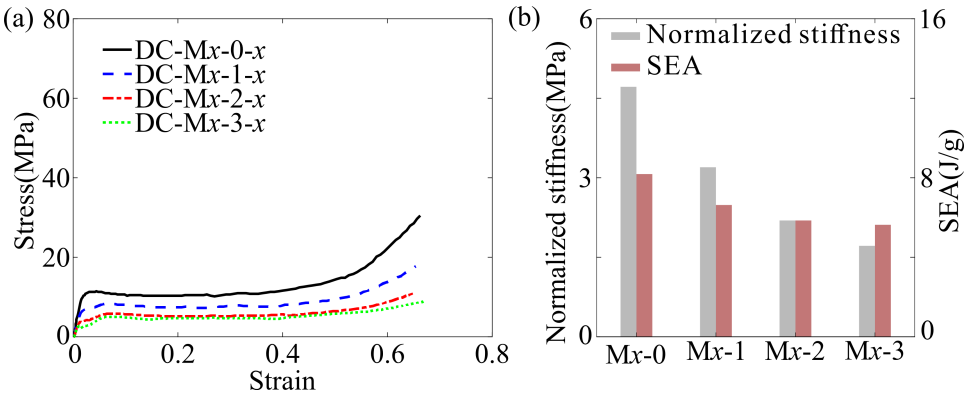

Fig. 3-15 (a) The stress versus strain curves of DC-M-0 to DC-M-3 when compressing in the *x* direction; (b) corresponding normalized stiffness and SEA.

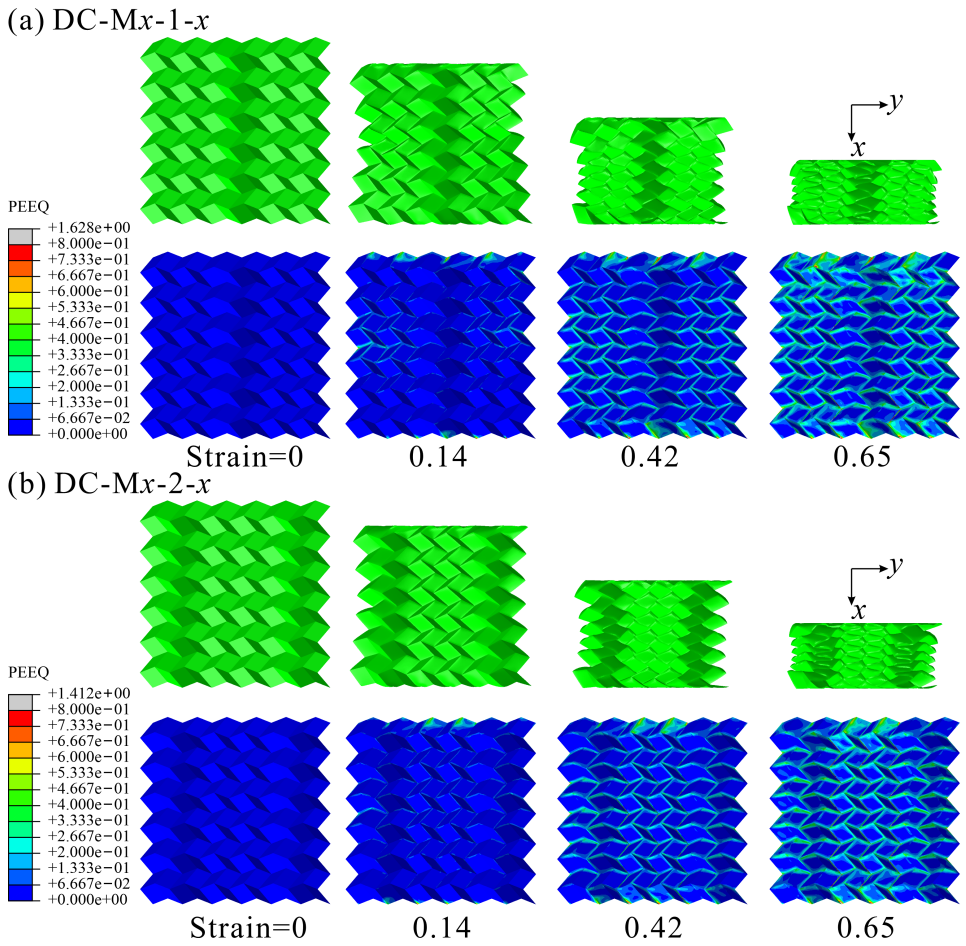

Fig. 3-16 Deformation processes and their corresponding PEEQ contour maps of the metamaterials when compressing in the *x* direction: (a) DC-M*x*-1; (b) DC-M*x*-2.

Table 3-2 The number of folding angles in metamaterials DC-M*x*-0 (DC-M*y*-0) to DC-M*x*-3 (DC-M*y*-3).

	$N(\varphi_i)$	$N(\theta_i)$	$N(\delta_i)$	$N(\gamma_i)$	$N(\varepsilon_i)$
DC-M*x*-0 (DC-M*y*-0)	528	528	48	48	0
DC-M*x*-1 (DC- M*y* -1)	528	432	48	48	96
DC-M*x*-2 (DC- M*y* -2)	528	336	48	48	192
DC-M*x*-3 (DC- M*y* -3)	528	240	48	48	288

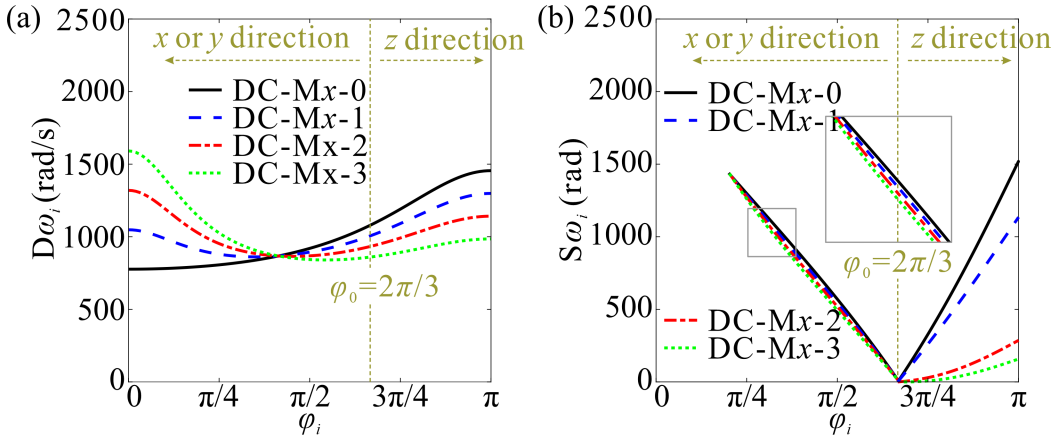

Fig. 3-17 (a) The rate of angle changes and (b) the magnitude of angle changes in DC-M*x*-0 to DC-M*x*-3.

Figure 3-18 presents the simulation results of DC-M*y* when subjected to compression in the *y* direction. Additionally, the deformation processes of DC-M*y*-1 and DC-M*y*-2 are illustrated in Figs. 3-19(a) and 3-19(b) respectively. In these cases, rigid folding is present, but the overall deformation process is still predominantly governed by buckling deformation. The following relationships can be obtained from Figs. 3-20(a) and 3-20(b) when compressing in the *y* direction: $D\omega_{My\text{-}0}>D\omega_{My\text{-}1}>D\omega_{My\text{-}2}>D\omega_{My\text{-}3}$ and $S\omega_{My\text{-}3}>S\omega_{My\text{-}2}>S\omega_{My\text{-}1}>S\omega_{My\text{-}0}$. The change in normalized stiffness aligns with the variation in $D\omega_i$, whereas the variation in SEA exhibits a completely opposite trend to that of $S\omega_i$. This contrast arises due to the predominance of buckling deformation when DC-M*y* is compressed in the *y* direction. Specifically, the DC-3 element within DC-M*y* experiences greater buckling deformation compared to the DC-4 element according to Figs. 3-11(c) and 3-11(d). Consequently, the greater the number

of DC-3 units present in the DC-M*y* metamaterials, the more pronounced the buckling deformation, resulting in a larger SEA.

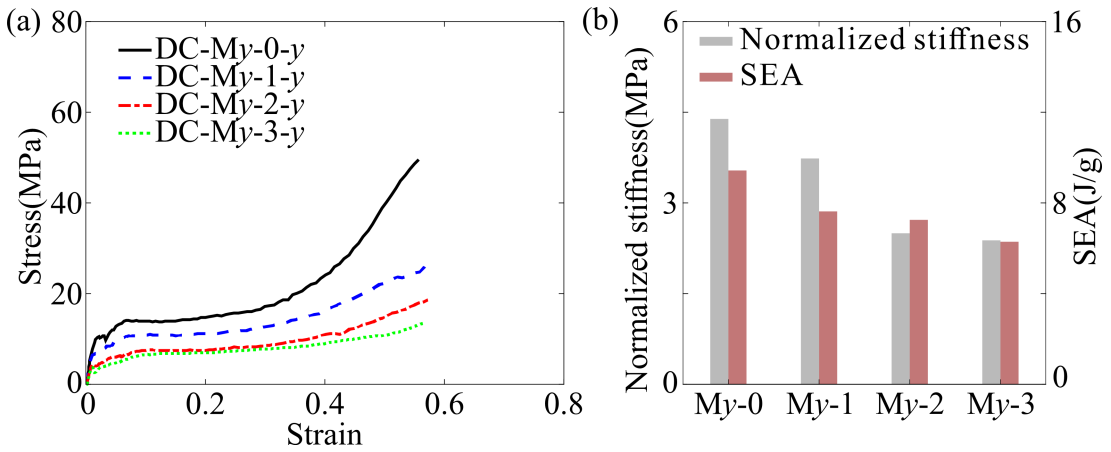

Fig. 3-18 (a) The stress versus strain curves of DC-M*y*-0 to DC-M*y*-3 when compressing in the *y* direction; (b) corresponding normalized stiffness and SEA.

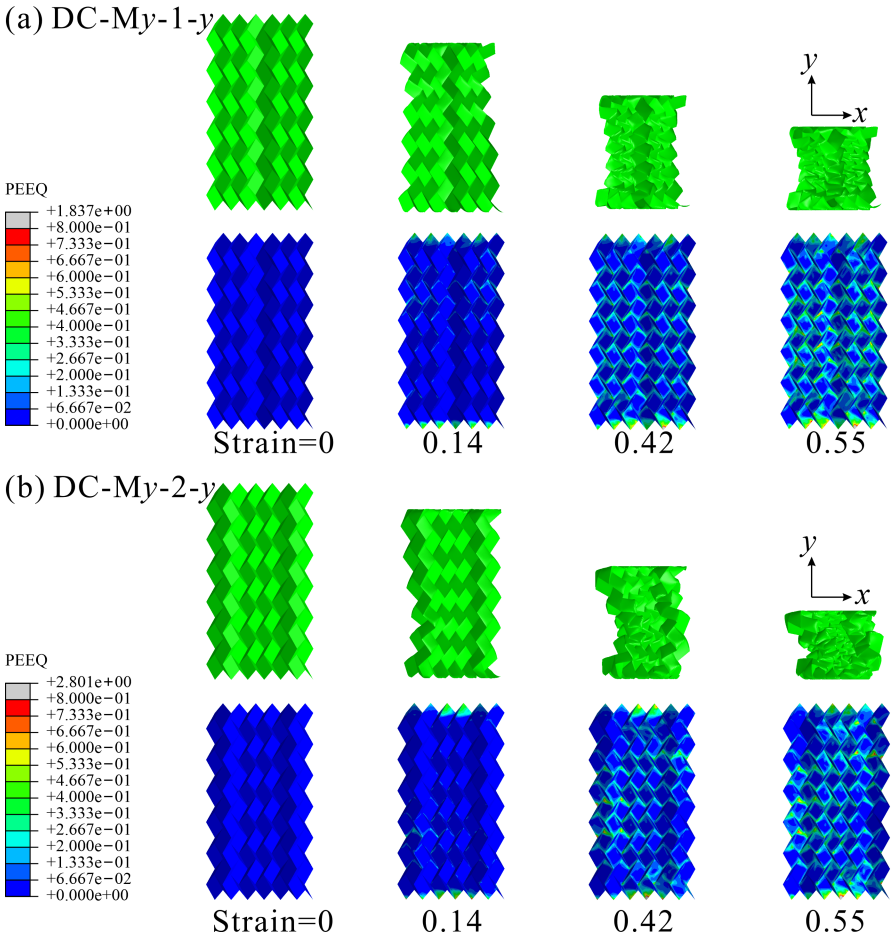

Fig. 3-19 Deformation processes and their corresponding PEEQ contour maps of the metamaterials when compressing in the *y* direction: (a) DC-M*y*-1; (b) DC-M*y*-2.

Figures 3-21(a) and 3-22(a) display the stress versus strain curves of the DC-M*x* and DC-M*y* when subjected to *z* direction compression, respectively. In contrast to the previous regularities, the mixed configurations DC-M*x*-1, DC-M*x*-2, DC-M*y*-1 and DC-M*y*-2 exhibit a step-shaped stress behavior, which is not observed in the uniform configurations such as DC-M*x*-0, DC-M*x*-3, DC-M*y*-0 and DC-M*y*-3.

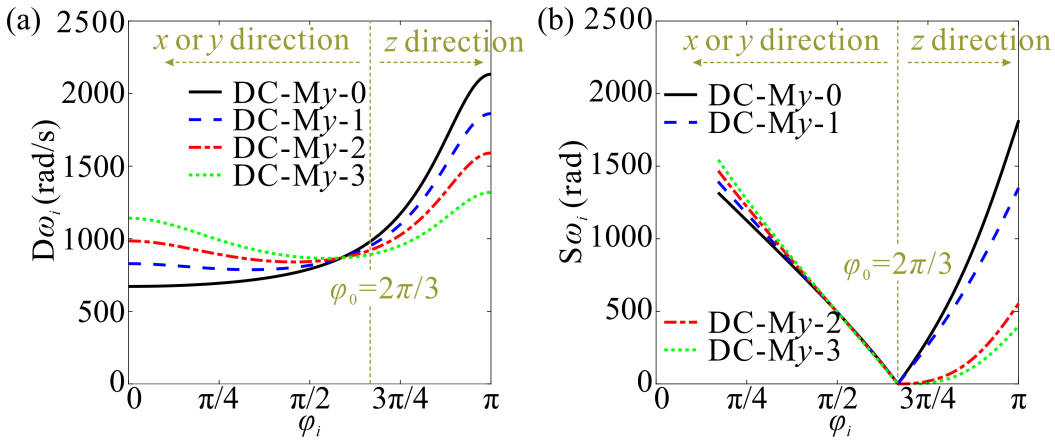

Fig. 3-20 (a) The rate of angle changes and (b) the magnitude of angle changes in DC-M*y*-0 to DC-M*y*-3.

Additionally, the stiffness demonstrates different variations compared to the previous cases, as shown in Figs. 3-21(b) and 3-22(b), which do not follow the relationships obtained from Figs. 3-17(a) and 3-20(a) when compressing in the *z* direction. This is due to the special deformation characteristic of the mixed configuration, as shown in Figs. 3-23 and 3-24. Taking DC-M*x*-1 shown in Fig. 3-23(a) as an example, due to the number of creases interconnecting the top two layers and the bottom two layers is noticeably reduced, the DC-2 units in DC-M*x*-1 undergo deformation initially, while the DC-1 units experience minimal deformation with a strain of around 0.14. Hence, the decreased involvement of creases in the deformation process is the reason for the sharp decrease in stiffness in the mixed configuration, which subsequently increases with the number of *n*. When the strain is further increased, the DC-1 units in the mixed configuration come into contact with each other, resulting in the second step in the stress-strain curves. Comparing the stress amplitudes between the two mixed configurations, it can be observed that DC-M*x*-2 exhibits higher stress amplitude during the first step, whereas DC-M*x*-1 demonstrates higher stress amplitude after the second step. This difference arises because, during the first step, a greater

number of units participate in deformation within DC-M*x*-2, while after the second step, all units undergo deformation. Besides, DC-1 units account for a larger proportion within DC-M*x*-1, leading to higher stress levels. A similar phenomenon can be observed in DC-M*y*-1 and DC-M*y*-2. The changes in SEA shown in Figs. 3-21(b) and 3-22(b) are consistent with the changes in Sω_i shown in Figs. 3-17(b) and 3-20(b).

For the DC-M*x* (DC-M*y*), the mechanical properties in the *x* direction (*y* direction) exhibit similar regularities as DC-1 and DC-2 (DC-3 and DC-4). In the *z* direction, the mixed configuration displays a distinct step-shaped stress curve, and the normalized stiffness presents a sharp decrease. These phenomena are closely related to the number and type of units involved in deformation during compression. Compression in the *z* direction of different metamaterials precisely follows the rigid origami folding mode. As a result, there exists a direct relationship between SEA and Sω_i.

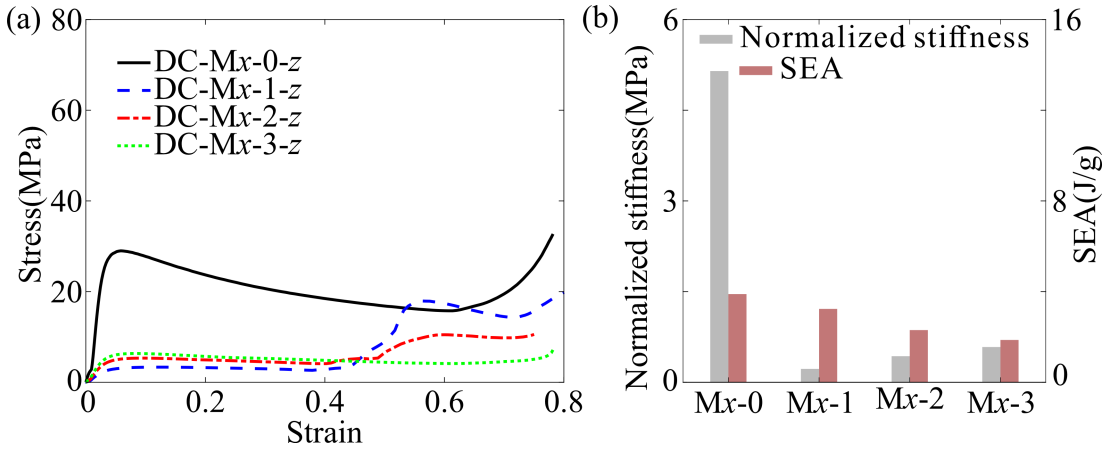

Fig. 3-21 (a) The stress versus strain curves of DC-M*x*-0 to DC-M*x*-3 when compressing in the *z* direction; (b) corresponding normalized stiffness and SEA.

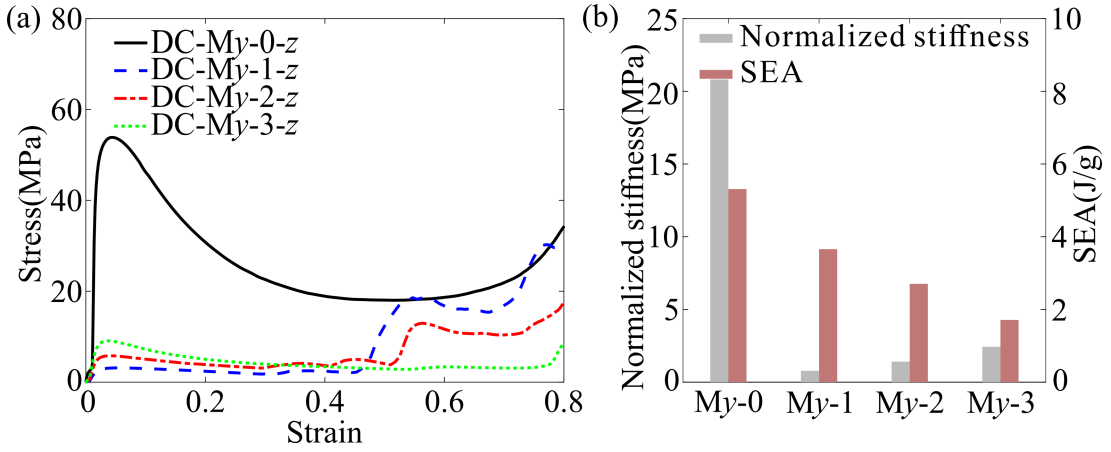

Fig. 3-22 (a) The stress versus strain curves of DC-M*y*-0 to DC-M*y*-3 when compressing in the *z* direction; (b) corresponding normalized stiffness and SEA.

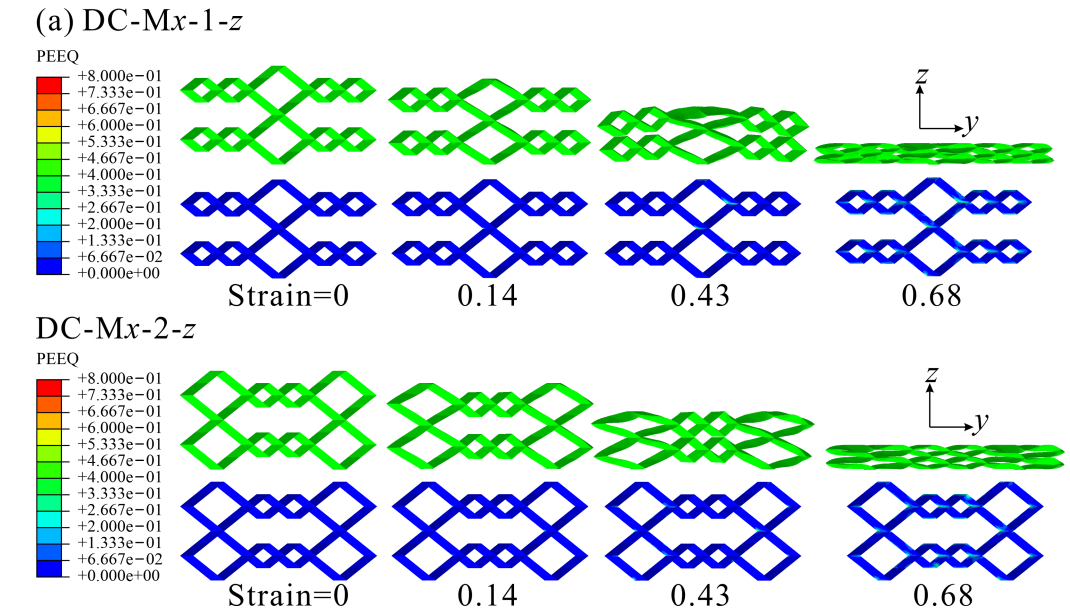

Fig. 3-23 Deformation processes and their corresponding PEEQ contour maps of the metamaterials when compressing in the *z* direction: (a) DC-M*x*-1; (b) DC-M*x*-2.

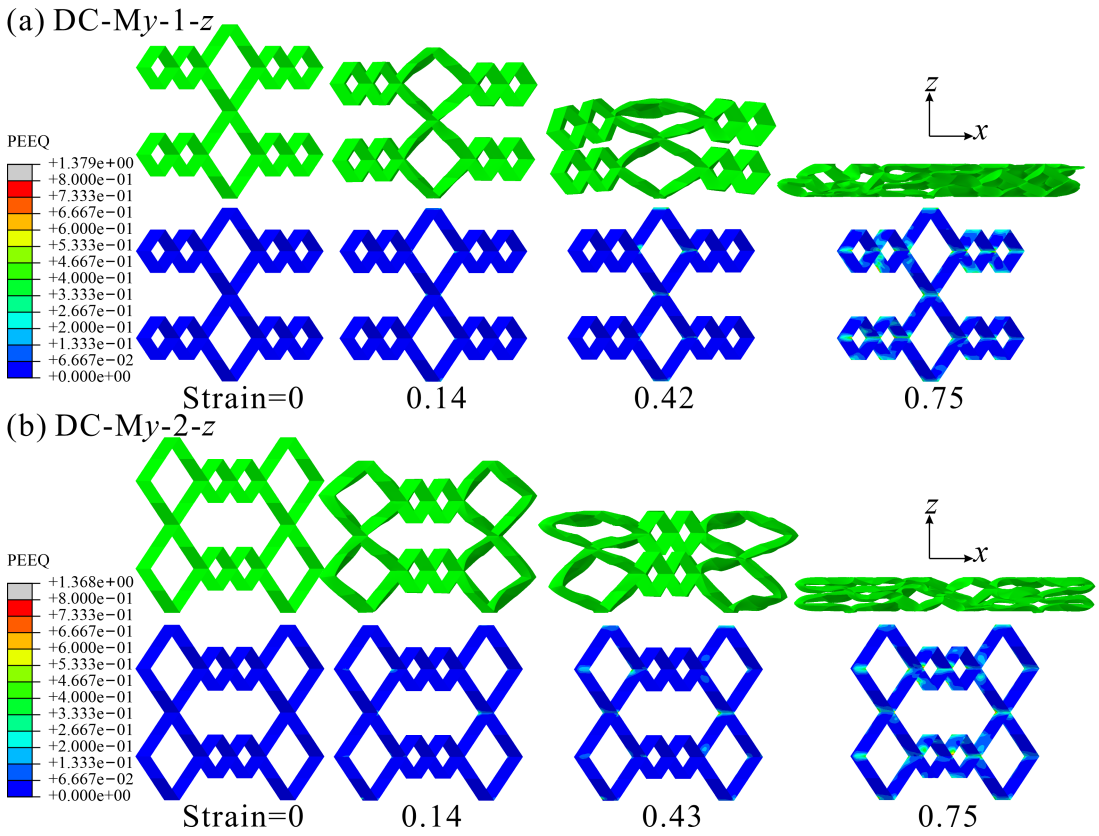

Fig. 3-24 Deformation processes and their corresponding PEEQ contour maps of the metamaterials when compressing in the *z* direction: (a) DC-M*y*-1; (b) DC-M*y*-2.

The results demonstrate that four uniform metamaterials, obtained through varying M-V assignments, exhibit different mechanical properties in their rigid foldable directions. Furthermore, by combining different origami units with the same Poisson's ratios, mixed metamaterials are created, whose mechanical properties can be programmed by adjusting the number of origami units.

Additionally, a graded stress response can be observed when compressing in the *z* direction due to the unique deformation mode of the mixed metamaterials. This confirms that the programmability of mechanical properties can be achieved by manipulating the M-V assignments. Moreover, after varying the M-V assignments, the mechanical properties can be further programmed by changing parameters such as design angle, folding angle, and wall thickness, as established in previous studies[95,131-132,153], thereby obtaining a wider range of mechanical properties. This work introduces a new dimension for the programmability of mechanical properties in origami metamaterials.

3.4 Acoustic Properties

Following the mechanical analysis, the focus now shifts to the acoustic wave propagation characteristics of the single-tubular metamaterials. COMSOL Multiphysics (Version 5.6) was utilized to model the band structure and transmission loss (TL) of the proposed origami metamaterial. The panels of the structure are modeled as sound-hard boundary walls, simulating the interactions of sound waves with the structure under Floquet periodicity for various wave vectors **k**. To validate the simulated results, the transmission loss was calculated using

$$\mathrm{TL} = 20\lg\left(\frac{P_i}{P_t}\right), \tag{3-12}$$

where P_i is the incident sound power and can be calculated as[22]

$$P_i = \int_{A_1} \frac{\left|p_1(\boldsymbol{r})\right|^2}{2c_{air}\rho_{air}}\mathrm{d}A \tag{3-13}$$

for the integration of pressure $p_1(\boldsymbol{r})$ in the integration plane A_1. The transmitted sound power P_t can be expressed as

$$P_t = \int_{A_2} \frac{\left|p_2(\boldsymbol{r})\right|^2}{2c_{air}\rho_{air}}\mathrm{d}A \tag{3-14}$$

for the integration of pressure $p_2(\boldsymbol{r})$ in the integration plane A_2. High TL may arise from either a directional bandgap in the considered propagation direction or a deaf band associated with symmetry-inactive Bloch modes. The 5×2×5 lattice with sound hard boundary conditions in the panels and sound soft boundary conditions in the boundaries except for the incident plane and the transmitted plane. The incident pressure field is a plane wave propagating along the *x* or *y* direction, and the pressure amplitude is set to p_0 = 1Pa.

To quantify these properties, a representative acoustic unit cell was extracted from the infinite array, as illustrated in Fig. 3-25. In the numerical simulations, the origami panels were modeled as sound-hard boundaries, assuming perfect reflection at the rigid walls without fluid-structure interaction. Consequently, the analysis focused solely on the propagation of airborne sound within the complex internal air domains. Based on the periodicity of the lattice, the corresponding reciprocal space and the Irreducible Brillouin Zone (IBZ) were identified, as shown in Fig. 3-26. The acoustic band structures were then obtained by solving the eigenvalue problem of the Helmholtz equation while sweeping the wave vector **k** along the characteristic boundaries of the IBZ (Γ–X–S–Y–Γ–Z–U–R–T–Z|Y–T|U–X|S–R). Here, the symbol "|" denotes a discontinuous jump between non-adjacent high-symmetry segments in the scanning path.

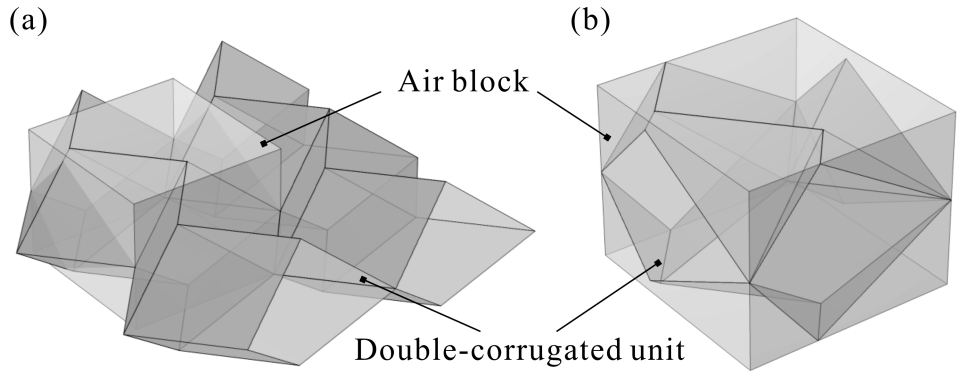

Fig. 3-25 Schematic representation of the acoustic unit cell. (a) The periodic array of the single-tubular metamaterial; (b) the extracted representative cubic unit cell used for acoustic calculations.

Sound transmission loss experiments for the specimens were conducted in square acoustic impedance tubes formed by sound-absorbing cotton (Fig. 3-27). Plane waves spanning 0.1-25 kHz were generated via a power amplifier (Brüel & Kjær, Type 2719).

Sound pressure data were collected through the microphone (Brüel & Kjær, Type 267) and output generator module (Brüel & Kjær, Type 3160-A-042), then analyzed via computer-controlled signal processing systems. The specimens were positioned equidistant (240 mm) from both the 3×3 speaker arrays and microphone.

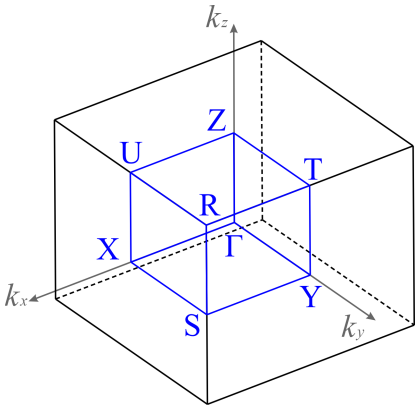

Fig. 3-26 The reciprocal space lattice and the IBZ corresponding to the cubic unit cell, with the characteristic wave vector scanning path Γ–X–S–Y–Γ–Z–U–R–T–Z|Y–T|U–X|S–R.

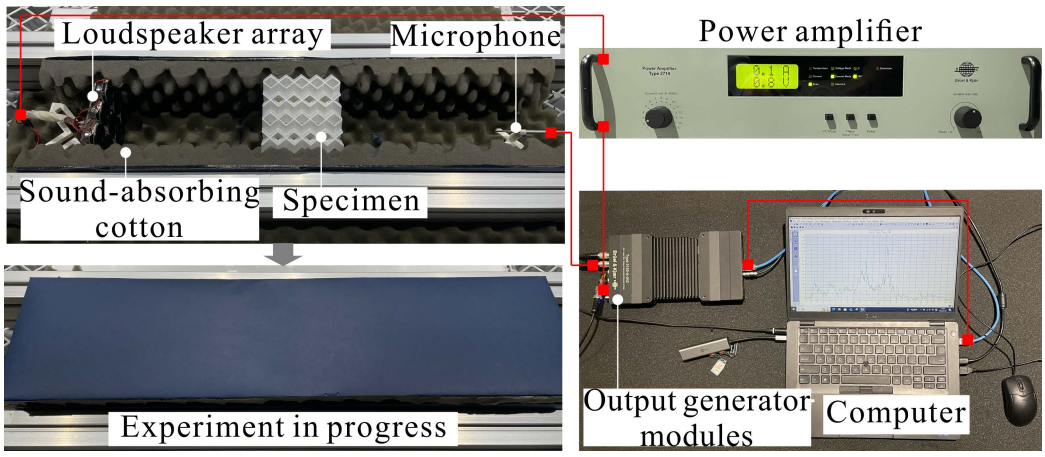

Fig. 3-27 Sound transmission loss measurement setup.

Experimental measurements of sound transmission loss were utilized to verify these computational assumptions. Figure 3-28 presents the calculated acoustic band structure alongside a comparison of the simulated and experimentally measured sound TL. Overall, good agreement is observed between the experimental and numerical results, which supports the validity of the adopted acoustic model. In addition to the attenuation associated with the directional bandgaps, a pronounced TL peak is observed at a frequency where propagating Bloch modes are still present in the band structure. This feature indicates the existence of a deaf band, rather than a bandgap. In other words,

although an eigenmode exists at this frequency, it cannot be efficiently excited by the incident plane wave because of modal symmetry mismatch.

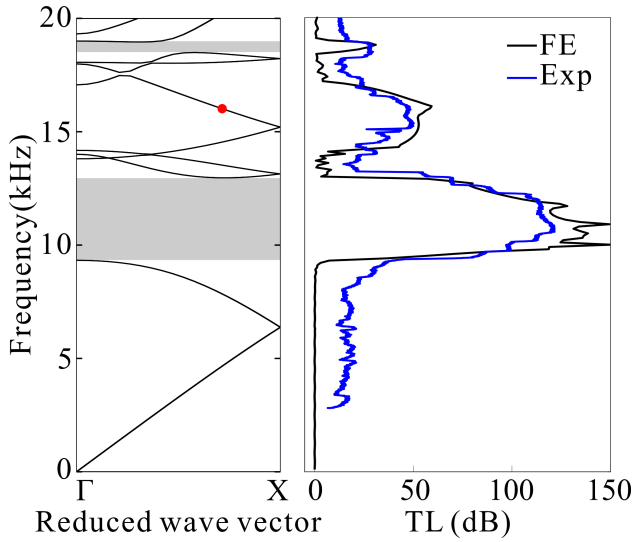

Fig. 3-28 Acoustic band structure and comparison of simulated and experimental TL.

To further clarify the physical origin of this attenuation mechanism, the acoustic pressure field distributions at the corresponding frequency are shown in Fig. 3-29. It can be seen that the relevant mode exhibits a strongly anti-symmetric pressure pattern inside the acoustic cavity. By contrast, the incident plane wave propagating along the prescribed direction possesses a symmetric excitation field. Owing to this mismatch in spatial symmetry, the incident wave cannot effectively couple with the corresponding Bloch mode, resulting in strongly suppressed transmission and, consequently, a high TL peak. Therefore, the observed attenuation at this frequency should be attributed to a deaf-band effect rather than to the opening of a directional bandgap.

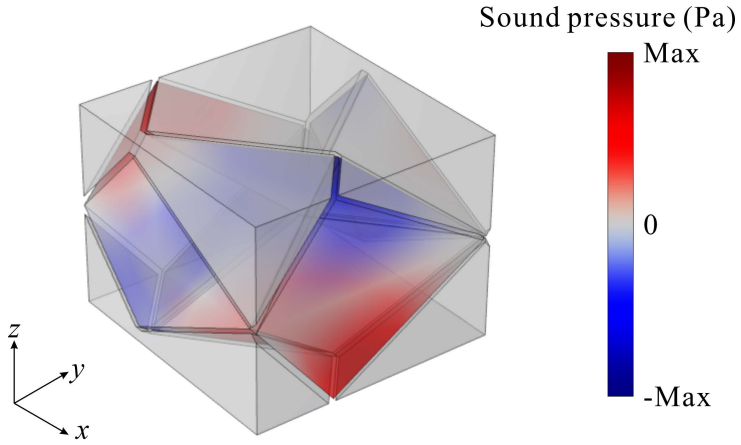

Fig. 3-29 Acoustic pressure field distributions of the anti-symmetric mode associated with the deaf-band effect.

3.4.1 Acoustic Properties of the Uniform Metamaterials

Building upon the validated numerical framework, the wave propagation mechanisms within the uniform metamaterials are systematically investigated. The periodic porous channels within these tubular structures undergo significant geometric transformations during the folding process. This kinematic behavior directly alters the internal air cavity profiles and provides a strong physical basis for manipulating sound waves.

To investigate the influence of topological configurations on acoustic performance, the dispersion relations of four distinct M-V assignment configurations (DC-1 to DC-4) were first compared under a fixed folding state of φ_i=120°. The band structures were plotted along the Γ–X direction for the DC-1 and DC-2 configurations and along the Γ–Y direction for the DC-3 and DC-4 configurations.

As shown in Fig. 3-30, the results reveal clear differences in the wave attenuation characteristics among the four configurations. Specifically, DC-1 and DC-3 exhibit pronounced directional bandgaps, highlighted by the gray regions, within which acoustic waves are prohibited from propagating along the considered directions. By contrast, DC-2 and DC-4 do not exhibit evident directional bandgaps within the investigated frequency range at this folding state. This comparison indicates that varying the M-V assignment significantly alters the acoustic dispersion characteristics of the metamaterials, even when the global geometric parameters and folding state remain unchanged. In other words, the M-V assignment provides an effective design variable for programming directional wave attenuation behavior.

Furthermore, a parametric analysis regarding the folding angle φ_i was conducted to investigate the evolution of the acoustic properties. Figure 3-31 shows the frequency ranges of the first directional bandgap for the DC-1 to DC-4 configurations as a function of the folding angle. It can be observed that the directional bandgap generally appears between the fourth and fifth acoustic bands. As the folding angle increases, the lower boundary frequencies of DC-1 and DC-3 exhibit a clear decreasing trend, as shown in Figs. 3-31(a) and 3-31(c). This trend is closely related to the geometric expansion of the unit cell during deployment. As the folding angle increases, the dimensions of the unit cell increase in both the x and y directions, as shown in Fig. 3-4. Although the internal cavity volume varies non-monotonically, the overall expansion effectively

increases the characteristic acoustic path length inside the structure. As a result, the corresponding characteristic frequencies shift toward lower values.

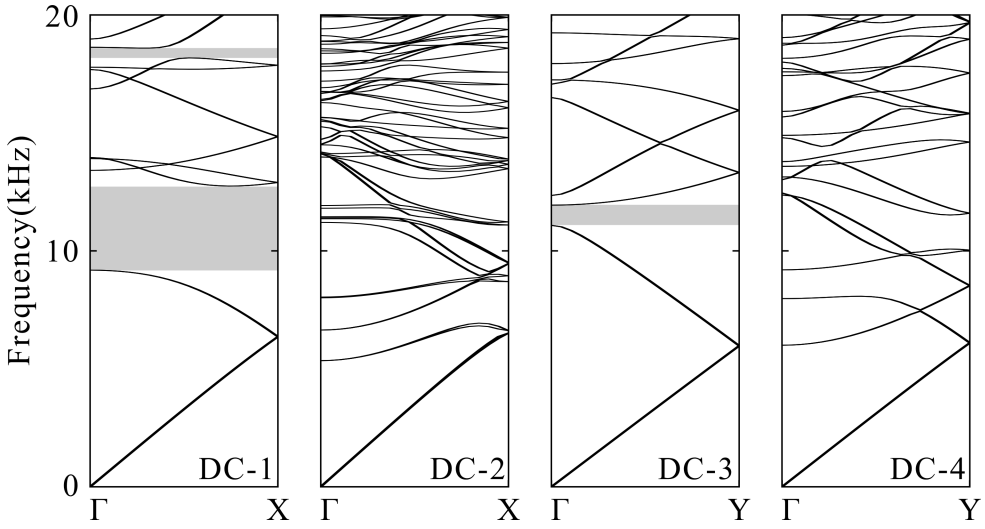

Fig. 3-30 Acoustic band structures of four different M-V configurations (DC-1, DC-2, DC-3, and DC-4) at a fixed folding angle of φ_i=120°. The gray shaded regions indicate the directional bandgaps along the considered propagation directions.

Although DC-2 and DC-4 do not exhibit bandgaps at φ_i=120°, a broader sweep of the folding angle reveals that such bandgaps can still be induced within specific folding ranges. As shown in Figs. 3-31(b) and (d), directional bandgaps can be opened in both DC-2 and DC-4 by adjusting the folding angle appropriately. This result indicates that the absence of a bandgap at a particular folding state is not an intrinsic limitation of the configuration, but rather a state-dependent feature governed by the instantaneous geometry during folding. The corresponding band structures of DC-2 at φ_2=140° and DC-4 at φ_4=40° are presented in Fig. 3-32, where distinct directional stopbands can be observed. This phenomenon suggests that changing the folding angle can effectively modify the internal channel geometry and the characteristic propagation paths of acoustic waves, thereby altering the dispersion relations and enabling the opening of bandgaps. Therefore, by manipulating both the M-V assignment and the folding angle, the acoustic attenuation behavior of single-tubular origami metamaterials can be effectively programmed, highlighting their potential for applications such as adaptive acoustic waveguides and tunable noise-control structures.

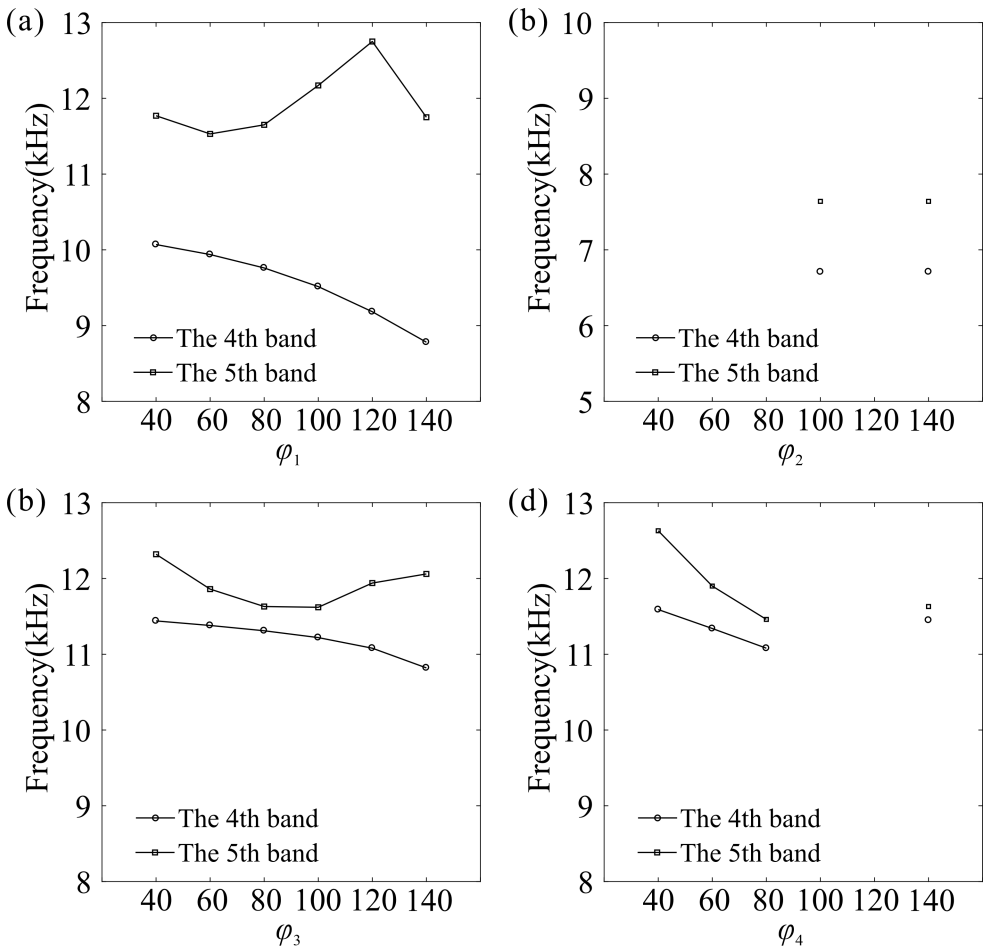

Fig. 3-31 Evolution of the frequency ranges of the first directional bandgap for (a) DC-1, (b) DC-2, (c) DC-3 and (d) DC-4 as a function of the folding angle φ_i.

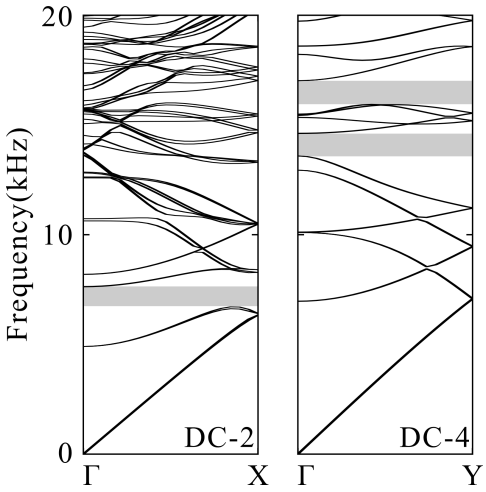

Fig. 3-32 Acoustic band structures of DC-2 along the Γ–X direction at φ_2=140° and DC-4 along the Γ–Y direction at φ_4=40°.

3.4.2 Acoustic Properties of the Mixed Metamaterials

Building upon the acoustic characteristics of the uniform configurations, this section further investigates wave propagation in mixed metamaterial assemblies. The design strategy is to spatially integrate DC-1 and DC-2, as well as DC-3 and DC-4, into mixed structures. By combining sub-domains with different bandgap characteristics, the resulting metamaterials can selectively guide acoustic waves along specific pathways. In this sense, the mixed designs function as programmable acoustic waveguides.

To demonstrate this frequency-dependent spatial filtering capability, a mixed assembly composed of DC-1 and DC-2 was subjected to incident acoustic waves at several representative frequencies. The corresponding simulated acoustic pressure field distributions are shown in Fig. 3-33. The pressure fields indicate that the transmission behavior of the mixed structure is highly sensitive to the excitation frequency. For clarity, the incident plane-wave side is treated as the input, and the transmission states at the terminal ends are represented by binary outputs. An output state of 1 denotes successful transmission, whereas an output state of 0 denotes blockage. The corresponding transmission states at different representative frequencies are summarized in Table 3-3.

At 16.2 kHz, both the DC-1 and DC-2 segments operate within their respective stopbands. As shown in Fig. 3-33(a), the incident acoustic waves are strongly attenuated within the structure, preventing transmission through either pathway and resulting in a globally blocked state. In contrast, a fully transmitted state is observed at 3.2 kHz. The pressure field in Fig. 3-33(b) shows that both sub-domains are in their passband regimes, allowing the incident sound waves to propagate through the entire mixed assembly. At intermediate frequencies, selective wave routing can be achieved. At 9.4 kHz, the DC-1 domain acts as an acoustic barrier, whereas the DC-2 domain still permits wave propagation, as shown in Fig. 3-33(c). Consequently, the acoustic energy is selectively guided through the DC-2 pathway. A reversed routing effect occurs at 2.4 kHz. As shown in Fig. 3-33(d), the acoustic waves propagate through the DC-1 section, while the DC-2 section blocks the incident energy due to its stopband behavior at this frequency. These four typical transmission states are listed in Table 3-3 for clarity.

It is worth noting that the transmission behavior of the DC-1 segment at 2.4 kHz shown in Fig. 3-33(d) appears inconsistent with the band structure characteristics

reported earlier. This discrepancy arises from the different boundary conditions adopted in the two analyses. In the band structure calculations, periodic boundary conditions were applied to the origami unit cell, representing an infinite periodic metamaterial. By contrast, only a finite number of cells are combined in the mixed metamaterial, and a soft acoustic boundary condition is used at the boundaries of the assembly. Consequently, the wave transmission observed in the finite mixed structure can deviate from the predictions of the infinite periodic band structure.

Similar programmable waveguiding behavior is also observed in the mixed configuration composed of DC-3 and DC-4. The simulated acoustic pressure field distributions under different excitation frequencies are shown in Fig. 3-34. As illustrated in Fig. 3-34(a), the incident waves are almost completely blocked when the excitation frequency falls within the overlapping stopbands of both sub-domains, leading to a global low-transmission state.

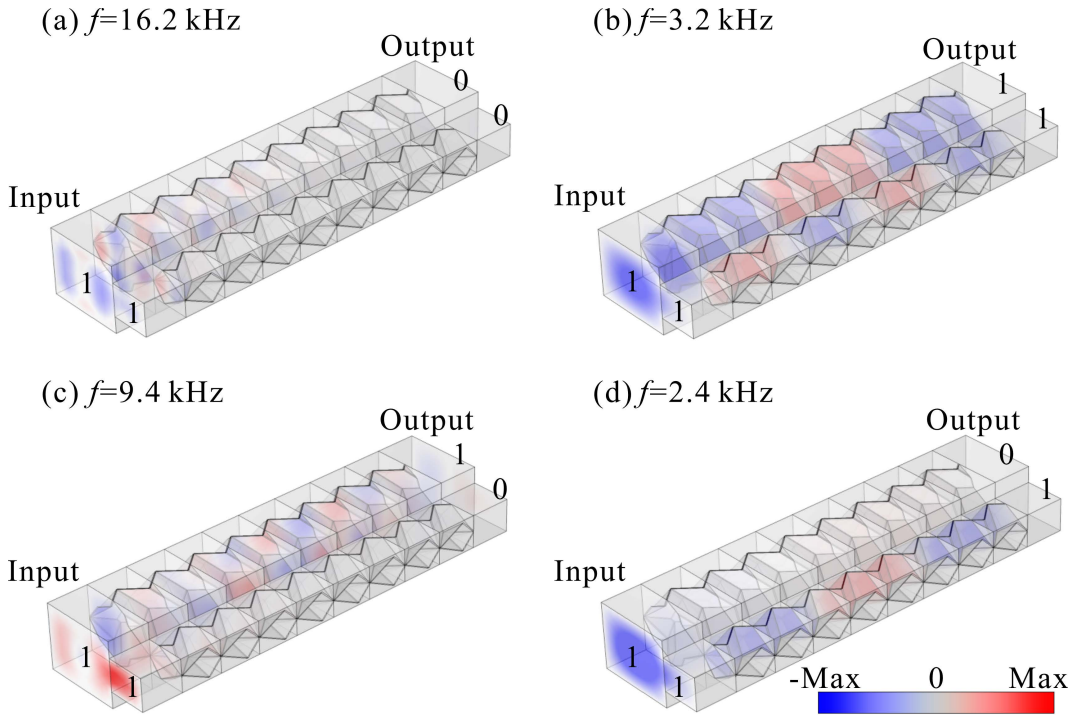

Fig. 3-33 Simulated acoustic pressure field distributions of the mixed DC-1 and DC-2 metamaterial under frequencies of (a) 16.2 kHz, (b) 3.2 kHz, (c) 9.4 kHz, and (d) 2.4 kHz. Binary indicators 0 and 1 represent the blocked and transmitted output states respectively. The same notation is used in the subsequent pressure maps.

Table 3-3 Frequency-dependent transmission states of the mixed metamaterials under representative frequencies.

Output	DC-1&DC-2	DC-3&DC-4
00	16.2 kHz	4.1 kHz
11	3.2 kHz	7.9 kHz
10	2.4 kHz	2.2 kHz
01	9.4 kHz	10.2 kHz

By contrast, Fig. 3-34(b) shows that when both sub-domains are in passband regimes, the acoustic energy can propagate through all available channels. The selective transmission states are illustrated in Figs. 3-34(c) and 3-34(d). In Fig. 3-34(c), the acoustic energy is guided exclusively through the DC-4 pathway because the adjacent DC-3 domain acts as a stopband filter. In Fig. 3-34(d), the situation is reversed: the DC-4 domain blocks wave propagation, while the DC-3 domain allows transmission, thereby switching the propagation pathway.

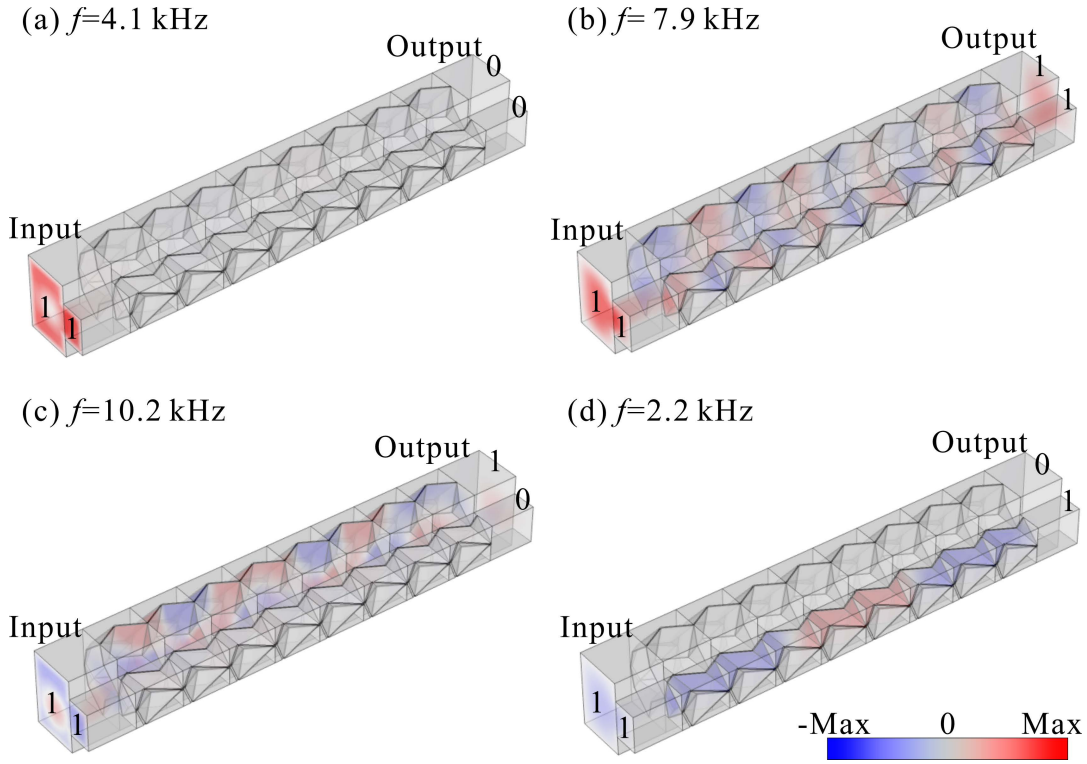

Fig. 3-34 Simulated acoustic pressure field distributions of the mixed DC-3 and DC-4 metamaterial under frequencies of (a) 4.1 kHz, (b) 7.9 kHz, (c) 10.2 kHz, and (d) 2.2 kHz.

These results demonstrate that combining different single-tubular metamaterial configurations enables frequency-dependent control of acoustic wave propagation. By exploiting the distinct stopband characteristics of different sub-domains, the mixed metamaterials can realize global blocking, full transmission, and selective wave routing under different excitation frequencies. This provides an effective strategy for programming acoustic functionalities in origami metamaterials and highlights their potential in adaptive waveguiding and acoustic filtering systems.

3.5 Conclusions and Discussion

In this chapter, a series of single-DOF rigid foldable origami metamaterials based on the double-corrugated pattern have been created by varying the M-V assignments. The geometric dimensions and Poisson's ratio of these metamaterials have been analyzed. To investigate the impact of M-V assignments on the mechanical properties, a finite element model has been established and experimentally validated. Furthermore, the acoustic band structures and their programmability have been explored to reveal the wave propagation characteristics.

Regarding the mechanical properties, the analysis of simulation results under compression in two rigid foldable directions indicates that metamaterials with identical Poisson's ratios exhibit similar deformation modes and mechanical responses. The findings of our research demonstrate that varying the M-V assignments effectively influences the mechanical properties through changing the rate and magnitude of angle changes. The normalized stiffness is influenced by the rate of angle changes. And the SEA is related to the magnitude of angle changes when the deformation of the metamaterials follows the rigid origami folding mode. For the mixed metamaterials, mechanical properties in the x and y directions are similar to those of the uniform metamaterials. While in the z direction, the mixed metamaterials display unique graded stress. These phenomena are determined by the number and type of units involved in deformation during the compression process.

In terms of acoustic properties, the results demonstrate that the M-V assignments play a key role in determining the wave attenuation behavior. Under the considered propagation directions, DC-1 and DC-3 exhibit pronounced directional bandgaps, whereas DC-2 and DC-4 do not show evident bandgaps at the same folding state within

the investigated frequency range. Parametric analysis further shows that these acoustic characteristics are highly sensitive to the folding state. By adjusting the folding angle, the location and width of the directional bandgaps can be effectively tuned, and directional stopbands can also be activated in configurations that do not exhibit them at other folding states. Moreover, by integrating different configurations into mixed metamaterials, frequency-dependent global blocking, full transmission, and selective waveguiding can be achieved. These results demonstrate that the acoustic properties of the proposed origami metamaterials can be programmed through the combined manipulation of M-V assignments and folding states.

Given the complexity of M-V assignments, this dissertation focuses exclusively on rigid foldable double-corrugated configurations. Future research will concentrate on exploring non-rigid folding kinematics to unlock a broader range of programmable mechanical and acoustic responses.

Chapter 4 Double-Tubular Metamaterials with Independently Programmable Mechanical and Acoustic Properties

4.1 Introduction

With the advance in mechanical metamaterials, recent research has increasingly focused on the multifunctional ones, as they can provide versatile cross-domain properties for complicated engineering applications, such as energy and sound absorption, vibration isolation, and noise attenuation. While Chapter 3 preliminarily investigated the factors influencing the mechanical and acoustic properties of origami metamaterials, in most cases, the multiple properties of existing metamaterials cannot be programmed independently, not to mention to be tuned post-fabrication.

Thus, the objective of this chapter is to achieve independent programmability and tunability of mechanical and acoustic properties. For this purpose, a series of double-tubular metamaterials are designed based on the criteria established in Chapter 2, followed by a systematic analysis of their geometric characteristics. Subsequently, the mechanical and acoustic properties are investigated to elucidate how these dual performances evolve with parametric variations. Furthermore, utilizing the nonlinear mapping between design parameters and physical responses, the independent programmability of the two properties is achieved. Finally, by incorporating thermoplastic polymers, geometric reconfiguration and property tunability are realized under thermomechanical stimuli.

The outline of this chapter is as follows. Section 4.2 details the geometric design and folding kinematics of the double-tubular origami units. Section 4.3 investigates the mechanical properties of the double-tubular metamaterials, followed by an analysis of their acoustic properties in Section 4.4. Building upon these analyses, Section 4.5 explores the advanced design strategies for these double-tubular metamaterials by demonstrating the independent programmability and tunability of their dual properties. This section not only establishes methodologies to simultaneously independently program the mechanical and acoustic behaviors, but also utilizes post-fabrication geometric reconfiguration to achieve tunable properties. Finally, Section 4.6 summarizes the main conclusions of the chapter.

4.2 Geometry and Folding Kinematics

The double-tubular origami unit presented in Fig. 4-1 features two perpendicular tubular pathways aligned along x and z axes, constructed through the connections of parallelogram panels, as shown in the front and top views in Fig. 4-2(a) and 4-2(b), respectively. The configuration comprises four distinct groups of geometrically defined parallelograms: Panels DHGC, CGFB, and CKJB share identical geometries with sector angle α_1 and length a_1, b_1; Panels DHEA, AEFB, AIJB are characterized by α_2, a_2, b_1. Panels HOLE, ELMF, ILMJ are characterized by α_3, a_2, b_2. Panels HONG, GNMF, KNMJ are characterized by α_4, a_1, b_2. Detailed definition of geometric parameters is presented in Table 4-1. In addition, to ensure a single-DOF motion of the unit cell, the design parameters should satisfy[154,155]

$$\begin{aligned} a_1\cos\alpha_1 &= a_2\cos\alpha_2, \\ a_1\cos\alpha_4 &= a_2\cos\alpha_3, \\ b_1\cos\alpha_1 &= b_2\cos\alpha_4. \end{aligned} \tag{4-1}$$

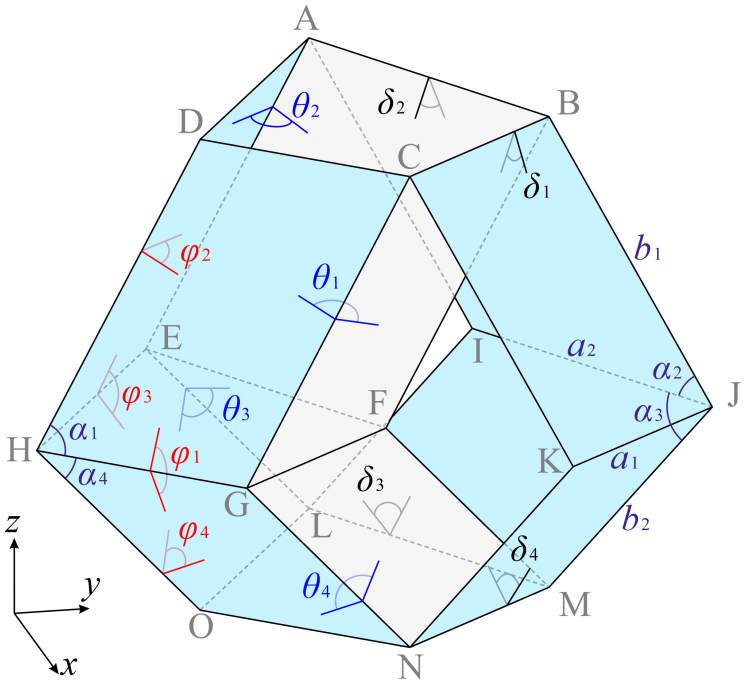

Fig. 4-1 Geometry of the double-tubular origami unit.

Hence, the folding kinematics of the unit cell can be described by Eqs. (4-2)-(4-5) in which the dihedral angle φ_1 is taken as the input to drive the rest dihedral angles φ_i, θ_i, and δ_i (i=1, 2, 3, 4)[87,147]. In this framework (see Fig. 4-1), φ_2, φ_4, and θ_i determine

the folding state of the unit cell in the x direction, while φ_1, φ_3, and δ_i similarly determine the folding state in the z direction

$$\begin{aligned}
\varphi_2 &= 180^\circ - 2\arctan\left[\frac{\cos^2\frac{\varphi_1}{2}\left(2\sin\alpha_2\sin\alpha_4\tan\varphi_1/2-\sqrt{P_1+4\sin^2\alpha_2\sin^2\alpha_4\tan^2\frac{\varphi_1}{2}}\right)}{\cos\alpha_3-\cos(\alpha_1-\alpha_2)\cos\alpha_4+\cos\varphi_1\sin(\alpha_1-\alpha_2)\sin\alpha_4}\right],\\
\varphi_3 &= \arccos\left(\cos\alpha_1\cos\alpha_4-\cos\alpha_2\cos\alpha_3+\frac{\sin\alpha_1\sin\alpha_4\cos\varphi_1}{\sin\alpha_2\sin\alpha_3}\right),\\
\varphi_4 &= 180^\circ - 2\arctan\left[\frac{\cos^2\frac{\varphi_1}{2}\left(2\sin\alpha_1\sin\alpha_3\tan\varphi_1/2-\sqrt{P_2+4\sin^2\alpha_1\sin^2\alpha_3\tan^2\frac{\varphi_1}{2}}\right)}{\cos\alpha_2-\cos\alpha_1\cos(\alpha_3-\alpha_4)-\cos\varphi_1\sin\alpha_1\sin(\alpha_3-\alpha_4)}\right],
\end{aligned} \tag{4-2}$$

$$\begin{aligned}
\theta_1 &= 180^\circ - 2\operatorname{arccot}\left(-\cos\alpha_1\cot\varphi_1+\cot\alpha_4\csc\varphi_1\sin\alpha_1\right),\\
\theta_2 &= 180^\circ - 2\operatorname{arccot}\left(-\cos\alpha_2\cot\varphi_3+\cot\alpha_3\csc\varphi_3\sin\alpha_2\right),\\
\theta_3 &= 180^\circ - 2\operatorname{arccot}\left(-\cos\alpha_3\cot\varphi_3+\cot\alpha_2\csc\varphi_3\sin\alpha_3\right),\\
\theta_4 &= 180^\circ - 2\operatorname{arccot}\left(-\cos\alpha_4\cot\varphi_1+\cot\alpha_1\csc\varphi_1\sin\alpha_4\right),
\end{aligned} \tag{4-3}$$

$$\begin{aligned}
\delta_1 &= 180^\circ - 2\operatorname{arccot}\left(-\cos\alpha_1\cot\varphi_2+\cot\alpha_2\csc\varphi_2\sin\alpha_1\right),\\
\delta_2 &= 180^\circ - 2\operatorname{arccot}\left(-\cos\alpha_2\cot\varphi_2+\cot\alpha_1\csc\varphi_2\sin\alpha_2\right),\\
\delta_3 &= 180^\circ - 2\operatorname{arccot}\left(-\cos\alpha_3\cot\varphi_4+\cot\alpha_4\csc\varphi_4\sin\alpha_3\right),\\
\delta_4 &= 180^\circ - 2\operatorname{arccot}\left(-\cos\alpha_4\cot\varphi_4+\cot\alpha_3\csc\varphi_4\sin\alpha_4\right),
\end{aligned} \tag{4-4}$$

in which

$$\begin{aligned}
P_1 &= -\sec^4\frac{\varphi_1}{2}\left[\cos\alpha_3-\cos(\alpha_1-\alpha_2)\cos\alpha_4+\cos\varphi_1\sin(\alpha_1-\alpha_2)\sin\alpha_4\right],\\
&\quad\left[\cos\alpha_3-\cos(\alpha_1+\alpha_2)\cos\alpha_4+\cos\varphi_1\sin(\alpha_1+\alpha_2)\sin\alpha_4\right]\\
P_2 &= -\sec^4\frac{\varphi_1}{2}\left[\cos\alpha_2-\cos\alpha_1\cos(\alpha_3-\alpha_4)-\cos\varphi_1\sin\alpha_1\sin(\alpha_3-\alpha_4)\right].\\
&\quad\left[\cos\alpha_2-\cos\alpha_1\cos(\alpha_3+\alpha_4)+\cos\varphi_1\sin\alpha_1\sin(\alpha_3+\alpha_4)\right]
\end{aligned} \tag{4-5}$$

And the relationship between the overall dimensions of the unit cell, l_x, l_y, l_z and the input angle φ_1 is

$$\begin{aligned}
l_x &= a_1\sin\alpha_1\sqrt{(1+\cos\theta_1)/2}+a_2\sin\alpha_2\sqrt{(1+\cos\theta_2)/2},\\
l_y &= 2a_1\sqrt{\frac{1+\cos^2\alpha_1-\sin^2\alpha_1\cos\theta_1}{2}}+2b_1\sqrt{\frac{1+\cos^2\alpha_1-\sin^2\alpha_1\cos\delta_1}{2}},\\
l_z &= b_1\sin\alpha_1\sqrt{(1+\cos\delta_1)/2}+b_2\sin\alpha_4\sqrt{(1+\cos\delta_4)/2}.
\end{aligned} \tag{4-6}$$

Table 4-1 Geometric significance of the parameters.

Parameter	Geometric significance
a_1	The length of HG, GF, KJ, DC, CB, ON and NM
a_2	The length of HE, EF, IJ, DA, AB, OL and LM
b_1	The length of DH, AE, CG, CK, AI, BF and BJ
b_2	The length of HO, EL, GN, KN, IL, FM and JM
α_1	The interior angle of parallelogram CDHG, BCGF and BCKJ
α_2	The interior angle of parallelogram ADHE, BAEF and BAIJ
α_3	The interior angle of parallelogram LOHE, MLEF and MLIJ
α_4	The interior angle of parallelogram NOHG, MNGF and MNKJ
φ_1	The dihedral angle between parallelogram CDHG and NOHG
φ_2	The dihedral angle between parallelogram CDHG and ADHE
φ_3	The dihedral angle between parallelogram ADHE and LOHE
φ_4	The dihedral angle between parallelogram LOHE and NOHG
θ_1	The dihedral angle between parallelogram CDHG and BCGF
θ_2	The dihedral angle between parallelogram ADHE and BAEF
θ_3	The dihedral angle between parallelogram LOHE and MLEF
θ_4	The dihedral angle between parallelogram NOHG and MNGF
δ_1	The dihedral angle between parallelogram BCJF and BCKJ
δ_2	The dihedral angle between parallelogram BAEF and BAIJ
δ_3	The dihedral angle between parallelogram MLEF and MLIJ
δ_4	The dihedral angle between parallelogram MNJF and MNKJ
γ_1	∠BAD
γ_2	∠DCB
ε_1	∠KCG
ε_2	∠GNK

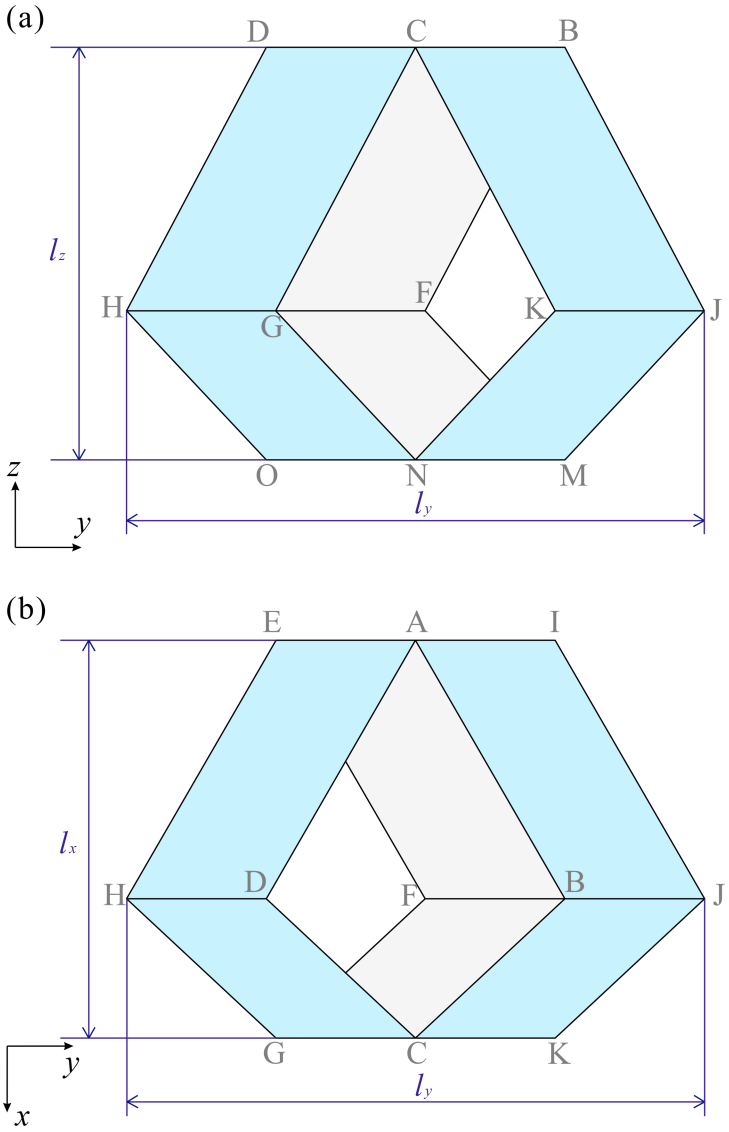

Fig. 4-2 (a) Front and (b) top views of the double-tubular origami unit.

By varying the geometric parameters, the flat foldability of the double-tubular origami unit cell can be modulated, leading to three different types with fundamentally distinct folding behaviors, referred to as C1, C2, and C3 hereafter. In general, the unit cell is not flat foldable along either tubular direction (x and z axes) as demonstrated by C1 in Fig. 4-3. As the dihedral angles and dimensions vary with input φ_1, neither l_x nor l_z can reach zero. At the upper or lower bound of the input φ_1, one side of the unit cell is flattened, and the unit cell is self-locked, corresponding to $\varphi_{\text{lock}x}$ =180° and $\varphi_{\text{lock}z} = 180° - \arccos\left[\cot\alpha_1 \cot\left(\alpha_3+\alpha_4\right) - \cos\alpha_2 \csc\alpha_1 \csc\left(\alpha_3+\alpha_4\right)\right]$.

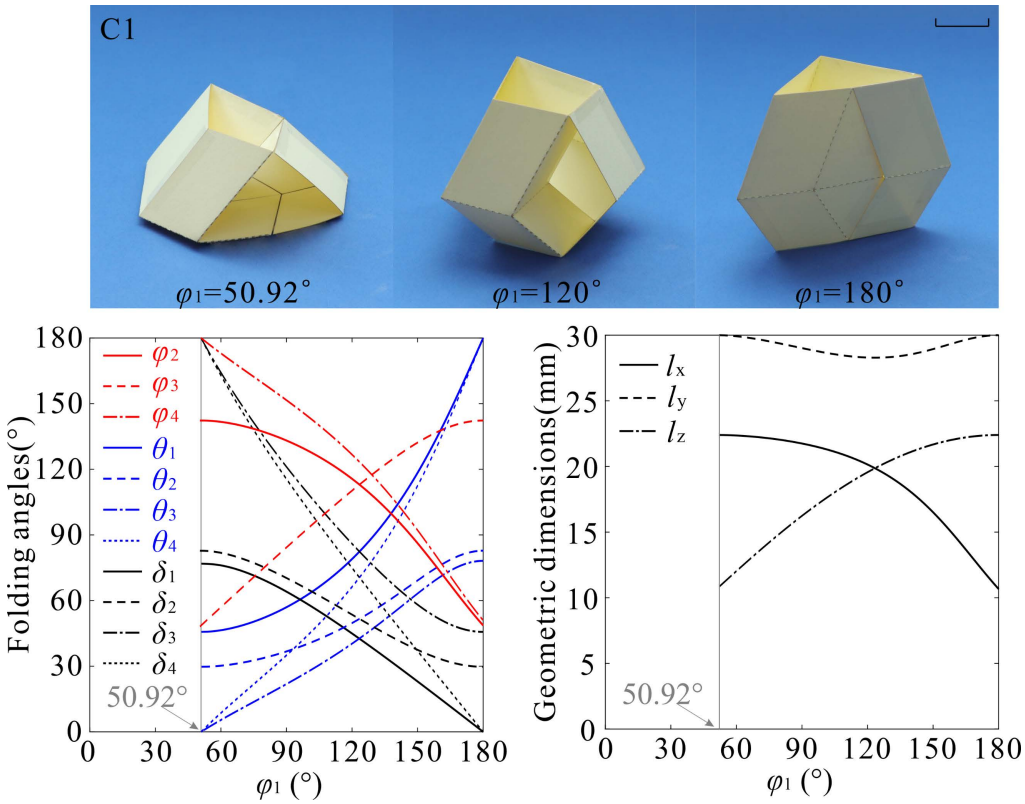

Fig. 4-3 Folding and deployment processes, along with the dihedral angles and geometric dimensions of the origami units C1, with a_1=b_2=15 mm, a_2=b_1=21.93 mm, α_1=α_3=70°, α_2=76.47°, α_4=60°. Scale bar: 10 mm.

To obtain flat foldability in one direction, for instance, the x direction, the design parameters should meet a_1=a_2, α_1=α_2, and α_3=α_4 so that the corresponding cross section becomes a rhombus, and the dihedral angles exhibit $\varphi_1 = \varphi_3$, $\theta_1 = \theta_2$, $\theta_3 = \theta_4$, $\delta_1 = \delta_2$, and $\delta_3 = \delta_4$. The folding behavior of a prototype of this type, C2, is presented in Fig. 4-4. Similarly, when b_1=b_2, α_1=α_4, and α_2=α_3, the unit cell is flat foldable along z direction. Therefore, when both conditions are satisfied, we obtain a very special case, C3, which is flat foldable in both directions (Fig. 4-5) with φ_3=φ_1, φ_2=φ_4= $180° - 2\arctan\left(\cos\alpha \tan\varphi_1/2\right)$, $\theta_i = 180° - 2\,\mathrm{arccot}\left(\cos\alpha \tan\varphi_1/2\right)$, and $\delta_i = 180° - 2\,\mathrm{arccot}\left(\cos\alpha \tan\varphi_2/2\right)$.

Specifically, C3 has a unique kinematic feature within the range of design parameter α as shown in Fig. 4-6(a) that the φ_2 versus φ_1 curve is symmetric about the 45° line, indicating that for any point (φ_1, φ_2) on curve φ_2, its transposed point (φ_2, φ_1) can also be found on the same curve. Such angular transposition also leads to a dimension transposition between the x and z axes. For example (Fig. 4-6(b)), for α = 60°, a_1 = a_2 = b_1 = b_2 = 15mm, φ_1 = 90°, φ_2 = 126.87°, l_x= 23.24mm, l_z= 18.37mm. After

transposition, φ_1 = 126.87°, φ_2 = 90°, and then l_x changes to 18.37mm while l_z becomes 23.24mm. Furthermore, when $\varphi_1 = \varphi_2 = 2\arctan\sqrt{\sec\alpha}$ (Fig. 4-7(a)), l_x and l_z are guaranteed to be equal (Fig. 4-7(b)).

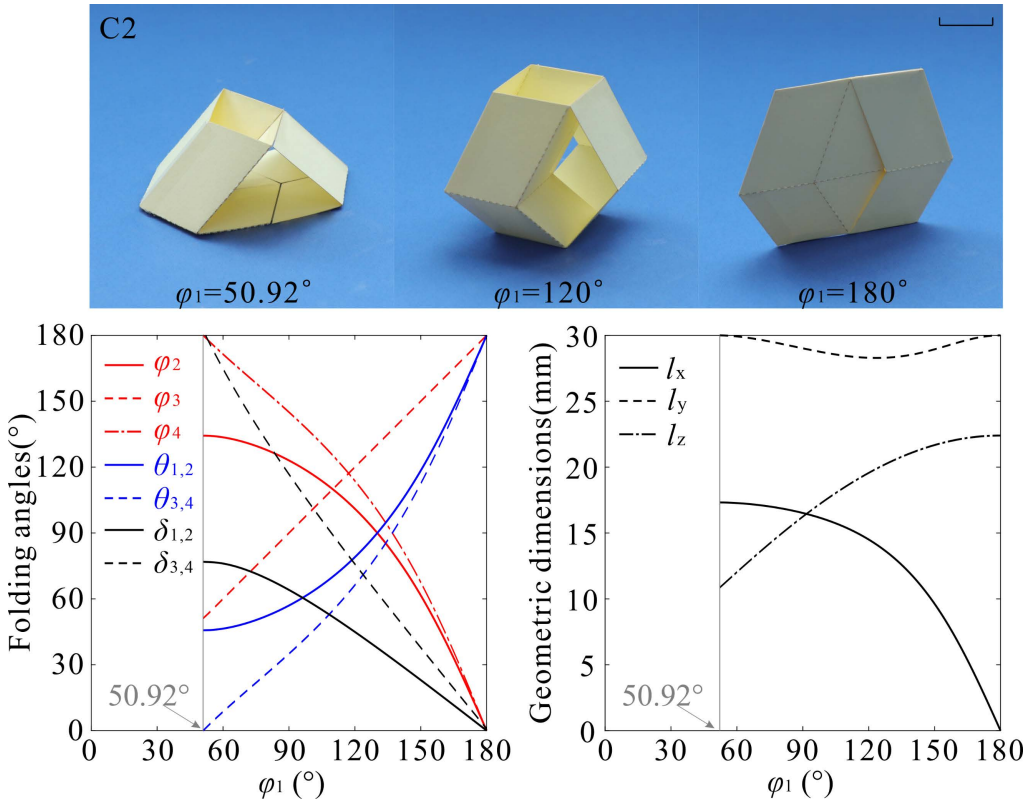

Fig. 4-4 Folding and deployment processes, along with the dihedral angles and geometric dimensions of the origami units C2, with a_1=a_2=b_2=15 mm, b_1=21.93 mm, α_1=α_2=70°, α_3=α_4=60°. Scale bar: 10 mm.

It is also worth noting that while C1 (with $\alpha_1 \neq \alpha_3$) and C2 can achieve identical dimensions in *x* and *z* directions under certain specific folding states. However, these two categories do not generally exhibit a universal geometric transposition feature throughout the entire deployment process. The inherent absence of structural symmetry dictates that their corresponding folding angles φ_1 and φ_2 maintain fundamentally distinct kinematic rates. Furthermore, the established categories from C1 to C3 comprehensively exhaust all possible rigid folding mechanisms permitted by the fundamental compatibility constraints defined in Eq. (4-1). While parametric variations (changing α_i, a_1, a_2 b_1 and b_2) generate infinite variants within these categories, they cannot produce new folding behaviors that violate the compatibility conditions.

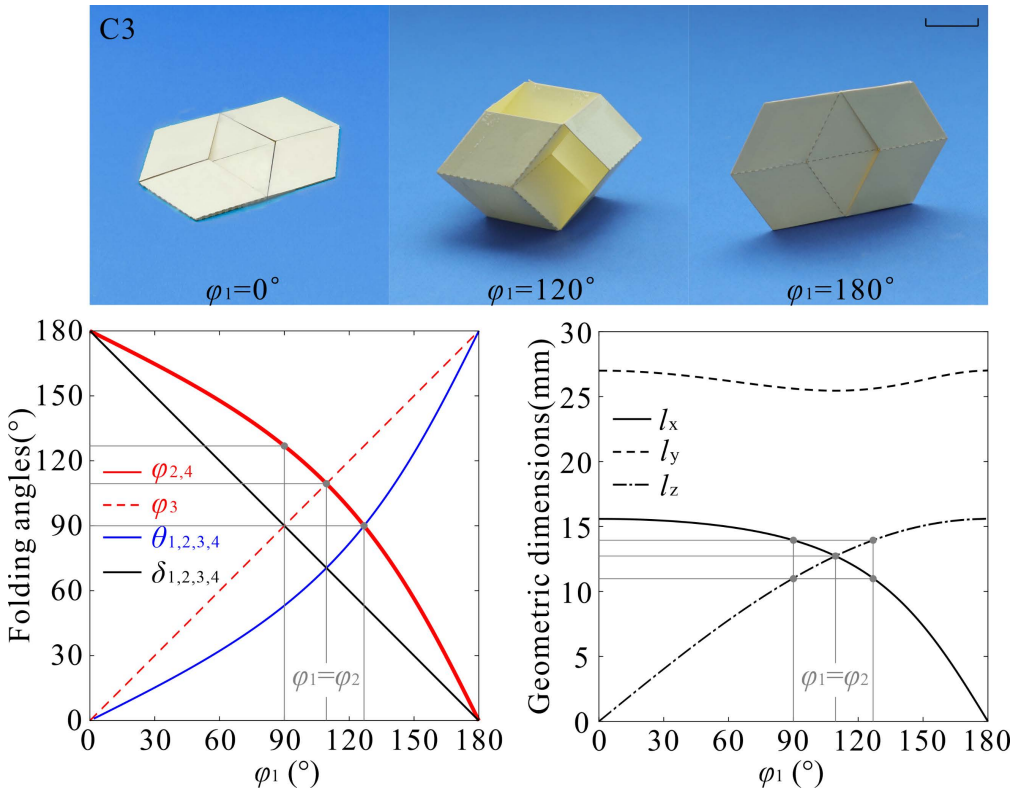

Fig. 4-5 Folding and deployment processes, along with the dihedral angles and geometric dimensions of the origami units C3, with $a_1=a_2=b_1=b_2=15$ mm, $\alpha_1=\alpha_2=\alpha_3=\alpha_4=60°$. Scale bar: 10 mm.

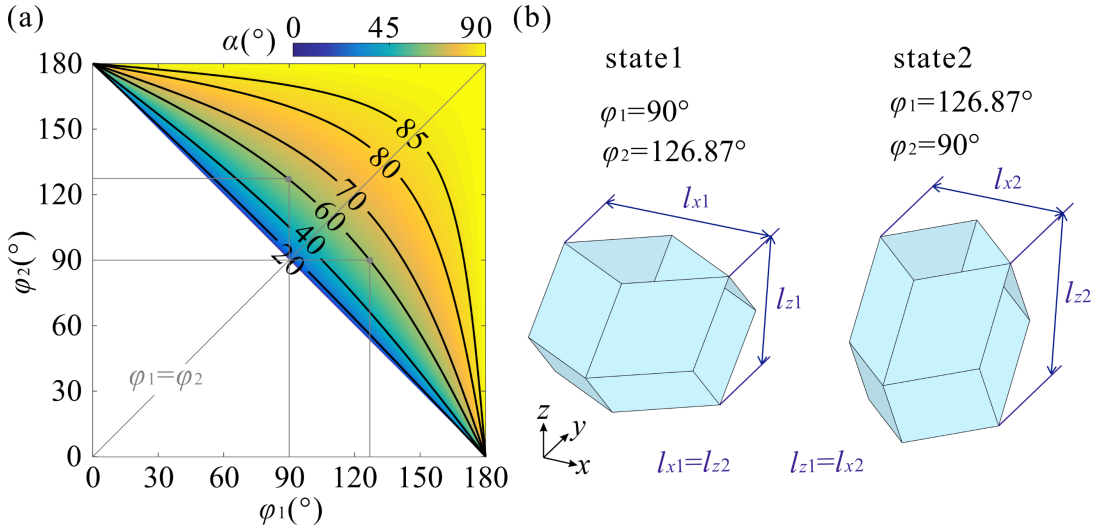

Fig. 4-6 (a) Relationships of φ_2 versus φ_1 with different α showing symmetry about the 45° line; (b) Two configurations featuring geometric transposition with $\alpha=60°$, $a_1=a_2=b_2=15$ mm, (φ_1, φ_2) = (90°, 126.87°) and (126.87°, 90°), respectively.

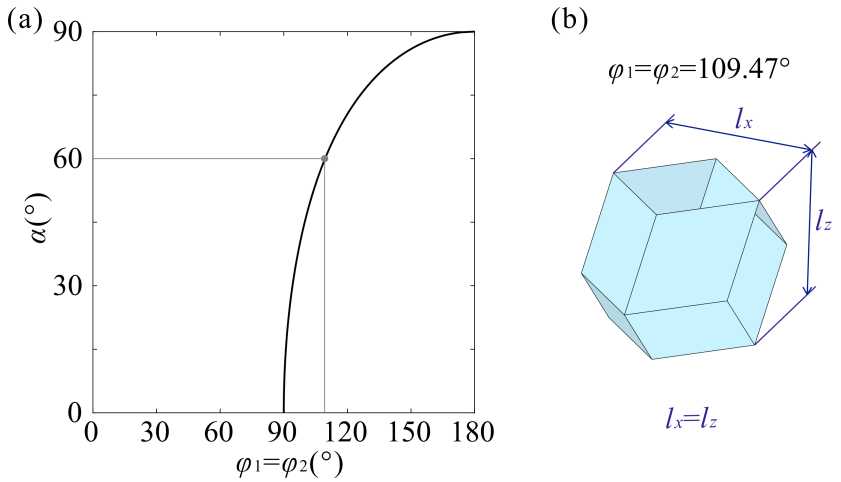

Fig. 4-7 (a) Relationships of α versus $\varphi_1=\varphi_2$; (b) configuration with α=60°, $a_1=a_2=b_2$=15 mm and $\varphi_1=\varphi_2$=109.47° featuring identical dimensions in the x and z directions ($l_x=l_z$).

Finally, 3D metamaterials can be assembled from the proposed unit cells following the procedure depicted in Fig. 4-8. First, the unit cell as previously shown in Fig. 4-1 is rotated along the x axis by 180°; second, both the original and rotated unit cells are tessellated along the z axis; third, the original and rotated multi-unit cells are shifted by half a unit along the z axis and then connected along the y axis by sharing the intersecting crease lines; last, the unit cell combination obtained from the previous step is tessellated along the x axis to form a 3D metamaterial with $m_x \times m_y \times m_z$ unit cells.

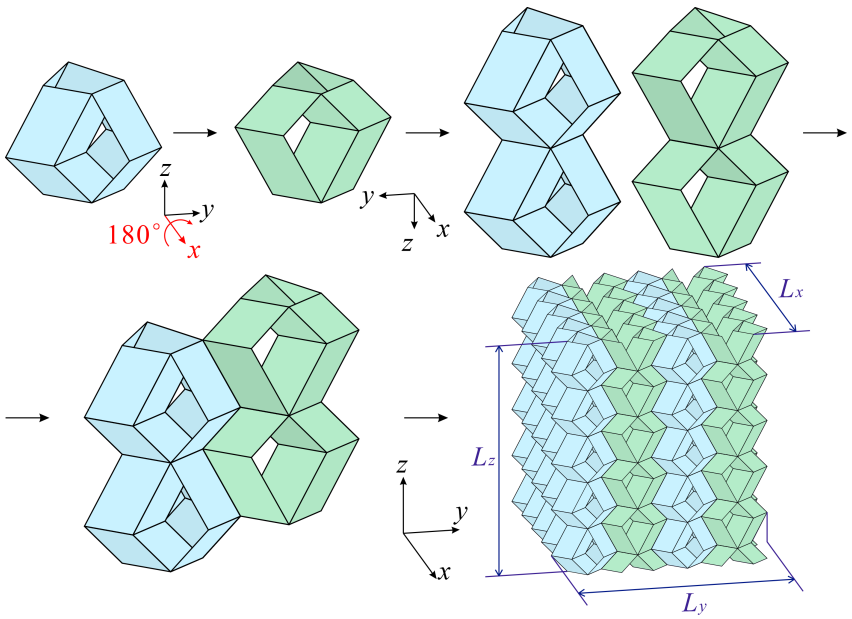

Fig. 4-8 Construction process of a 5×2×5 double tubular origami metamaterial.

We name the metamaterials formed solely by unit cell C1-C3 as MC1-MC3, respectively, the overall dimensions of which are defined by L_x, L_y, and L_z and can be calculated using

$$\begin{aligned} L_x &= m_x\left(a_1\cos\frac{\gamma_2}{2}+a_2\cos\frac{\gamma_1}{2}\right), \\ L_y &= \begin{cases} m_y\left(2a_1\sin\dfrac{\gamma_2}{2}+b_1\sin\dfrac{\varepsilon_1}{2}\right) & \text{when } m_y \text{ is even} \\ 2m_y a_1\sin\dfrac{\gamma_2}{2}+\left(m_y+1\right)b_1\sin\dfrac{\varepsilon_1}{2} & \text{when } m_y \text{ is odd} \end{cases}, \\ L_z &= m_z\left(b_1\cos\frac{\varepsilon_1}{2}+b_2\cos\frac{\varepsilon_2}{2}\right). \end{aligned} \tag{4-7}$$

4.3 Mechanical Property of Double-Tubular Metamaterials

Taking advantage of the rigid origami folding mode and the previously established folding kinematics of the unit cell C3, we develop an analytical model for the stiffness and SEA of MC3 in the *x* and *z* directions based on the assumptions that all creases are characterized as elastic-plastic hinges while the panels are rigid without deformation. The bending moment per unit length can be expressed as

$$M_{\varphi 1}=\begin{cases} \dfrac{ah^2\sigma_0 E\left(\varphi_1-\varphi_{1\mathrm{i}}\right)}{12p}, \text{when } \varphi_1\le\varphi_{\mathrm{el}}\left(elastic\right) \\ \dfrac{\sigma_0 t^2}{4}, \text{when } \varphi_1>\varphi_{\mathrm{el}}\left(plastic\right) \end{cases}, \tag{4-8}$$

where a and t represent the length and thickness of the parallelogram panel, respectively, $\varphi_{1\mathrm{i}}$ is the initial folding angle, p represents the size of the elastically deformed part and is usually considered to range between $2t$ and $5t$. To take strain hardening effects into account, plastic flow stress σ_0 is used in the calculation, as

$$\sigma_0=\frac{\sigma_y+\sigma_u}{2}, \tag{4-9}$$

φ_{el} is the limit of the elastic dihedral angle, and can be calculated as

$$\varphi_{\mathrm{el}}=\varphi_{1\mathrm{i}}+3n\sigma_0/E. \tag{4-10}$$

Similar equations can be obtained by replacing the φ_1 related parameters of Eqs. (4-8) and (4-10) with dihedral angles φ_i, θ_i and δ_i. The energy balance equation, which accounts for the external work and dissipated energy within the origami metamaterial,

defines the force-displacement characteristic:

$$F\mathrm{d}D=\sum_{i=1}^{4}\left(n_{\varphi i}l_{\varphi i}M_{\varphi i}\mathrm{d}\varphi_i+n_{\theta i}l_{\theta i}M_{\theta i}\mathrm{d}\theta_i+n_{\delta i}l_{\delta i}M_{\delta i}\mathrm{d}\delta_i+n_{\gamma i}l_{\gamma i}M_{\gamma i}\mathrm{d}\gamma_i\right), \tag{4-11}$$

in which n represents the number of the corresponding dihedral angles in the metamaterial, D represents the displacement: $D=L_x(\varphi_{1i})-L_x(\varphi_1)$ under x direction compression and $D=L_z(\varphi_{1i})-L_z(\varphi_1)$ under z direction compression, l represents the length of the hinge, which is equal to a_1, a_2, b_1 or b_2 depending on different dihedral angles. By considering the folding angle φ_1 as the governing variable, Eq. (4-11) can be expressed as

$$\begin{aligned}F\frac{\partial D}{\partial\varphi_1}\mathrm{d}\varphi_1&=n_{\varphi1}a_1M_{\varphi1}\mathrm{d}\varphi_1+\sum_{i=2}^{4}\left(n_{\varphi i}l_{\varphi i}M_{\varphi i}\frac{\partial\varphi_i}{\partial\varphi_1}\mathrm{d}\varphi_1\right)\\&+\sum_{i=1}^{4}\left(n_{\theta i}l_{\theta i}M_{\theta i}\frac{\partial\theta_i}{\partial\varphi_1}\mathrm{d}\varphi_1+n_{\delta i}l_{\delta i}M_{\delta i}\frac{\partial\delta_i}{\partial\varphi_1}\mathrm{d}\varphi_1+n_{\gamma i}l_{\gamma i}M_{\gamma i}\frac{\partial\gamma_i}{\partial\varphi_1}\mathrm{d}\varphi_1\right).\end{aligned} \tag{4-12}$$

Hence, the reaction force F can be obtained by

$$F=\frac{\begin{aligned}&n_{\varphi1}a_1M_{\varphi1}+\sum_{i=2}^{4}\left(n_{\varphi i}l_{\varphi i}M_{\varphi i}\frac{\partial\varphi_i}{\partial\varphi_1}\right)\\&+\sum_{i=1}^{4}\left(n_{\theta i}l_{\theta i}M_{\theta i}\frac{\partial\theta_i}{\partial\varphi_1}+n_{\delta i}l_{\delta i}M_{\delta i}\frac{\partial\delta_i}{\partial\varphi_1}+n_{\gamma i}l_{\gamma i}M_{\gamma i}\frac{\partial\gamma_i}{\partial\varphi_1}\right)\end{aligned}}{\frac{\partial D}{\partial\varphi_1}}. \tag{4-13}$$

Substituting Eqs. (4-2)-(4-5) into Eq. (4-13), the reaction force F during compression can be obtained. It is assumed that the metamaterial undergoes homogeneous deformation during quasi-static compression, with all cells deforming simultaneously. The maximum displacement of the metamaterial occurs at a specific value of the folding angle $\varphi_{1\mathrm{d}}$. By equating the volume occupied by the parallelogram panels and metamaterial volume at $\varphi_1=\varphi_{1\mathrm{d}}$ the maximum displacement can be obtained from the relationship

$$\begin{aligned}&t\left(n_{\alpha1}a_1b_1\sin\alpha_1+n_{\alpha2}a_2b_1\sin\alpha_2+n_{\alpha3}a_2b_2\sin\alpha_3+n_{\alpha4}a_1b_2\sin\alpha_4\right)\\&=L_{\mathrm{x}}\left(\varphi_{1\mathrm{d}}\right)L_{\mathrm{y}}\left(\varphi_{1\mathrm{d}}\right)L_{\mathrm{z}}\left(\varphi_{1\mathrm{d}}\right),\end{aligned} \tag{4-14}$$

To facilitate comparison among metamaterials with different design parameters, we assess the mechanical response through two main indices, i.e., the initial stiffness $k=\mathrm{d}F/\mathrm{d}D$ within the elastic range, and specific energy absorption $\mathrm{SEA}=\int_0^D FdD/W$ upon the metamaterial is fully folded, in which W represents the weight of the metamaterial.

Having obtained the folding kinematics and the analytical models of the double-tubular origami metamaterials, we subsequently investigate their mechanical response when compressed along the *x* and *z* directions, respectively. Notice that compression along the *y* direction is not considered as the deformation mode does not follow the origami pattern. The compression simulations were implemented in Abaqus/Explicit utilizing the foundational framework established in Chapter 3, Section 3.3. The assembly was compressed between a fixed base plate and a moving top plate to achieve an 85% nominal height reduction. The element type (S4R), friction coefficient (μ=0.3), and energy convergence criteria remain identical to those detailed previously. Based on these established parameters, a global mesh size of 1 mm and an analysis time of 0.1 s were maintained to ensure quasi-static conditions and mitigate hourglass distortion.

Quasi-static compression tests were performed to validate the theoretical and numerical models using a YAW-600 micro-computer controlled electro-hydraulic servo system (500 kN load cell, ±1% accuracy) (Fig. 4-9). Specimens were vertically placed between a stationary rigid plate and a moving rigid plate and subjected to uniaxial displacement control at 5 mm/min until achieving 85% nominal height reduction, with three replicates per configuration. The origami metamaterials were fabricated out of 316L stainless steel due to its high yield strength and plasticity [93,125], with a thickness of 0.8 mm through the 3D printing technique. The printing method employed is selective laser melting with a double laser powder sintering process. The material properties obtained from the uniaxial tensile test are as follows: elastic modulus E=175 GPa, Poisson's ratio v=0.3, yield stress σ_y=486.82 MPa, ultimate stress σ_u=846.0 MPa, ultimate strain ε_u=28.98%. The density of the material is ρ=7.85 g/cm^3.

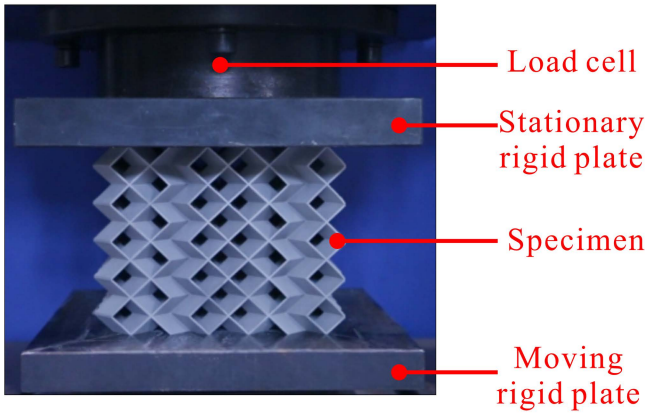

Fig. 4-9 Quasi-static compression setup using the YAW-600.

For metamaterial MC1 with self-locking at both directions in Fig. 4-10(a), the stress versus strain curve in either direction is characterized by a prolonged plateau when the metamaterial deforms primarily through a rigid origami folding mode with localized bending along the creases, followed by a remarkably raised stress when the strain passes through the self-locking point (strain=0.39) and panel deformation becomes dominant. For MC2 with flat foldability along *x* direction and self-locking along *z* direction in Fig. 4-10(b), the curve in the *z* direction shows similar characteristics as that for MC1, while a stable plateau stress is maintained in the *x* direction until the metamaterial is fully squeezed. For the special design MC3 which is flat foldable along both directions, a rigid origami folding mode and a plateau reaction strain are observed in either direction, see the experimental results in Fig. 4-11.

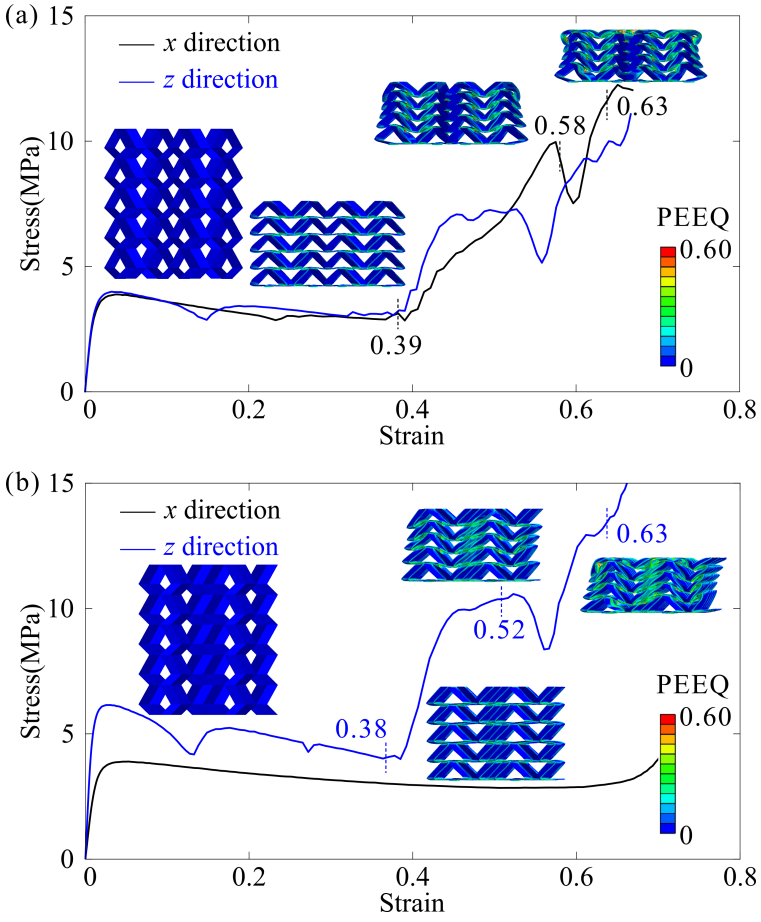

Fig. 4-10 Mechanical properties of the double-tubular origami metamaterials: (a) and (b) Comparative stress versus strain curves under axial compression along *x* and *z* directions for (a) MC1 (a_1=b_2=15 mm, a_2=b_1=21.93 mm, α_1=α_3=70°, α_2=76.47°, α_4=60°, φ_{1i}=119.16°) and (b) MC2 (a_1=a_2=b_2=15 mm, b_1=21.93 mm, α_1=α_2=70°, α_3=α_4=60°, φ_{1i}=119.16°), with corresponding deformation modes and PEEQ distributions.

The analytical stress versus strain curve, stiffness, and specific energy absorption of the MC3 prototype are presented in Fig. 4-11. In the theoretical model, material nonlinearity was considered, as defined in Eqs. (4-8)-(4-10), which account for strain hardening through the plastic flow stress term σ_0. The mechanical properties investigated in this study, including stiffness and SEA, show good agreement between the theoretical predictions and the experimental results, with errors of no more than 2.5% for stiffness and 5.3% for SEA, respectively, as shown in Fig. 4-11. The slight discrepancies observed in the stress-strain curves are mainly attributed to non-ideal factors in the experiments, including non-uniform deformation during quasi-static compression, contact friction, boundary effects, and manufacturing tolerances.

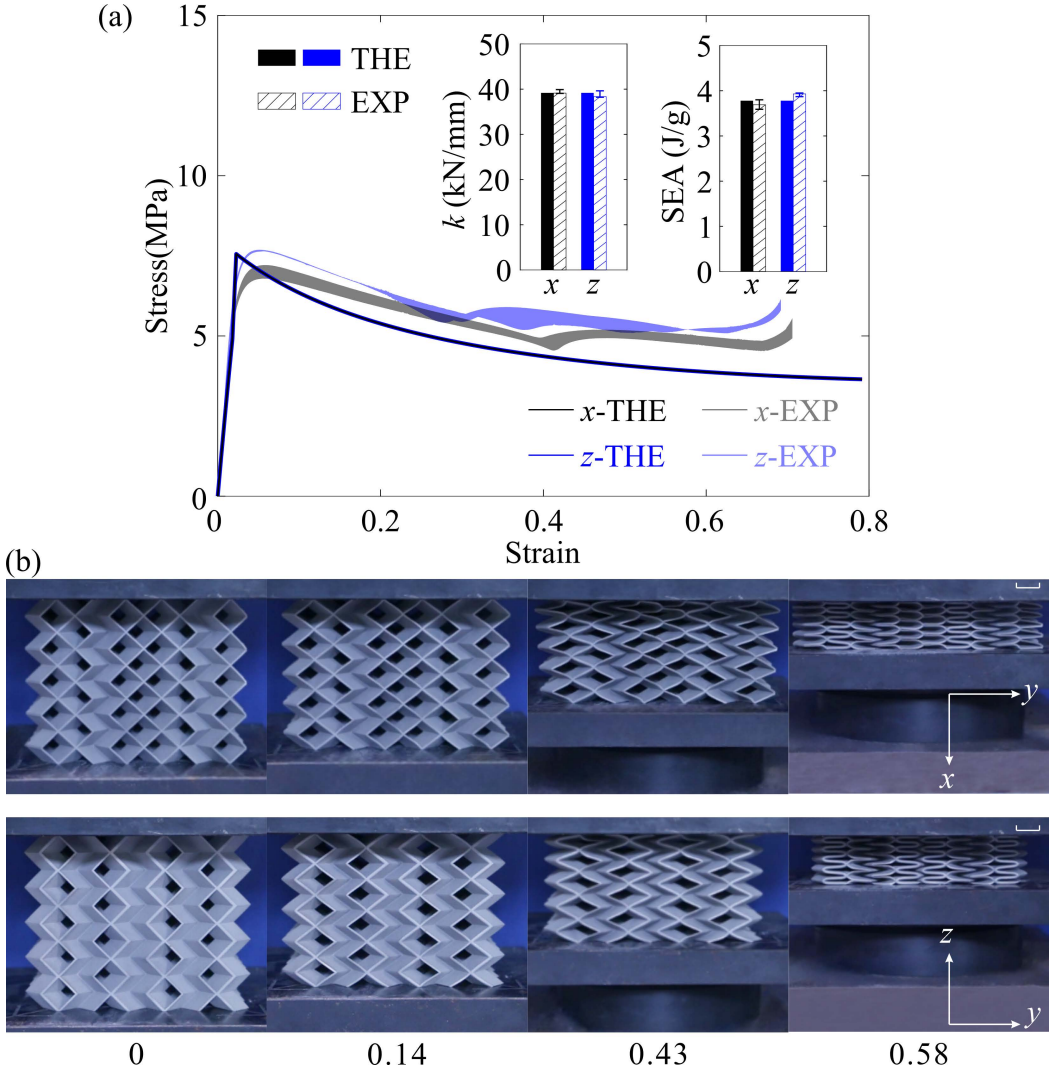

Fig. 4-11 Experimental results of MC3. (a) Theoretical and experimental stress versus strain curves, stiffness and SEA of MC3 (a_1=a_2=b_1=b_2=15 mm, α=60°, φ_{1i}=109.47°) when compressing in the x and z directions; (b) deformation modes of MC3 in two directions. Scale bar: 7 mm.

Utilizing the analytical model, we are able to precisely program the mechanical property of MC3 through the initial folding angles φ_{1i} and the sector angle α. As shown in Fig. 4-12(a)-(b), both k_x and SEA_x are negatively correlated to φ_{1i}. This is because φ_{1i} determines the initial folding state of the metamaterials. A smaller φ_{1i} leads to a less folded initial configuration and thus larger stiffness and specific energy absorption. The correlation between k_x, SEA_x, and α shows a non-monotonic trend due to the complicated kinematic relationship between α and the dihedral angles. Moreover, if we select the geometric parameters by following the contour lines, we can achieve identical k_x or SEA_x out of a variety of distinct configurations.

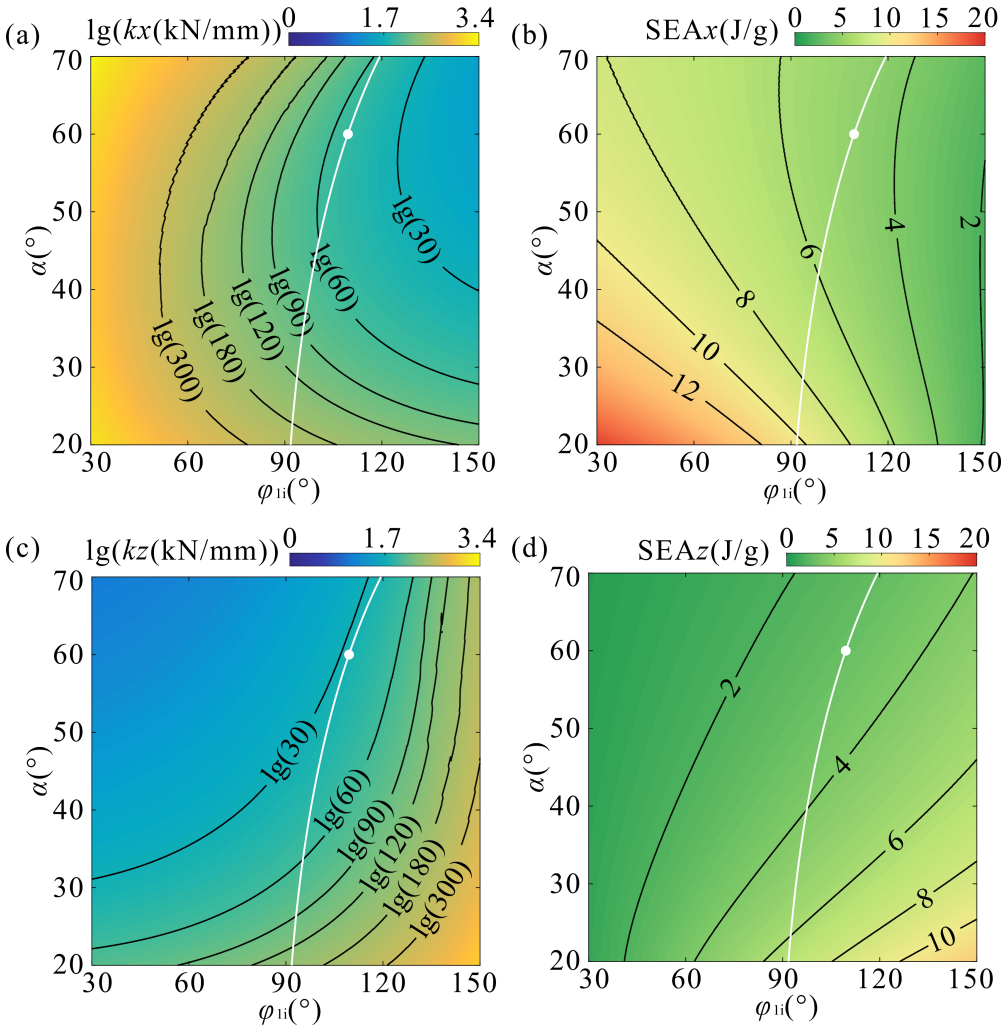

Fig. 4-12 Parametric analysis of stiffness and SEA of MC3 when changing design angle α and initial folding angle φ_{1i}. (a) and (b) Stiffness and SEA in the x direction; (c) and (d) corresponding mechanical properties in the z direction. To enhance visualization clarity of stiffness, all data are subjected to base-10 logarithmic transformation prior to plotting. The white lines represent the configuration at the $\varphi_1=\varphi_2$ state, and the white dots represent the selected configuration in Fig. 4-11.

In contrast, compression along the *z* direction induces completely opposite variation trends as shown in Fig. 4-12(c)-(d) because a less folded initial configuration in the *x* direction corresponds to a more folded one in the *z* direction. Finally, recall that for each α, there exists a special configuration for MC3 that the dimensions in the *x* and *z* directions are identical (Fig. 4-7(a)). The analytical model predicts that at this special configuration, the stiffness and SEA are respectively identical in both directions (white lines in Fig. 4-12), see Appendix A for more details. Overall, by changing the design parameters, the stiffness and SEA can be varied as much as 175 times and 30 times, respectively.

4.4 Acoustic Property of Double-Tubular Metamaterials

Beyond the mechanical properties, we further explore the acoustic properties of the double-tubular origami metamaterials. The structural unit of acoustic metamaterial is obtained by extracting a rectangular unit from the structure (Fig. 4-13). The geometric dimensions of the unit cell can be calculated as

$$\begin{aligned} l_{x'} &= l_x, \\ l_{y'} &= 4a_1\sqrt{\frac{1+\cos^2\alpha_1-\sin^2\alpha_1\cos\theta_1}{2}}+2b_1\sqrt{\frac{1+\cos^2\alpha_1-\sin^2\alpha_1\cos\delta_1}{2}}. \\ l_{z'} &= l_z. \end{aligned} \tag{4-15}$$

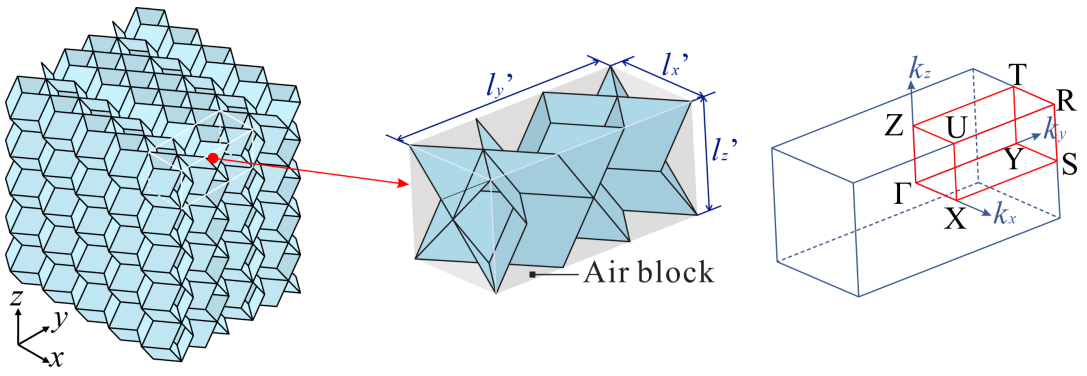

Fig. 4-13 Structural unit geometry and the IBZ.

The primitive lattice is an orthorhombic lattice, and the k-path is determined as Γ–X–S–Y–Γ–Z–U–R–T–Z|Y–T|U–X|S–R for the band structure calculations. The acoustic wave propagation in air follows the classical wave equation[156],

$$\nabla \cdot \left(-\frac{1}{\rho_0} \nabla p \right) - \frac{\omega^2 p_0}{\rho_0 c^2} = 0, \tag{4-16}$$

where c are the speeds of sound; p is the pressure field; ρ_0 is the mass density; $\omega=2\pi f$ is the angular frequency. The sound speed of air is c_{air}=343 m/s, the mass density of air is ρ_{air}=1.29 kg/m^3. The band structure can be calculated by imposing periodic boundary conditions on the lateral sides of the unit cell. According to Bloch's theorem, the wave field should adopt the following form: $p(\mathbf{r})=e^{\iota(\mathbf{k}\cdot\mathbf{r})}\, p_k(\mathbf{r})$ where $p_k(\mathbf{r})$ denotes the periodic function of the position vector, $\iota=\sqrt{-1}$, $\mathbf{k}$ is the Bloch wave vector; and $\mathbf{k}=(k_x, k_y, k_z)$ when the proposed structure possesses periodicity along the x, y, and z directions, respectively. $p(\mathbf{r}+\boldsymbol{L})=e^{\iota(\mathbf{k}\cdot\mathbf{L})}p(\mathbf{r})$, where $\boldsymbol{L}=(l_{x'}, l_{y'}, l_{z'})$ denotes the lattice translation vectors. The band structure, which illustrates the relationship between eigenfrequencies ω and Bloch wave vectors $\mathbf{k}$, can be determined by sweeping the $\mathbf{k}$ along the boundaries of the irreducible Brillouin zone.

Here, we employ FE simulations (via COMSOL Multiphysics) and experimental measurements to investigate the acoustic band structures and TL of the proposed double-tubular metamaterials. The fundamental numerical framework and the experimental data acquisition systems follow the exact procedures detailed in Section 3.4. For the specific structural designs investigated in this chapter, a 5×2×5 finite lattice was constructed. Sound-hard boundary conditions were applied to the internal structural panels. Sound-soft boundary conditions were assigned to all exterior boundaries excluding the designated incident and transmitted planes. An incident plane wave with a pressure amplitude of p_0=1 Pa was applied along either the x or z direction. As further illustrated in Fig. 4-14, this supplementary figure provides additional details of the experimental setup and shows that, for measurements along different directions, the spatial orientation of the specimen was adjusted accordingly to align the tested direction with the incident sound field. The resulting TL spectra were then compared with the calculated band structures to validate the attenuation characteristics of the proposed metamaterials.The resulting TL spectra were then compared with the calculated band structures to validate the attenuation characteristics of the proposed metamaterials.

In the experimental evaluation, the fabricated metamaterial specimens were positioned 240 mm equidistant from both the speaker arrays and the microphone to evaluate the plane wave propagation across the 0.1-25 kHz frequency range. Our

primary focus lies on the band structures along the Γ–X and Γ–Z directions. The full band structures are provided in Appendix B.

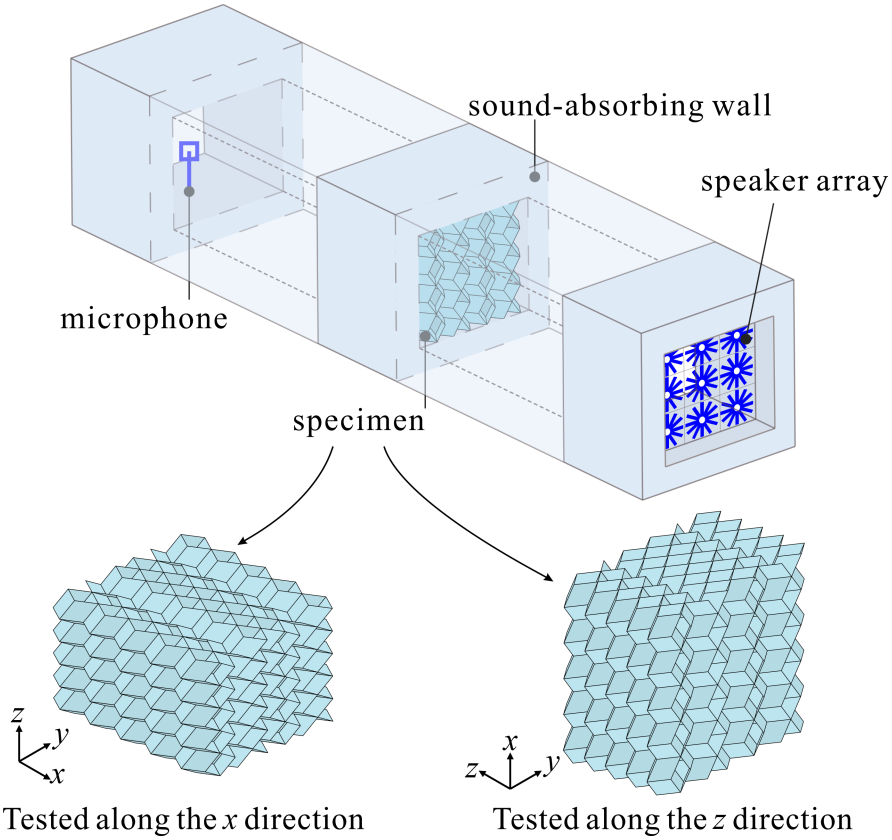

Fig. 4-14 Details of the experimental setup for acoustic TL measurements along different directions.

For MC1 at φ_{1i}=119.16° (l_x=l_z) with kite-shaped cross-sections in both x and z directions, four bandgaps are observed at 7.26-7.76 kHz, 12.82-13.27 kHz, 16.84-17.43 kHz, and 20.44-20.69 kHz, respectively (Fig. 4-15(a), grey shaded regions). In contrast, MC2 at φ_{1i}=119.16° (l_x≠l_z) with kite shape in x and rhombus in z generates partial (direction-dependent) bandgaps spanning 14.94-16.09 kHz in x direction and 8.83-9.91 kHz in z direction (Fig. 4-15(b)). For MC3, the simulation and experimental analysis at φ_1 =φ_2 =109.47° reveals two bandgaps spanning 9.56-12.47 kHz and 16.93-18.49 kHz (Fig. 4-15(c)) with identical TLs in both x and z directions.

It should be noted that discrepancies remain between the simulated and experimental TL spectra in Fig. 4-15(c). In the passband regions, the experimentally measured TL is generally higher than the simulated prediction, primarily because the ideal pressure-acoustics model neglects additional dissipation mechanisms present in the experiment, particularly thermoviscous losses within the narrow air channels. In the bandgap regions, however, the experimental TL can be either higher or lower than the

simulated result at different frequencies. This behavior is likely caused by the combined influence of thermoviscous dissipation, non-ideal experimental boundary conditions, slight fabrication induced geometric deviations from the nominal symmetric configuration, as well as minor imperfections in specimen. Because the bandgaps of MC3 are highly sensitive to geometric symmetry and folding state, these factors can induce slight shifts of the bandgap boundaries and local variations in attenuation level, while the overall agreement in bandgap position and trend is still maintained.

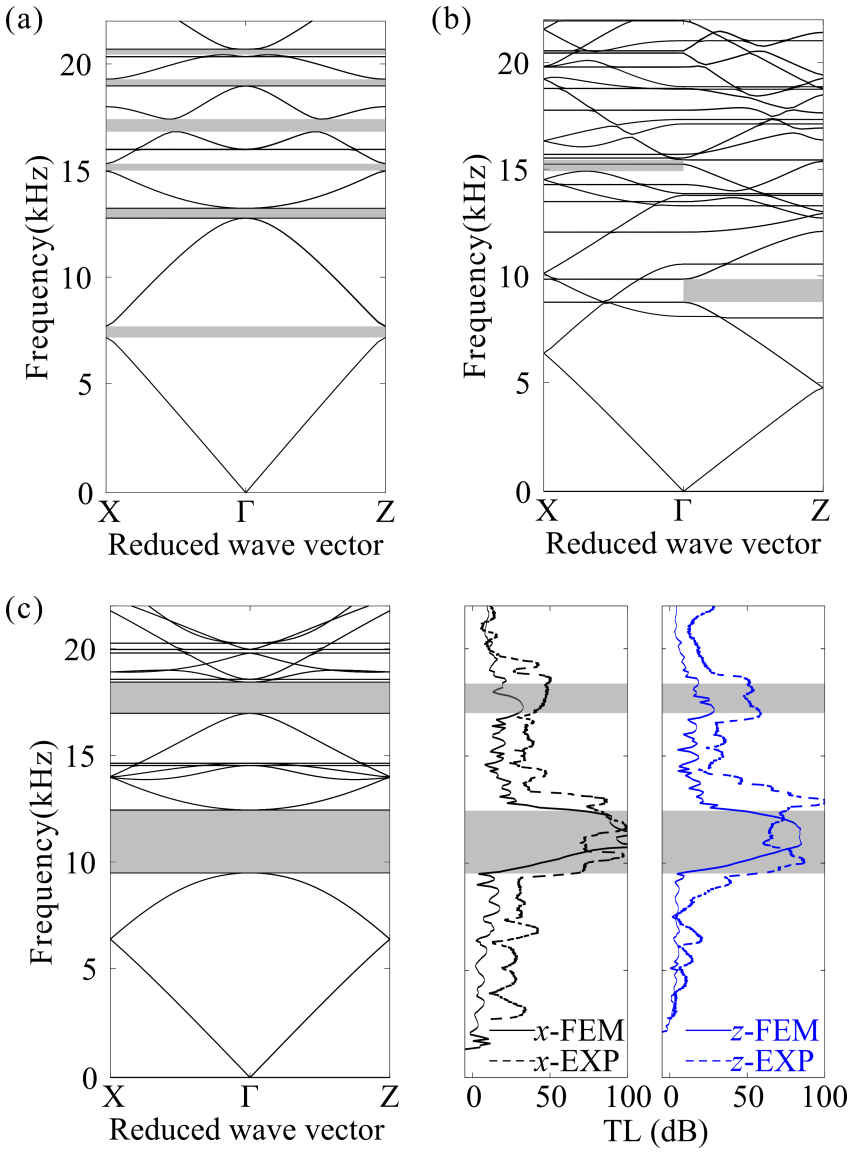

Fig. 4-15 Band structures of (a) MC1 (a_1=b_2=15 mm, a_2=b_1=21.93 mm, α_1=α_3=70°, α_2=76.47°, α_4=60°, φ_{1i}=119.16°), (b) MC2 (a_1=a_2=b_2=15 mm, b_1=21.93 mm, α_1=α_2=70°, α_3=α_4=60°, φ_{1i}=119.16°); (c) band structures and TLs of MC3 (a_1=a_2=b_1=b_2=15 mm, α (α_1=α_2=α_3=α_4)=60°, φ_{1i}=109.47°).

The observed bandgaps are mainly attributed to Bragg-type scattering induced by the periodic arrangement of the unit cells. Notably, geometric symmetry is favorable for the formation of bandgaps, because it tends to produce similar wave propagation characteristics along orthogonal directions. Specifically, the periodic tessellation of MC1 and MC3 produces symmetric structural characteristics along the *x* and *z* directions, which in turn leads to similar wave-propagation behaviors in the two orthogonal directions and facilitates the opening of bandgaps. By contrast, the geometric asymmetry of MC2 gives rise to distinct wave-propagation characteristics along the orthogonal directions, resulting in partial, direction-dependent bandgaps.

To further investigate the acoustic programmability of the proposed metamaterials, finite element simulations were performed for MC3 over a parameter space defined by the sector angle $\alpha \in [40°, 70°]$ and initial folding angle $\varphi_{1i} \in [20°, 160°]$. As shown in Fig. 4-16(a), the first bandgap persists between the 12th and 13th bands throughout the investigated parameter range, and its maximum width is achieved at the $\varphi_1=\varphi_2$ state (denoted by solid dots in Fig. 4-16(a). At this state, the geometric dimensions in the *x* and *z* directions are identical, and the structural symmetry is maximized, which is beneficial to the formation of the widest bandgap.

The bandgap decreases progressively as the initial folding angle deviates from the $\varphi_1=\varphi_2$ state due to increasing dimensional disparities between orthogonal directions. By adjusting both design parameters and folding states, the frequency range of the bandgap can be programmed to vary over 23.7 times. For asymmetric configurations with $\varphi_1 \neq \varphi_2$, direction-dependent TL characteristics arise from different wave propagation in orthogonally oriented directions with distinct geometries, as demonstrated in Fig. 4-16(b) with $\alpha=70°$ and $\varphi_{1i}=130°$.

4.5 Independent Programmability and Tunability of Dual Properties

4.5.1 Independent Programmability

Through investigating the programmability of both mechanical and acoustic properties, we discover that a given mechanical or acoustic characteristic can be associated with multiple configurations, revealing a one-to-many relationship between metamaterial properties and design parameters. This finding enables the independent programming of mechanical and acoustic properties, i.e., one property can be widely varied while the other remains unchanged.

To modulate the bandgap characteristics while preserving the mechanical properties, we can select the design parameters along the contour lines in Fig. 4-12. As shown in Fig. 4-17(a), the selected configurations (solid dots) possess identical stiffness of 30 kN/mm in the *z* direction, while exhibiting programmable bandgap widths through parameter variation (Fig. 4-17(b)). This independent programmability enables a 10.4-time variation in the frequency range of the bandgap under constant stiffness, exemplified by two parameter sets (α=40°, φ_{1i}=106.11° vs. α=70°, φ_{1i}=115.49°) showing distinct bandgap ranges (Fig. 4-18).

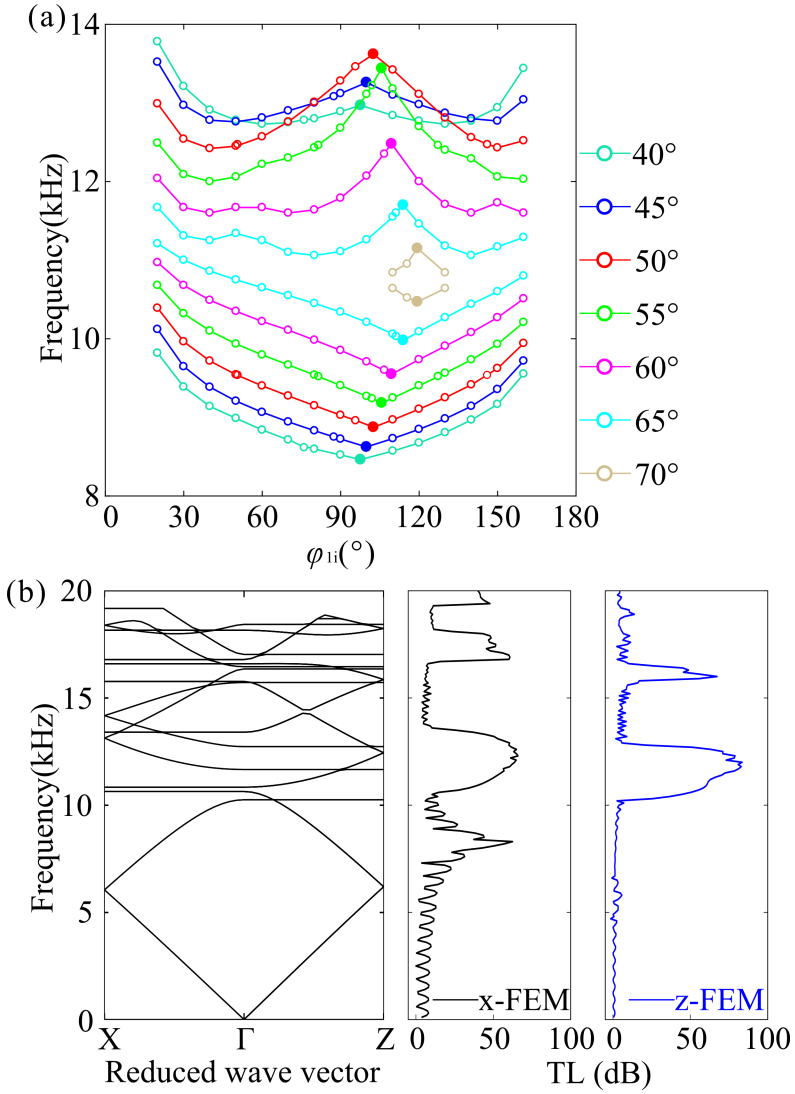

Fig. 4-16 (a) Parametric analysis of the first bandgaps of MC3 with different design angle α and initial folding angle φ_{1i}; (b) Band structures of MC3 with a_1=a_2=b_1=b_2=15 mm, α=70°, and φ_{1i}=130°, along with TLs in the *x* and *z* directions.

Similarly, the mechanical properties can also be independently programmed without altering the bandgap frequencies. The bandgap's nonlinear dependence on design parameters (Fig. 4-16(a)) enables distinct configurations with identical bandgaps but varying mechanical responses. More interestingly, by utilizing the unique geometric transposition of unit cell C3, we can even achieve transposed mechanical properties under the constraint of invariable bandgap frequencies. This is exemplified by configurations $1^{\#}$-$5^{\#}$ in which $1^{\#}$&$5^{\#}$, $2^{\#}$&$4^{\#}$ respectively form transposed pairs while $3^{\#}$ serves as a symmetric case (Fig. 4-19(a)).

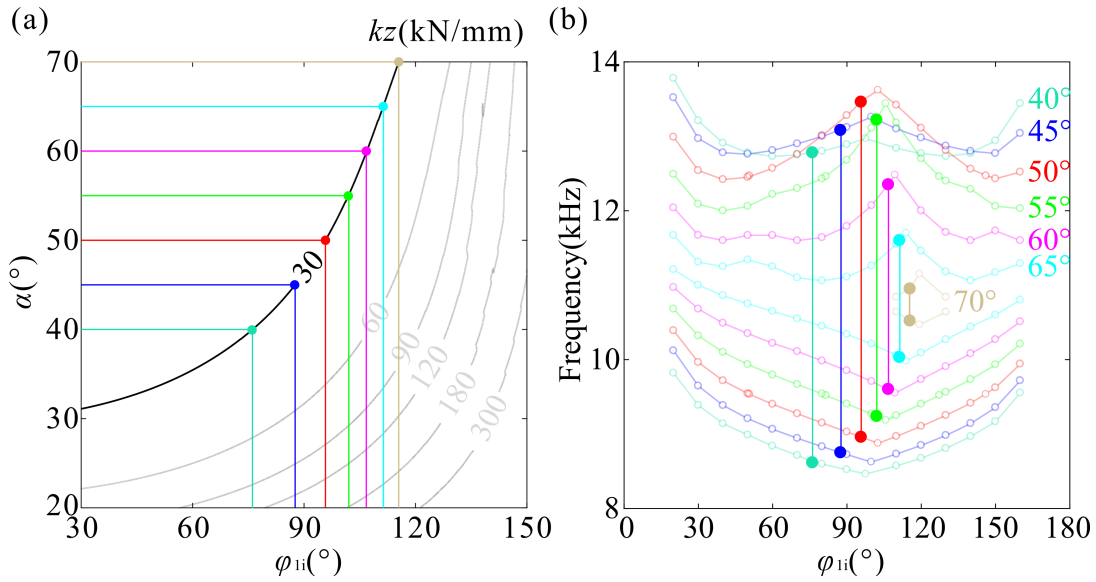

Fig. 4-17 (a) Selected configurations exhibiting identical stiffness in the *z* direction and (b) distinct bandgap characteristics.

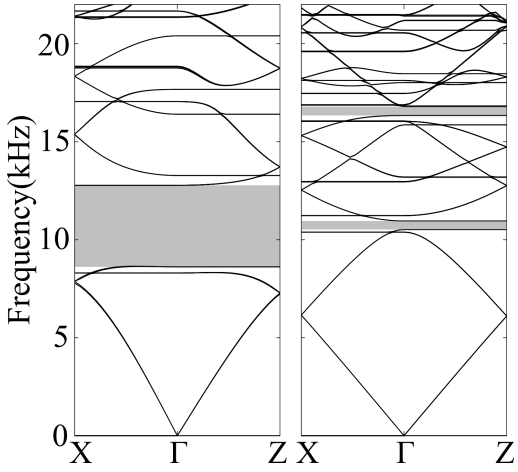

Fig. 4-18 Comparative bandgap ranges between parameter sets: α=40°, φ_{1i}=76.11° (left) and α=70°, φ_{1i}=115.49° (right).

These configurations share identical bandgap frequencies as shown in Fig. 4-19(b), but their stress versus strain curves, stiffness and SEA not only exhibit broad ranges of programmability but also transposed features between the pairs, i.e., $k_{x1}=k_{z5}$, $SEA_{x1}=SEA_{z5}$, $k_{x2}=k_{z4}$, and $SEA_{x2}=SEA_{z4}$ as shown in Fig. 4-19(c)-(d) (detailed derivation in Appendix C). A special case is configuration 3# which has identical stiffness and SEA in the two orthogonal directions. These configurations achieve stiffness variations of 16.9 times and SEA variations of 5.4 times without altering the bandgap.

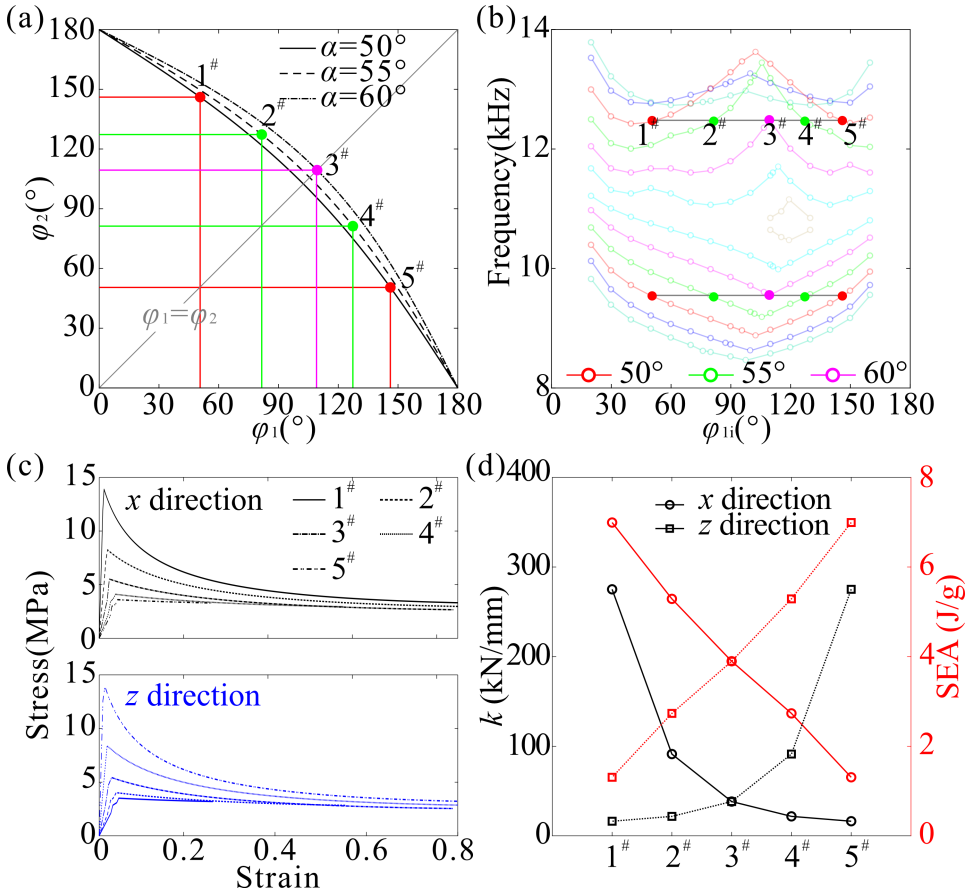

Fig. 4-19 (a) Configurations 1#-5# with transposition pairs 1# & 5# (α=50°, φ_{1i}=50.67° and φ_{1i}=146.15°), 2# & 4# (α=55°, φ_{1i}=81.59° and φ_{1i}=127.33°) and symmetric configuration 3# (α=60°, $\varphi_1=\varphi_2$=109.47°) demonstrate (b) identical bandgap frequencies; (c-d) direction-dependent mechanical performance showing transposed stress versus strain curves, stiffness and SEA between paired configurations (1# & 5#, 2# & 4#) along orthogonal axes (x and z directions), with configuration 3# maintaining identical properties.

In existing studies, a 1.79-time variation in SEA together with a 6-fold variation in the sound-absorption frequency range has been achieved [145], while a 10-time variation in strength together with an 8-fold variation in the sound-absorption frequency range has also been reported [143]. The proposed design achieves a 5.4-time variation in SEA, a 10.4-fold variation in the bandgap frequency range, and an 11.77-fold variation in strength (calculated according to the methodology in Ref. [143]), highlighting its superior capacity for independently programming multiple properties while preserving structural integration. To summarize, these results establish a strategy for independent programmability of multiple properties by utilizing the inherent non-unique mapping between design parameters and physical properties. And the methodology extends beyond the demonstrated cases to enable control of individual properties while preserving complementary functionalities.

4.5.2 Geometric Reconfiguration and Properties Tunability

A key characteristic of advanced origami-inspired metamaterials lies in their ability to achieve post-fabrication geometric reconfiguration. Unlike traditional mechanical metamaterials that are structurally static and possess fixed properties once manufactured, reconfigurable origami structures can transition among various folding states. This morphological flexibility enables the on-demand, geometry-dependent tunability of their physical properties. To demonstrate this feature, we design an MC3 metamaterial with a sector angle of α=65°. To facilitate the physical reconfiguration process, prototypes with a uniform panel thickness of 1.2 mm were fabricated via 3D printing using thermoplastic polyurethane (TPU). TPU was specifically selected owing to its high deformability, low glass transition temperature, and exceptional thermomechanical responsiveness. These characteristics allow the structure to undergo significant plastic deformation at elevated temperatures and subsequently lock into new target geometries upon cooling, successfully demonstrating post-fabrication tunability.

The material properties obtained from the uniaxial tensile test are as follows: elastic modulus E=52.82 MPa, Poisson's ratio ν=0.3, yield stress σ_y=8.32 MPa, ultimate stress σ_u=11.25 MPa, ultimate strain ε_u=50.03%. The density of the material is ρ=1.10 g/cm^3. The compression experiments employed an Instron 5982 universal testing

machine (100 kN load cell, ±1% accuracy) (Fig. 4-20) under identical speed (5 mm/min) with 1.5% height reduction.

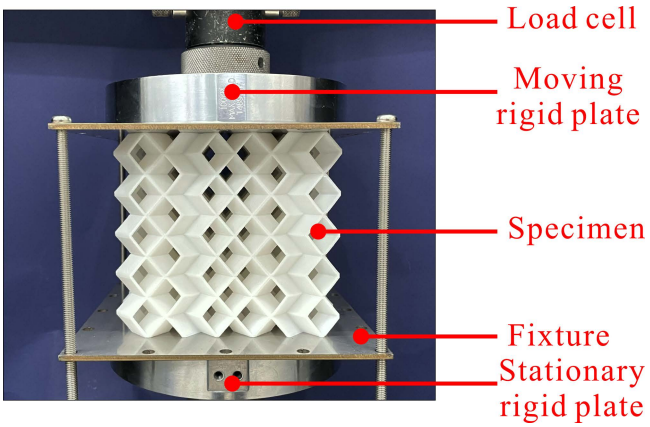

Fig. 4-20 Quasi-static compression setup using the Instron 5982.

The reconfiguration process of the specimen presented in Fig. 4-21 involves the following steps: First, a custom-designed fixture assembly comprising paired 3 mm-thick 316L stainless steel components (shown in Fig. 4-19) was mounted to the sample. Subsequently, controlled compressive forces were applied to plastically deform the specimen into the predetermined target geometry, followed by mechanical locking of the fixture position using threaded fasteners. The constrained system was then transferred to a constant temperature oven (Yamato, DKN612C) for isothermal heating at 130°C ± 2°C for 30 minutes. Following heat treatment, the assembly underwent passive cooling to room temperature (25°C) over 90 minutes before careful disassembly of the fixture components.

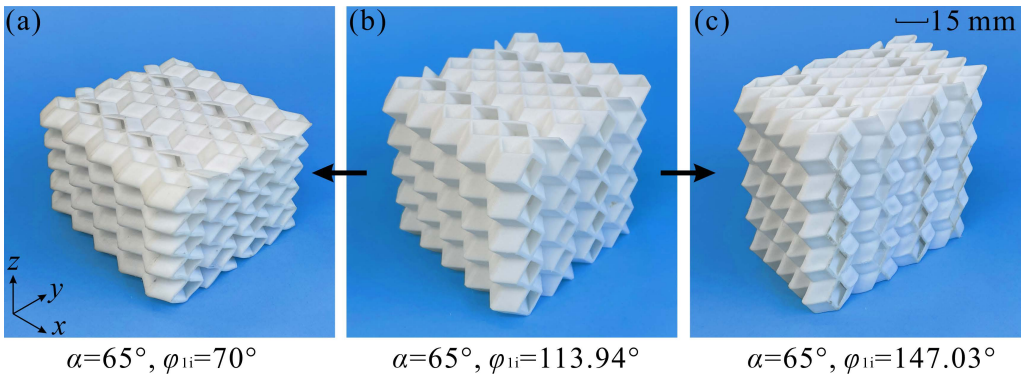

Fig. 4-21 Geometric reconfiguration of the double-tubular origami metamaterial made by TPU. MC3 with α=65° at (a) φ_{1i}=70°, (b) φ_{1i} =113.94°, and (c) φ_{1i} =147.03°, respectively.

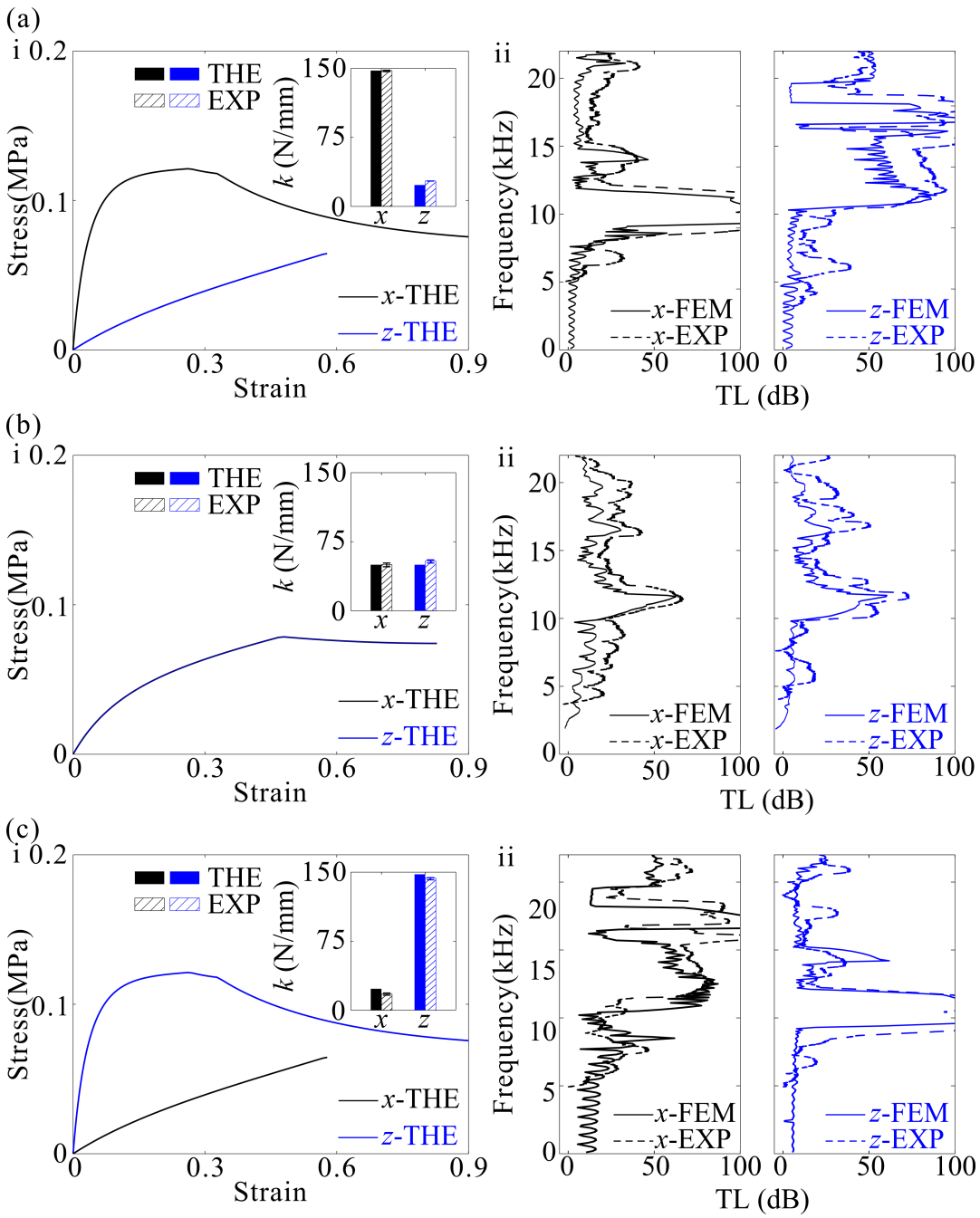

Fig. 4-22 Properties tunability of the double-tubular origami metamaterial. (a) i. Stress versus strain curves and stiffness and ii. TLs in the *x* and *z* directions of MC3 at φ_{1i}=70°, demonstrating direction-dependent properties along the orthogonal directions; (b) identical (i) mechanical responses and (ii) TLs in both directions at φ_{1i}=113.94°; (c) transposed properties at φ_{1i}=147.03° along the two directions compared to Fig. 4-21(a).

Initially, when the structure is set to the symmetric configuration with a dihedral angle of φ_{1i}=113.94°, the metamaterial exhibits nearly identical stress versus strain

curves and stiffness along both *x* and *z* directions (Fig. 4-22(b)-i), and the transmission loss peaks in both directions occur in the frequency ranges of 9.98–11.7 kHz and 16.4–17.6 kHz (Fig. 4-22(b)-ii). Reconfiguring the metamaterial from its symmetric state to a general configuration characterized by φ_{1i}=70° introduces pronounced directional difference in both mechanical and acoustic behaviors. Specifically, the *x* direction shows substantial enhancement in stress and stiffness relative to the *z* direction (Fig. 4-22(a)-i). And different transmission loss profiles emerge: the *x* direction demonstrates transmission loss peaks at 9.3–12.1 kHz, 14.1–15.2 kHz, and 21–22 kHz, while the *z* direction shows distinct frequencies at 10.5–15.7 kHz, 16.5–18.1 kHz, and 19.6–22 kHz (Fig. 4-22(a)-ii). When reconfigured to the transposed configuration with φ_{1i}=147.03° corresponding to that with φ_{1i}=70°, a swap of mechanical and acoustic properties occurs along both directions, see Fig. 4-22(c). Therefore, by reconfiguring the metamaterials post-fabrication, we can realize simultaneous tunability of the mechanical and acoustic properties.

4.6 Conclusions and Discussion

To conclude, a novel class of double-tubular origami metamaterials with independently programmable and tunable mechanical and acoustic properties is proposed. Based on rigid-origami principles, three representative designs, namely C1, C2, and C3, are developed, each exhibiting distinct folding characteristics. Specifically, C1 is not flat-foldable in either orthogonal direction, C2 is flat-foldable in only one direction, and C3 is uniquely flat-foldable in both orthogonal directions. Among them, C3 exhibits a remarkable geometric transposition feature, which enables dimensional and functional transposition between the *x* and *z* axes. Owing to this characteristic, the structure can either display transposed mechanical and acoustic properties or maintain identical responses in the two directions at specific folding states.

Through analytical modeling, numerical simulation, and experimental validation, it is demonstrated that the mechanical properties, including stiffness and SEA, as well as the acoustic characteristics, including bandgaps and TL, can be independently programmed. By systematically varying the geometric parameters and initial folding states, the independent programmability of these two categories of properties is successfully achieved. For example, the frequency range of the acoustic bandgap can be tuned by up to 10.4 times while keeping the mechanical stiffness nearly unchanged.

Conversely, the stiffness and SEA can be varied by up to 16.9 times and 5.4 times, respectively, while preserving the bandgap interval. These results confirm that the proposed design framework provides an effective route for decoupling and coordinating mechanical and acoustic functionalities within a single origami metamaterial system.

Furthermore, 3D-printed prototypes fabricated from TPU showcase dynamic, post-fabrication tunability through thermomechanical reconfiguration. This material responsiveness enables the metamaterial to physically reconfigure between symmetric and transposed states, allowing for on-site, directional swapping of its mechanical and acoustic profiles. These advancements firmly position the proposed metamaterials as highly promising candidates for complex, multifunctional engineering systems that require simultaneous energy absorption, noise attenuation, and adaptive performance.

Despite these advances, the present design framework still has certain limitations. First, the tuning of one property while maintaining another nearly unchanged is currently achieved only within specific feasible regions of the parameter space, rather than over the entire design domain. This indicates that the multifunctional design space is still subject to certain constraints. Future work could therefore adopt multi-objective optimization and collaborative design strategies to enable a more comprehensive exploration of the parameter space and to further improve the flexibility and generality of multifunctional design. Second, the proposed metamaterials are presently constructed through the uniform periodic tessellation of identical unit cells. Future studies may further introduce geometric gradients or heterogeneous unit-cell arrangements into the tessellated architecture to achieve richer and more diversified multifunctional responses.

Chapter 5 Triple-Tubular Metamaterials with Programmable Orthotropic Mechanical Properties

5.1 Introduction

Unlike materials such as steel or rubber, which typically exhibit isotropic mechanical properties, origami metamaterials are inherently anisotropic, which grants metamaterials a more diverse and customizable range of mechanical properties. However, most origami metamaterials are designed and optimized to achieve specific targets, such as smooth force response or high energy absorption. Consequently, it remains difficult for a single origami structure to bear distinct mechanical behaviors in different directions simultaneously.

Thus, the objective of this chapter is to propose an origami metamaterial capable of exhibiting distinct mechanical behaviors in three orthotropic directions. For this purpose, based on the double-tubular origami metamaterial presented in Chapter 2 and Chapter 4, a single DOF triple-tubular origami metamaterial is designed. When compressed along the *x*, *y*, and *z* axes, this metamaterial demonstrates three fundamentally different deformation modes: a rigid deformation mode, a non-rigid deformation mode, and a mixed mode combining rigid and non-rigid deformations, respectively. These kinematic differences translate into significant anisotropy in mechanical properties, enabling the structure to meet diverse load-bearing and energy-absorption requirements within a single unit.

The outline of this chapter is as follows. Section 5.2 introduces the geometric design and tessellation method of the proposed metamaterial, accompanied by a theoretical analysis of its folding kinematics along the three orthogonal directions. Following this, Section 5.3 details the compression test results for a representative triple-tubular origami metamaterial. Section 5.4 explores the programmability of these mechanical properties through analytical models and a comprehensive parametric analysis. Finally, the main conclusions of the chapter are summarized in Section 5.5.

5.2 Geometric Design

For multi-layer origami metamaterials, the primary folding modes include rigid folding, non-rigid folding, and self-locking. Our goal is to combine these modes in different directions, thereby designing metamaterials with distinct mechanical

performance orthogonally. The origami unit is illustrated in Fig.5-1(a). By mirroring part 1 about the *xoy* plane and connecting it with part 2 along the corresponding edges, the origami unit shown in Fig. 5-1(b) is obtained. Part 1 retains the folding pattern of the double-tubular origami structure introduced in Chapter 4, whose cross-section is a parallelogram. To extend this motion pattern to the present triple-tubular configuration while preserving kinematic compatibility, part 2 is introduced between the two mirrored part 1 substructures, as shown in Fig. 5-1(c). Although part 2 is composed of rectangular panels, its crease arrangement forms a parallelogram mechanism rather than introducing an additional independent motion. As a result, its edges remain geometrically constrained throughout the folding process, ensuring kinematic compatibility and coordinated deformation of the connected substructures. Therefore, the entire origami unit exhibits a single-DOF.

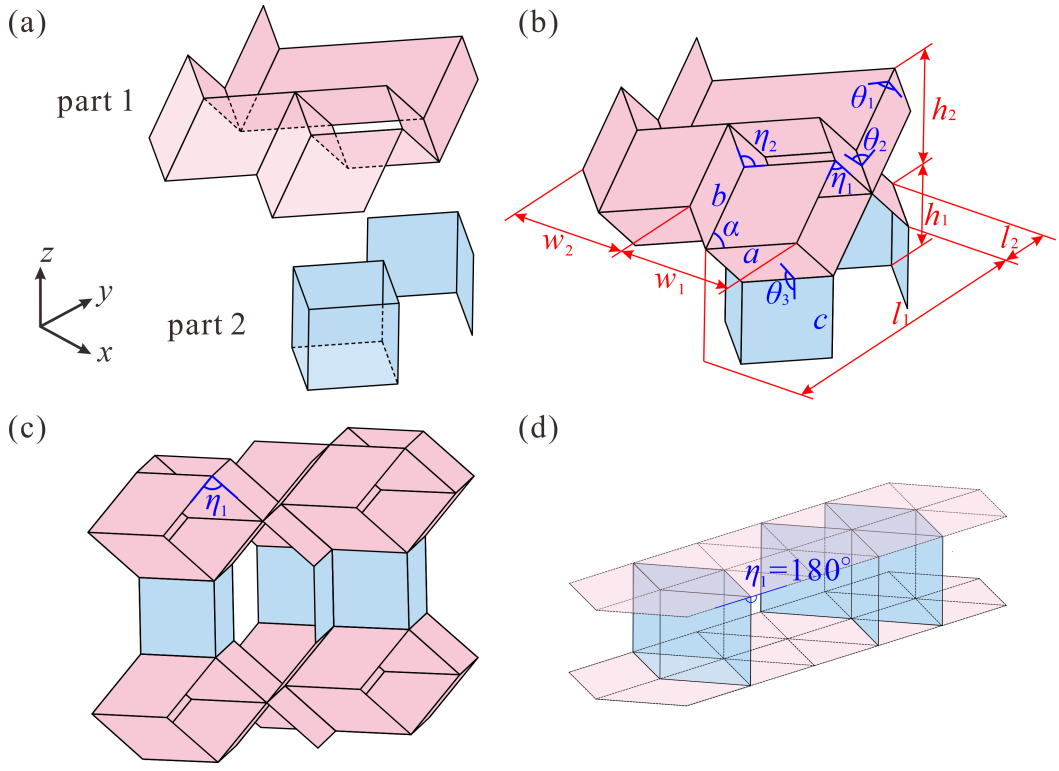

Fig. 5-1 (a) and (b) Geometric design of the origami unit; origami structure with (c) η_1=90°, and (b) η_1=180°.

The parallelogram panel is defined by the side lengths *a*, *b*, and the internal angle α, while the rectangle panel has a side length of *a* and *c*. The line angle η_1 is selected as

the parameter to characterize the folding state of the unit, and other angles, such as the panel dihedral angles θ_1, θ_2 and θ_3, and the line angle η_2, can be calculated as

$$\cos\theta_1 = \frac{\cos\eta_2 - \cos^2\alpha}{\sin^2\alpha}, \tag{5-1}$$

$$\cos\theta_2 = \frac{\cos\eta_1 + \cos^2\alpha}{\sin^2\alpha}, \tag{5-2}$$

$$\cos\theta_3 = -\frac{\cos\left[\arcsin\left(\sin\frac{\eta_1}{2}/\sin\alpha\right)\right]}{\cos\varphi\cdot\sqrt{1+\cos^2\left[\arcsin\left(\sin\frac{\eta_1}{2}/\sin\alpha\right)\right]\tan^2\alpha}}, \tag{5-3}$$

$$\cos\eta_2 = \frac{4\cos^2\alpha}{(1-\cos\eta_1)} - 1. \tag{5-4}$$

Figures 5-1(c) and 5-1(d) illustrate two representative configurations of the origami unit corresponding to η_1=90° and η_1=180°, respectively. Combined with the folding sequence shown in Fig. 5-2(a), the deformation behavior of the structure in the two opposite directions can be further understood. When the structure folds along the *x* direction, η_1 gradually decreases, and part 2 folds flat together with part 1, corresponding to the transition from configuration II to configuration I in Fig. 5-2(a). In contrast, when the structure folds along the *z* direction, η_1 gradually increases. After part 1 reaches its flattened state, part 2 is still unable to fold flat, which leads to a self-locking configuration, as shown in Fig. 5-1(d) and in the transition from configuration II to configuration III in Fig. 5-2(a).

Based on the above equations, the relationships between η_1 and other folding angles can be plotted in Fig. 5-2(b). The geometric dimensions labeled in Fig. 5-1(b) can be determined by

$$\begin{aligned} w_1 &= 2a\sin\frac{\eta_2}{2}, \\ w_2 &= 2a\sin\frac{\eta_2}{2}, \end{aligned} \tag{5-5}$$

$$\begin{aligned} l_1 &= 2\left(a\cos\frac{\eta_2}{2} + b\sin\frac{\eta_1}{2}\right), \\ l_2 &= a\cos\frac{\eta_2}{2}, \end{aligned} \tag{5-6}$$

$$\begin{aligned} h_1 &= c, \\ h_2 &= 2b\cos\frac{\eta_1}{2}. \end{aligned} \tag{5-7}$$

The origami metamaterial can be constructed by tessellating origami units in 3D space forming a triple-tubular origami metamaterial, and its folding and deployment process is presented in Fig. 5-2(a). For a $n \times n \times n$ metamaterial, the geometric dimensions of the metamaterial in the *x*, *y*, and *z* directions are denoted as *W*, *L*, and *H*, respectively, which are related with folding angle η_1

$$W = 2\left(2n-1\right)a\sin\frac{\eta_2}{2}, \tag{5-8}$$

$$L = 2n\left(a\cos\frac{\eta_2}{2} + b\sin\frac{\eta_1}{2}\right), \tag{5-9}$$

$$H = \left(n-1\right)c + 2nb\cos\frac{\eta_1}{2}, \tag{5-10}$$

as plotted in Fig. 5-2(c).

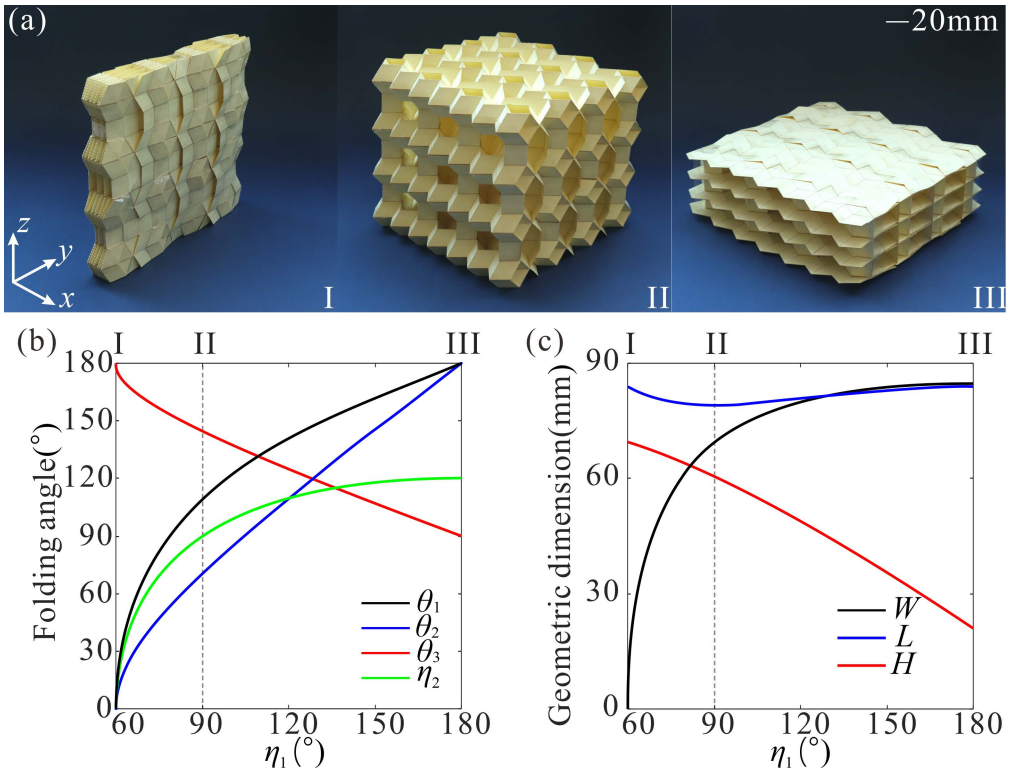

Fig. 5-2 (a) Folding and deployment of a 4×4×4 triple-tubular origami metamaterial made of 250 g/m^2 card paper; (b) and (c) variations in folding angles and geometric dimensions, in which a=b=c=7 mm and α=60°.

Figure 5-2(c) shows that the geometric scale in the *y* direction undergoes minimal changes, preventing the metamaterial from flattening when compressed. Self-locking occurs when η_1 reaches 180°, as shown in Fig. 5-1(d), corresponding to the

displacement in the *z* direction

$$H_L = 2nb\cos\frac{\eta_1}{2}. \tag{5-11}$$

Equations (5-1)-(5-14) demonstrate kinematic analysis. When considering a continuum structure with thickness, the ratio of panel thickness to edge length should be less than 0.1 to ensure it functions as a shell[157], so as to make the metamaterial deform in the rigid origami folding mode.

5.3 Mechanical Properties of a Typical Origami Metamaterial

In this section, a typical origami metamaterial is investigated through experiments and numerical simulations. As the geometric design parameters are parallelogram angle α, side length ratio a/b and a/c, and edge angle η_1, the metamaterials are named as α-a/b-a/c-η_1, and they are in a 4×4×4 configuration and a=7 mm in this paper. A set of experimental specimens 60-1-1-90, i.e., the metamaterial with α=60°, a/b=1, a/c=1 and η_1=90°, are fabricated with 316L stainless steel with a thickness of 0.5mm by metal 3D printing technique. Three sets of Dogbone specimens were printed, and subsequent tensile tests were conducted to obtain the material properties. The average mechanical properties are elastic modulus E=175 GPa, Poisson's ratio υ=0.3, yield stress σ_y=487.11 MPa, ultimate stress σ_u=846.07 MPa, ultimate strain ε_u=28.97%. The density of the material is ρ=7.85 g/cm^3. The quasi-static compression experiments were conducted on a SINOTEST testing machine with a load cell of 300 kN. The experimental setup is illustrated in Fig. 5-3(a), with the maximum displacement load set to 73% of the total height of the model and a loading rate of 2 mm/min. Three sets of experiments were conducted in each direction.

Meanwhile, the numerical simulations were conducted using the commercial FE software Abaqus/Explicit. The model was placed on a completely fixed rigid plate while being compressed by another moving rigid plate, as shown in Fig. 5-3(b). The DOFs of the moving rigid panel were restricted except for the compression direction. A prescribed downward displacement of 73% of the model dimension in the corresponding direction was assigned to the free DOF of the moving rigid plate to control the compression process, and the loading rate was controlled using the built-in smooth analysis step in Abaqus/Explicit. Four-node shell elements with reduced integration S4R were used to mesh the structure. General contact was employed to

model the contacts between different parts of the model and the contacts between the model and the upper and lower rigid plates. Friction was also considered in the analysis, with a friction coefficient μ set to 0.3. The material properties in simulations are the same as those given in Section 5.4.

Prior to the finite element analysis, convergence tests were conducted following the energy criteria established in Chapter 3, Section 3.3.1. To accurately maintain quasi-static conditions and effectively mitigate the hour-glassing effect, the global mesh size was set to 0.5 mm and the analysis time was specified as 0.03 s.

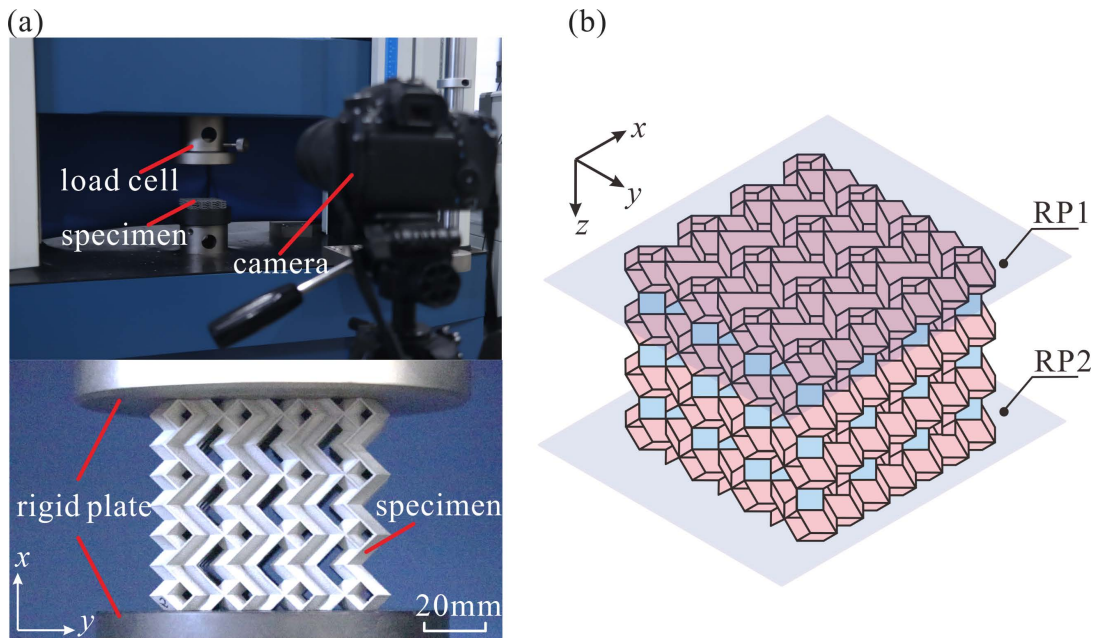

Fig. 5-3 (a) Experimental setup, zoomed-in view of the specimen and (b) compression setup of FE.

The deformed configurations at various stages of compression, the corresponding PEEQ contour maps drawn on the undeformed shapes, and the stress versus strain curves of the metamaterial in three orthogonal directions are extracted from the numerical results and compared with the experimental data in Fig. 5-4, 5-5 and 5-6 with good agreement. The SEA and compressive stiffness k_c, calculated from the experiments and numerical simulations are summarized in Figs. 5-7 and 5-8. The numerical results for SEA and k_c are all within 5.0% of the averaged experimental values, indicating that the numerical model is capable of producing reliable results. Therefore, in the subsequent discussions, the numerical results will be utilized to reveal further details.

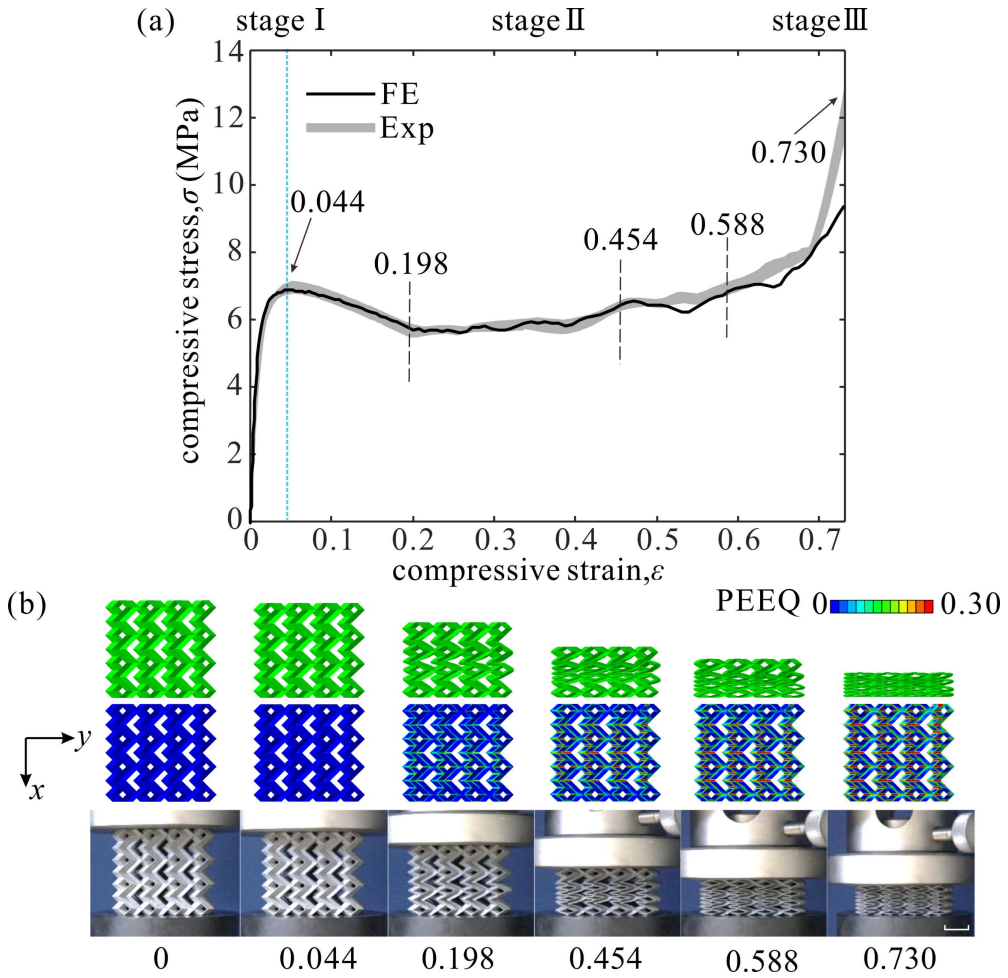

Fig. 5-4 (a) The stress versus strain curves and (b) the deformation modes, PEEQ drawn on the undeformed shapes obtained from experiments and numerical simulations of 60-1-1-90 under compression in the *x* direction.

Firstly, the compression in the *x* direction is studied, as shown in Fig. 5-4. The deformation process can be divided into three stages. In stage I, before reaching a compressive strain of 0.044, the model primarily deforms within the elastic range, resulting in a rapid increase in stress with compressive strain. Moving into stage II, which spans a compressive strain range of 0.044 to 0.730, the deformation predominantly follows the folding mode of rigid origami. The creases become bent into the plastic range, forming fixed plastic hinges, while the panels undergo minimal plastic deformation. As a result, a long plateau is observed in the stress versus strain curve. It should be noted that although the non-uniform deformation during compression may affect the smoothness of the curve to some extent, its impact on the overall deformation mode remains minimal. This non-uniform deformation is primarily influenced by

boundary conditions, resulting in initial deformation occurring in the middle two layers of the model, as can be seen in Fig. 5-4(a) near the strain of 0.198 and 0.454. Upon exceeding a compressive strain of 0.730, the model enters stage III, where all layers are flattened and compressed together, entering the densification stage. In this stage, the model solidifies and becomes resistant to further compression, resulting in a significant increase in stress.

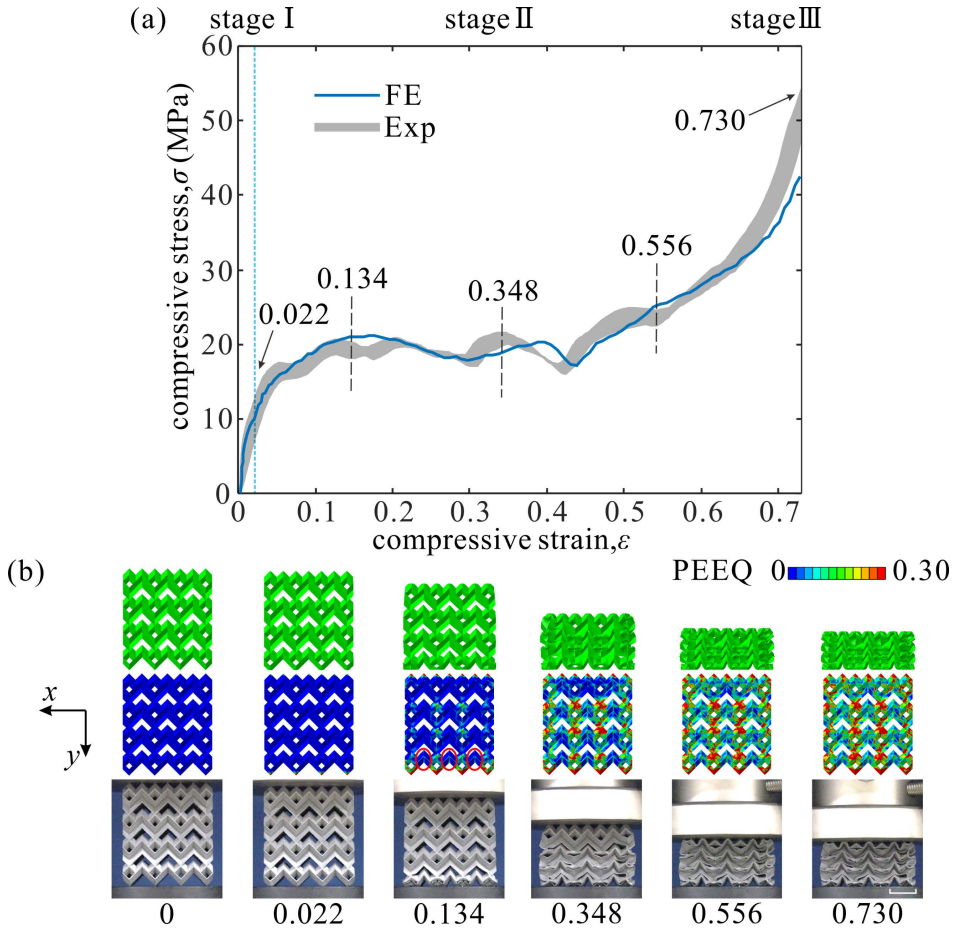

Fig. 5-5 (a) The stress versus strain curves and (b) the deformation modes, PEEQ drawn on the undeformed shapes obtained from experiments and numerical simulations of 60-1-1-90 under compression in the *y* direction.

Next, the compression of the 60-1-1-90 in the *y* direction is investigated, and the corresponding results are presented in Fig. 5-5. The compression process can be divided into three stages. In stage I within a strain of 0.022, when a small strain is applied to the model, elastic deformation occurs. As compression progresses to stage II, stress concentration leads to small buckling deformations at the tips of the model.

Subsequently, buckling of the top and bottom panels of the metamaterial takes place. Plastic hinges also form at certain creases, as indicated by the red circles in Fig. 5-5(a) near a strain of 0.134. This buckling behavior and plastic hinge formation persist as different layers of the metamaterial collide within the compressive strain range of 0.134 to 0.730. When the compressive strain exceeds 0.730, the structure enters the densification stage. In contrast to the previous case, the compression in the *y* direction is characterized by the prevalence of buckling deformation in the panels throughout the entire deformation process.

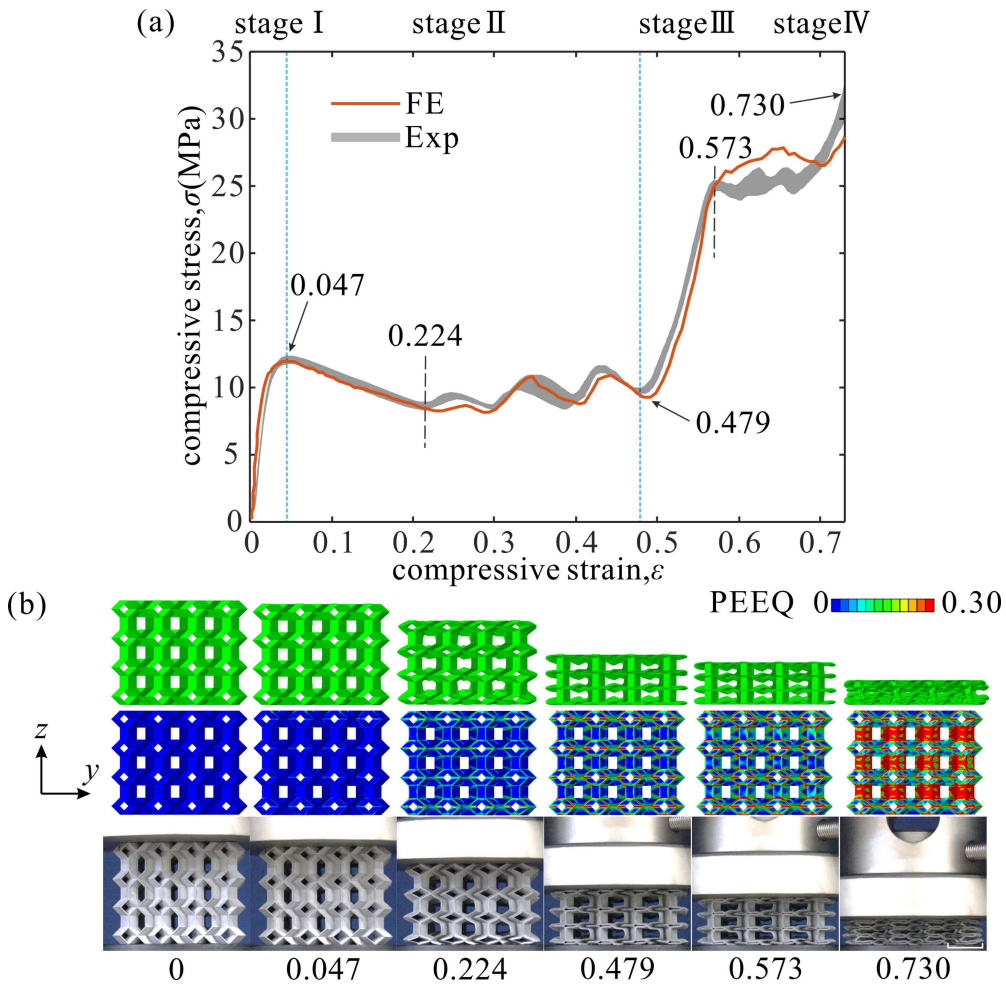

Fig. 5-6 (a) The stress versus strain curves and (b) the deformation modes, PEEQ drawn on the undeformed shapes obtained from experiments and numerical simulations of 60-1-1-90 under compression in the *z* direction.

In the *z* direction, the corresponding results are illustrated in Fig. 5-6. The deformation process can be divided into four stages. In stages I and II, similar to the

behavior observed in the *x* direction, the model undergoes elastic deformation followed by plastic deformation at the creases. However, within the compressive strain range of 0.224-0.479, the deformation becomes non-uniform, leading to variations in the smoothness of the stress versus strain curve. During this range, the model predominantly follows the rigid origami folding mode. When the compressive strain reaches 0.479, the self-locking of the model becomes evident, accompanied by the emergence of graded stiffness. Subsequently, in stage III (strain range: 0.479-0.730), the deformation primarily involves the buckling of the rectangle panels. Finally, in stage IV, when the compressive strain exceeds 0.730, the model enters the densification stage.

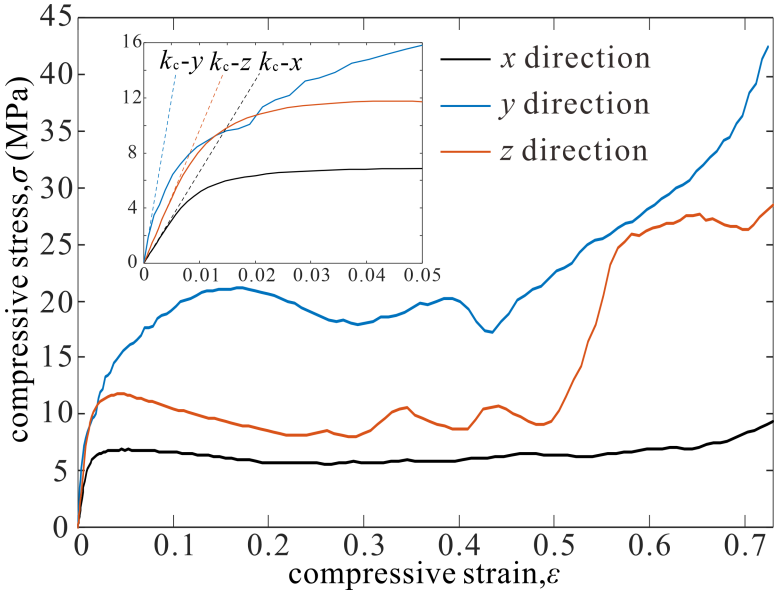

Fig. 5-7 The comparison of finite element simulation results in three directions.

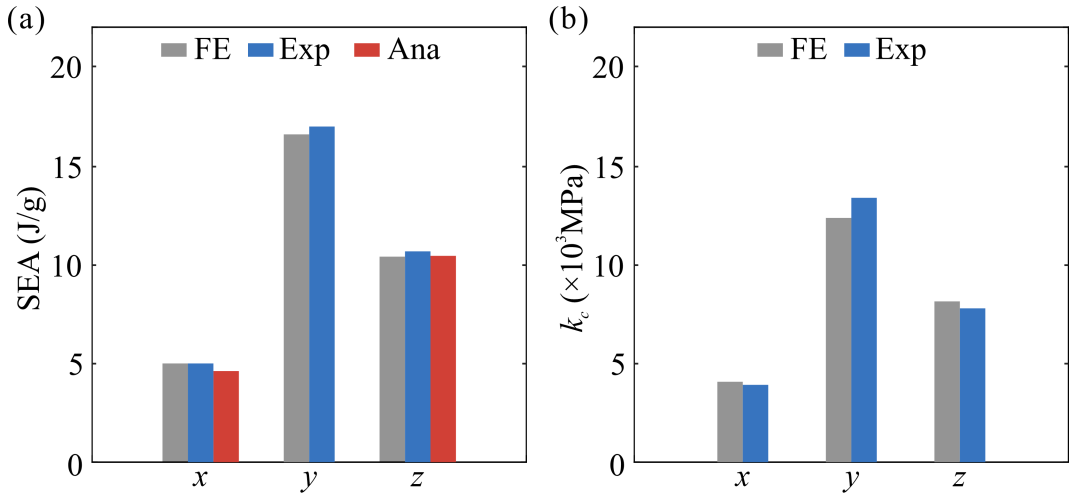

Fig. 5-8 (a) SEA and (b) stiffness comparison between the finite element simulations, experiments and theoretical analysis.

From the experimental and numerical simulation results discussed earlier, it is clear that the proposed metamaterial exhibits distinct anisotropic mechanical properties in three orthotropic directions, as shown in Fig. 5-7. When subjected to loading in the *x* direction, the deformation strictly follows the rigid origami folding mode. Plastic deformation primarily occurs at the creases, resulting in lower energy absorption and stiffness compared to the other directions. On the other hand, when the metamaterial is loaded in the *y* direction, it demonstrates significantly higher stiffness and SEA, with values three times greater than those observed in the *x* direction, as presented in Figs. 5-8(a) and (b). This substantial increase can be attributed to the buckling deformation in the *y* direction. In the *z* direction, the behavior of the metamaterial is characterized by a combination of initial rigid origami folding, followed by a transition to a panel buckling mode. Consequently, a graded response is observed, with intermediate levels of stiffness and SEA compared to the *x* and *y* directions. Overall, these findings highlight the anisotropic characteristic of the metamaterial, with its mechanical properties varying significantly depending on the loading directions.

5.4 Programmability of Mechanical Properties

5.4.1 Analytical Models

In this section, the analytical models are derived for the mechanical property in the *x* and *z* directions due to the character of rigid origami folding[96]. When ductile metal stainless steel is used to create origami structures, significant localized plastic deformations occur along the creases during continuous compressing. These deformations can be modeled as plastic hinges. Here, we assume that the base material is perfectly plastic, and energy dissipation solely occurs through these large plastic deformations, with elasticity being neglected[95]. The geometric design parameters are parallelogram angle α, side length ratio a/b and a/c, and edge angle η_1.

Because the metamaterial dimension in the *y* direction (L) has very limited variation (Fig. 5-2(c)), compressing in this direction will cause panel buckling without a specific mechanism such as rigid origami mode, plastic hinge flow[158] or honeycomb crushing[133,159]. Consequently, it is rather difficult to predict the deformation and establish an analytical model. Hence, this study does not include theoretical analysis in

the *y* direction, but instead employs numerical simulations to explore the impact of parameters on mechanical performances.

When compressing in the *x* direction, the deformation follows the rigid origami folding mode, as can be seen in Fig. 5-2(a), from state II to state I. The energy balance equation, which considers the external work and dissipated energy within the origami metamaterial, is utilized to define the force-displacement characteristic, $F_c(x)$, resulting from the compression in the *x* direction:

$$F_c\left(x\right)dx_c = bm_{\theta_1}M_{\theta_1}d\theta_1 + am_{\theta_2}M_{\theta_2}d\theta_2 + am_{\theta_3}M_{\theta_3}d\theta_3 + cm_{\eta_2}M_{\eta_2}d\eta_2, \tag{5-12}$$

$$M_{\theta_1} = M_{\theta_2} = M_{\theta_3} = M_{\eta_2} = M_0 = \frac{\sigma_0 t^2}{4}, \tag{5-13}$$

in which $m_{\theta 1}=24n^3-10n^2-5n$, $m_{\theta 2}=32n^3-18n^2+6n$, $m_{\theta 3}=8n^3-6n^2-6n$, and $m_{\eta 2}=5n^3-6n^2-n$ represent the number of corresponding creases in the metamaterial. $x_c=W(\eta_1)-W(\eta_{1i})$ represents the displacement in the loading direction relative to the initial configuration with a folding angle η_{1i}. F_c denotes the applied compression force, M_0 represents the fully plastic bending moment per unit length, *t* corresponds to the wall thickness. To take strain hardening effects into account, flow stress σ_0 is used as[160]

$$\sigma_0 = \sqrt{\frac{\sigma_y \sigma_u}{\varsigma + 1}}, \tag{5-14}$$

where ς is the strain hardening exponent of the thin-walled material and set as 0.25. The stress versus strain curve of the material and the flow stress are presented in Fig. D1 of Appendix D, which demonstrates the relationship between σ_y, σ_u and σ_0. By considering the folding angle η_1 as the governing variable, Eq. (5-12) can be expressed as follows

$$\begin{aligned} F_c\left(x\right)\frac{\partial W}{\partial \eta_1}d\eta_1 = {} & bm_{\theta_1}M_{\theta_1}\frac{\partial \theta_1}{\partial \eta_1}d\eta_1 + am_{\theta_2}M_{\theta_2}\frac{\partial \theta_2}{\partial \eta_1}d\eta_1 + am_{\theta_3}M_{\theta_3}\frac{\partial \theta_3}{\partial \eta_1}d\eta_1 \\ & + cm_{\eta_2}M_{\eta_2}\frac{\partial \eta_2}{\partial \eta_1}d\eta_1. \end{aligned} \tag{5-15}$$

in which the compressive force is denoted by F_c.

It is assumed that the metamaterial undergoes homogeneous deformation during quasi-static compression, where all the cells deform simultaneously. In order to study the mechanical properties of the metamaterial in different directions, the stress versus strain curves, SEA, and initial compressive stiffness are calculated. The compressive stress σ and strain ε can be calculated as[27]

$$\sigma = \frac{F_c}{S_u}, \quad \varepsilon = \frac{x_c}{H_c}, \tag{5-16}$$

in which the compressive displacement is represented by x_c. H_c is used to represent the height of the structure when compressed in different directions, and S_u refers to the projected area in the compressive direction. The initial compressive stiffness k_c is also investigated in this study, which represents the bearing capacity of metamaterials in the elastic range. Understanding k_c is vital for designing structures and components that can withstand specific loads without undergoing undesirable plastic deformations[161]. The initial compressive stiffness k_c is defined as the initial tangent slope of the stress versus strain curve divided by the relative density of the metamaterial[162,163]. In Eqs. (5-17) and (5-18), ρ_v represents the relative density of the metamaterial, t is the thickness of the panels, and S_m represents the sum of the surface area of the panels.

$$S_m = 2na\left(14n^2b\sin\alpha + 3n^2c - 4nc - 10nb\sin\alpha - c - 2b\sin\alpha\right), \tag{5-17}$$

$$\rho_v = \frac{S_m \cdot t}{WLH}. \tag{5-18}$$

The maximum displacement of the metamaterial occurs at a specific value of the folding angle η_{1d}. By equating the volume occupied by the walls with the volume at $\eta_1=\eta_{1d}$, that is, relative density, $\rho_v(\eta_{1d})=1$, the maximum displacement can be determined by

$$S_m \cdot t = W\left(\eta_{1d}\right)L\left(\eta_{1d}\right)H\left(\eta_{1d}\right). \tag{5-19}$$

Thus, the SEA, defined as the energy absorption per unit mass, is

$$\mathrm{SEA}_x = \frac{\int_0^{W(\eta_{1i})-W(\eta_{1d})} F_c\left(x\right)dx}{M}, \tag{5-20}$$

where M represents the mass of metamaterial.

During compression in the z direction, the deformation process can be divided into two stages. In the first stage, the deformation follows the folding mode of rigid origami, as illustrated in Fig. 5-2(a), from state II to state III. Self-locking occurs at state III, transforming the metamaterial into a multi-layer honeycomb structure. Subsequent compression induces buckling deformation in the rectangular panels. In the first stage, the analytical model corresponds to the x direction discussed in section 5.3.1. By substituting x_c in Eq. (5-12) with z_c=H(η_1)-(n-1)c, Eq. (5-15) can be recalculated as

$$\begin{aligned} F_{c1}\left(z\right)\frac{\partial H}{\partial \eta_1}d\eta_1 = {} & bm_{\theta_1}M_{\theta_1}\frac{\partial \theta_1}{\partial \eta_1}d\eta_1 + am_{\theta_2}M_{\theta_2}\frac{\partial \theta_2}{\partial \eta_1}d\eta_1 + \\ & am_{\theta_3}M_{\theta_3}\frac{\partial \theta_3}{\partial \eta_1}d\eta_1 + cm_{\eta_2}M_{\eta_2}\frac{\partial \eta_2}{\partial \eta_1}d\eta_1. \end{aligned} \tag{5-21}$$

The compression force can be determined, and the end of this stage is at η_{1d}=180°. Consequently, the SEA during the first stage can be obtained by

$$\mathrm{SEA}_{z1}=\frac{\int_0^{H(\eta_{1i})-H(\eta_{1d})}F_{c1}(z)\,dz}{M}. \tag{5-22}$$

Figure 5-1(c) presents the initial configuration, while Fig. 5-1(d) illustrates the configuration at the completion of the first stage, wherein the parallelogram panels are fully folded. Subsequently, during the second stage deformation, the primary mode of deformation involves the buckling of the rhombic honeycomb formed by the rectangular panels. The honeycomb structure consists of three types of elements: Type I and Type II corner elements with sector angles of π-β and β, respectively, and Type III X-shaped intersection elements, whose cross-section is shown in Fig. 5-9. The mean crushing force for each type of element can be calculated as[133,159,164,165]

$$F_{\mathrm{I}}=\frac{1}{2\varepsilon_2}\sigma_0\left(\frac{a}{2}\right)^{\frac{1}{3}}t^{\frac{5}{3}}\left(\frac{2\pi\tan(\pi/2-\beta/2)}{0.163[\tan(\pi/2-\beta/2)+0.06/\tan(\pi/2-\beta/2)]}\right)^{\frac{1}{2}}, \tag{5-23}$$

$$F_{\mathrm{II}}=\frac{1}{2\varepsilon_2}\sigma_0\left(\frac{a}{2}\right)^{\frac{1}{3}}t^{\frac{5}{3}}\left(\frac{2\pi\tan(\alpha/2)}{0.163[\tan(\beta/2)+0.06/\tan(\beta/2)]}\right)^{\frac{1}{2}}, \tag{5-24}$$

$$F_{\mathrm{III}}=\frac{2}{\varepsilon_2}\sigma_0\left(\frac{a}{2}\right)^{\frac{1}{2}}t^{\frac{3}{2}}\left(\pi\tan(\beta/2)+4\pi\sec(\beta/2)\left(\frac{2t}{a}\right)^{\frac{1}{2}}\right)^{\frac{1}{2}} \quad \text{for } \beta\in(0,\pi/2],$$

$$F_{\mathrm{III}}=\frac{2}{\varepsilon_2}\sigma_0\left(\frac{a}{2}\right)^{\frac{1}{2}}t^{\frac{3}{2}}\left(\pi\tan(\pi/2-\beta/2)+4\pi\sec(\pi/2-\beta/2)\left(\frac{2t}{a}\right)^{\frac{1}{2}}\right)^{\frac{1}{2}} \quad \text{for } \beta\in[\pi/2,\pi), \tag{5-25}$$

where ε_2 represents the densification strain of the second stage deformation with a value of 0.73 in this study. For a multi-layer origami metamaterial, the upper and lower layers of the metamaterial contact with the rigid loading plate during compression process. The presence of friction results in different boundary conditions for the upper/lower layers and the middle layers. Hence, non-uniform deformation might cause the honeycombs between different layers to deform asynchronously. As a result, the mean crushing force of n-layer honeycombs is less than n times the force of a single-layer honeycomb. To account for this, a coefficient λ is introduced, which is set to 0.4 for the 4×4×4 metamaterial in this study, based on subsequent finite element simulations. The

mean crushing force of the $n\times n\times n$ origami metamaterial during the second stage when compressed in the z direction is given by

$$F_{c2}(z)=\lambda(n-1)\left(\left(n^2+n\right)F_{\mathrm{I}}+2n^2F_{\mathrm{II}}+\left(n^2-n\right)F_{\mathrm{III}}\right). \tag{5-26}$$

The SEA during the second stage can be calculated as

$$\mathrm{SEA}_{z2}=\frac{\int_0^{\varepsilon_{2C}}F_{c2}(z)\,dz}{M}. \tag{5-27}$$

The SEA when compressing in the z direction is the sum of SEA_{z1} and SEA_{z2}.

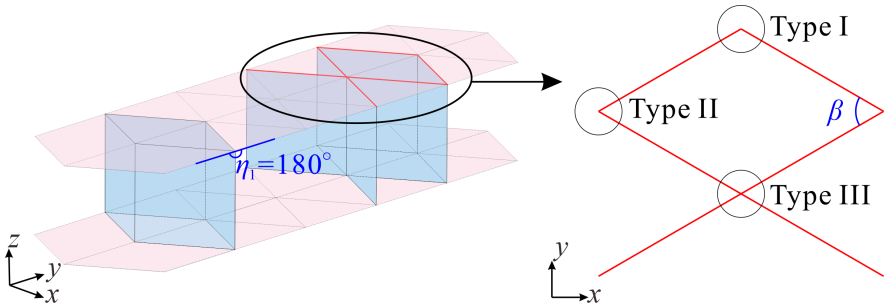

Fig. 5-9 Two types of corner element (I and II) and the X-shaped intersection element (III).

5.4.2 Parametric Analysis

Having investigated the anisotropic mechanical properties of a typical origami metamaterial, the influence of three design parameters (α, a/b, and a/c) and one folding parameter (η_1) are further studied in this section to fulfill the task of programmability. To facilitate comparison, all metamaterials feature an equal number of 4×4×4 units, while the relative density ρ_v is maintained at 11.44% through adjustments to the thickness of different models. The geometries of all the structures are listed in Tables 5-1 to 5-4. Figure 5-10 presents the stress versus strain curves in the x direction for the numerical models listed in Tables 5-5 to 5-8.

Analysis of Fig. 5-10(a) demonstrates a positive correlation between the stress amplitude and changes in the design angle α. When the structure is compressed in the x direction, the folding angle η_2 transitions from η_{2i} to 0, where η_{2i} represents the folding angle corresponding to η_1=90°. As indicated by Eq. (5-4), there exists a positive relationship between α and η_{2i}. Additionally, Eq. (5-8) reveals that the compressive displacement in the x direction (W) increases with η_{2i}. It requires greater stress to compress a model with a higher folding extent in the x direction. Consequently, there is a gradual increase in stress as the design angle increases.

Table 5-1 Geometric parameters of different origami metamaterials when varying α.

Model	α (°)	a (mm)	a/b	a/c	η_1 (°)	t (mm)	ρ_v (%)	M (g)
50-1-1-90	50	7.0	1	1	90	0.372	11.44	201
55-1-1-90	55	7.0	1	1	90	0.465	11.44	265
60-1-1-90	60	7.0	1	1	90	0.500	11.44	299
65-1-1-90	65	7.0	1	1	90	0.504	11.44	312
70-1-1-90	70	7.0	1	1	90	0.487	11.44	311

Table 5-2 Geometric parameters of different origami metamaterials when varying a/b.

Model	α (°)	a (mm)	a/b	a/c	η_1 (°)	t (mm)	ρ_v (%)	M (g)
60-0.6-1-90	60	7.0	0.6	1	90	0.616	11.44	571
60-0.7-1-90	60	7.0	0.7	1	90	0.573	11.44	464
60-0.8-1-90	60	7.0	0.8	1	90	0.542	11.44	391
60-0.9-1-90	60	7.0	0.9	1	90	0.518	11.44	338
60-1-1-90	60	7.0	1.0	1	90	0.500	11.44	299
60-1.1-1-90	60	7.0	1.1	1	90	0.485	11.44	268
60-1.2-1-90	60	7.0	1.2	1	90	0.474	11.44	244

Table 5-3 Geometric parameters of different origami metamaterials when varying a/c.

Model	α (°)	a (mm)	a/b	a/c	η_1 (°)	t (mm)	ρ_v (%)	M (g)
60-1-0.78-90	60	7.0	1	0.78	90	0.524	11.44	328
60-1-0.875-90	60	7.0	1	0.875	90	0.512	11.44	313
60-1-1-90	60	7.0	1	1	90	0.500	11.44	299
60-1-1.17-90	60	7.0	1	1.17	90	0.487	11.44	284
60-1-1.4-90	60	7.0	1	1.4	90	0.474	11.44	269

Table 5-4 Geometric parameters of different origami metamaterials when varying η_1.

Model	α (°)	a (mm)	a/b	a/c	η_1 (°)	t (mm)	ρ_v (%)	M (g)
60-1-1-70	60	7.0	1	1	70	0.391	11.44	234
60-1-1-80	60	7.0	1	1	80	0.471	11.44	281
60-1-1-90	60	7.0	1	1	90	0.500	11.44	299
60-1-1-100	60	7.0	1	1	100	0.505	11.44	302
60-1-1-110	60	7.0	1	1	110	0.496	11.44	296
60-1-1-120	60	7.0	1	1	120	0.476	11.44	284

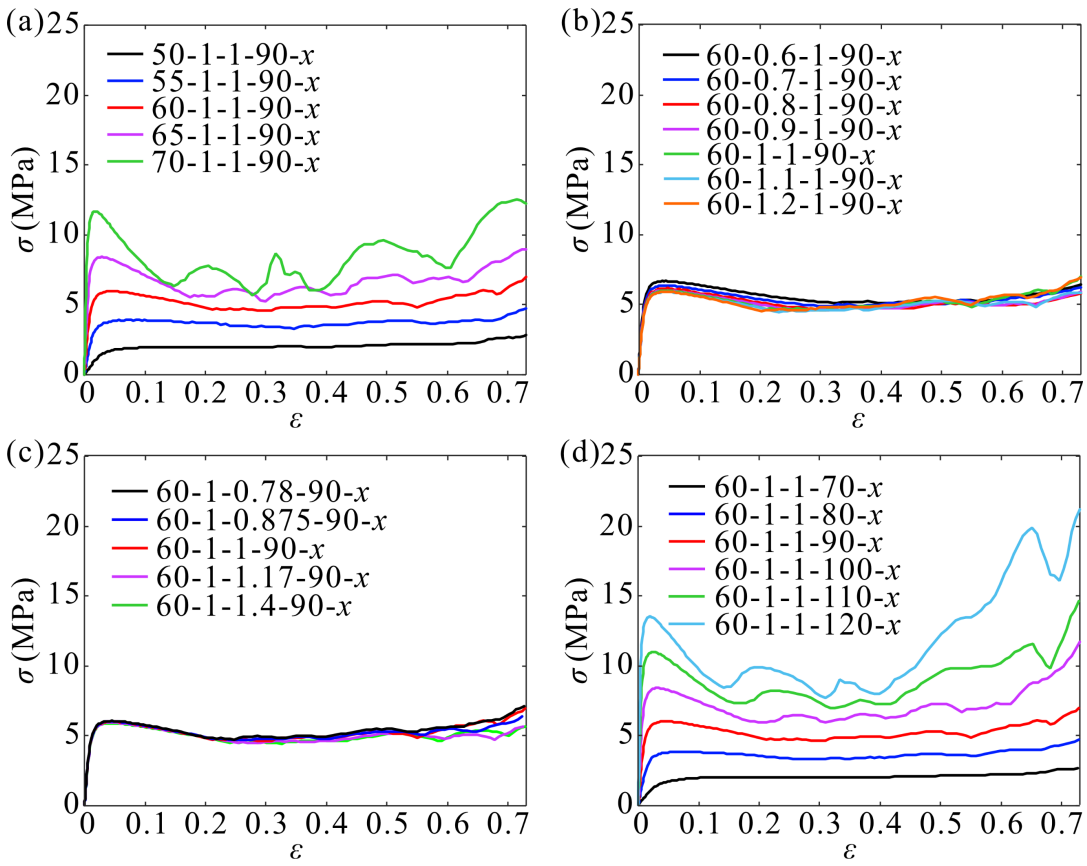

Fig. 5-10 The stress versus strain curves in the *x* direction when varying: (a) α, (b) *a*/*b*, (c) *a*/*c*, and (d) η_1 for different design parameters.

Notably, significant fluctuations in the stress curve occur at α values of 65° and 70°, attributed to non-uniform deformation during the compression process, as shown in Fig. 5-11. Figures 5-10(b) and (c) indicate that variations in the parameters *a*/*b* and *a*/*c* have minimal impact on the stress versus strain curve. Firstly, deformation in the *x* direction follows the rigid origami folding mode, where plastic deformation concentrates on the creases. Therefore, longer or thicker creases require more force during compression. Secondly, to maintain relative density consistency, the design parameter, *a*/*b* or *a*/*c*, and panel thickness are changed based on Eqs. (5-17) and (5-18), in which length and panel thickness are always changed oppositely, as shown in Tables 5-2 and 5-3, resulting in limited effect on stress. Figure 5-10(d) reveals significant changes in the amplitude of the stress versus strain curves when varying the folding angle η_1. Models with larger folding angles η_1 require a greater force for compression along the *x* direction, whereas the opposite is observed for the *z* direction, which will be discussed in the subsequent section. Moreover, the fluctuation observed in the curve

is attributable to localized non-uniform deformation, similar to the aforementioned scenario.

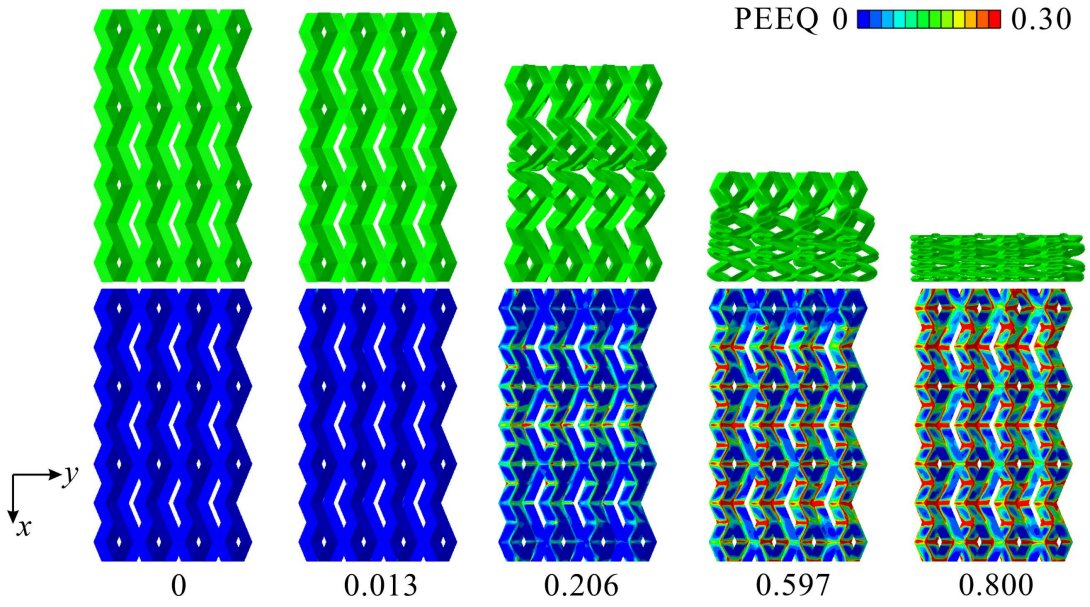

Fig. 5-11 Deformation process and corresponding PEEQ contour maps of 70-1-1-90 in the *x* direction.

Table 5-5 SEA and k_c obtained from simulations of different origami metamaterials when varying α.

Model	SEA-*x* (J/g)	SEA-*y* (J/g)	SEA-*z* (J/g)	k_c-*x* (MPa)	k_c-*y* (MPa)	k_c-*z* (MPa)
50-1-1-90	1.83	18.74	16.61	488.81	18303.94	29738.24
55-1-1-90	3.27	17.71	13.80	1915.88	16181.09	17766.79
60-1-1-90	4.52	15.06	10.39	4624.10	13715.90	9519.31
65-1-1-90	6.31	14.54	9.45	9401.56	11603.66	6336.63
70-1-1-90	7.85	14.33	7.05	18944.47	8390.52	4076.80

Table 5-6 SEA and k_c obtained from simulations of different origami metamaterials when varying a/b.

Model	SEA-*x* (J/g)	SEA-*y* (J/g)	SEA-*z* (J/g)	k_c-*x* (MPa)	k_c-*y* (MPa)	k_c-*z* (MPa)
60-0.6-1-90	5.05	15.30	9.11	5424.19	14150.18	6939.03
60-0.7-1-90	4.88	15.10	9.24	5045.23	14234.03	7503.29
60-0.8-1-90	4.66	15.32	9.79	4852.84	13922.12	8268.75
60-0.9-1-90	4.60	14.75	9.98	4660.68	14164.39	8957.74
60-1-1-90	4.52	15.06	10.39	4624.10	13715.90	9519.31
60-1.1-1-90	4.33	15.36	10.87	4562.86	14114.53	10325.46
60-1.2-1-90	4.27	14.71	11.36	4501.20	13872.92	11558.31

Table 5-7 SEA and k_c obtained from simulations of different origami metamaterials when varying a/c.

Model	SEA-x (J/g)	SEA-y (J/g)	SEA-z (J/g)	k_c-x (MPa)	k_c-y (MPa)	k_c-z (MPa)
60-1-0.78-90	4.93	16.04	12.09	4689.10	13569.35	11424.11
60-1-0.875-90	4.60	15.68	11.25	4650.53	13815.66	10686.37
60-1-1-90	4.52	15.06	10.39	4624.10	13715.90	9519.31
60-1-1.17-90	4.36	16.02	9.65	4474.13	13518.78	8859.85
60-1-1.4-90	4.32	15.94	8.85	4404.20	13695.17	7803.49

Table 5-8 SEA and k_c obtained from simulations of different origami metamaterials when varying η_1.

Model	SEA-x (J/g)	SEA-y (J/g)	SEA-z (J/g)	k_c-x (MPa)	k_c-y (MPa)	k_c-z (MPa)
60-1-1-70	1.77	13.32	15.74	481.68	13195.01	31886.22
60-1-1-80	3.13	14.40	12.77	1930.61	14372.98	16686.06
60-1-1-90	4.52	15.06	10.39	4624.10	13715.90	9519.31
60-1-1-100	7.15	16.18	9.86	8393.36	14068.77	5516.49
60-1-1-110	8.38	15.70	8.87	13858.10	13152.43	3236.90
60-1-1-120	10.98	15.88	8.31	19372.91	12455.00	1915.37

Figures 5-12(a)-(d) illustrate stress versus strain curves for compression in the y direction. As previously discussed in Fig. 5-5, primary deformation in this direction manifests as panel buckling. Therefore, the main factors affecting the stress in the y direction are the thickness of the panel and the projected area on the xoz plane. When the thickness and projected area have minimal changes, the stress does not undergo significant changes, as shown in Figs. 5-12(b) and (c). However, when the projected area undergoes significant variations due to changes in the design angle and folding angle, the amplitude of the stress curve also exhibits corresponding trends, as shown in Figs. 5-12(a) and (d). According to Eqs. (5-4), (5-8) and (5-10), the project area S_{WH} for compressing in the y direction can be expressed as

$$S_{WH} = 2\left(2n\text{-}1\right)a\sin\sqrt{1-\frac{2\cos^2\alpha}{1-\cos\eta_1}}\left[\left(n-1\right)c+2nb\cos\frac{\eta_1}{2}\right]. \tag{5-28}$$

An increase in α correlates with an increased projected area, while an increase in η_1 yields an inverse effect. As a result, stress versus strain curves reflect corresponding trends.

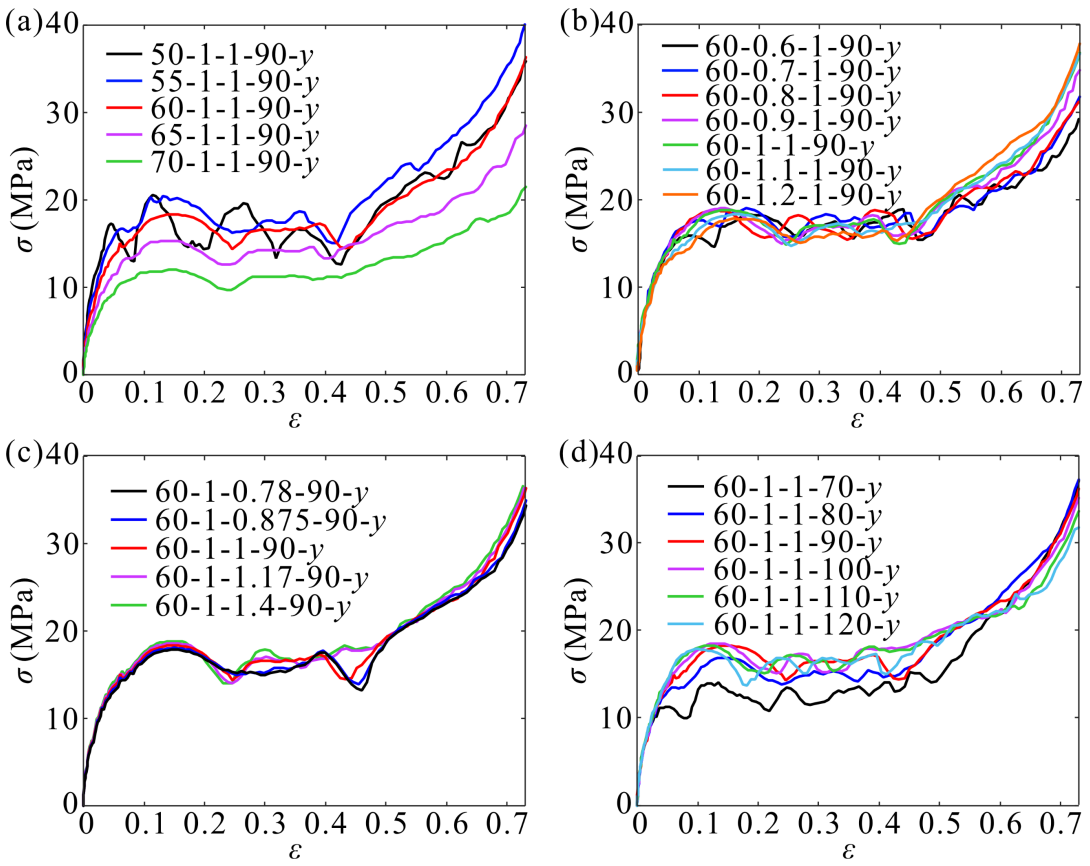

Fig. 5-12 The stress versus strain curves in the *y* direction when varying: (a) α, (b) *a*/*b*, (c) *a*/*c*, and (d) η_1 for different design parameters.

The finite element simulation results in the *z* direction are presented in Fig. 5-13, where Fig. 5-13(a) illustrates variations in the stress versus strain curve of the metamaterial in response to changes in α. As previously discussed, variations in α lead to changes in η_2, subsequently affecting stress, with a trend opposite to that observed in the *x* direction. This phenomenon is related to the single DOF folding characteristic of the origami metamaterial. As shown in Fig. 5-2(c), the folding extent in the *x* and *z* directions is always opposite, leading to an opposite trend in the mechanical properties. Similar results can be obtained in Fig. 5-13(d) when altering η_1. Figure 5-13(b) presents the results when changing *a*/*b*. Two primary alterations are observed: firstly, a slight increase in the initial peak stress can be observed, attributed to alterations in thickness; secondly, a progressive advancement of the self-locking strain point with increasing *a*/*b*. Based on Eqs. (5-10) and (5-11), the self-locking strain point ε_L can be calculated as

$$\varepsilon_L = \frac{2nb\cos\frac{\eta_1}{2}}{(n-1)c + 2nb\cos\frac{\eta_1}{2}}. \tag{5-29}$$

Thus, it is evident that an increase in *a*/*b* leads to a decrease in the self-locking strain. Similarly, a decrease in *a*/*c* also produces the same effect, as shown in Fig. 5-13(c).

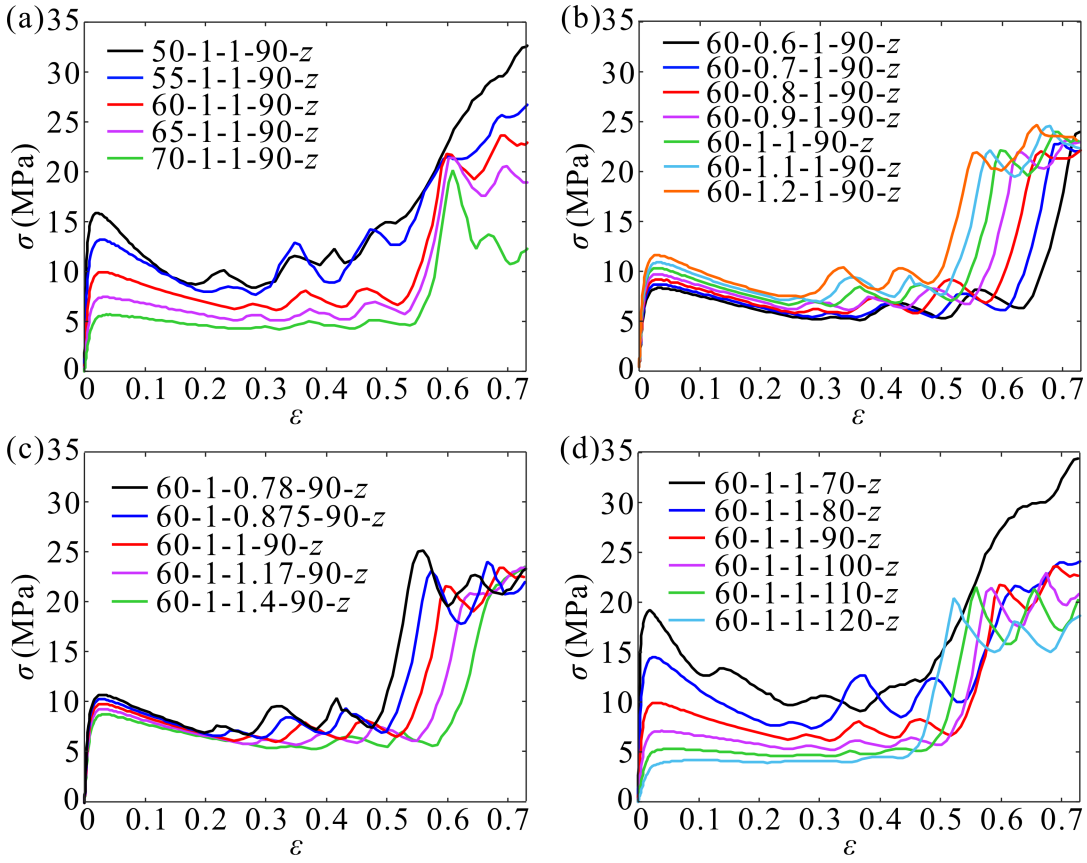

Fig. 5-13 The stress versus strain curves in the *z* direction when varying: (a) α, (b) *a*/*b*, (c) *a*/*c*, and (d) η_1 for different design parameters.

Figure 5-14 and Tables 5-5 to 5-8 illustrate the trends in SEA and k_c as different parameters are varied. Overall, there is a consistent influence of the parameters on both SEA and k_c. In other words, modifying the parameters leads to similar trends in SEA and k_c in the same direction. The mechanical properties exhibit distinct anisotropic characteristics in different directions. The results also include the theoretical analysis results of SEA in the *x* and *z* direction, as shown in Figs. 5-14(a), 5-14(c), 5-14(e), and 5-14(g). Significant errors are observed in the theoretical analysis at extreme design and folding angles, as shown in Figs. 5-14(a) and 5-14(g). When there is an error in the

x direction, the *z* direction fits well, and vice versa. This discrepancy arises because the deformation occurring in the structure at these parameter values deviates from the rigid origami folding mode. The occurrence of buckling deformation results in higher SEA in the finite element simulations, as can be seen in Fig. 5-11. The mechanical properties of the metamaterial exhibit different dependencies based on the direction. In the *x* direction, the design angle and folding angle play primary roles, while length parameters like *a*/*b* and *a*/*c* have minimal impact. The mechanical properties in the *y* direction are primarily affected by the design angle. Moreover, in the *z* direction, the mechanical properties increase with higher values of *a*/*b* and lower values *a*/*c*. Changes in the design angle and folding angle result in an opposite trend of mechanical properties in the *z* direction compared to the *x* direction.

Based on the analytical models developed in Section 5.4.1, the contour maps of SEA when varying parameters are presented in Figs. 5-15 and 5-16. Regarding the length parameters, as shown in Fig. 5-15(a), the SEA in the *x* direction exhibits a stable response, fluctuating narrowly between 4.02 J/g and 4.88 J/g. It is barely affected by the variations in length ratios *a*/*b* or *a*/*c*. This insensitivity arises because the deformation in the *x* direction is dominated by the rigid origami folding mode, where energy dissipation is primarily concentrated at the plastic hinges of the creases rather than the panel surfaces. Consequently, changes in panel aspect ratios have a negligible impact on the plastic hinge formation per unit mass.

In contrast, Fig. 5-16(a) demonstrates that the SEA in the *z* direction is highly sensitive to these geometric proportions; it increases significantly with an increase in *a*/*b* and a decrease in *a*/*c*. This is physically attributed to the fact that the *z* direction deformation involves the buckling of rectangular panels (part 2). Altering *a*/*b* or *a*/*c* directly changes the slenderness ratio of these panels, thereby significantly influencing their critical buckling loads and the resulting energy absorption capacity.

Regarding the angular parameters, Figs. 5-15(b) and 5-16(b) reveal a clear competing relationship between the SEA in the *x* and *z* directions. As the design angle η_1 and folding angle α vary, the two directional responses generally exhibit opposite trends. In addition, it should be noted that the design space is restricted by geometric compatibility conditions. Specifically, configurations satisfying $\eta_1<\pi-2\alpha$ are physically unattainable and are therefore identified as an invalid region, shown as the gray area in the figures.

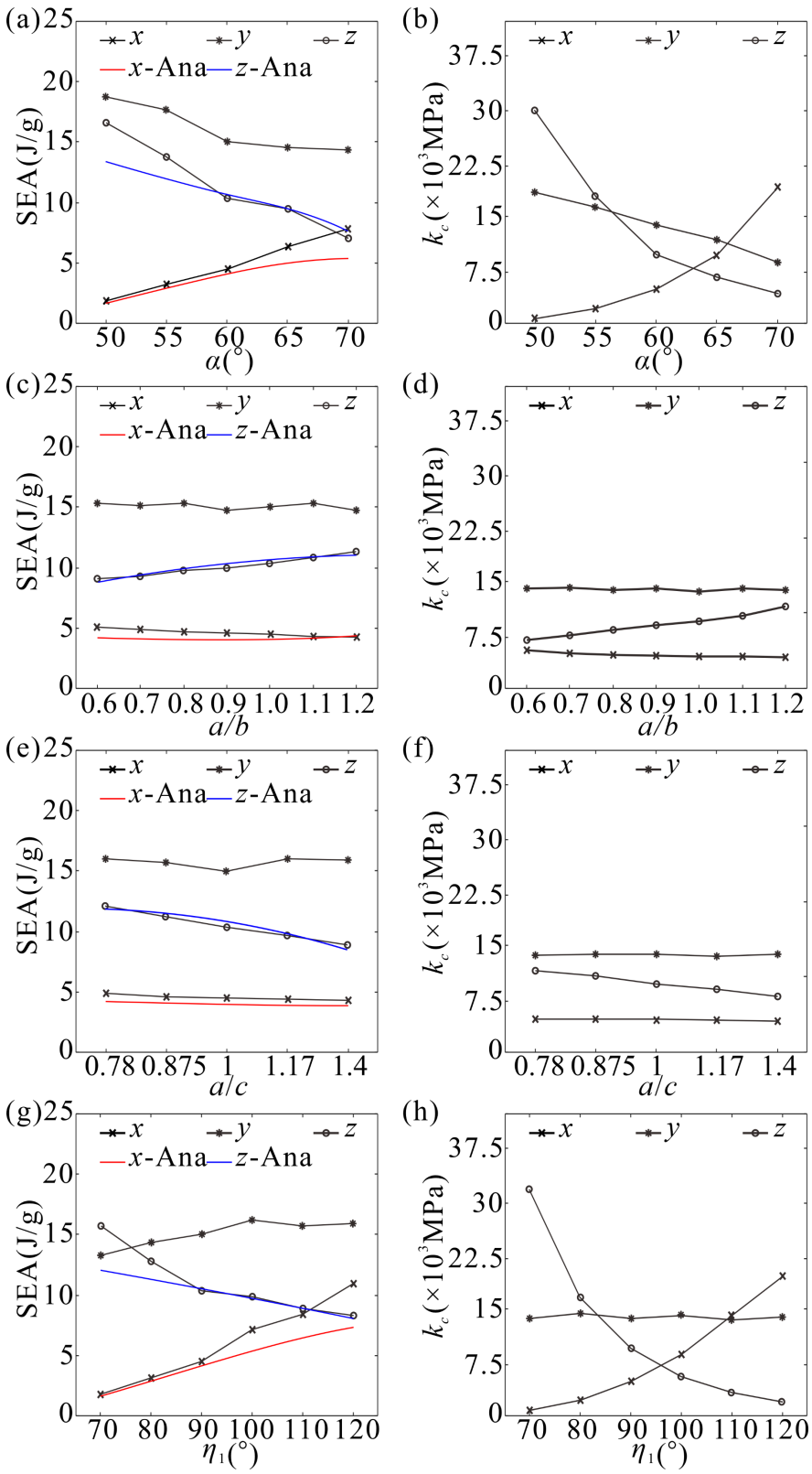

Fig. 5-14 Comparison of SEA and k_c in different directions when varying: (a-b) α, (c-d) a/b, (e-f) a/c, and (g-h) η_1 for different design parameters, with SEA in the x and z direction obtained from theoretical analysis plotted on the corresponding figures.

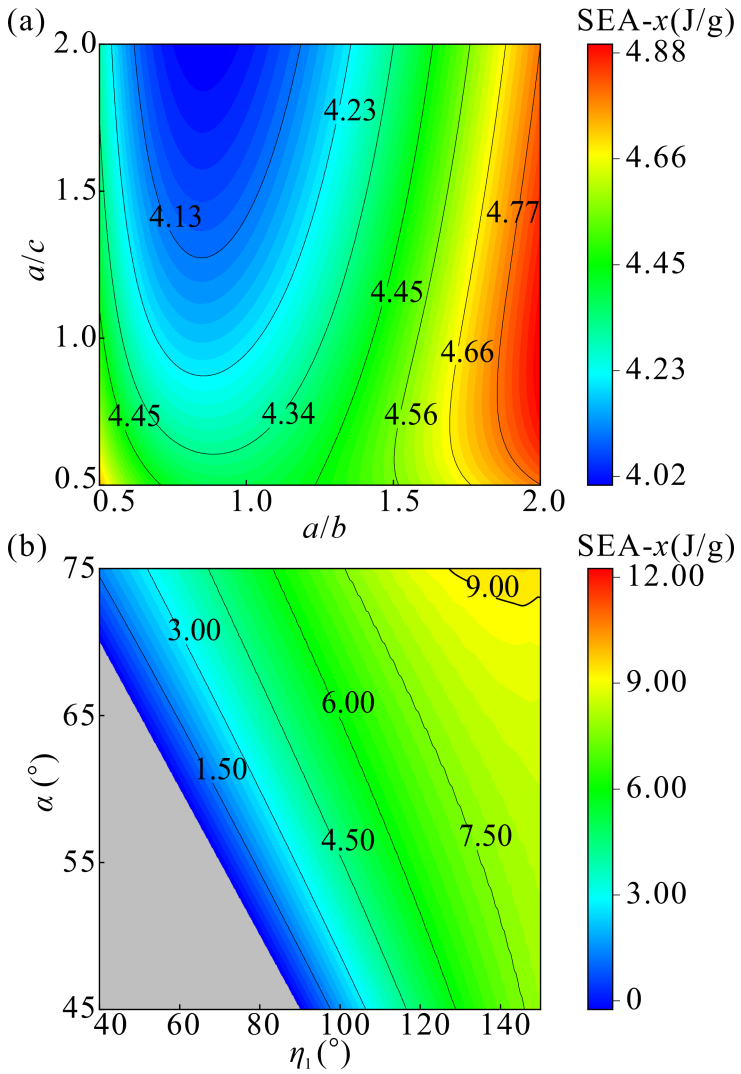

Fig. 5-15 Parametric analysis of SEA in the *x* direction: (a) SEA in the *x* direction when varying length parameters *a*/*b* and *a*/*c*; (b) SEA in the *x* direction when varying angle parameters α and η_1.

In the vicinity of this boundary, the SEA in the *x* direction remains relatively low, whereas the SEA in the *z* direction exhibits an intriguing non-monotonic trend. This phenomenon is a direct consequence of the constraint to maintain a constant relative density across all models. According to Eq. (5-18), as the configuration approaches the limit $\eta_1 \approx \pi\text{-}2\alpha$, the total surface area S_m changes, forcing the panel thickness t to decrease to keep ρ_v constant. Since the *z* direction strength relies heavily on panel buckling—which is cubically related to thickness—the reduction in t counteracts the geometric benefits of the angles, causing a drop in SEA. Conversely, if the angles are reduced independently without the thickness constraint, the *z* direction SEA would

strictly increase. Therefore, the observed non-monotonicity is the result of a trade-off between geometric configuration and the required reduction in wall thickness.

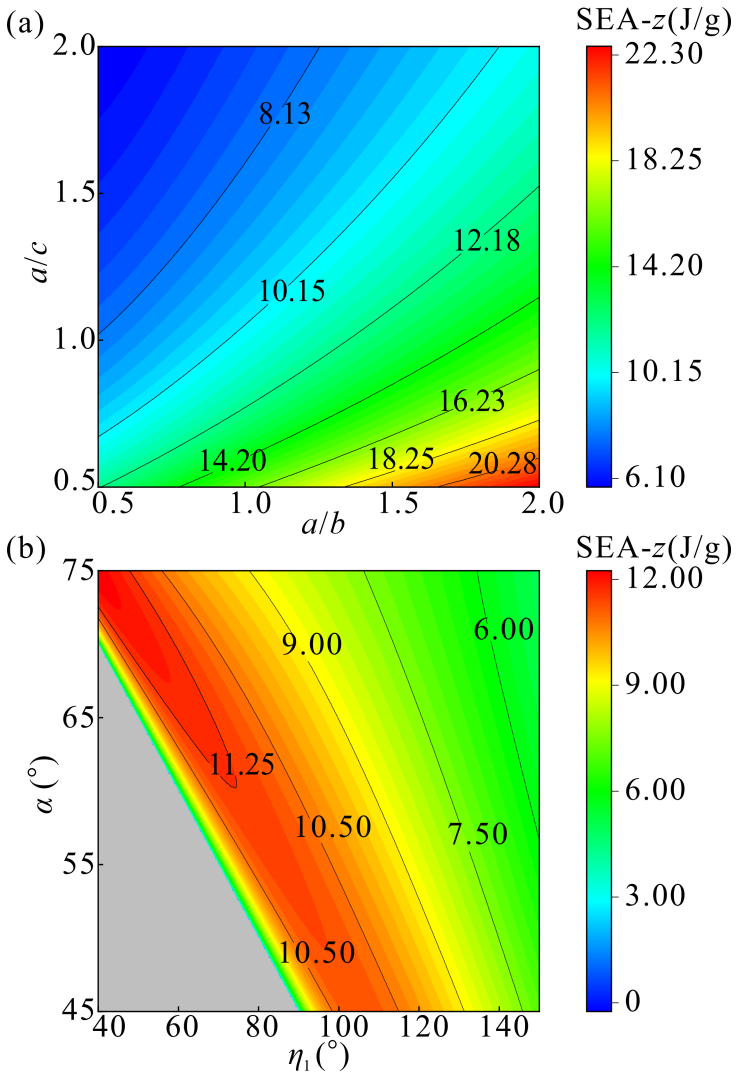

Fig. 5-16 Parametric analysis of SEA in the *z* direction: (a) SEA in the *z* direction when varying length parameters *a*/*b* and *a*/*c*; (b) SEA in the *z* direction when varying angle parameters α and η_1.

5.5 Conclusions and Discussion

In this chapter, a novel origami metamaterial featuring distinct anisotropic mechanical properties in three orthotropic directions has been proposed, designed, and systematically analyzed. A theoretical model based on rigid origami kinematics and plastic hinge theory has been established to predict the SEA in the *x* and *z* directions. These analytical predictions have been corroborated by experimentally validated finite element simulations, showing high consistency. The results reveal that the proposed

metamaterial is not merely anisotropic in magnitude but exhibits fundamentally distinct deformation mechanisms in each orthogonal direction. In the *x* direction, the deformation strictly follows a rigid origami folding mode with minimal panel distortion. This mechanism results in a predictable, stable, but relatively low SEA and compressive stiffness, making it suitable for applications requiring compliant deployment. In the *y* direction, the behavior is governed by the buckling of vertical panels throughout the entire compression process. Consequently, this direction exhibits the highest mechanical performance, with SEA and stiffness values reaching approximately three times those observed in the *x* direction. In the *z* direction, the metamaterial demonstrates a unique two-stage response, initially undergoing rigid folding followed by a transition to panel buckling. This results in intermediate mechanical properties that lie between the other two directions, offering a graded stiffness response. Furthermore, the extensive parametric analysis highlights the programmability of this metamaterial.

In addition to the comprehensive mechanical characterization, the acoustic properties of the proposed metamaterial have also been investigated using finite element simulations. The numerical results indicate that, unlike the aforementioned origami configurations, this specific triple-tubular origami structure does not exhibit acoustic bandgap characteristics, as shown in Fig. E1 in Appendix E. This absence can be primarily attributed to the lack of independent wave propagation pathways across the three orthogonal directions.

This work elucidates the comprehensive anisotropic mechanical framework of the proposed origami metamaterial, proving its capability to integrate conflicting mechanical requirements, such as high load-bearing capacity and deployability, into a single unitary architecture. By successfully programming the mechanical responses in orthogonal directions, this design offers a versatile platform for multi-functional engineering applications, ranging from impact energy absorbers to reconfigurable aerospace structures.

Beyond the uniform tessellations studied here, future investigations will focus on functionally graded designs and dynamic impact behaviors to further tailor the mechanical performance and energy absorption efficiency for complex loading scenarios.

Chapter 6 Main achievements and Future Works

6.1 Conclusions

This dissertation focuses on the intersection of origami kinematics and multifunctional metamaterial design. A generalized analytical framework for the kinematic synthesis of tubular origami structures is established, and, on this basis, several classes of origami metamaterials with programmable mechanical and acoustic properties are developed. Through theoretical analysis, numerical simulation, and experimental validation, this work systematically reveals the mapping relationships between geometric configuration, folding kinematics, and multiphysical performance, thereby providing both a theoretical foundation and a design methodology for the development of origami metamaterials.

First, a generalized kinematic synthesis framework for single-DOF tubular origami structures composed of 4-crease vertices is established. By combining the D-H matrix method with spatial loop-closure constraints, explicit compatibility conditions are derived for tubular assemblies with spatial polygonal cross-sections and further extended to generalized multi-vertex systems. Based on these compatibility conditions, a class of double-tubular origami structures is constructed, and a rotational tessellation strategy is developed to assemble the corresponding 3D metamaterials while preserving rigid foldability. This part of the work provides a general theoretical basis for the rational design of subsequent single-, double-, and triple-tubular structures.

Second, for single-tubular origami metamaterials, the influence of M-V assignments on both mechanical and acoustic properties is systematically clarified. The results show that M-V assignments significantly affect the mechanical response by altering the rate and magnitude of folding-angle variation, and also govern the occurrence and programmability of directional bandgaps in the acoustic response. These findings demonstrate that M-V assignment not only determines the geometric topology of the metamaterial, but also an effective and independent design variable for programming the multiphysical properties of origami metamaterials.

Third, a class of double-tubular origami metamaterials with independently programmable mechanical and acoustic properties is proposed. Owing to the nonlinear mapping between the design parameters, initial folding states, and physical responses, one property can be programmed over a wide range while the other remains nearly

unchanged. In particular, the frequency range of the acoustic bandgap can be varied by up to 10.4 times while maintaining an almost constant mechanical stiffness, whereas the stiffness can be varied by up to 16.9 times while preserving the bandgap interval. In addition, post-fabrication thermomechanical reconfiguration further enables the on-demand tunability of both mechanical and acoustic properties.

Finally, a triple-tubular origami metamaterial with highly programmable anisotropic mechanical behavior is developed. The proposed structure exhibits distinct deformation mechanisms under compression along three orthogonal directions. Specifically, rigid folding dominates in the *x* direction, resulting in relatively low stiffness and SEA; panel buckling dominates in the *y* direction, leading to high stiffness and significantly enhanced SEA; and a coupled deformation mode involving rigid folding followed by panel buckling occurs in the *z* direction, producing a graded mechanical response. These results further expand the design space of origami metamaterials for directional mechanical programmability.

Overall, this research not only lays a robust theoretical foundation for the configurational synthesis and functional design of origami metamaterials, but also provides vital technical support for their practical engineering applications.

6.2 Innovations

The main innovations of this dissertation are summarized as follows.

(1) A generalized kinematic synthesis framework for single-DOF tubular origami structures composed of 4-crease vertices is established. This framework extends tubular origami design from specific planar cross-sections to generalized spatial polygonal cross-sections, providing a unified theoretical basis for the design of tubular origami metamaterials.

(2) M-V assignment is identified as an independent design dimension for programming the mechanical and acoustic properties of single-tubular metamaterials. This work demonstrates that varying M-V assignments can effectively program mechanical responses and acoustic wave attenuation characteristics, thereby providing a new strategy for the functional design of origami metamaterials.

(3) A double-tubular origami metamaterial with independently programmable and tunable mechanical and acoustic properties is proposed. By exploiting the nonlinear mapping between design parameters and physical responses, this work achieves

independent programmability of the two properties and further realizes post-fabrication tunability through thermomechanical reconfiguration.

(4) A triple-tubular origami metamaterial with programmable anisotropic mechanical properties in three orthogonal directions is developed. The proposed structure enables distinct deformation modes and highly differentiated mechanical responses along three orthogonal directions, expanding the design space of anisotropic origami metamaterials.

6.3 Future Works

The research reported in this dissertation establishes a generalized theoretical framework for the kinematic synthesis of tubular origami structures and systematically investigates the mapping mechanisms between geometric configurations and multiphysical performance. To further enhance the functional versatility and practical engineering applications of the proposed origami metamaterials, several potential topics can be further explored.

First, the kinematic synthesis framework developed in this study is currently mainly focused on 4-crease vertices subject to flat-foldability constraints. Future work could extend this framework to more generalized 4-crease vertices, thereby broadening the range of admissible tubular origami configurations and enriching the design space of origami metamaterials.

Second, in the construction of the double-tubular and triple-tubular origami metamaterials, this study mainly adopts a uniform tessellation strategy. Future research could introduce geometric gradient designs at the unit-cell level, for example by gradually varying the design angle, folding angle, or unit type along the tessellation direction, so as to achieve more diverse programmable performances.

Third, the present acoustic simulations are based on rigid-wall assumptions, where the structural walls are treated as sound-hard boundaries and fluid-structure interaction is neglected. Future studies could further incorporate wall flexibility and fluid-structure coupling to more accurately capture the acoustic behavior of origami metamaterials.

Forth, for the reconfiguration of origami metamaterials, future research could further explore the integration of origami structures with smart materials. By introducing stimuli-responsive materials with optical, thermal, or magnetic responsiveness, it may become possible to achieve active reconfiguration of structural

geometries and endow these metamaterials with richer multiphysical functionalities.

Finally, in addition to the commonly used 3D printing methods, future efforts should also explore the feasibility of employing conventional manufacturing techniques for the mass production of origami metamaterials, thereby supporting their practical engineering applications.

References

[1] Veselago V G. The electrodynamics of substances with simultaneously negative values of ε and μ[J]. Soviet Physics Uspekhi, 1968, 10(4): 509-514.

[2] Pendry J B, Schurig D, Smith D R. Controlling electromagnetic fields[J]. Science, 2006, 312(5781): 1780-1782.

[3] Pendry J B. Negative refraction makes a perfect lens[J]. Physical Review Letters, 2000, 85(18): 3966-3969.

[4] Mei J, Ma G, Yang M, et al. Dark acoustic metamaterials as super absorbers for low-frequency sound[J]. Nature Communications, 2012, 3: 756.

[5] Ma Z, Song K, Zhou X. An AI-based bidirectional design framework for energy-absorbing cubic origami metamaterials from plane tessellation patterns[J]. Thin-Walled Structures, 2026, 225: 114750.

[6] Barchiesi E, Spagnuolo M, Placidi L. Mechanical metamaterials: A state of the art[J]. Mathematics and Mechanics of Solids, 2019, 24: 212-234.

[7] Hurairah M A, Lee S. Auxetic mechanical metamaterials (AMMs): A state-of-the-art review on advances in design, fabrication, and applications[J]. Journal of Mechanical Science and Technology, 2026, 40(2): 1093–1122.

[8] Haver D, Acuña D, Janbaz S, et al. Elasticity and rheology of auxetic granular metamaterials[J]. Proceedings of the National Academy of Sciences, 2024, 121(14): e2317915121.

[9] Giri T R, Mailen R. Controlled snapping sequence and energy absorption in multistable mechanical metamaterial cylinders[J]. International Journal of Mechanical Sciences, 2021, 204: 106541.

[10] Ren Z, Qi D, Liu Z, et al. Multistable chiral-twist metamaterials with reconfigurable deformation modes: Mechanical design, simulations and experimental demonstrations[J]. Thin-Walled Structures, 2026, 225: 114784.

[11] Mei T, Meng Z, Zhao K, et al. A mechanical metamaterial with reprogrammable logical functions[J]. Nature Communications, 2021, 12: 7234.

[12] Hou X, Sheng T, Xie F, et al. Mechanical logic gate design based on multi-stable metamaterial with multi-step deformation[J]. Composite Structures, 2024, 335: 118001.

[13] Xu C, Gallant B M, Wunderlich P U, et al. Three-dimensional Au microlattices

as positive electrodes for Li–O_2 batteries[J]. ACS Nano, 2015, 9(6): 5876-5883.

[14] Greiner A M, Richter B, Bastmeyer M. Micro-engineered 3D scaffolds for cell culture studies[J]. Macromolecular Bioscience, 2012, 12(10): 1301-1314.

[15] Maldovan M. Sound and heat revolutions in phononics[J]. Nature, 2013, 503(7475): 209-217.

[16] Arjunan A, Baroutaji A, Robinson J, et al. Acoustic metamaterials for sound absorption and insulation in buildings[J]. Building and Environment, 2024, 251: 111250.

[17] Paul D D. Optical metamaterials: fundamentals and applications[J]. Physics Today, 2010, 63(9): 57-58.

[18] Li Y, Li W, Han T, et al. Transforming heat transfer with thermal metamaterials and devices[J]. Nature Reviews Materials, 2021, 6(6): 488-507.

[19] Lee K W, Lim W, Jeon M S, et al. Visibly clear radiative cooling metamaterials for enhanced thermal management in solar cells and windows[J]. Advanced Functional Materials, 2022, 32: 2105882.

[20] Jiang S, Liu X, Liu J, et al. Flexible metamaterial electronics[J]. Advanced Materials, 2022, 34(52): 2200070.

[21] Jang K I, Chung H U, Xu S, et al. Soft network composite materials with deterministic and bio-inspired designs[J]. Nature Communications, 2015, 6: 6566.

[22] Zhang X, Huang X, Lu G. Tunable bandgaps and acoustic characteristics of perforated Miura-ori phononic structures[J]. International Journal of Mechanical Sciences, 2023, 253: 108389.

[23] Zhao P, Zhang K, Deng Z. Origami-inspired lattice for the broadband vibration attenuation by Symplectic method[J]. Extreme Mechanics Letters, 2022, 54: 101771.

[24] Cai J, Estakhrianhaghighi E, Akbarzadeh A. Functionalized graphene origami metamaterials with tunable thermal conductivity[J]. Carbon, 2022, 191: 610-624.

[25] Rahardjo A S, Navaratnam S, Zhang G. Reconfigurable origami-based metamaterials with a transition between compact flat-foldable and load-bearing states[J]. Mechanics Research Communications, 2026, 154: 104678.

[26] Li S, Zhang W, Ding S, et al. A comprehensive review on energy-absorbing mechanical metamaterials: From mechanisms to applications[J]. Composites Part B: Engineering, 2025, 311: 113222.

[27] Ma J, Dai H, Chai S, et al. Energy absorption of sandwich structures with a kirigami-inspired pyramid foldcore under quasi-static compression and shear[J]. Materials & Design, 2021, 206: 109808.

[28] Yan Q, Shi H, Bai C, et al. Triple-layered multifunctional woven lattice truss sandwich panels with multifunction of load carrying and sound absorbing[J]. Composite Structures, 2025, 357: 118934.

[29] Li X, Yu X, Chua J W, et al. Microlattice metamaterials with simultaneous superior acoustic and mechanical energy absorption[J]. Small, 2021, 17(24): 2100336.

[30] Zhang X, Ye H, Wei N, et al. Design optimization of multifunctional metamaterials with tunable thermal expansion and phononic bandgap[J]. Materials & Design, 2021, 209: 109990.

[31] Lv S, Xu W, Bai L, et al. Thermal tuning of band gap properties in planar stretch-dominated lattices with tailorable coefficient of thermal expansion[J]. Applied Physics A, 2021, 127(6): 425.

[32] Xu W, Lv S, Bai L, et al. Multifunctional design of triangular lattice metamaterials with customizable thermal expansion and tunable bandgap properties[J]. Journal of Applied Physics, 2021, 130(8): 085106.

[33] Lee H Y, Liang C G. A new vector theory for the analysis of spatial mechanisms[J]. Mechanism and Machine Theory, 1988, 23(3): 209-217.

[34] Wu W, You Z. Modelling rigid origami with quaternions and dual quaternions[J]. Proceedings of the Royal Society A: Mathematical, Physical and Engineering Sciences, 2010, 466(2119): 2155-2174.

[35] Wei G, Ding X, Dai J S. Mobility and geometric analysis of the hoberman switch-pitch ball and its variant[J]. Journal of Mechanisms and Robotics, 2010, 2(3): 031010.

[36] Zhang K, Fang Y, Fang H, et al. Geometry and constraint analysis of the three-spherical kinematic chain based parallel mechanism[J]. Journal of Mechanisms and Robotics, 2010, 2(3): 031014.

[37] Gu Y, Zhang X, Wei G, et al. Sarrus-inspired deployable polyhedral mechanisms[J]. Mechanism and Machine Theory, 2024, 193: 105564.

[38] Tarnai T. Infinitesimal and finite mechanisms[M]. Vienna: Springer, 2001, 412: 113-142.

[39] Yang F, Chen Y, Kang R, et al. Truss transformation method to obtain the non-overconstrained forms of 3D overconstrained linkages[J]. Mechanism and Machine Theory, 2016, 102: 149-166.

[40] Chen Y, Chai W H. Bifurcation of a special line and plane symmetric Bricard linkage[J]. Mechanism and Machine Theory, 2011, 46(4): 515-533.

[41] Gan W W, Pellegrino S. A numerical approach to the kinematic analysis of deployable structures forming a closed loop[J]. Proceedings of the Institution of Mechanical Engineers, Part C: Journal of Mechanical Engineering Science, 2006, 220(7): 1045-1056.

[42] Kumar P, Pellegrino S. Computation of kinematic paths and bifurcation points[J]. International Journal of Solids and Structures, 2000, 37(46-47): 7003-7027.

[43] Denavit J, Hartenberg R S. A kinematic notation for lower-pair mechanisms based on matrices[J]. Journal of Applied Mechanics, 1955, 22(2): 215-221.

[44] Chen Y, Lv W, Peng R, et al. Mobile assemblies of four-spherical-4R-integrated linkages and the associated four-crease-integrated rigid origami patterns[J]. Mechanism and Machine Theory, 2019, 142: 103613.

[45] Zhang K, Dai J S. Classification of origami-enabled foldable linkages and emerging applications[C]//International Design Engineering Technical Conferences and Computers and Information in Engineering Conference. Portland, Oregon, USA: American Society of Mechanical Engineers, 2013, 55942: V06BT07A024.

[46] Zimmermann L, Stanković T. Rigid and flat foldability of a degree-four vertex in origami[J]. Journal of Mechanisms and Robotics, 2020, 12(1): 011004.

[47] Cai J, Zhang Q, Feng J, et al. Modeling and kinematic path selection of retractable kirigami roof structures[J]. Computer-Aided Civil and Infrastructure Engineering, 2019, 34(4): 352-363.

[48] Peng R, Ma J, Chen Y. The effect of mountain-valley folds on the rigid foldability of double corrugated pattern[J]. Mechanism and Machine Theory, 2018, 128: 461-474.

[49] Budinski N. Mathematics and origami: The art and science of folds[M]//Handbook of the Mathematics of the Arts and Sciences. Cham: Springer International Publishing, 2021: 317-348.

[50] Justin J. Mathematical remarks about origami bases[J]. Symmetry: Culture and

Science, 1994, 5(2): 153-165.

[51] Lang R J. Twists, tilings, and tessellations: Mathematical methods for geometric origami[M]. Boca Raton: AK Peters/CRC Press, 2017, 33-42.

[52] 邹凯, 赵昌方, 刘浩, 等. 多向拉胀折纸超材料的力学行为研究[J]. 塑料科技, 2025, 53(1): 16-21.

Zou K, Zhao H, Liu H, et al. Study on mechanical behaviours of multi-directional auxetic origami meta-materials[J]. Plastics Science & Technology/Suliao Ke-Ji, 2025, 53(1): 16-21. (in Chinese)

[53] Meng F, Chen S, Zhang W, et al. Negative Poisson's ratio in graphene Miura origami[J]. Mechanics of Materials, 2021, 155: 103774.

[54] Pratapa P P, Liu K, Paulino G H. Geometric mechanics of origami patterns exhibiting Poisson's ratio switch by breaking mountain and valley assignment[J]. Physical Review Letters, 2019, 122(15): 155501.

[55] Yasuda H, Yang J. Reentrant origami-based metamaterials with negative Poisson's ratio and bistability[J]. Physical Review Letters, 2015, 114(18): 185502.

[56] Zhou Y, Jiang D, Wang L, et al. Cushioning performance of origami negative Poisson's ratio honeycomb steel structure[J]. Thin-Walled Structures, 2024, 204: 112284.

[57] 王海瑞, 申薛靖, 王宙恒, 等. 折纸超材料折展稳态特性研究[J]. 力学学报, 2022, 54(10): 2726-2732.

Wang H, Shen X, Wang Z, et al. Study on folding stability of origami metamaterials[J]. Chinese Journal of Theoretical and Applied Mechanics, 2022, 54(10): 2726-2732. (in Chinese)

[58] Grasinger M, Gillman A, Buskohl P R. Multistability, symmetry and geometric conservation in eightfold waterbomb origami[J]. Proceedings of the Royal Society A: Mathematical, Physical and Engineering Sciences, 2022, 478(2268): 20220270.

[59] Waitukaitis S, Menaut R, Chen B G ge, et al. Origami multistability: From single vertices to metasheets[J]. Physical Review Letters, 2015, 114(5): 055503.

[60] Xi K, Chai S, Ma J, et al. Multi-stability of the extensible origami structures[J]. Advanced Science, 2023, 10(29): 2303454.

[61] Tiwari A K, Upadhyay S H, Mukhopadhyay T. Nonlinear wave propagation and dynamic control in multi-unit Kresling origami metamaterials with conical

architectures[J]. Mechanical Systems and Signal Processing, 2026, 244: 113737.

[62] Mukhopadhyay T, Ma J, Feng H, et al. Programmable stiffness and shape modulation in origami materials: Emergence of a distant actuation feature[J]. Applied Materials Today, 2020, 19: 100537.

[63] Tomita S, Oyama S, Shimanuki K, et al. Tunable stiffness via laminar jamming of aluminum sheets and 3D-printed origami structures[J]. Smart Materials and Structures, 2025, 34(7): 075027.

[64] Yuan L, Dai H, Song J, et al. The behavior of a functionally graded origami structure subjected to quasi-static compression[J]. Materials & Design, 2020, 189: 108494.

[65] Schenk M, Guest S D. Geometry of Miura-folded metamaterials[J]. Proceedings of the National Academy of Sciences of the United States of America, 2013, 110(9): 3276-3281.

[66] Feng H, Peng R, Ma J, et al. Rigid foldability of generalized triangle twist origami pattern and its derived 6R linkages[J]. Journal of Mechanisms and Robotics, 2018, 10(5): 051003.

[67] Hull T. Counting mountain-valley assignments for flat folds[J]. Ars Combinatoria, 2003, 67: 175-188.

[68] Ma J, Zang S, Feng H, et al. Theoretical characterization of a non-rigid-foldable square-twist origami for property programmability[J]. International Journal of Mechanical Sciences, 2021, 189: 105981.

[69] Feng H, Peng R, Zang S, et al. Rigid foldability and mountain-valley crease assignments of square-twist origami pattern[J]. Mechanism and Machine Theory, 2020, 152: 103947.

[70] Wei J, Chen Y, Zhang X. Rigid-foldable hexagon-twist origami patterns[C]//International Meeting on Origami in Science, Mathematics and Education. Singapore: Springer Nature Singapore, 2024, 1: 171-185.

[71] Tachi T. Designing freeform origami tessellations by generalizing Resch's patterns[J]. Journal of Mechanical design, 2013, 135(11): 111006.

[72] Chen Y, Feng H, Ma J, et al. Symmetric waterbomb origami[J]. Proceedings of the Royal Society A: Mathematical, Physical and Engineering Sciences, 2016, 472(2190): 20150846.

[73] Zhang X, Chen Y. Vertex-splitting on a diamond origami pattern[J]. Journal of

Mechanisms and Robotics, 2019, 11(3): 031014.

[74] Deng A, Ji B, Zhou X, et al. Geometric design and mechanical properties of foldcores based on the generalized Resch patterns[J]. Thin-Walled Structures, 2020, 148: 106516.

[75] Kshad M A E, Popinigis C, Naguib H E. 3D printing of Ron-Resch-like origami cores for compression and impact load damping[J]. Smart Materials and Structures, 2019, 28(1): 015027.

[76] Kuribayashi K, Tsuchiya K, You Z, et al. Self-deployable origami stent grafts as a biomedical application of Ni-rich TiNi shape memory alloy foil[J]. Materials Science and Engineering: A, 2006, 419(1-2): 131-137.

[77] Fang H, Zhang Y, Wang K W. Origami-based earthworm-like locomotion robots[J]. Bioinspiration & Biomimetics, 2017, 12(6): 065003.

[78] Onal C D, Wood R J, Rus D. An origami-inspired approach to worm robots[J]. IEEE/ASME Transactions on Mechatronics, 2013, 18(2): 430-438.

[79] Stavric M, Wiltsche A. Quadrilateral patterns for rigid folding structures[J]. International Journal of Architectural Computing, 2014, 12(1): 61-79.

[80] Ma J, Feng H, Chen Y, et al. Folding of tubular waterbomb[J]. Research, 2020, 2020: 1735081.

[81] Li Y. Motion paths finding for multi-degree-of-freedom mechanisms[J]. International Journal of Mechanical Sciences, 2020, 185: 105709.

[82] Yu Y, Chen Y, Paulino G H. On the unfolding process of triangular Resch patterns: A finite particle method investigation[C]//International Design Engineering Technical Conferences and Computers and Information in Engineering Conference. Anaheim, California, USA: American Society of Mechanical Engineers, 2019, 59247: V05BT07A048.

[83] Yang K, Xu S, Shen J, et al. Energy absorption of thin-walled tubes with pre-folded origami patterns: Numerical simulation and experimental verification[J]. Thin-Walled Structures, 2016, 103: 33-44.

[84] Masana R, Dalaq A S, Khazaaleh S, et al. The Kresling origami spring: A review and assessment[J]. Smart Materials and Structures, 2024, 33(4): 043002.

[85] Zhang J, Wang C. Deployment behavior and mechanical property analysis of Kresling origami structure[J]. Composite Structures, 2024, 341: 118234.

[86] Tachi T. One-DOF cylindrical deployable structures with rigid quadrilateral

panels[C]//Proceedings of the International Association for Shell and Spatial Structures (IASS) Symposium 2009. Universidad Politecnica de Valencia, Spain: Editorial Universitat Politècnica de València. 2009, 2295-2305.

[87] Liu S, Lv W, Chen Y, et al. Deployable prismatic structures with rigid origami patterns[J]. Journal of Mechanisms and Robotics, 2016, 8(3): 031002.

[88] Chen Y, Lv W, Li J, et al. An extended family of rigidly foldable origami tubes[J]. Journal of Mechanisms and Robotics, 2017, 9(2): 021002.

[89] Filipov E T, Tachi T, Paulino G H. Origami tubes assembled into stiff, yet reconfigurable structures and metamaterials[J]. Proceedings of the National Academy of Sciences, 2015, 112(40): 12321-12326.

[90] Filipov E T, Paulino G H, Tachi T. Origami tubes with reconfigurable polygonal cross-sections[J]. Proceedings of the Royal Society A: Mathematical, Physical and Engineering Sciences, 2016, 472(2185): 20150607.

[91] Kamrava S, Ghosh R, Wang Z, et al. Origami-inspired cellular metamaterial with anisotropic multi-stability[J]. Advanced Engineering Materials, 2019, 21(2): 1800895.

[92] Liu Z, Fang H, Xu J, et al. A novel origami mechanical metamaterial based on Miura-variant designs: Exceptional multistability and shape reconfigurability[J]. Smart Materials and Structures, 2021, 30(8): 085029.

[93] Mirzajanzadeh M, Pasini D. Smooth doubly curved origami shells with reprogrammable rigidity[J]. Nature Communications, 2026, 17: 2729.

[94] Zhai Z, Wang Y, Jiang H. Origami-inspired, on-demand deployable and collapsible mechanical metamaterials with tunable stiffness[J]. Proceedings of the National Academy of Sciences, 2018, 115(9): 2032-2037.

[95] Zhang J, Karagiozova D, You Z, et al. Quasi-static large deformation compressive behaviour of origami-based metamaterials[J]. International Journal of Mechanical Sciences, 2019, 153: 194-207.

[96] Karagiozova D, Zhang J, Lu G, et al. Dynamic in-plane compression of Miura-ori patterned metamaterials[J]. International Journal of Impact Engineering, 2019, 129: 80-100.

[97] Dang X, Lu L, Duan H, et al. Deployment kinematics of axisymmetric Miura origami: Unit cells, tessellations, and stacked metamaterials[J]. International Journal of Mechanical Sciences, 2022, 232: 107615.

[98] Eidini M. Zigzag-base folded sheet cellular mechanical metamaterials[J]. Extreme Mechanics Letters, 2016, 6: 96-102.

[99] Zhang J, Karagiozova D, Lu G, et al. Quasi-static in-plane compression of zig-zag folded metamaterials at large plastic strains[J]. Thin-Walled Structures, 2021, 159: 107285.

[100] Yasuda H, Gopalarethinam B, Kunimine T, et al. Origami-based cellular structures with in situ transition between collapsible and load-bearing configurations[J]. Advanced Engineering Materials, 2019, 21(12): 1900562.

[101] He R, Chen Y, Ye W, et al. Geometrically graded kiri-origami beams with enhanced energy absorption performance[J]. International Journal of Mechanical Sciences, 2026: 111378.

[102] Miura K, Tachi T. Synthesis of rigid-foldable cylindrical polyhedra[J]. Symmetry: Art and Science, 2010, 2010: 204-213.

[103] Yasuda H, Yein T, Tachi T, et al. Folding behaviour of Tachi-Miura polyhedron bellows[J]. Proceedings of the Royal Society A: Mathematical, Physical and Engineering Sciences, 2013, 469(2159): 20130351.

[104] Yamaguchi K, Yasuda H, Tsujikawa K, et al. Graph-theoretic estimation of reconfigurability in origami-based metamaterials[J]. Materials & Design, 2022, 213: 110343.

[105] Tomita S, Shimanuki K, Nishigaki H, et al. Origami-inspired metamaterials with switchable energy absorption based on bifurcated motions of a Tachi-Miura polyhedron[J]. Materials & Design, 2023, 225: 111497.

[106] 刘杰, 李志勇, 何俊峰, 等. TMP 折纸防护的双稳态软体机器人[J]. 力学学报, 2023, 55(10): 2331-2343.
Liu J, Li Z, He J, et al. A TMP origami-shell reinforced bistable soft robot. Chinese Journal of Theoretical and Applied Mechanics, 2023, 55(10): 2331-2343. (in Chinese)

[107] Lv C, Krishnaraju D, Konjevod G, et al. Origami based mechanical metamaterials[J]. Scientific Reports, 2014, 4: 5979.

[108] Lee D Y, Kim J S, Kim S R, et al. The deformable wheel robot using magic-ball origami structure[C]//International Design Engineering Technical Conferences and Computers and Information in Engineering Conference. Portland, Oregon, USA: American Society of Mechanical Engineer. 2013, 55942: V06BT07A040.

[109] Li S, Vogt D M, Rus D, et al. Fluid-driven origami-inspired artificial muscles[J]. Proceedings of the National Academy of Sciences, 2017, 114(50): 13132-13137.

[110] Feng H, Ma J, Chen Y, et al. Twist of tubular mechanical metamaterials based on waterbomb origami[J]. Scientific Reports, 2018, 8: 9522.

[111] Silverberg J L, Na J H, Evans A A, et al. Origami structures with a critical transition to bistability arising from hidden degrees of freedom[J]. Nature Materials, 2015, 14(4): 389-393.

[112] Liu K, Tachi T, Paulino G H. Invariant and smooth limit of discrete geometry folded from bistable origami leading to multistable metasurfaces[J]. Nature Communications, 2019, 10: 4238.

[113] Hou X, Zhao X, Xie F, et al. Energy absorption of multicellular diamond origami tubes based on additive manufacturing: Experimental, numerical, and theoretical studies[J]. Composite Structures, 2025, 373: 119633.

[114] Ma J, You Z. Energy absorption of thin-walled square tubes with a prefolded origami pattern—Part I: geometry and numerical simulation[J]. Journal of Applied Mechanics, 2014, 81(1): 011003.

[115] Ming S, Song Z, Zhou C, et al. The crashworthiness design of metal/CFRP hybrid tubes based on origami-ending approach: Experimental research[J]. Composite Structures, 2022, 279: 114843.

[116] Song Z, Ming S, Du K, et al. Energy absorption of metal-composite hybrid tubes with a diamond origami pattern[J]. Thin-Walled Structures, 2022, 180: 109824.

[117] Ye H, Ma J, Zhou X, et al. Energy absorption behaviors of pre-folded composite tubes with the full-diamond origami patterns[J]. Composite Structures, 2019, 221: 110904.

[118] 刘永文, 邵伟平, 郝永平. 多种超材料结构的缓冲吸能特性研究分析[J]. 建模与仿真, 2025, 14: 86.

Liu Y, Shao W, Hao Y. Study on energy absorption characteristics of various metamaterial buffer structures[J]. Modeling and Simulation, 2025, 14(12): 86-94. (in Chinese)

[119] Zhou Y, Li Z, Li X, et al. Axial compression performance of honeycomb structure with diamond origami tube[J]. Construction and Building Materials, 2025, 481: 141602.

[120] Masana R, Dalaq A S, Khazaaleh S, et al. The Kresling origami spring: A review

and assessment[J]. Smart Materials and Structures, 2024, 33(4): 043002.

[121] Kresling B. Origami-structures in nature: lessons in designing “smart” materials[J]. MRS Proceedings. 2012, 1420: mrsf11-1420-oo02-01.

[122] Dalaq A S, Daqaq M F. Experimentally-validated computational modeling and characterization of the quasi-static behavior of functional 3D-printed origami-inspired springs[J]. Materials & Design, 2022, 216: 110541.

[123] Tao R, Ji L, Li Y, et al. 4D printed origami metamaterials with tunable compression twist behavior and stress-strain curves[J]. Composites Part B: Engineering, 2020, 201: 108344.

[124] Zhai Z, Wang Y, Jiang H. Origami-inspired, on-demand deployable and collapsible mechanical metamaterials with tunable stiffness[J]. Proceedings of the National Academy of Sciences of the United States of America, 2018, 115(9): 2032-2037.

[125] Ming S, Song Z, Li T, et al. The energy absorption of thin-walled tubes designed by origami approach applied to the ends[J]. Materials & Design, 2020, 192: 108725.

[126] Wang B, Zhou C. The imperfection-sensitivity of origami crash boxes[J]. International Journal of Mechanical Sciences, 2017, 121: 58-66.

[127] Wang H, Zhao D, Jin Y, et al. Study of collapsed deformation and energy absorption of polymeric origami-based tubes with viscoelasticity[J]. Thin-Walled Structures, 2019, 144: 106246.

[128] Yang K, Xu S, Zhou S, et al. Multi-objective optimization of multi-cell tubes with origami patterns for energy absorption[J]. Thin-Walled Structures, 2018, 123: 100-113.

[129] Yuan L, Shi H, Ma J, et al. Quasi-static impact of origami crash boxes with various profiles[J]. Thin-Walled Structures, 2019, 141: 435-446.

[130] Gao J, You Z. Origami-inspired Miura-ori honeycombs with a self-locking property[J]. Thin-Walled Structures, 2022, 171: 108806.

[131] Karagiozova D, Zhang J, Chen P, et al. Response of graded Miura-ori metamaterials to quasi-static and dynamic in-plane compression[J]. Journal of Aerospace Engineering, 2022, 35(4): 04022035.

[132] Ma J, Song J, Chen Y. An origami-inspired structure with graded stiffness[J]. International Journal of Mechanical Sciences, 2018, 136: 134-142.

[133] Li Z, Yang Q, Fang R, et al. Origami metamaterial with two-stage programmable compressive strength under quasi-static loading[J]. International Journal of Mechanical Sciences, 2021, 189: 105987.

[134] De Waal L, Lu G, Zhang J, et al. Dynamic behaviour of graded origami honeycomb[J]. International Journal of Impact Engineering, 2021, 157: 103976.

[135] Ye H, Liu Q, Cheng J, et al. Multimaterial 3D printed self-locking thick-panel origami metamaterials[J]. Nature Communications, 2023, 14: 1607.

[136] Jiang W, Yin G, Xie L, et al. Multifunctional 3D lattice metamaterials for vibration mitigation and energy absorption[J]. International Journal of Mechanical Sciences, 2022, 233: 107678.

[137] Zhang L, Bai Z, Chen Y. Dual-functional hierarchical mechanical metamaterial for vibration insulation and energy absorption[J]. Engineering Structures, 2022, 271: 114916.

[138] Han S, Han Q, Li C. Muiltifunctionality-driven customization of sandwich origami-based topological metamaterials with mechanical robustness[J]. Composites Communications, 2025, 54: 102250.

[139] Feng J, Qiao J, Xu Q, et al. Accelerated design of acoustic-mechanical multifunctional metamaterials via neural network[J]. International Journal of Mechanical Sciences, 2025, 287: 109920.

[140] Liu W, Wu L, Sun J, et al. Tunable multifunctional metamaterial sandwich panel with quasi-zero stiffness lattice cores: Load-bearing, energy absorption, and vibration isolation[J]. Advanced Materials Technologies, 2024, 9(4): 2301586.

[141] Wang J X, Liu X, Yang Q S, et al. A novel programmable composite metamaterial with tunable Poisson’s ratio and bandgap based on multi-stable switching[J]. Composites Science and Technology, 2022, 219: 109245.

[142] Montgomery S M, Wu S, Kuang X, et al. Magneto-mechanical metamaterials with widely tunable mechanical properties and acoustic bandgaps[J]. Advanced Functional Materials, 2021, 31(3): 2005319.

[143] Li Z, Li X, Wang Z, et al. Multifunctional sound-absorbing and mechanical metamaterials via a decoupled mechanism design approach[J]. Materials Horizons, 2022, 10: 75-87.

[144] Li X, Yu X, Zhao M, et al. Multi-level bioinspired microlattice with broadband sound-absorption capabilities and deformation-tolerant compressive response[J].

Advanced Functional Materials, 2023, 33(2): 2210160.

[145] Li Z, Wang X, Zeng K, et al. Unprecedented mechanical wave energy absorption observed in multifunctional bioinspired architected metamaterials[J]. NPG Asia Materials, 2024, 16(45): 1-14.

[146] Pei H, Yang H, Zhang N, et al. Moth-wing-inspired multifunctional metamaterials[J]. Advanced Materials, 2025, 38(9): e15350.

[147] Cervantes-Sánchez J J, Medellín-Castillo H I. A robust classification scheme for spherical 4R linkages[J]. Mechanism and Machine Theory, 2002, 37(10): 1145-1163.

[148] Evans T A, Lang R J, Magleby S P, et al. Rigidly foldable origami gadgets and tessellations[J]. Royal Society Open Science, 2015, 2(9): 150067.

[149] Zhou X, Zhang L, Zhang H, et al. 3D cellular models with negative compressibility through the wine-rack-type mechanism[J]. Physica Status Solidi (b), 2016, 253(10): 1977-1993.

[150] Dudek K K, Attard D, Caruana-Gauci R, et al. Unimode metamaterials exhibiting negative linear compressibility and negative thermal expansion[J]. Smart Materials and Structures, 2016, 25(2): 025009.

[151] Caruana-Gauci R, Degabriele E P, Attard D, et al. Auxetic metamaterials inspired from wine-racks[J]. Journal of Materials Science, 2018, 53(7): 5079-5091.

[152] Thornton P H. Energy absorption in composite structures[J]. Journal of Composite Materials, 1979, 13(3): 247-262.

[153] Zhu H, Chen S, Shen T, et al. CFRP origami metamaterial with tunable buckling loads: A numerical study[J]. Materials, 2021, 14(4): 917.

[154] Li S, Wang K W. Fluidic origami: A plant-inspired adaptive structure with shape morphing and stiffness tuning[J]. Smart Materials and Structures, 2015, 24(10): 105031.

[155] Fang H, Li S, Wang K W. Self-locking degree-4 vertex origami structures[J]. Proceedings of the Royal Society A: Mathematical, Physical and Engineering Sciences, 2016, 472(2195): 20160682.

[156] Elford D P, Chalmers L, Kusmartsev F V, et al. Matryoshka locally resonant sonic crystal[J]. Journal of the Acoustical Society of America, 2011, 130(5): 2746-2755.

[157] Hartmann F, Zotemantel R. The direct boundary element method in plate bending[J]. International Journal for Numerical Methods in Engineering, 1986,

23(11): 2049-2069.

[158] Liu K, Li P, Wang Z. Buckling-regulated origami materials with synergy of deployable and undeployable features[J]. International Journal of Mechanical Sciences, 2023, 247: 108167.

[159] Zhang X, Zhang H. Theoretical and numerical investigation on the crush resistance of rhombic and kagome honeycombs[J]. Composite Structures, 2013, 96: 143-152.

[160] Santosa S P, Wierzbicki T, Hanssen A G, et al. Experimental and numerical studies of foam-filled sections[J]. International Journal of Impact Engineering, 2000, 24(5): 509-534.

[161] Yu X, Zhou J, Liang H, et al. Mechanical metamaterials associated with stiffness, rigidity and compressibility: A brief review[J]. Progress in Materials Science, 2018, 94: 114-173.

[162] Gümrük R, Mines R A W. Compressive behaviour of stainless steel micro-lattice structures[J]. International Journal of Mechanical Sciences, 2013, 68: 125-139.

[163] Fan Y, Shen H S. Non-symmetric stiffness of origami-graphene metamaterial plates[J]. Composite Structures, 2022, 297: 115974.

[164] Wierzbicki T, Abramowicz W. On the crushing mechanics of thin-walled structures[J]. Journal of Applied Mechanics, 1983, 50(4a): 727-734.

[165] Abramowicz W, Jones N. Dynamic progressive buckling of circular and square tubes[J]. International Journal of Impact Engineering, 1986, 4(4): 243-270.

[166] Mao Y, Yu K, Isakov M S, et al. Sequential self-folding structures by 3D printed digital shape memory polymers[J]. Scientific reports, 2015, 5: 13616.

[167] Zaghloul A, Bone G M. 3D shrinking for rapid fabrication of origami-inspired semi-soft pneumatic actuators[J]. IEEE Access, 2020, 8: 191330-191340.

[168] Kuang X, Roach D J, Wu J, et al. Advances in 4D printing: materials and applications[J]. Advanced Functional Materials, 2019, 29(2): 1805290.

[169] Momeni F, Liu X, Ni J. A review of 4D printing[J]. Materials & design, 2017, 122: 42-79.

[170] Kim W, Byun J, Kim J K, et al. Bioinspired dual-morphing stretchable origami[J]. Science robotics, 2019, 4(36): eaay3493.

[171] Wang H, Zhao D, Jin Y, et al. Modulation of multi-directional auxeticity in hybrid origami metamaterials[J]. Applied Materials Today, 2020, 20: 100715.

[172] Zhang L, Pan F, Ma Y, et al. Bistable reconfigurable origami metamaterials with high load-bearing and low state-switching forces[J]. Extreme Mechanics Letters, 2023, 63: 102064.

[173] Yamaguchi K, Miyazawa Y, Yasuda H, et al. Post-fabrication tuning of origami-inspired mechanical metamaterials based on Tachi-Miura Polyhedron[J]. Materials & Design, 2023, 233: 112170.

[174] Liu K, Pratapa P P, Misseroni D, et al. Triclinic metamaterials by tristable origami with reprogrammable frustration[J]. Advanced Materials, 2022, 34(43): 2107998.

[175] Wang Y, Guo J, Fang Y, et al. Ultralight metamaterial for sound absorption based on Miura-Ori tessellation structures[J]. Advanced Engineering Materials, 2021, 23(12): 2100563.

[176] Wang X Q, Chan K H, Cheng Y, et al. Somatosensory, light-driven, thin-film robots capable of integrated perception and motility[J]. Advanced Materials, 2020, 32(21): 2000351.

Appendix

A. Dihedral angle variations of C3 at $\varphi_1=\varphi_2$ when compressing in *x* and *z* directions

The dihedral angle variations of the symmetric C3 configuration at $\varphi_1=\varphi_2$ under compressive deformation were analyzed (Fig. A1). When compressed along the *x* direction (black traces), the dihedral angles φ_1 and φ_3 exhibit monotonous expansion from 109.47° to 180°, while angles φ_2 and φ_4 contract from 109.47° to 0°. The tetrahedral angles $\theta_{1\text{-}4}$ and $\delta_{1\text{-}4}$ also demonstrate symmetric variations spanning 70.53° to 180° and 70.53° to 0°, respectively. Conversely, under *z* direction compression (blue traces), the transformation is directionally inverted: φ_1 and φ_3 compress from 109.47° to 0°, while φ_2 and φ_4 expand to 180°, with $\theta_{1\text{-}4}$ and $\delta_{1\text{-}4}$ traversing inverted ranges (0°-70.53° and 180°-70.53° respectively). Notably, the angular disparities for both compression directions exhibit quantitative equivalence in both total angular changes and the initial tangent slopes at $\varphi_1=\varphi_2$. This symmetry results in identical SEA and stiffness across the *x* and *z* directions according to theoretical analysis.

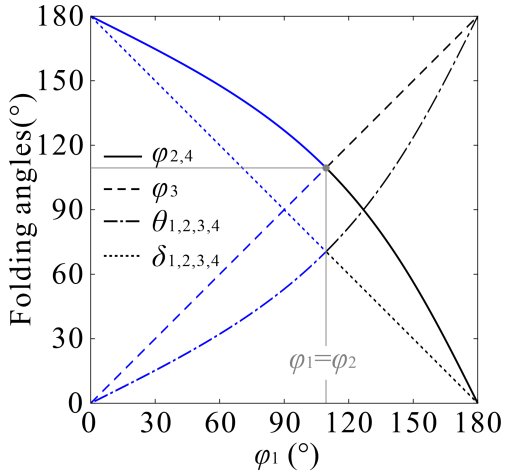

$$3\times(\varphi_1+\varphi_3)(109.47°\rightarrow180°)+3\times(\varphi_2+\varphi_4)(109.47°\rightarrow0°)$$
$$+4\times\theta_{1\text{-}4}(70.53°\rightarrow180°)+4\times\delta_{1\text{-}4}(70.53°\rightarrow0°)$$

$$\|$$

$$3\times(\varphi_2+\varphi_4)(109.47°\rightarrow180°)+3\times(\varphi_1+\varphi_3)(109.47°\rightarrow0°)$$
$$+4\times\delta_{1\text{-}4}(70.53°\rightarrow180°)+4\times\theta_{1\text{-}4}(70.53°\rightarrow0°)$$

Fig. A1 Dihedral angle variations of C3 at $\varphi_1=\varphi_2$ when compressing in the *x* (black) and *z* directions (blue).

B. Full band structures of the double-tubular origami metamaterial

The full band structures discussed in the main text are systematically presented in this section (Figs. B1-B5). Since no continuous propagation pathway exists in the *y* direction of the double-tubular origami metamaterial, the band structures along the *y* direction are not presented here.

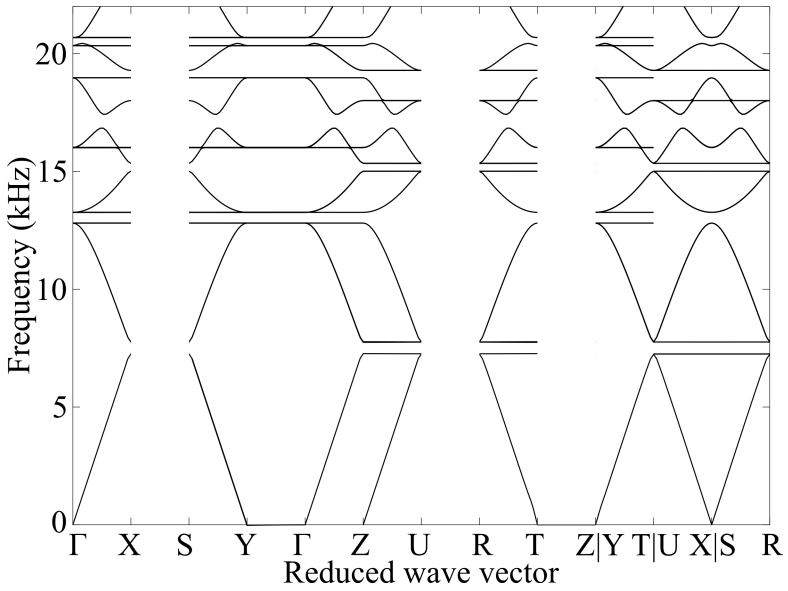

Fig. B1 Band structures of MC1 (corresponding to Fig. 4-15(a) in the main text) with $a_1=b_2=15$mm, $a_2=b_1=21.93$mm, $\alpha_1=\alpha_3=70°$, $\alpha_2=76.47°$, $\alpha_4=60°$, $\varphi_{1i}=119.16°$.

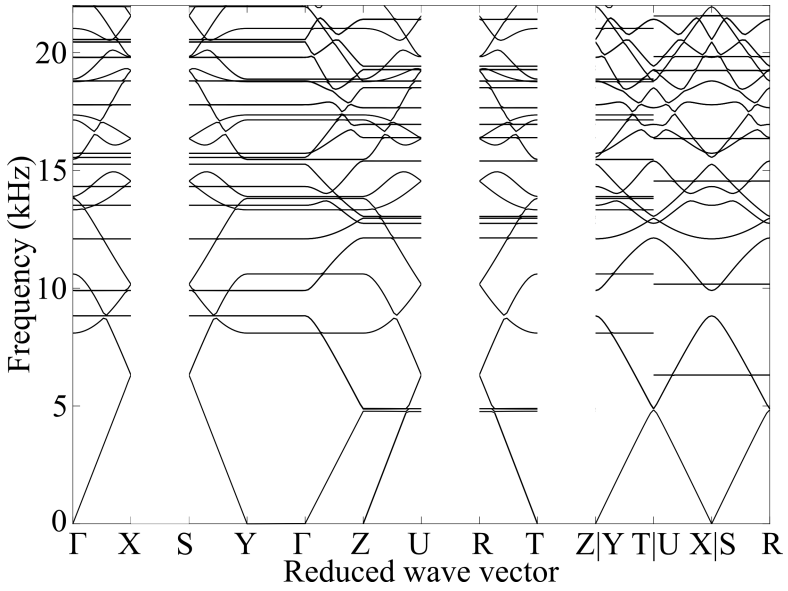

Fig. B2 Band structures of MC2 (corresponding to Fig. 4-15(b) in the main text) with $a_1=a_2=b_2=15$mm, $b_1=21.93$mm, $\alpha_1=\alpha_2=70°$, $\alpha_3=\alpha_4=60°$, $\varphi_{1i}=119.16°$.

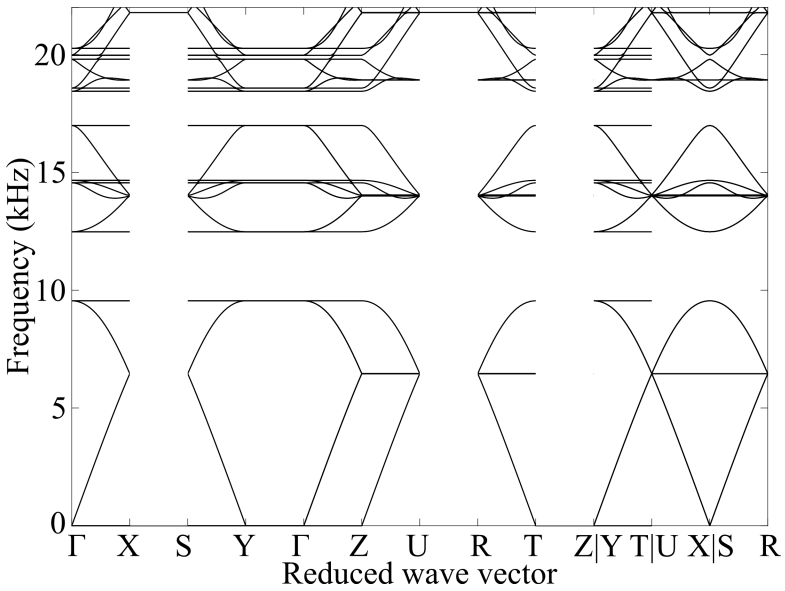

Fig. B3 Band structures of MC3 (corresponding to Fig. 4-15(c) in the main text) with $a_1=a_2=b_1=b_2$=15mm, α ($\alpha_1=\alpha_2=\alpha_3=\alpha_4$)=60°, φ_{1i} =109.47°.

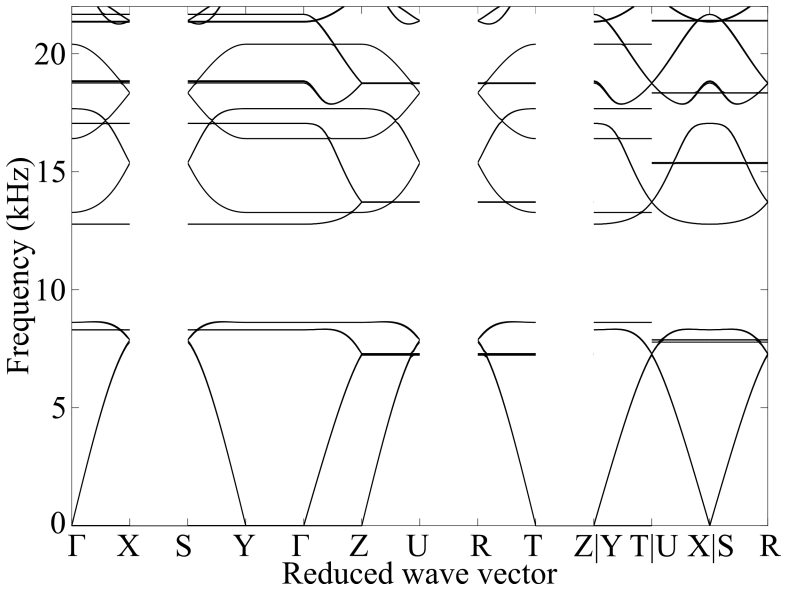

Fig. B4 Band structures of MC3 (corresponding to Fig. 4-18 left in the main text) with $a_1=a_2=b_1=b_2$=15mm, α ($\alpha_1=\alpha_2=\alpha_3=\alpha_4$)=40°, φ_{1i}=76.11°.

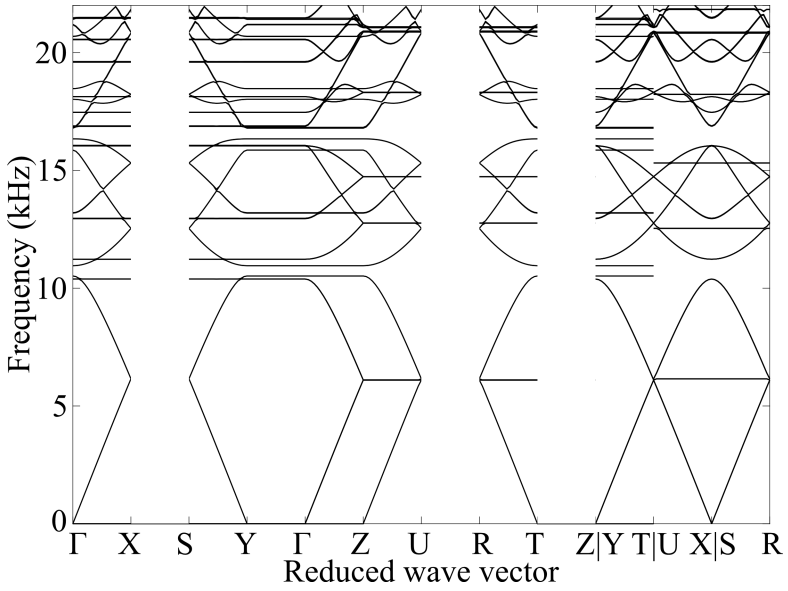

Fig. B5 Band structures of MC3 (corresponding to Fig. 4-18 right in the main text) with a_1=a_2=b_1=b_2=15mm, α (α_1=α_2=α_3=α_4)=70°, φ_{1i}=115.49°.

C. Dihedral angle variations of C3 at transposed states when compressing in *x* and *z* directions

When geometrically transposed configurations (Fig. C1, configurations $1^{\#}$/$5^{\#}$ and $2^{\#}$/$4^{\#}$) undergo directional compression, their dihedral angles display complementary evolution patterns along the *x* (black traces) and *z* directions (blue traces). For configuration $1^{\#}$ (Fig. C1(i)), compression in the *x* direction drives monotonic expansion of dihedral angles φ_1 and φ_3 from 50.67° to 180° with concurrent contraction of φ_2 and φ_4 from 146.15° to 0°, while dihedral angles $\theta_{1\text{-}4}$ and $\delta_{1\text{-}4}$ span 33.85°-180° and 129.33°-0°, respectively. Conversely, compression in the *z* direction inverts these trends: φ_1 and φ_3 contract to 0° as φ_2 and φ_4 expand to 180°, accompanied by reversed dihedral angle variations ($\theta_{1\text{-}4}$: 33.85°→0°; $\delta_{1\text{-}4}$: 129.33°→180°). Configuration $5^{\#}$ (Fig. C1(ii)) exhibits transposed angular responses: its compression in the *x* direction exhibits trends identical to those of $1^{\#}$ under compression in the *z* direction (φ_1 and φ_3: 146.15°→0°; φ_2 and φ_4: 50.67°→180°; $\theta_{1\text{-}4}$ and $\delta_{1\text{-}4}$ mirroring $1^{\#}$'s $\delta_{1\text{-}4}$ and $\theta_{1\text{-}4}$ trajectories), while its compression in the *z* direction precisely replicates $1^{\#}$'s compression in the *x* direction behavior. This geometric transposition directly establishes the identical relations k_{x1}=k_{z5}, and SEA_{x1}=SEA_{z5}. Configurations $2^{\#}$ and $4^{\#}$ in Fig. C1(b) demonstrate analogous transposition, resulting in k_{x2}=k_{z4}, and SEA_{x2}=SEA_{z4}.

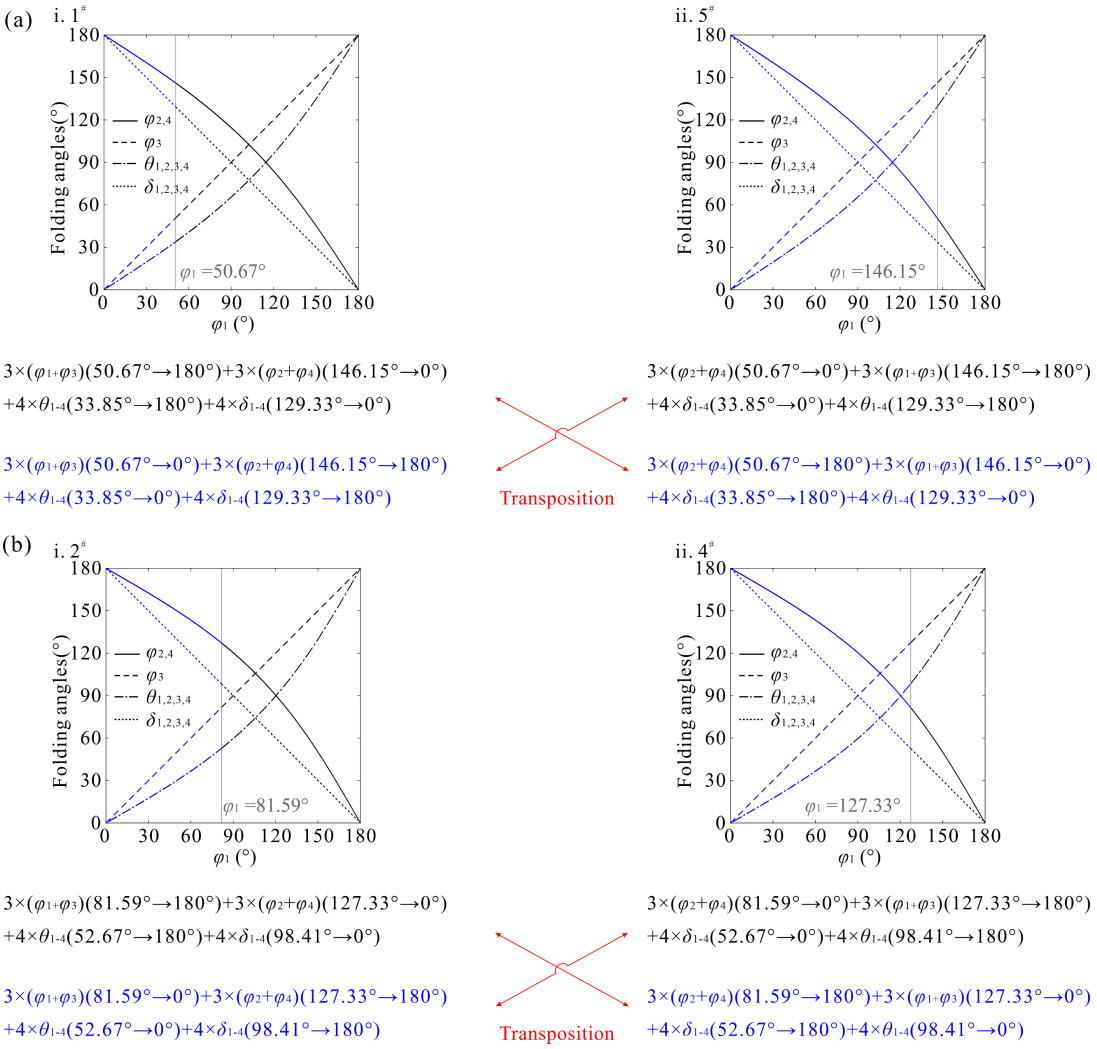

Fig. C1 Dihedral angle variations of C3 at transposed states when compressing in the *x* (black) and *z* directions (blue): (a) Transposed pairs 1# (α=50°, φ_{1i}=50.67°) and 5# (α=50°, φ_{1i}=146.15°); (b) Transposed pairs 2# (α=55°, φ_{1i}=81.59°) and 4# (α=50°, φ_{1i}=127.33°).

D. Stress versus strain curves of the 316L stainless steel

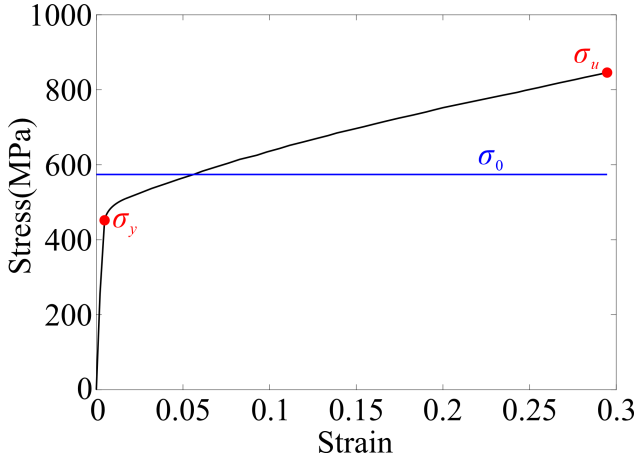

Fig. D1 Stress versus strain curve of 316L stainless steel.

E. Band structures of triple-tubular origami metamaterial

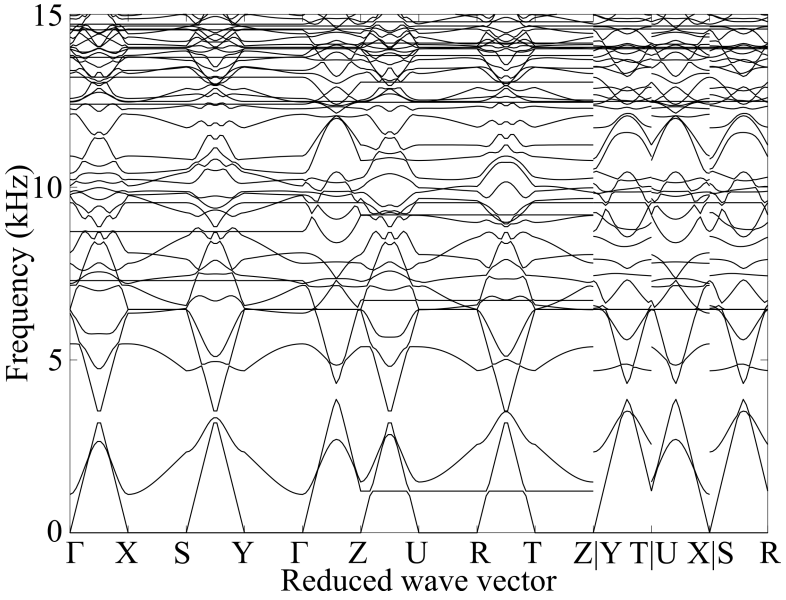

Fig. E1 Band structures of triple-tubular origami metamaterial.

中文大摘要

折纸结构作为一种将二维平面材料通过折叠转化为三维空间结构的艺术形式，近年来已发展成为极具潜力的工程设计方法。其中，管状折纸结构凭借其优异的折展比、独特的折展特性和可定制的截面形状，被广泛应用于可展机构、软体机器人骨架以及能量吸收装置中。伴随超材料概念的不断深化，将管状折纸作为周期性胞元进行三维空间镶嵌，催生了兼具独特运动学行为与超常物理响应的新型折纸超材料。这类结构能通过几何参数与折痕拓扑的编程设计，实现对宏观力学响应与动态波传播的有效操控，为实现结构轻量化与多功能一体化提供了全新的解决方案。因此，探索新型管状折纸超材料的构型综合理论，并揭示其多物理场性能的编程机制，已成为力学、声学及材料科学交叉领域的研究热点。

尽管折纸超材料在工程领域展现出广阔的应用前景，但其构型设计与性能编程仍面临诸多挑战。首先，在构型综合层面，现有的管状折纸多依赖经验设计或特定几何图案（如 Miura-ori 及其变体），截面形状往往局限于传统的平面多边形。这种针对任意空间多边形截面的广义运动学综合理论的缺失，已成为制约管状折纸构型创新的核心瓶颈。因此，利用机构学原理建立基于四折痕顶点的单自由度管状结构通用设计理论，突破平面截面的几何束缚，是实现多样化空间填充与复杂变形模式的关键前提。其次，在性能编程层面，折纸超材料的物理属性不仅取决于连续的几何尺寸（如设计角、边长），更高度依赖于折痕图案的山谷线分布。然而，现有性能编程研究多聚焦于几何参数的连续变化，鲜有从山谷线分布的角度，系统探究其对力学、声学等多物理场特性的决定性影响。

另一方面，尽管折纸超材料以及其他拓扑超材料在力学性能编程方面已经取得了大量研究进展，但现代工程应用对材料的要求正在不断提高，研究重点也正由单一物理性能优化逐步转向多功能集成。进一步地，在超材料从单一功能向多功能集成的跨越中，物理属性间的强耦合效应成为了关键制约因素。传统多功能超材料的设计普遍陷入参数强耦合的困境：由于力学、声学等不同维度的物理特性往往依赖于同一套设计参数，在调整几何构型以优化某一特定性能时，极易引发其他性能的非预期偏移。这种固有的参数依赖性，使得在单一结构中同时实现多物理场性能的精准协同与按需定制变得异常困难。因此，如何打破这种物理性能的固有博弈，通过创新的拓扑构型与机制设计，实现力学与声学性能的独立编程与动态调控，是当前该领域亟待攻克的科学难题。此外，多功能超材料的内涵不仅局限于跨物理场的性能协同，更延伸至单一结构内部多种不同力学响应机制

的集成。针对复杂工程环境中对方向依赖性承载的特殊需求，如何通过微观几何设计在单一结构中集成多种截然不同的变形模式，进而实现高度可编程的各向异性力学响应，也是拓展折纸超材料工程应用维度的重要研究方向。

由于超材料的性能编程和结构变形是高度相关的，对于现有的这些多功能超材料来说，他们的变形是强非线性和不可预测的。相比之下，折纸结构，尤其是刚性折纸，其变形过程与机构运动学之间具有明确而紧密的对应关系，这为建立结构构型、运动学行为与物理性能之间的解析联系提供了可能。基于机构学与力学理论，有望构建连接设计参数、变形模式与功能响应的解析模型，从而为多功能超材料性能的精准设计以及独立编程提供理论基础。

综上所述，系统性地构建新型折纸超材料，并实现其运动学综合与多物理场性能的编程研究，需要完成的核心工作包括：(1) 建立基于四折痕顶点的管状折纸广义运动学综合理论，突破传统平面截面构型的限制，为新型超材料的创新设计提供通用的几何胞元与空间镶嵌策略；(2) 系统探究山谷线分布对超材料力学与声学性能的影响，揭示构型与物理响应之间的关系；(3) 通过性能编程研究，建立设计参数与物理性能之间的非唯一映射关系，实现力学与声学性能的独立编程与动态调控；(4) 设计具备复杂结构变形模式的折纸超材料，在单一结构中集成不同的力学机制，实现高度可编程的多功能各向异性响应。

本文聚焦于折纸超材料的运动学设计与多物理场性能编程，旨在建立一套从构型综合到性能编程的完整理论体系与研究方法。本文首先基于 D-H 矩阵法与空间闭环约束方程，构建了基于四折痕顶点的单自由度管状折纸结构的广义综合框架，推导了具有空间多边形截面管状结构的几何协调条件，并提出了双通路结构的构造方法及其空间镶嵌策略。其次，深入探究了山谷线分布对单通路折纸超材料多物理场性能的影响，建立了空间构型与泊松比、刚度及声学带隙之间的关系。然后，本文提出了一系列在正交方向上具有独特折叠特性的双通路折纸超材料，通过建立设计参数与物理性能的非唯一映射关系，成功实现了力学与声学性能的独立编程与动态调控。最后，本文设计了一种在三个正交方向上具备不同折叠模式折纸超材料，揭示了其在正交方向上的变形机理，实现了正交各向异性的力学响应。本文的主要研究成果为多功能折纸超材料的创新设计与工程应用提供了坚实的理论基础与技术路径。本文主要工作包括以下四部分：

- **基于四折痕顶点的单自由度管状折纸结构运动学综合**

本文第二章建立了一套用于四折痕顶点构成的单自由度管状折纸结构的通用运动学综合框架。首先，利用 D-H 矩阵与空间闭环约束相结合的方法，对由

四个四折痕顶点组成的基本闭环组件进行了运动学建模。推导出的显式协调性条件证明了刚性可折叠管状结构的截面设计不必局限于平面多边形，而是可以扩展至空间多边形。在此基础上，本章将运动学分析推广至由多个四折痕顶点组成的广义管状折纸结构。通过将复杂的多顶点闭环分解为离散的几何链，建立了由多个四折痕顶点组成的折纸管状结构协调性条件。

为了进一步拓展设计空间，本章提出了一种基于约束几何耦合的双通路折纸结构构建方法。该方法以单管结构为基础单元，利用其边界接口作为连杆基础，耦合具有特定空间方向的次级折纸单元，从而合成了具有单自由度运动特性的双通路折纸单元。针对广义双通路单元缺乏固有对称性的问题，制定了一种特定的旋转镶嵌策略。通过对原始单元进行空间旋转生成互补配置，并遵循严格的连接规则，实现了双通路折纸单元在三维空间中的系统化镶嵌，得到了三维折纸超材料。

本章建立的广义运动学框架有效消除了传统设计中对共面截面的假设限制，极大地扩展了刚性可折叠管状折纸结构的可行设计空间。所提出的从基本四顶点回路到广义多顶点链的解析方法，以及后续的双通路结构构造与镶嵌策略，为设计具有多功能空间配置的复杂折纸超材料提供了坚实的理论基础和系统的方法论。

- **基于山谷线分布的单通路折纸超材料力学与声学性能编程**

本文第三章致力于通过改变山谷折痕的分配方式，对基于 double-corrugated 顶点的单通路（single-tubular）折纸超材料的力学和声学性能进行编程设计。首先，基于上一章的协调性条件，构造出了四种具有不同山谷线分布的单自由度刚性可折叠折纸单元（命名为 DC-1 至 DC-4）。几何与运动学分析表明，尽管山谷线分布不同，但 DC-1 与 DC-2、DC-3 与 DC-4 分别具有相同的几何尺寸关系和泊松比。基于这些单元的运动学等价性，本章不仅构建了四种均一超材料，还通过在同一层内组合具有相同泊松比的不同单元（如 DC-1 与 DC-2 组合），构建了多种混合折纸超材料。

为了深入探究山谷线分布对力学性能的影响，本章采用了有限元模拟与实验相结合的方法。对均一超材料的研究发现，在刚性折叠方向上，具有相同泊松比的超材料表现出相似的变形模式和力学响应；其归一化刚度主要由折叠角度的变化率决定，而比吸能则主要取决于折叠角度的变化总量。对于混合超材料，其在 x 和 y 方向的力学性能与均匀超材料相似，但在 z 方向压缩时表现出独特的阶梯状应力响应，且归一化刚度出现急剧下降。这种特殊的力学行为归因于混合配置

中不同单元在变形初期的参与程度不同，从而证实了通过操纵山谷线分布可以实现对超材料力学性能的有效编程。

在声学性能方面，本章系统揭示了拓扑构型与空间组合方式对声波传播的决定性影响。针对均一单通路超材料，研究发现特定山谷线分布（如 DC-1 和 DC-3）具备带隙，能够有效阻挡声波传播，而 DC-2 和 DC-4 则表现为通带。参数化分析进一步表明，改变折叠角度不仅能显著调节现有带隙的频率范围与带宽，还能在特定几何状态下为原本无带隙的构型开启带隙。在此基础上，通过在空间上组合具有不同带隙特性的子区域，混合超材料成功打破了波传播的空间对称性，使其能够根据入射频率实现声波的全局透射、全局阻断以及沿特定物理通道的选择性声波通路。

本文第三章提出的基于山谷线配置的性能编程策略，有效拓展了单通路折纸超材料的多功能设计空间。所阐明的山谷线拓扑排布与宏观力学及声学特性间的关系，确立了通过离散折痕配置实现多物理场性能编程的新策略。

- **具有独立可编程力学及声学特性的双通路折纸超材料**

本文第四章提出了一类具有独立可编程与动态可调控特性的多功能双通路（double-tubular）折纸超材料。首先，基于第二章的理论基础，构建了在 x 和 z 两个正交方向上具有管状通道的折纸单元。运用刚性折纸理论，详细分析了单元的几何参数与折叠变化规律。根据几何参数的协调性条件，将该类胞元划分为三种具有不同折叠行为的构型：非平整折叠型（C1）、单向平整折叠型（C2）以及双向平整折叠型（C3）。特别地，C3 型胞元被证明具有独特的双向平折能力和“几何转置”特性，即在两个正交方向（x 轴与 z 轴）上可通过改变折叠状态实现几何对称性或互换性，这为后续实现多物理场性能的独立编程提供了关键的运动学基础。

针对具有优异运动特性的 C3 型超材料，分别探究了其力学与声学特性并进行了深入的参数化分析。在力学方面，建立了理论模型，推导了准静态压缩下的刚度与比吸能解析公式，并通过有限元仿真与实验验证了该理论模型的准确性；参数化分析表明，初始折叠角与扇形角是决定力学响应的关键因素。在声学方面，采用有限元仿真计算了声学能带结构及传输损失，并进行了实验验证。声学参数化分析揭示了晶格几何对称性对带隙形成的决定性作用：正交方向几何尺寸的一致性有利于最大化带隙宽度，而几何非对称性则会导致带隙的破缺或窄化。

基于上述参数化分析结果，本章利用物理性能与几何参数之间存在的非唯一映射特性，实现了力学与声学性能的独立编程。通过在设计域内搜寻等性能路径，

不仅能够在保持力学刚度恒定的前提下，使带隙的频率范围发生大范围调节（变化幅度达 10.4 倍）；反之，亦可在维持声学带隙频率范围不变的约束下，显著调节刚度（变化幅度达 16.9 倍）与比吸能（变化幅度达 5.4 倍）。此外，为了进一步验证超材料的后制造可调性，采用热塑性聚氨酯制备了实体样机，并利用热机械加载实现了超材料几何构型的重构与性能的调控。

本文第四章提出了一种同时具有力学和声学特性的双通路折纸超材料，利用设计参数与物理性能之间的非唯一映射关系实现了两种性能的独立编程，结合热塑性材料实现了超材料的构型重构和性能调控。为开发新一代集能量吸收、噪声抑制及动态适应能力于一体的智能工程材料开辟了新途径。

- **具有可编程正交各向异性力学性能的三通路折纸超材料**

本文第五章提出了一种具有显著正交各向异性力学性能的三通路（triple-tubular）折纸超材料。首先，通过组合双通路折纸单元与矩形面板的几何构建策略，设计了具有单自由度特性的三通路基本折纸胞元。利用运动学建模，推导了描述胞元折叠状态的显式方程。通过在三维空间中对胞元进行周期性阵列，构建了三维折纸超材料。运动学分析表明，该超材料在三个正交方向具有截然不同的运动特性：在 *x* 方向上，结构遵循刚性折纸模式，可实现完全平折；在 *y* 方向上，其几何尺寸在折展过程中变化微小；而在 *z* 方向上，由于矩形面板引入的几何约束，结构在折叠过程中会产生自锁现象，导致无法完全折平。

针对超材料在三个正交方向上迥异的变形机制，分别建立了相应的力学理论预测模型与数值分析框架。对于 *x* 方向，基于刚性折纸假设，认为塑性变形主要集中于折痕处，利用塑性铰理论与能量平衡方程，推导了准静态压缩下的力学响应与比吸能解析公式。对于 *z* 方向，揭示了其独特的两阶段变形模式，即初始的刚性折叠阶段与随后的面板屈曲阶段；为此，结合刚性折纸理论与蜂窝结构平均压溃力理论，构建了分阶段的力学解析模型。利用金属 3D 打印技术制备了 316L 不锈钢实验样机，并通过准静态压缩实验与有限元仿真验证了理论模型的准确性。研究结果表明，该超材料在 *x* 方向表现为低刚度与低吸能的刚性折叠模式；在 *y* 方向表现为高刚度与高吸能的屈曲模式，其比吸能约为 *x* 方向的三倍；而在 *z* 方向则呈现出先折叠后屈曲的梯度力学响应特征。

为了实现超材料力学性能的可编程设计，系统地探究了设计参数以及初始折叠角对三个方向力学性能的影响规律。参数化分析表明，设计角与初始折叠角是影响 *x* 与 *z* 方向力学性能的关键因素。值得注意的是，这两个方向的力学性能随参数变化往往呈现出相反的演化趋势：例如，增大设计角会导致 *x* 方向的平台应

力增加，但会降低 z 方向的屈曲强度。此外，边长比参数虽然对 x 方向的刚性折叠行为影响有限，但显著改变了 z 方向的自锁应变点及随后的屈曲行为。基于这些非线性的参数映射关系，通过调整几何设计参数与初始折叠状态，可以实现对该折纸超材料在三个正交方向上刚度与吸能特性的性能编程。

本章所提出的三通路折纸超材料突破了传统结构难以在单一构型中同时集成多种截然不同力学行为的限制。通过巧妙融合刚性折叠与结构屈曲两种变形机制，该超材料成功实现了在不同加载方向上刚度特性从低到高的切换。这种独特的力学特性，使其在多功能抗冲击防护、定向能量吸收以及自适应工程结构设计等领域具有重要的应用潜力，为折纸超材料的功能化设计提供了新的技术路径。

- **结论与展望**

本文着眼于折纸运动学与多功能超材料设计的交叉融合，建立了适用于管状折纸结构的通用运动学综合理论框架，并基于该框架提出了一系列具有独特折叠行为的创新折纸超材料。通过系统探究几何构型与多物理场性能之间的映射机制，实现了力学与声学性能的独立编程与动态调控，并成功开发出具有可编程各向异性特性的新型超材料。本研究不仅为折纸超材料的构型综合与功能化设计奠定了强有力的理论基础，也为其实际工程应用的发展提供了有效的技术支撑。

此外，本文的研究工作还可以在如下几方面进行进一步的深入研究：

(1) 本文目前建立的运动学综合理论主要面向带有可平折相关约束的四折痕顶点。未来可进一步将该理论框架推广至一般化四折痕顶点，从而拓展管状折纸结构的构型设计空间，丰富折纸超材料的构型设计方法。

(2) 本文在双通路及三通路折纸超材料构造中主要采用均匀镶嵌策略。未来可在单元层面引入几何渐变设计，例如沿镶嵌方向逐渐改变设计角、折叠角或单元类型，以实现更加丰富的性能编程。

(3) 本文的声学仿真采用刚性壁面假设，未考虑壁面柔性及流固耦合效应。后续研究可进一步引入流固耦合分析，以更全面、更准确地揭示折纸超材料的声学响应规律。

(4) 针对折纸超材料的动态调控，未来可进一步探索折纸架构与智能材料的融合。通过引入光响应、热响应、磁响应等刺激响应材料，有望实现结构构型的主动重构，并赋予其更丰富的多物理场性能。

(5) 除目前常用的 3D 打印方法外，未来还应进一步探索传统制造技术在折纸超材料批量化制备中的可行性，从而为其工程化应用提供支撑。

关键词： 刚性折纸；折纸超材料；管状折纸结构；多物理场性能编程

Publications and Research Projects

Journal Papers:

[1] Li M#, Ma J#, Tang X-L, Wang Y-F*, Chen Y*. Double-tubular origami metamaterials with independently programmable and tunable mechanical and acoustic properties[J]. Composites Part B: Engineering, 2025, 306: 112804. (Co-author)

[2] Li M#, Chen H#, Ma J*, Chen Y*. An origami metamaterial with distinct mechanical properties in three orthotropic directions[J]. International Journal of Mechanical Sciences, 2024, 283: 109713. (Co-author)

[3] Li M, Peng R, Ma J*, Chen Y*. Programming the mechanical properties of double-corrugated metamaterials by varying mountain-valley assignments[J]. Philosophical Transactions of the Royal Society A: Mathematical, Physical and Engineering Sciences, 2024, 382(2283): 20240004.

[4] Li M, Zhou Z, Hao B, Chen F, Chen Y, Ma J*. Design and deformation analysis of an inflatable metallic cylinder based on the Kresling origami pattern[J]. Thin-Walled Structures, 2023, 188: 110859.

[5] Li M, Gu Y, Ma J, Chen Y*. Kinematic synthesis of single-DOF tubular origami structures composed of 4-crease vertices[J]. Mechanism and Machine Theory, 2026. (Accept)

Patents:

[1] 马家耀、李梦岳、陈厚华、陈焱，一种可折展与可承载的折纸结构，授权号：ZL202311085740.5，发明专利，授权公告日：2023.12.08.

[2] 陈焱、李梦岳、马家耀、周志勇、余晨帆、郝宝新、高峰、李小琪、许久远、鲍煊，一种基于四个球面四连杆机构的单自由度可折展管状结构，授权号：ZL202210163731.2，发明专利，授权公告日：2022.10.18.

Research Projects Participated in:

[1] 国家自然科学基金委员会，杰出青年基金项目，机构运动学与折展结构，项

目编号 51825503.

[2] 国家自然科学基金委员会，优秀青年基金项目，52422502，折纸超材料，项目编号 52422502.

[3] 国家自然科学基金委员会，重点项目，可编程超材料的构建理论与性能调控策略研究，项目编号 52035008.

[4] 国家重点研发计划，集成微芯片的高密度感驱控一体化智能无线微米机器人，项目编号 2024YFB4707800.

Acknowledgments

First and foremost, I would like to express my deepest gratitude to my supervisors, Prof. Yan Chen and Prof. Jiayao Ma, for their visionary guidance, rigorous scholarly standards, and unwavering patience throughout my doctoral study. Their profound insights not only illuminated my research path but also profoundly shaped my development as an independent researcher. I would also like to sincerely thank Prof. Yan-Feng Wang for his valuable support, insightful suggestions, and continuous encouragement, which have greatly benefited both my research and academic growth.

My sincere thanks also go to all current and former members of the MSL laboratory for making research a truly collaborative endeavor. I am deeply thankful to Dr. Xiao Zhang, Dr. Yuanqing Gu, Dr. Weiqi Liu, and Dr. Tianshu Wang for their insightful discussions and guidance. To Mr. Zhenhao Jia, Mr. Zhibo Wei, Ms. Kaili Xi, Mr. Sibo Chai, Mr. Yuehao Zhang, Mr. Chuhan Xu, Mr. Chenhao Zhang, and Ms. Yuening Du, thank you for your daily assistance and the vibrant atmosphere we shared; I will always cherish our late-night discussions. I also acknowledge the graduated alumni: Dr. Weilin Lv, Dr. Xiaochen Yang, Mr. Xinfeng Sun, Mr. Jinrui Yu, Mr. Lei Fu, and Mr. Houhua Chen, whose shared experiences and legacy of excellence greatly benefited my work.

Furthermore, I am deeply grateful to my close friends outside the laboratory: Mr. Jiawei Cheng, Mr. Zhenyang Chu, Mr. Hongwei Gu, Mr. Xinrui Liu, Mr. Wei Wang, Mr. Fan Zhang, Mr. Yan Zhang, and Mr. Qi Zong. Thank you for your unwavering companionship. Your willingness to listen during bottlenecks and celebrate my triumphs provided the emotional anchor I needed to keep moving forward.

Finally, I dedicate my most heartfelt gratitude to my family. To my parents and brother: your decades of hard work, silent sacrifices, and unconditional love have built the solid foundation of my life. You have always been my safe harbor, and this milestone belongs as much to you as it does to me. The conclusion of my Ph.D. is merely the starting point of a new chapter. Carrying this gratitude, I will continue to march forward with reverence for science and a passion for life.